University of Glasgow | James Watt School of Engineering

Analytical and Numerical investigation of heat and mass transport in catalytic microreactors

Graeme Robert Hunt

Submitted in fulfilment of the requirements for the Degree of Doctor of Philosophy in Mechanical Engineering at the University of Glasgow

James Watt School of Engineering

College of Science and Engineering

University of Glasgow

September 2019

Abstract

Microreactors for chemical synthesis and combustion have attracted increased attention in recent years. Due to the high degree of thermal control exhibited by microreactors, exothermic catalytic activity features heavily in these devices and thus advective-diffusive transport is of key importance in their analyses.

An analytical study of the transport phenomena in a single microchannel microreactor filled with a porous medium is presented, first as a one-dimensional, then expanded to a two-dimensional model with catalytic activity. The systems under investigation include fluid and porous solid phases inside the microchannel under local thermal non-equilibrium (LTNE), in addition to the enclosing structure of thick walls subject to distinct thermal loads. The thermal diffusion of mass, viscous dissipation of the fluid flow is examined for both a heterogeneous catalyst placed on the channel wall and for a homogeneous reaction process. The axial and transverse variations of heat and mass transfer processes are considered to provide two-dimensional solutions of both the temperature and concentration fields. These are then used to calculate the local and total entropy generation within the system. A novel extension of an existing LTNE model capable of taking into account the enclosing structure as well as the porous solid and fluid phases is presented. The thickness of this enclosing structure is shown to have a major influence on heat and mass transport within the system, particularly the Nusselt number. Irreversibilities in the system are found to be dominated by the mass transfer contributions and the influence of the Soret effect as well as the Damköhler number.

A numerical investigation is undertaken to examine the effect of hydrodynamics upon the activity of a heterogeneous catalyst. Three corrugated wall channel configurations with varying phase difference between upper and lower walls were generated. Low Reynolds number flows of fuel lean methane in air were catalytically combusted over platinum in the numerical model. Hydrodynamic reflux features were observed in the out of phase cases. Coinciding with these zones, the site surface concentration of carbon dioxide was observed to vary significantly as compared to the base case.

The extension of the LTNE model significantly increases the capability of modelling the interface between thick walls and a porous medium under thermal load, permitting more accurate modelling of microreactors. The effect of the reflux feature on the surface site fraction of product for the corrugated channels reveals the complex interaction between hydrodynamics and catalytic activity.

Table of Contents

List of Tables

List of Figures

Acknowledgement

There are many people who are deserving of thanks for aiding me in the completion of this PhD. Firstly, I would like to thank EPSRC and the University of Glasgow for seeing fit to grant me the scholarship that made it possible for me to enter into the PhD programme in the first place.

I would like to thank my supervisor, Dr Nader Karimi for his guidance, insight and patience during the course of this project. I am grateful for his encouragement, guidance and criticism where necessary to improve my work.

Additionally, I thank all the other members of academic staff, IT staff, technical and teaching staff at the School of Engineering who have enriched my time here in countless ways.

Thanks are also due to the people with whom I have shared an office over these past four years. Their support and camaraderie throughout the ups and downs of the progress, and occasionally lack thereof, of this project have been invaluable.

For their support and belief in me during this process, I thank my family. My father and mother for their pride in my work and my sister, Shona, for her wit and humour. Finally, I would like to thank my wife, Alice, who never doubted me even when I doubted myself throughout the course of this degree programme. She has patiently endured my frustrations and shared my happiness when things worked well. I am deeply indebted to her for her constant encouragement.

Author's Declaration

Part of the work presented in this thesis has been published in the following articles:

Hunt, G., Karimi, N., Yadollahi, B. and Torabi, M. (2019) The effects of exothermic catalytic reactions upon combined transport of heat and mass in porous microreactors. International Journal of Heat and Mass Transfer, 134, pp. 1227-1249. (doi:10.1016/j.ijheatmasstransfer.2019.02.015)

Hunt, G., Karimi, N. and Torabi, M. (2018) Two-dimensional analytical investigation of coupled heat and mass transfer and entropy generation in a porous, catalytic microreactor. International Journal of Heat and Mass Transfer, 119, pp. 372-391. (doi:10.1016/j.ijheatmasstransfer.2017.11.118)

Hunt, G., Torabi, M., Govone, L., Karimi, N. and Mehdizadeh, A. (2018) Two-dimensional heat and mass transfer and thermodynamic analyses of porous microreactors with Soret and thermal radiation effects: An analytical approach. Chemical Engineering and Processing: Process Intensification, 126, pp. 190-205. (doi:10.1016/j.cep.2018.02.025)

Hunt, G., Karimi, N. and Torabi, M. (2017) Analytical investigation of heat transfer and classical entropy generation in microreactors - the influences of exothermicity and asymmetry. Applied Thermal Engineering, 119, pp. 403-424. (doi:10.1016/j.applthermaleng.2017.03.057)

I declare that, except when explicit reference is made to the contribution of others, this thesis is my own work and it has not been submitted for any other degree at the University of Glasgow or any other institution.

Signed …….

Graeme Hunt

September 2019

Publications

Journal articles

Saeed, A., Karimi, N., Hunt, G., Torabi, M. and Mehdizadeh, A. (2019) Double-diffusive transport and thermodynamic analysis of a magnetic microreactor with non-Newtonian biofuel flow. Journal of Thermal Analysis and Calorimetry, pp. 1-25 (doi:10.1007/s10973-019-08629-3)

Saeed, A., Karimi, N., Hunt, G. and Torabi, M. (2019) On the influences of surface heat release and thermal radiation upon transport in catalytic porous microreactors-A novel porous-solid interface model. Chemical Engineering and Processing: Process Intensification, 143, pp. 107602 (doi:10.1016/J.CEP.2019.107602)

Hunt, G., Karimi, N., Yadollahi, B. and Torabi, M. (2019) The effects of exothermic catalytic reactions upon combined transport of heat and mass in porous microreactors. International Journal of Heat and Mass Transfer, 134, pp. 1227-1249. (doi:10.1016/j.ijheatmasstransfer.2019.02.015)

Hunt, G., Karimi, N. and Torabi, M. (2018) Two-dimensional analytical investigation of coupled heat and mass transfer and entropy generation in a porous, catalytic microreactor. International Journal of Heat and Mass Transfer, 119, pp. 372-391. (doi:10.1016/j.ijheatmasstransfer.2017.11.118)

Hunt, G., Torabi, M., Govone, L., Karimi, N. and Mehdizadeh, A. (2018) Two-dimensional heat and mass transfer and thermodynamic analyses of porous microreactors with Soret and thermal radiation effects: An analytical approach. Chemical Engineering and Processing: Process Intensification, 126, pp. 190-205. (doi:10.1016/j.cep.2018.02.025)

Govone, L., Torabi, M., Hunt, G. and Karimi, N. (2017) Non-equilibrium thermodynamic analysis of double diffusive, nanofluid forced convection in microreactors with radiation effects. Entropy, 19(12), 690. (doi:10.3390/e19120690)

Elliott, A., Torabi, M., Hunt, G. and Karimi, N. (2017) Erratum to “On the effects of internal heat sources upon forced convection in porous channels with asymmetric thick walls” [Int.

Comm. Heat Mass Trans. 73 (2016) 100–110]. International Communications in Heat and Mass Transfer, 85, pp. 76-80. (doi:10.1016/j.icheatmasstransfer.2017.05.002)

Hunt, G., Karimi, N. and Torabi, M. (2017) Analytical investigation of heat transfer and classical entropy generation in microreactors - the influences of exothermicity and asymmetry. Applied Thermal Engineering, 119, pp. 403-424. (doi:10.1016/j.applthermaleng.2017.03.057)

Conference Proceedings

15th International Conference on Microreaction Technology (2018),
Two-Dimensional Analytical Models for Heat and Mass Transport in Microreactors
G. Hunt[1]; N. Karimi[1]; M. Torabi[2]; [1] University of Glasgow, Glasgow/UK; [2] Georgia Institute of Technology, Atlanta/USA

15th UK Heat Transfer Conference (2017),
A Two-Dimensional Analytical Model for Transport and Entropy Generation in Microreactors. G. Hunt[1]; N. Karimi[1]; M. Torabi[2]; [1] University of Glasgow, Glasgow/UK; [2] Georgia Institute of Technology, Atlanta/USA

15th UK Heat Transfer Conference (2017),
On The Effects Of Microstructure Upon The Thermal And Second Law Performance Of Microreactors. G. Hunt[1]; N. Karimi[1]; M. Torabi[2]; [1] University of Glasgow, Glasgow/UK; [2] Georgia Institute of Technology, Atlanta/USA

Poster Presentations

UK-Japan Engineering Education League Workshop (2017),
Analytical study of transport and entropy generation in microreactors. G. Hunt[1]; N. Karimi[1]; M. Torabi[2]; [1] University of Glasgow, Glasgow/UK; [2] Georgia Institute of Technology, Atlanta/USA

Prizes

Third prize in the poster presentation competition at the UK-Japan Engineering Education League Workshop (2017).

List of Symbols

Roman Symbols

a_{sf}	Interfacial area per unit volume of porous media, (m^{-1})
A_r	Pre-exponential factor for reaction, r
A_X	Cross-sectional area (m^2)
Bi	Biot number
Br'	Modified Brinkman number
C	Mass species concentration (kg m^{-3})
C_0	Inlet concentration (kg m^{-3})
C_p	Specific heat capacity (J K^{-1} kg^{-1})
$C_{p,i}$	Specific heat capacity of species, i
D	Mass diffusion coefficient (m^2 s^{-1})
$D_{i,m}$	Molecular diffusivity of species, i
Da	Darcy number
D_H	Hydraulic diameter (m)
D_T	Coefficient of thermal mass diffusion (K^{-1} kg^{-1} m^{-1} s^{-1})
E_a	Activation energy (kJ mol^{-1})
$g_{i,r}$	The stoichiometric coefficients of the products minus that of the reactants

h	Enthalpy (J)
h_i	Enthalpy of species, i (J)
h_1	Half-thickness of the microchannel to lower wall (m)
h_2	Half-thickness of the microchannel to upper wall (m)
h_3	Thickness from outer surface of lower wall to inner surface of upper wall (m)
h_4	Total thickness of microchannel (m)
h_3	Half-height of microchannel (m)
h_{sf}	Interstitial heat transfer coefficient (W K^{-1} m^{-2})
H_m	Mass transfer coefficient
H_w	Wall heat transfer coefficient (W K^{-1} m^{-2})
$J_{i,j}$	Diffusive flux of species, i in direction, j (kg m^{-2} s^{-1})
k	Effective thermal conductivity ratio of the fluid and the porous solid
k_1	Thermal conductivity of wall 1 (W K^{-1} m^{-1})
k_2	Thermal conductivity of wall 2 (W K^{-1} m^{-1})
k_{e1}	Ratio of thermal conductivity of wall 1 and thermal conductivity of the porous solid
k_{e2}	Ratio of thermal conductivity of wall 2 and thermal conductivity of the porous solid
k_{ef}	Effective thermal conductivity of the fluid phase (W K^{-1} m^{-1})

k_{es}	Effective thermal conductivity of the solid phase of the porous medium (W K^{-1} m^{-1})
k_R	Reaction rate constant (m s^{-1})
L	Length of the microchannel (m)
M	Viscosity Ratio
N_b	Number of bulk species
N_g	Number of gas species
N_{reac}	Number of surface reactions
N_{DI}	Dimensionless diffusive irreversibility
N_{FF}	Dimensionless fluid friction irreversibility
N_{int}	Dimensionless interstitial heat transfer irreversibility
N_f	Dimensionless fluid and interstitial irreversibility
$N_{f,ht}$	Dimensionless fluid heat transfer irreversibility
N_s	Dimensionless porous solid and interstitial irreversibility
$N_{s,ht}$	Dimensionless heat transfer irreversibility
N_1	Dimensionless lower wall irreversibility
N_2	Dimensionless upper wall irreversibility
N_{pm}	Dimensionless total porous medium irreversibility
N_{Tot}	Dimensionless total entropy

Nu	Nusselt number
p	Pressure (Pa)
P_R	Wetted perimeter (m)
Pe	Peclet number
Pr	Prandtl number
Q	Wall heat flux ratio
Q_1	Dimensionless volumetric heat source term in wall 1
Q_2	Dimensionless volumetric heat source term in wall 2
q_r	Radiation parameter
$\dot{q_1}$	Volumetric heat source in wall 1
$\dot{q_2}$	Volumetric heat source in wall 2
q_c''	Total catalytic heat flux (W m^{-2})
q_{w1}''	Lower wall heat flux (W m^{-2})
q_{w2}''	Upper wall heat flux (W m^{-2})
Re	Reynolds number
Rd	Dimensionless radiation parameter
R	Specific gas constant (J K^{-1} kg^{-1})
$\hat{R}_i$	Net rate of production of species, i

s_f	Volumetric heat source in fluid phase
s_S	Volumetric heat source in solid porous phase
S	Shape factor of the porous medium
Sh	Sherwood number
$\dot{S}'''_{Di}$	Volumetric entropy generation due to mass diffusion (W K^{-1} m^{-3})
$\dot{S}'''_{FF}$	Volumetric entropy generation due to fluid friction (W K^{-1} m^{-3})
$\dot{S}'''_{f}$	Volumetric entropy generation in the fluid (W K^{-1} m^{-3})
$\dot{S}'''_{s}$	Volumetric entropy generation in the porous solid (W K^{-1} m^{-3})
$\dot{S}'''_{w1}$	Volumetric entropy generation rate from lower wall (W K^{-1} m^{-3})
$\dot{S}'''_{w2}$	Volumetric entropy generation rate from upper wall (W K^{-1} m^{-3})
Sr	Soret number
T	Temperature (K)
T_C	Temperature at upper wall limit (K)
T_H	Temperature at Lower wall limit (K)
$\bar{T}_f$	Mean bulk temperature (K)
u	Fluid velocity, x component (m s^{-1})
U	Dimensionless fluid velocity, x component (m s^{-1})
$\bar{u}$	Average velocity over cross-section (m s^{-1})

$\overline{U}$	Dimensionless Average velocity over cross-section (m s^{-1})
v	Fluid velocity, y component (m s^{-1})
w	Fluid velocity, z component (m s^{-1})
x	Dimensional axial coordinate
X	Dimensionless axial coordinate
$[X_i]$	Site species concentration of species, i
y	Dimensional transverse coordinate
Y	Dimensionless transverse coordinate
Y_i	Species mass fraction
z	Dimensional out of plane coordinate

Greek Symbols

β	Temperature exponent
Γ	Site surface density (kmol m^{-2})
μ	Dynamic viscosity (N s m^{-2})
κ	Permeability (m^2)
κ^*	Rosseland mean extinction coefficient
ρ	Density (kg m^{-3})

σ^* Stefan-Boltzmann constant

θ Dimensionless temperature

Θ_i Site species concentration of species, i

ϕ Volume fraction of nanoparticles

Φ Dimensionless concentration

ξ Aspect ratio of the microchannel

ε Porosity of the porous medium

γ Damköhler number

ω Dimensionless heat flux

φ Irreversibility distribution ratio

η_{ir} Site coverage dependence constant for species, i and reaction, r

μ_{ir} Site coverage dependence constant for species, i and reaction, r

ε_{ir} Site coverage dependence constant for species, i and reaction, r

$\upsilon_{(i,r)}$ Rate exponent for species,i in reaction, r

ω_f Dimensionless fluid phase volumetric heat source term

ω_S Dimensionless solid porous phase volumetric heat source term

Ω Temperature gradient

Subscripts

C	Cold
e	Prefix for “effective”
f	Fluid
$f1$	Porous Fluid
$f2$	Clear fluid
H	Hot
i	Placeholder defined as necessary in text
j	Placeholder defined as necessary in text
nf	Nanofluid
p	nanoparticle
REF	Reference
s	porous solid
$w1$	Surface of wall 1
$w2$	Surface of wall 2
1	lower wall
2	upper wall

List of Abbreviations

AEL	Alkaline electrolysis
CAES	Compressed air energy storage
CCGT	Combined cycle gas turbines
CFD	Computational fluid dynamics
CPO	Catalytic partial oxidation
IP	In Phase
LIF	laser induced fluorescence
LTE	Local thermal equilibrium
LTNE	Local thermal non-equilibrium
OoP	Out of Phase
P1	Partially out of phase
P2G	Power to gas
PEM	Polymer electrolyte membranes
PSH	Pumped storage hydroelectric
SOEC	Solid oxide electrolysis
SNG	Synthetic natural gas
STP	Standard temperature and pressure, (298.15K and 1 bar)
UPS	Uninterruptable power supply

Chapter 1 Introduction

The UK government has set the target of 15% of the energy demand to be met by renewable sources by 2020 in the UK Renewable Energy Roadmap [1]. More ambitious targets were set by the Northern Ireland Executive of 40% renewable electricity and by the Scottish Government of 100% renewable electricity by 2020 [1]. To achieve this, a combination of wind, solar energy and hydroelectric must play a vital role. In 2015 electricity from renewable sources were the greatest contributor of electricity in Scotland [2]. Furthermore, this high share of the electricity supply contributed 42% of Scotland's electricity output that year [2]. By way of comparison, a mere 10 years previously, in 2005, the combined total of hydroelectric and "Other renewables" achieved a 14% share of the electricity generated [3]. Wind and solar sources provided 20% of the UK electricity generated [4] in 2018 totalling some 15.15 TWh (TeraWatt hours) in the third quarter of 2018. These figures clearly demonstrate the increase in dependence upon renewable sources for electricity generation. Specifically, wind and solar generated electricity accounting for by far the greatest proportion of renewable electricity generation [4]. This phenomenon is not limited to the UK, however. By way of example, in Germany, wind and solar combined provided 29% of the electricity generated [5]. In fact, the EU has set out a target of 20% renewable energy generation in its member states by 2020 [6]. In the intervening years, these targets have been updated to even more ambitions targets for 2050. The UK government has set targets for greenhouse gas emission reduction of a minimum of 80% by 2050 as compared to 1990 levels [7]. The UK is not alone in this drive, the EU has set goals for 2050 of cutting greenhouse gas emissions to 80-95% below 1990 levels over that timeframe [8]. Even these targets have been deemed insufficient and the EU has updated its target to now be carbon neutral by 2050 [9]. Consider, not just these targets themselves but also the evolution of the targets. This points to an ongoing and increasing demand for sustainable energy production that will see an increase of the likes of solar and wind generation penetration into the energy market.

1.1 A Move Toward Renewable Power Generation

This increasing reliance on solar and wind as sources of electricity generation is not without its drawbacks. Since both wind and solar energy can fluctuate and provide intermittent power, they must be balanced to provide grid stability. In the UK, the greatest share of power storage is in the form of pumped storage hydroelectric (PSH), however as can be seen from Figure 1-1, while the share of renewable energy has increased from 2.3GW

to 44.3GW, the change in capacity of PSH is negligible by comparison [10]. Not all renewable sources are intermittent, but it is worth noting that wind and solar provide over a quarter of renewable energy (see Figure 1-2) in the UK [10]. Without such energy storage options surplus energy is wasted and energy deficit could lead to power loss to certain areas [11]. Construction of the grid allows for some degree of erraticism in both supply and demand, but not large-scale swings in either direction [12].

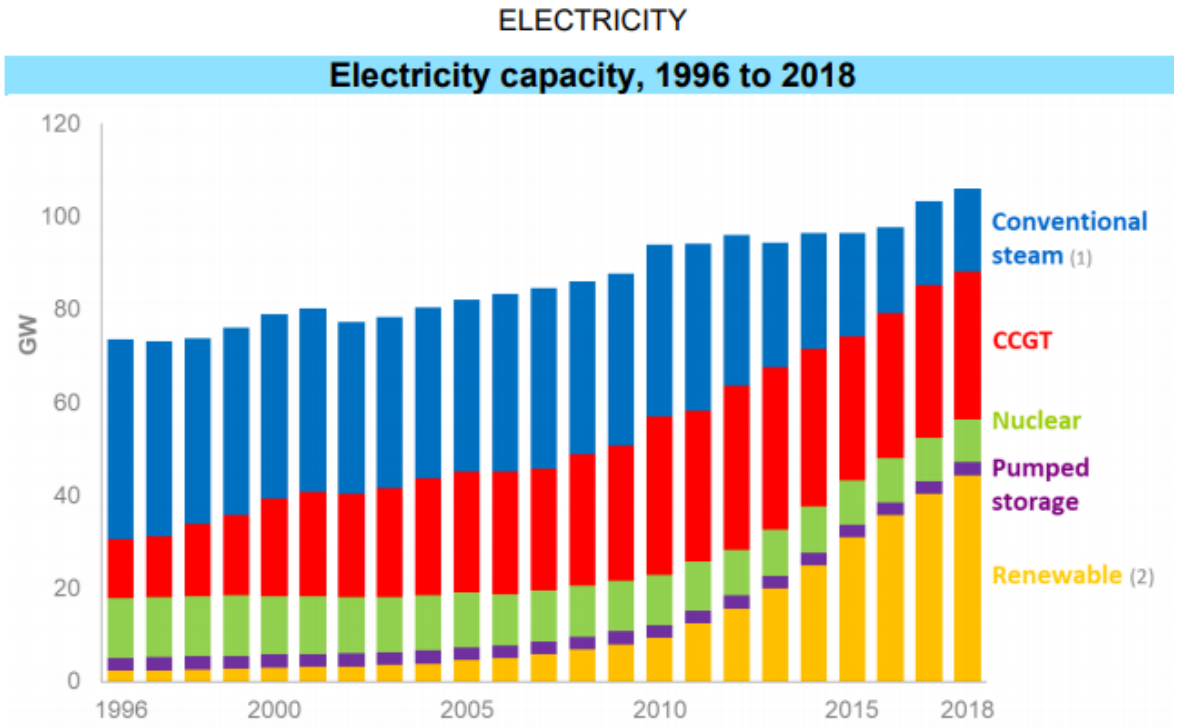

GW

	1996	2000	2005	2010	2017	2018
Conventional Steam	43.0	39.7	37.1	37.1	18.0	18.0
CCGT	12.7	21.1	25.9	34.0	32.9	31.7
Nuclear	12.9	12.5	11.9	10.9	9.4	9.3
Pumped Storage	2.8	2.8	2.8	2.7	2.7	2.7
Renewable	2.3	3.0	4.5	9.3	40.3	44.3
Total	**73.6**	**79.0**	**82.1**	**94.0**	**103.3**	**106.1**

Figure 1-1 Electricity capacity in the UK, 1996 to 2018 [10]

This leads to the requirement for a form of electricity storage capacity that is both long term and substantial (the figures quoted above demonstrate the scale of the requirement) in addition to having a significant reserve production capacity. In order to function correctly, the power grid needs to be balanced, that is to say the power supply and demand should match at any given time [12]. To meet this requirement, there must be an increased degree of flexibility build into the grid to allow such balance to be maintained [12].

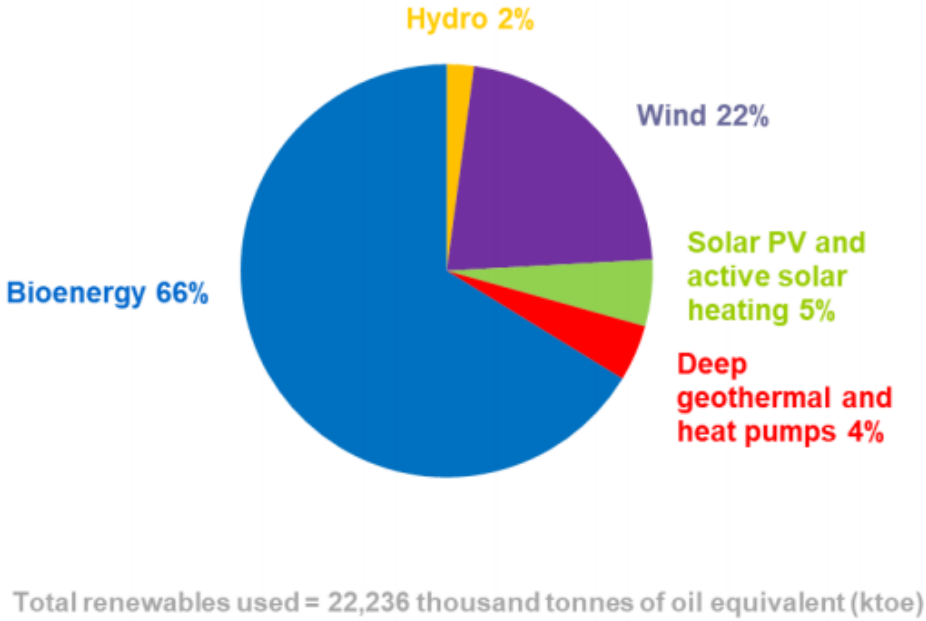

	Thousand tonnes of oil equivalent				
	1990	**2000**	**2010**	**2017**	**2018**
Solar PV and active solar heating	6	11	41	1,039	1,158
Wind	1	81	884	4,268	4,893
Hydro (large & small) and wave	448	437	309	508	473
Landfill gas	80	731	1,725	1,419	1,298
Sewage gas	138	169	295	401	409
Wood (domestic and industrial)	174	458	1,653	2,370	2,560
Municipal waste combustion (biodegradable)	101	375	632	1,278	1,496
Heat pumps and deep geothermal	1	1	23	964	980
Transport biofuels	-	-	1,218	997	1,364
Cofiring	-	-	625	18	0
Other bioenergy	72	265	1,054	6,581	7,606
Total	**1,021**	**2,529**	**8,460**	**19,843**	**22,236**

Figure 1-2 Share of different renewables types in Thousand tonnes of oil equivalent [10]

This leads to the need for several different functions to be fulfilled in terms of energy storage or demand side management (see Figure 1-3). The first of these functions is system or frequency regulation, which incorporates energy storage technologies to meet short-term needs such as to resolve, random fluctuations, temporary power outages, voltage sags and surges [13]. Following this are reduction techniques such as peak shaving, which stores energy from the energy peaks in the minutes to hours scale on a daily basis, and conservation, which is simply reducing the load (see Figure 1-3) [13]. The reverse of these are the increasing demand procedures of valley filling and load growth. Lastly, there is load shifting which can involve storing energy generation surpluses during off-peak times (e.g. overnight) and releases the stored energy to meet demands at peak times (see Figure 1-3) [13]. Load

shifting is particularly advantageous as it permits variability in demand without affecting the generation of power [12].

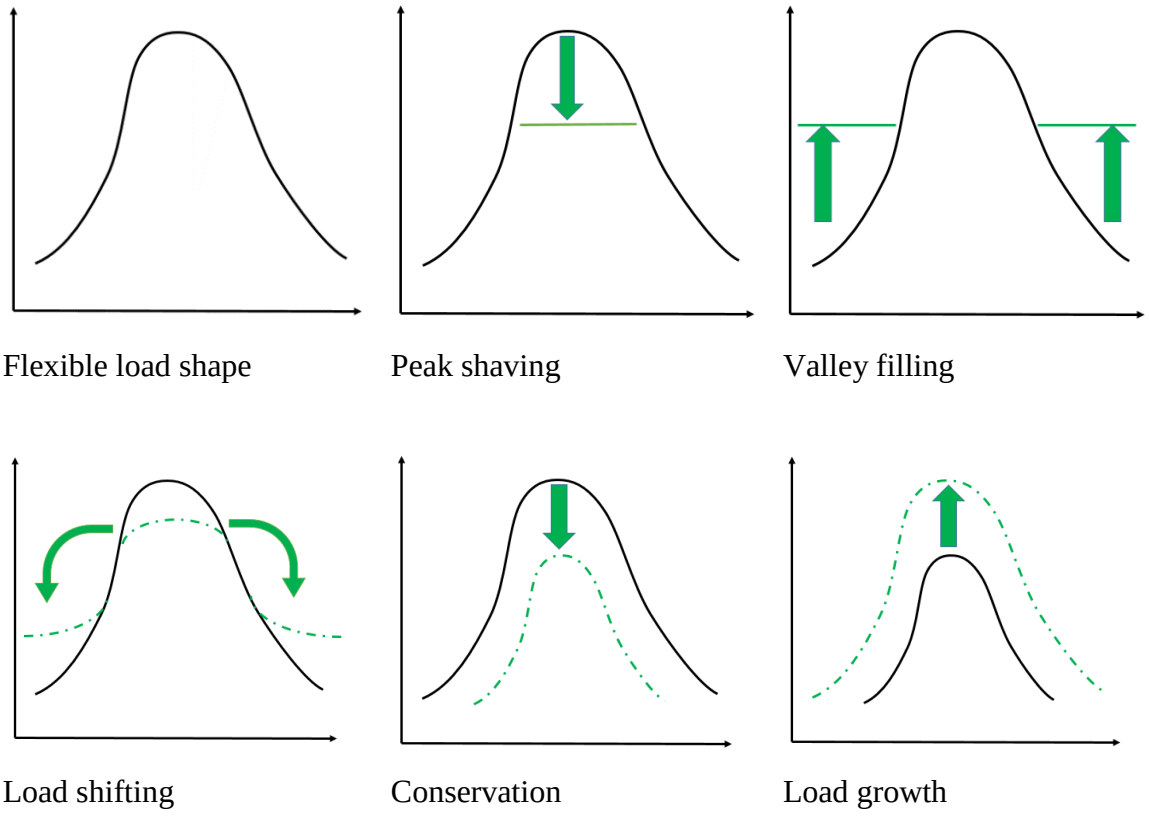

Figure 1-3 Categories of load management adapted from [14]

1.1.1 Flexibility

To accomplish this requires facilities that exhibit flexibility in one form or another as appropriate to the needs of the grid under different conditions. There are three main characteristics by which this flexibility may be measured [15]. First is simply the quantity of the range of power that is required, i.e. the number of MW. Resources that fall into this category are deemed flexible in that due to their large range of absolute power output between the minimum and maximum operating capacity. This allows them to adjust their output level to accommodate fluctuating power requirements. Secondly, the speed at which this output can be achieved, or ramp rate, i.e. MW per minute. High ramp rates (or in some cases, fast start-up times) allow systems in the second category to respond rapidly to changes in power demand. Finally, there is the duration for which this output can be maintained, i.e. how many MWh. Systems that fall into this category have the capacity to maintain energy levels for greater durations, enabling them to meet power demands in sustained conditions [16].

1.2 Energy Storage Technologies

A number of energy storage technologies have been developed over some considerable time. Highlighted here are some of main forms of energy storage that are in use and being developed today. Consideration is given to each mentioned technology in the context of the definitions of flexibility described in the previous section such that a comparison may be made.

1.2.1 Hydroelectric

Historically, response to variability and fluctuation in the system is provided by rapid response thermal generation. However, factors such as restriction on emissions, have led to an increase in interest in storage technologies with a low carbon footprint. Currently by far the greatest share of energy storage is provided by pumped storage hydroelectric (PSH) stations [17]. There are currently 4 pumped storage hydro facilities in the UK with a total capacity of 2,828MW and a combined energy storage capacity of 26.7GWh [17] as shown in Table 1-1.

Table 1-1 Pumped storage Hydro facilities in the UK

Pumped Hydro facility	Power (MW)	Energy Capacity (GWh)
Dinorwig Power Station	1,728	9.1
Cruachan Power Station	440	10.0
Ffestiniog Pumped Hydro Power Plant	360	1.3
Foyers Pumped Storage Power Station	300	6.3

Pumped storage facilities consist, typically, of two interconnected water reservoirs for storage of energy in the form of gravitational potential energy. During off-peak times, water is pumped from the lower to the upper reservoir. The upper reservoir of Ffestiniog PSH facility is shown in Figure 1-4.Thus, when the energy is required, the water stored can be released from the upper reservoir back to the lower through turbines to generate the electricity and balance the load on the grid. This is a mature technology, for which the most recent developments have been in variable-speed and ternary plants [18]. Variable speed plants, as the name suggests, are capable of changing their rotational speed to avoid

resonance related issues and are overall more efficient and flexible than standard hydro plants [18]. Similarly, ternary plants also offer improved efficiency over standard plants, while significantly improving flexibility. This is achieved by the plants ability to operate simultaneously as both a pump and a turbine. This permits operation of the plant as both a pump and a generator. Unlike most reversible machines, it does not require to stop before changing direction and as such can switch rapidly from full pumping mode to full generating mode [18].

Figure 1-4 The upper reservoir (Llyn Stwlan) and dam of the Ffestiniog Pumped Storage Scheme in north Wales. (Taken by Adrian Pingstone)

The main advantage that pumped storage hydroelectric has over other forms of energy storage lies in precisely this maturity of technology. However, when looking at the figures outlined on the first page of this introduction, it is clear that the future requirement for storage will significantly outstrip the current capacity. This leads to the main disadvantage of pumped storage hydroelectric facilities, which is their inherent size and geographical requirements. There are a limited number of sites at which such facilities could be constructed [19].

1.2.2 Flywheel

Another energy storage system is flywheel energy storage (see Figure 1-5 for example). These facilities are physically smaller that pumped storage hydroelectric and so

have less in the way of geographic limitations. In addition, however, they typically have lower power levels. Beacon Power runs two flywheel stations in the USA, each with 200 flywheels, one in Stephentown, New York operating at 20MW (with a 40 MW overall range) and another at Hazle Township, Pennsylvania with a capacity of 20 MW [20]. Lower power aside, flywheel facilities have high efficiency levels and energy densities [19]. While they lack flexibility as determined by range of power and limited operational duration of 1-100s [21], they exhibit great flexibility in their ramp speeds and can be used in the millisecond to second range [19].

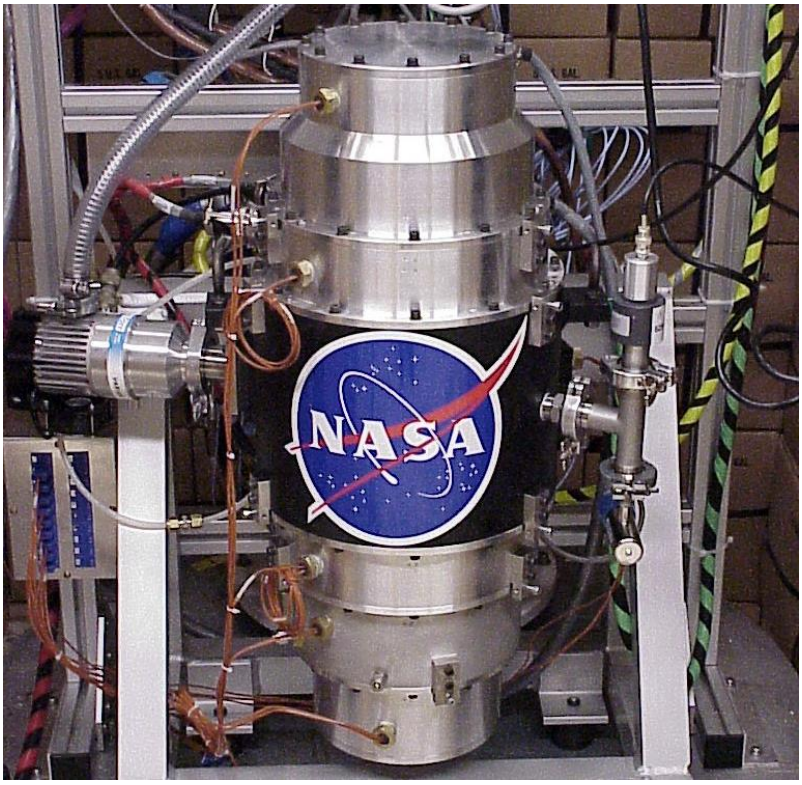

Figure 1-5 G2 Flywheel Module, NASA (Image http://space-power.grc.nasa.gov/ppo/projects/flywheel/gallery.html)

1.2.3 Compressed Air

Another technology capable of storing energy at times when demand is low in order to release that energy when demand picks up again (load shifting) is Compressed air energy storage (CAES). Like pumped storage hydroelectric facilities, CAES is a mature technology for energy storage and is capable of high power and long term applications as required for load levelling purposes [22]. Load levelling evens out the peaks and troughs of electricity demand to a near constant value in a similar value to load shifting. This constant level permits baseload power stations to operate at higher efficiencies and mitigates against the need for peaking power stations [12]. Excess energy from the power grid is used to compress

air to 60-70 bar, followed by cooling it and then pump it into a cavern where it is stored. The choice of storage location is usually in underground salt caverns hard rock caverns or saline aquifers [23]. Rock salt has very low permeability, which helps guarantee its tightness against gas leakage [24], other types of rock caverns require some form of lining or hydrodynamic containment to achieve the required air tightness [25].

Once demand increases the compressed air is extracted from the cavern, heated and then used to power a gas turbine [26]. Facilities for CAES can be on the small, modular scale or up to the hundred MWh plus scale such as that found in Huntdorf, Germany, which has a power capacity of 290MW [22]. Similarity to PSH does not end with the maturity of the technology though, the capital costs are also similar, and in the same way that PSH has geographic requirements with regards to bodies of water in order to function, CAES has geographic requirement of caverns to store the compressed air [19]. A further disadvantage is the low efficiency levels of below 55% as compared to PSH of approximately 75% [19]. In order to address this deficiency, advances in CAES have led to projects involving adiabatic CAES systems, which increase the efficiency by storing the heat energy extracted during the cooling process separately. This heat can then be recombined with the air as it is expanded through an air turbine [26].

1.2.4 Battery

Batteries with rechargeable properties have existed as an energy storage, in the form of chemical energy, for over one hundred years. They consist of one or more electrochemical cell, each of which utilises an electrolyte to bridge the anode and the cathode. The battery functions as a source of power by means of reversible electrochemical reactions, which occur at each electrode. The reversibility of the reactions allows for power to be stored when the reactions proceed in one direction and for power to be supplied when the reaction proceeds in the other direction.

The ability of batteries to rapidly react to changes in the load of a system, coupled with their generally high efficiencies (60-95%) and low standby losses stands firmly in their favour [27]. Batteries find their main use at the utility scale and are frequently employed in cases where uninterruptable power supply (UPS) is required (e.g. hospitals etc.). However, utilisation of battery technology on a large scale is not common due to factors such as short lifespan, limited capacity and expense of facility maintenance [27]. In 1988, Southern California Edison at Chino, California, a 10MW facility was created and tested for load

levelling over a two year period [28]. Recently Hitachi unveiled a demonstration project in Germany of a hybrid power storage system featuring both Lithium-ion and NaS batteries with a total storage capacity of 11.5MW [29].Furthermore, most batteries currently in use contain materials which are highly toxic (e.g. cadmium and lead) [12], necessitating control measures to govern their disposal [27].

Examples of batteries in common use include lead acid batteries, familiar to most people in the form of car batteries. This type of battery is highly cost effective, in addition to the previously mentioned general advantages of batteries, thus adding to its attractiveness. On the downside, however, lead acid batteries do not perform well at low temperatures and have a relatively short lifespan (500-1000 cycles) [27]. This has not prevented their use in larger scale facilities, in fact lead-acid batteries that were used in the Chino facility mentioned previously and are frequently found in photovoltaic systems especially in China [30]. Other, smaller, but nonetheless large-scale energy management facilities have been constructed in Germany, Spain and Puerto Rico [27].

Nickel Cadmium (NiCd) batteries have been used for energy storage almost as long as lead acid and so also represent a mature technology [27]. They benefit from a higher energy density and longer life (2000-2500 cycles) [30]. Their primary use has historically been in small portable devices, but this use is decreasing, as they are known to suffer from the "memory effect". That is not to say that their use is limited to only smaller devices, in fact Golden Valley Electric Authority constructed a battery energy storage system using NiCd batteries, which was rated at 27MW for 15 minutes [31].

The most prolific large-scale energy storage battery is the Lithium-ion (Li-ion) battery. This is due to its high efficiency (almost 100%) and long life cycle (up 10000 cycles), on the downside, they are expensive [27]. This has not discouraged both the USA and Japan from constructing plants in the tens of MW scale using this technology. Japan with its 40MW/20 MWh power station in Sendai in the Miyagi Prefecture in 2013 for frequency regulation [32]. To resolve energy shortages in San Diego, the 30MW/120MWh lithium battery storage facility in Escondido, San Diego was constructed [32]. Many other forms of battery technology are in use or research phase, including but not limited to flow batteries, sodium sulphur batteries, etc. They find use in various different applications and have their own distinct pros and cons. In all cases, though there is the question of battery technology's flexibility in terms of duration since they can only be used in the seconds to hours timescale.

1.2.5 Power to Gas

Though batteries are the most well-known form of chemical energy storage, another contender is that known as power to gas (P2G). The gas concerned is typically either methane, which can be used by existing infrastructure for using natural gas for power generation, or hydrogen, which can likewise be converted to water to provide a return on energy invested (see Figure 1-6) [33].

In the case of power to hydrogen storage system a combination of three components is required. Firstly, an electrolyser which produces the hydrogen through hydrolysis of water to liberate both the required hydrogen and oxygen. A fuel cell to reverse this process and liberate electrical energy, and finally some form of storage system, for the hydrogen during the interim between supply and demand requirements [13]. These storage systems can be either aboveground storage facilities or rock salt caverns. Due to the visco-elastic properties of rock salt it is extremely tight to both hydrogen and methane even under high pressures, make it the logical choice for large scale storage of hydrogen [34].

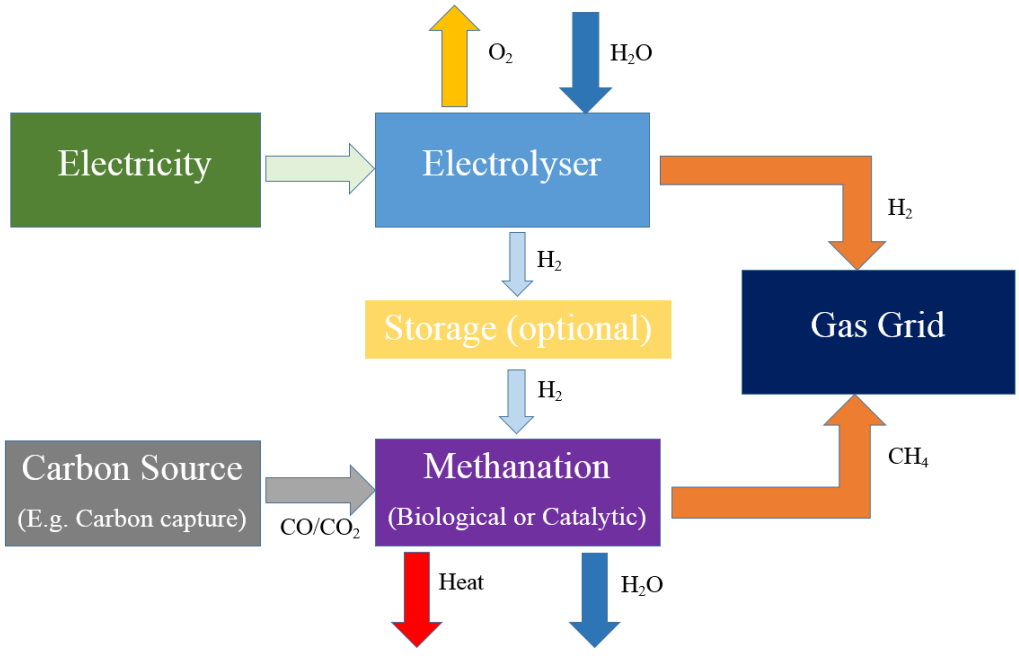

Figure 1-6 Power to gas process chain adapted from [33]

Alternatively, convert the hydrogen to methane, which can then be used by existing natural gas infrastructure to generate electricity. This last is one of the major advantages of P2G, an infrastructure of storage, distribution, and electricity production already exists. This permits excess energy from renewable sources to be temporarily stored in the form of hydrogen or methane either in the gas network or in storage facilities. From there, the

distribution network is already available to transport it to other locations during times of increased demand [19].

1.3 Examination of Energy Storage Capacities

To get a clearer picture of the scale involved in the UK alone, the electricity generated in the UK in 2018 by renewable sources was 110 TWh, some 33% of the total electricity generated in the UK that year. It is significant that combined onshore and offshore wind generation accounted for almost half of that (49%) [35]. That accounts for about 55 TWh of electricity generation through intermittent technologies. To achieve an energy storage of that capacity based on the four PSH facilities currently extant in the UK would require (based on Table 1-1 figures) would require a further 2033 PSH facilities to be built. Clearly, that is not feasible. Even if only say, 10% is required to be stored, then that would still require an additional 200 facilities. Again this is not practical. A similar situation arises when examining the other storage capacities, with one exception. Since existing natural gas facilities range in hundreds of terawatt-hours scale (881 TWh in 2018 for overall energy demands [35]), they represent the largest potential for energy storage capacity [19]. Using synthetic natural gas (SNG) produced in the P2G process using methane, rather than natural gas produced from fossil fuel sources would also significantly reduce the carbon footprint.

There are various methods and associated technologies by which the SNG may be produced. A discussion of these will be provided in Chapter 2 examining the pros and cons of each. While all technologies presented are viable options, the focus, is upon catalytic microreactor technology. The key areas of interest in this thesis for microreactor technology are heat and mass transfer processes. Heat transfer processes for the required high degree of thermal control and mass transfer for improving product yield. Understanding of these processes and the effects that other design parameters have on them is the aim of the work presented herein.

Specifically, the objectives of this work are:

- To develop a one-dimensional analytical model of a microreactor with a view to investigating the effects of various parameters upon the heat transfer properties of the microreactor.

- To realise a novel two-dimensional analytical model that will incorporate coupled heat and mass transfer. Both heterogeneous and homogeneous catalysed reactive systems will be investigated.

- To design a novel boundary model to examine the effects of heterogeneous catalytic surface featuring exothermic or endothermic reactions.

- To undertake detailed numerical simulations to determine the impact of hydrodynamics of a bluff body or changing wall geometry can have upon catalytic activity.

Chapter 2 Literature review

2.1 Introduction

In the drive towards increased use of renewable energy, wind and solar energy sources play a pivotal role. An increased penetration into the energy production market of the sources has been observed in recent years and is likely to continue in years to come. However, as discussed in Chapter 1, both wind and solar exhibit fluctuations and can be intermittent in their energy provision. As such, they require to be balanced for the purpose of grid stability. This presents the need for energy storage solutions that are both long term and high capacity to provide the required balance in the grid. In addition, to allow for the use of such techniques as load shifting (which was discussed in Chapter 1), there is the necessity for the existence of a reserve energy storage capacity.

Many energy storage solutions were considered in Chapter 1 and the forms of flexibility exhibited by each examined. Some showed high flexibility in terms of ramp rate, others in terms of storage capacity. In addition, the environmental impact was also considered, including issues relating to use of toxic chemicals in, for example, batteries. To geographical considerations associated with, for example, PSH facilities.

Of the many different forms of energy storage discussed in Chapter 1, power to gas exhibits great flexibility and low impact on the environment. Depending on the requirements, power to gas can operate on small scale for local supply purposes or in large-scale facilities. In addition, it allows for a link from the power grid to the gas grid taking advantage of existing infrastructure.

An outline of power to gas is now presented including a discussion of the various technologies which may be used in the process. The focus will then narrow to the use of microreactor technology as a key option for accomplishing the methanation reactions. The thermal properties, which make microreactors a prime option for exothermic flow chemistry reactions, will be outlined. This leads to the need for greater understanding of heat and mass transfer properties in microreactors. To further this, a review of analytical and numerical techniques that may be applied to resolving this knowledge gap are reviewed.

2.2 Power to gas

Even with renewable power generation penetration of 85% (model based in Germany), P2G was able to counterbalance surplus energy provision [32]. As touched on in Chapter 1, P2G has two primary forms, the first of which involves production of hydrogen and then injection of this hydrogen into the existing natural gas infrastructure. This method has the main limitation that the amount of hydrogen that can be accepted by the gas grid is variable. For example, in Germany the maximum amount of hydrogen in the gas grid is 5% depending on both end user requirements and restrictions on compressors for example [34]. As such, any feed of hydrogen into the grid in any given country is dependent upon that countries limits for hydrogen fraction in its natural gas grid. Bypassing this limitation, the hydrogen liberated from the electrolysis of water can be converted to synthetic natural gas (SNG).

2.2.1 Electrolyser

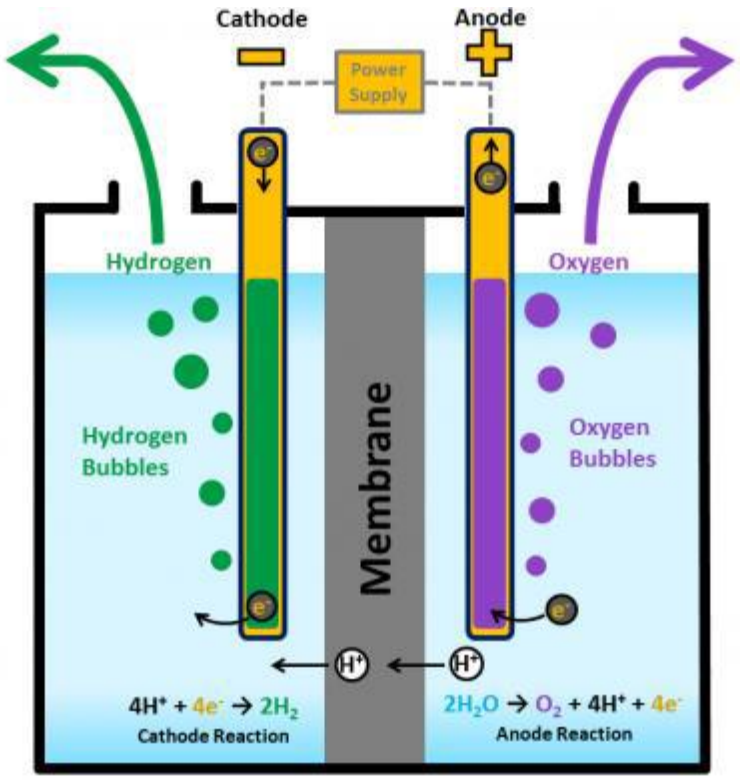

Figure 2-1 Schematic of electrolysis of water in which the charge carrier is H^+. Image from: www.energy.gov/eere/fuelcells/hydrogen-production-electrolysis

The electrolysis of water to yield hydrogen and oxygen is a technology that has been available for over a century, the effect having first been discovered in 1800 [35]. The overall reaction for splitting water in to hydrogen and oxygen is shown in equation (2-1). At the

cathode, the reduction reaction shown in equation (2-2) takes place, whereas at the anode the oxidation reaction shown in equation (2-3) occurs. The reaction enthalpy, ΔH_R^0 = 285.9 kJ mol^{-1} is required under standard temperature and pressure (STP; 298.15 K and 1 bar) [36]. Depending on which electrolyser technology is utilised, the charge carrier can be OH^-, H^+, or O^{2-} [36]. An example where the charge carrier is H^+ is shown in Figure 2-1.

$$H_2O_{(l)} + \Delta H_R^0 \rightarrow H_{2(g)} + \frac{1}{2}O_{2(g)} \quad (2\text{-}1)$$

$$H_2O + 2e^- \rightarrow H_2 + O^{2-} \quad (2\text{-}2)$$

$$O^{2-} \rightarrow \frac{1}{2}O_2 + 2e^- \quad (2\text{-}3)$$

The Gibbs free energy of electrolysis of water, ΔG_R^0, may also be calculated and is found to be 237 kJ mol^{-1} [36]. From the Gibbs free energy and the Faraday constant, *F* the reversible equilibrium cell voltage, V_{rev}^0 may be determined using equation (2-4) for n electrons [36].

$$V_{rev}^0 = \frac{\Delta G_{rev}^0}{n\,F} \quad (2\text{-}4)$$

For the purposes of energy storage and re-release, the most important factors for any electrolysis technology are efficiency, flexibility and lifetime. Efficiency since it is clearly of interest that as much hydrogen as possible is produced per given amount of energy. Flexibility is again important, for example, rapid ramp up times are clearly beneficial. Finally, lifetime is important in this technology since a long operational lifetime reduces the need for replacement. Since electrolysis of water is a mature technology that has been well understood for a considerable time, it may be achieved in many ways. For the sake of brevity, only the two main electrolyser technologies will be considered here. These are alkaline electrolysis (AEL), and polymer electrolyte membranes (PEM). It is worth mentioning that an additional electrolyser technology also shows promise; this is the solid oxide electrolysis (SOEC). In this system, steam rather than water is used to slit into hydrogen and oxygen at elevated temperatures. However, this technology is still in the development stage [37].

The most mature of the electrolyser technologies considered is AEL, which has been operating commercially for several decades [35]. As the name suggests, an aqueous alkaline solution (KOH or NaOH) is used as the electrolyte in AEL. While AEL can operate either

at atmospheric pressure, increased pressure is detrimental to the overall reaction as can be seen by application of Le Chatelier's principle to equation (2-1). This is evidenced by the lower efficiency and purity of the products in pressurised AEL as compared to atmospheric AEL [38]. However, the great advantage of pressurised AEL is that, when compared to atmospheric AEL, it produces pressurised hydrogen for a lower energy cost [38]. This is because the decrease in electrical efficiency of the pressurised system is less that the energy required to pressurise the hydrogen produced from the atmospheric system. On the downside, the minimum load is typically 25-50% (though some are reported as low as 5-10%) of normal operating power and the system has a relatively long ramp up time and takes some 30-60 minutes to restart from shut down [39]. This limitation tends to make AEL electrolysers less suitable than PEM for intermittent and fluctuating power sources [40]. In addition, there are the maintenance problems caused by the highly caustic nature of the electrolyte itself. This leads to the requirement for a general overhaul every 7-15 years and an lifespan of up to 30 years [38].

In the late 1970s early commercial PEM electrolysers were developed by General Electric [37]. This technology uses a gas-tight polymer membrane, which is strongly acidic, permitting the charge carrier H^+ to conduct via ion exchange [37]. In comparison to AEL technologies, PEM demonstrated faster ramp up speed and can operate from as little as 5% of nominal operating power [40]. This makes their suitability for fluctuating and intermittent power sources much more favourable. An additional advantage is in the very high purity of hydrogen obtained from the electrolyser [37,40]. One of the disadvantages of PEM systems is in their cost due to both the polymer itself and the use of noble metals in its construction [37]. A second problem lies with the lifetime of the system being only about 5 years [40]. Lastly, they do not have the capacity that AEL technology exhibits [40].

2.2.2 Methanation

Two main avenues exist for the methanation process; these are biological and catalytic methanation reactors. While biological methanation reactor have their own advantages and disadvantages, the focus of this work is primarily concerned with catalytic methanation reactors. The methanation process typically involves a number of key reactions including, the Sabatier reaction (2-5), CO hydrogenation (2-6), and the reverse water gas shift reaction (2-7) [41]. Both the Sabatier reaction and CO hydrogenation are equilibrium limited, fast and highly exothermic [42]. Catalysts often used include Co, Ni, Rh and Ru

[43] which are found to be highly selective [44]. The most common choice of catalyst is Ni, due to its high activity and relatively low cost [45].

$$CO_2 + 4\,H_2 \rightleftharpoons CH_4 + H_2O \qquad \Delta H = -165\ \text{kJ/mol} \qquad (2\text{-}5)$$

$$CO + 3\,H_2 \rightleftharpoons CH_4 + H_2O \qquad \Delta H = -206\ \text{kJ/mol} \qquad (2\text{-}6)$$

$$CO_2 + H_2 \rightleftharpoons CO + H_2O \qquad \Delta H = +41\ \text{kJ/mol} \qquad (2\text{-}7)$$

The methanation process (2-5) is generally viewed as a combination of the reverse water gas shift reaction and CO hydrogenation [41]. Due to Le Chatelier's principle, the methanation process (2-5) is favoured at lower temperature and higher pressures. High temperature increase the reaction rate of both forward and reverse reactions, but due to the exothermic nature of the reaction favour the reverse process. Further, an increase in temperature can also result in carbon deposition (coke) due to CO decomposition, and methane cracking [42]. This cannot be completely avoided, due to the thermal conditions of the reaction, and presents a significant problem for industry [46]. Thus in order to obtain a respectable reaction rate, a balance between elevated temperature and pressure is used in conjunction with one of the metal catalysts mentioned previously [41].

To demonstrate the highly exothermic nature of the Sabatier reaction (2-5) consider that an increase of about 1% in the molar gas fraction of methane in the product gas increases the temperature by approximately 60 K [45].This poses a significant issue for any catalytic methanation reactor, the necessity for a high degree of temperature control. As mentioned above, lower temperatures are favoured for the forward reaction, so the temperature must be controlled to for this reason and to avoid the potential for catalyst sintering temperatures above 550^{o}C [45]. Conversely, the temperature cannot be permitted to drop below 200^{o}C for the nickel based catalyst as this can lead to the formation of highly toxic nickel carbonyl compounds [45]. The requirement to realise high temperature control has led to the development of the following steady-state reactors, fixed-bed, fluidised-bed, three-phase and structured reactors.

Operating conditions for the adiabatic fixed bed reactor technology have a broad range of temperature, some 250-700^{o}C. However, with fixed-bed reactors, limitations imposed by the poor heat transfer in both axial and radial directions means that potential problems of catalyst sintering or cracking arise [47]. As such, the need arises to utilise a

cooling mechanism between a series of reactors rather than using a single reactor. This may be accomplished with either via the use of outlet gas cooling and recirculation or intermediate gas cooling steps [45]. Another technique for temperature control involves use of cooled bed reactors. Typically, this type of reactor is constructed using bundles of cooling tubes, or cooled plates [48].

A high degree of thermal control can be achieved using a fluidised-bed reactor (Figure 2-2). Fluidised solid catalyst particles mixed with the gas feed allow for high heat and mass transfer [48]. They also have the advantage the additional catalyst can be added or removed to the reactor during the process [48]. However, high mechanical load of fluidisation results in attrition of both the catalyst and the reactor walls themselves [45,48]. Consequently, the catalyst becomes increasingly deactivated, especially as partial pressures of CO increase caused by incomplete CO_2 conversion due to bubbling [49]. This is due to formation of $Ni(CO)_4$ as large crystallites [47] and can even lead to loss of the nickel metal in extreme cases [49]. Superficial gas velocity is a controlling factor within a fluidised-bed reactor, with higher velocities increasing the heat transfer properties. However, high gas velocities also cause higher rates of gas bypassing though the bed as bubbles [50].

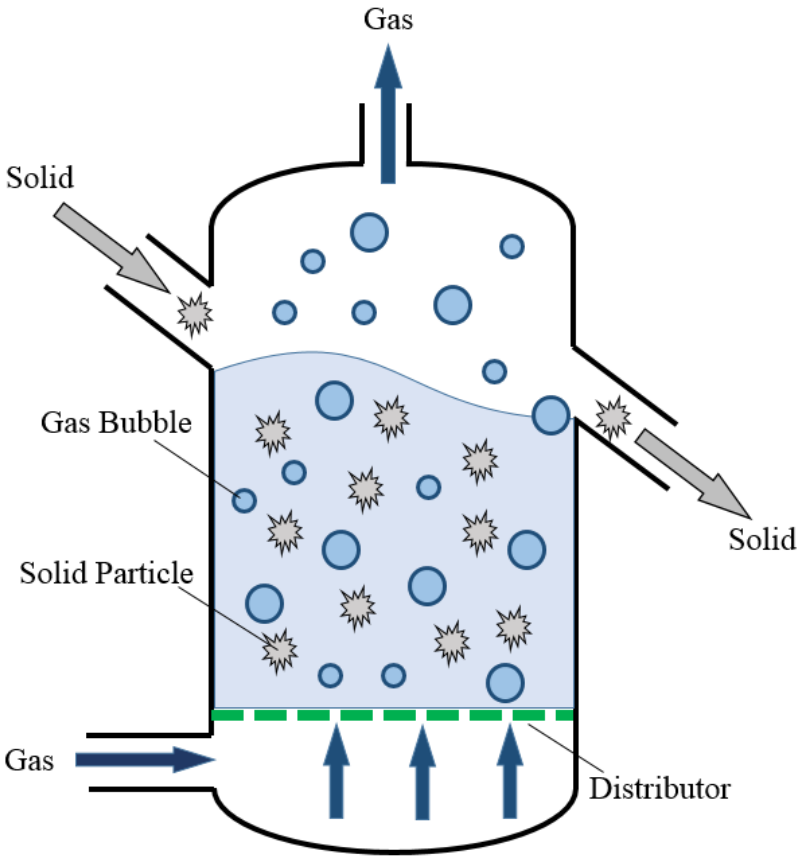

Figure 2-2 Schematic of a generalised fluidised bed reactor.

The three-phase reactors involve a slurry reactor filled with a high heat transfer liquid phase such as dibenzyltoluene [51]. Into this liquid phase, fine catalyst particles are dispersed and are suspended by gas flow. The high heat capacity of the liquid phase permits a high degree of thermal control of the reactor by removing the most of the heat of reaction completely from the system [51]. Thus, the reactor is able to operate under almost isothermal conditions. Additionally, the high heat capacity of the liquid reduces the impact of rapid temperature changes that can be a problem for two-phase reactors [51]. However, the presence of the extra phase adds an extra boundary to be overcome so gas liquid mass transfer resistance poses a significant problem to three-phase reactors [52]. Problems associated with evaporation and decomposition in the heat transfer liquid are further drawbacks associated with three-phase reactors [51].

Development of structured reactors (for example, monolith reactors) has been ongoing in order to counteract the drawbacks associated with adiabatic fixed-bed reactors as described above. Monolith reactor technology consists of the monolith itself, which contains a large number of channels running parallel to one another bounded by thin walls and the catalyst washcoat. This design increases the surface area as compared to one large channel. The monolith acts as a support on which the catalyst washcoat of choice is added. As compared to fixed-bed reactors, monolithic supported catalyst offer the advantages of greatly reduced pressure drop and improved radial heat transfer [53]. The latter may be further enhanced by use of a metal monolith support [53]. The interconnected channels form a solid matrix via which heat may be conducted away from the reaction zone [53]. One potential disadvantage for this technology type is that due to the catalyst being coated on the monolith support, it may prove susceptible to coke deposition [54]. A further advance in structured reactor technology is the microreactor. Key features of these reactors include their large surface-to-volume ratio and enhanced thermal control, aiding in the reduction of hot spots [55]. In turn this enhances the selectivity, which may be affected by hot spots, thus increasing the efficiency of the technology [44].

Table 2-1 Comparison of advantages and disadvantages for differing reactor technologies.

	Advantages	Disadvantages
Fixed bed	• Broad temperature range	• Susceptible to sintering/cracking • Difficulty with rapid temperature change/hot spots
Fluidised bed	• Effective heat removal	• Attrition of walls and catalyst • Deactivation of catalyst
Three phase	• Accurate temperature control	• Gas liquid mass transfer resistances • Decomposition and evaporation of suspension fluid
Microreactors	• Enhanced radial heat transport • Small pressure drop	• Complex catalyst deposition and replacement procedure

Due to their small size, they are suitable for both small-scale applications and by numbering up (increasing the number of reactors rather than size of the reactor) also the large scale. Accounting for the properties associated with each of the methanation technologies discussed allows for a comparison of their advantages and disadvantages. This is summarised in Table 2-1.

While it is clear that, each individual methanation technology has both advantages and disadvantages, microreactors have more in their favour on balance. Further improvements in microreactor technology could further increase this lead.

2.3 Why Microreactors

With the provision of low cost and commercial micro manufacturing techniques, micro process engineering facilities are becoming more popular in both academia and industry [56]. Amongst these, microreactors are one of the recently growing tools [57,58]. They have a broad range of applications from distributed fuel production [59] and methanol steam reforming [60] to process intensification [58] and nanoparticle generation [61]. Most of these processes involve multiple reactants and exothermic/endothermic stages. Therefore, microreactors should feature very efficient mixing and heat transfer characteristics. Furthermore, over the last two decades, there have been sustained attempts for developing micro-combustors for the purpose of micro power generation [62].

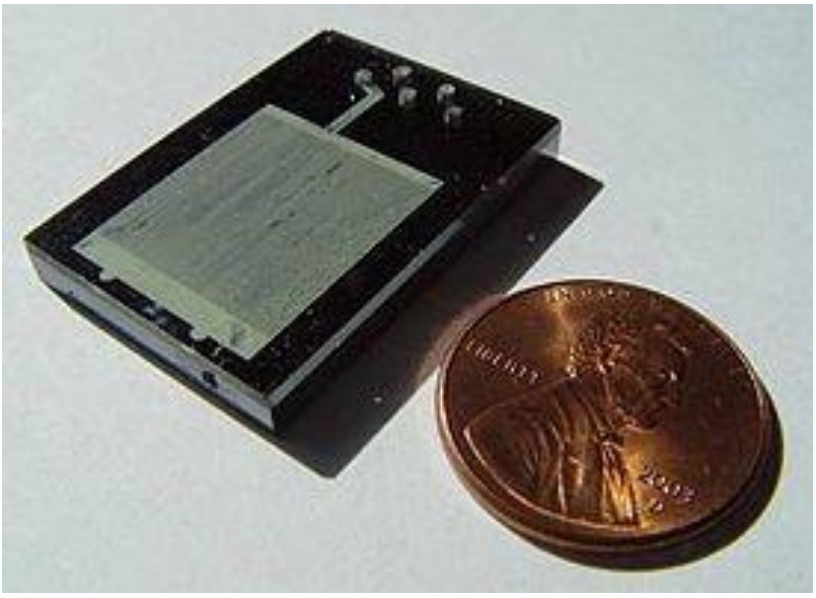

Figure 2-3 Microreactor next to coin for scale. Image source: United States DoE

In comparison with traditional reactors, microreactors occupy smaller volumes (as shown in Figure 2-3) and feature other benefits such as performance enhancement, increased temperature control and operation under continuous flow mode [63,64]. As such, there exist major incentives for the development of micro-structured chemical reactors [55,65]. However, due to their smaller size, micro-structured reactors are relatively more sensitive to the variations in the surrounding temperature and thermal modifications of their external boundaries can affect their performance [58,59]. In general, microreactors are most suited to catalytic systems featuring highly exothermic and/or endothermic reactions [55,59]. This is essential because of the fact that transport phenomena are highly enhanced in microreactors and hence thermal energy can be readily added to or removed from these systems [66,67].

Microreactors typically consist of a bundle of microchannels [68]. By filling these microchannels with porous materials, the microreactor provides a more uniform temperature distribution compared with those lacking porous inserts [69,70]. Additionally, the porous medium can serve as a means of introducing catalysts [71]. Recent examples can be found in continuous flow hydrogenation systems [72,73]. As mentioned previously, porous microreactors can be an efficient tool for processes with large heat of reactions as they offer highly improved ability to transport heat by their massive surface to volume ratio [67]. This permits a high degree of control upon the thermal conditions within the microreactor in addition to a very efficient mixing of reactants, which enables a greater degree of selectivity as compared to traditional reactors [74,75].

2.4 Analytical modelling

There are still ground for improvement of microreactor technology, which is not yet a mature technology. To aid any design improvements an understanding of the heat and mass transfer processes taking place within the microreactors is a key factor. Most microreactors consist of microchannels and therefore share their heat transfer characteristics with them. This has led to a number of studies of microchannels to obtain a better understanding of the transport processes taking place. The fluid dynamics and mass transfer behaviours of microreactors have been already subject to significant investigations [76,77]. Although there has been some works on the exchanges of heat between the microreactors and surrounding [65], the internal heat transfer aspects of these devices remain largely unexplored. The existing heat transfer analyses in microreactors have already revealed that the internal heat transfer processes could significantly affect the chemical performance of the reactor [65,78]. Further, recent studies strongly emphasised the importance of microstructure, features within the microreactor including the enclosing structure, design in the optimal functioning of microreactors [58]. Indeed, any detailed design of microstructure calls for comprehensive thermal analyses of microreactors under varying configurations. Besides, microchannels may use porous materials for further enhancement of heat transfer [55,79]. In microreactors, porous inserts are also used to introduce catalysts and increase the rate of mass transfer [80,81]. Temperature fields and heat transfer in microreactors have been already examined experimentally, e.g. Refs. [82,83]. Nevertheless, the small size of microreactors makes them a challenging medium for experimental measurements and equally amenable to numerical and theoretical investigations [84].

To aid in the design process by virtue of increasing understanding of heat transfer processes, numerical and analytical modelling techniques have been employed. To analyse a single porous reactor there are two well-known volume average approaches to follow [70]. The first traditional approach is to consider the porous solid and the fluid phases as a single phase material and specify average thermo-physical properties to each point of the porous section of the reactor [85,86]. In this relatively new approach, the solid and fluid phases within the porous medium are analysed separately, and specific thermos-physical properties are assigned to each phase.

2.4.1 LTE and LTNE

Typically, the porous inserts are attached to the walls of the channel and may vary in thickness and structural characteristics. Many investigators have examined porous microchannels

and the treatment of the heat flux at the boundary between the walls and the porous materials has received different types of treatment. The simplest way to examine such a system is by treating the fluid phase and porous matrix as a homogeneous medium [87,88], assuming that both phases are at equal temperatures. This is known as the one-equation or local thermal equilibrium (LTE) model. A more detailed, and accurate, approach is taken by the local thermal non-equilibrium (LTNE) model, which treats the solid and fluid phases as separate entities with explicit thermal properties [89]. Thus, two energy equations are required, one for each phase of the porous medium. The transport of heat in solid and fluid phases of the porous medium are co-related through an internal heat exchange, and hence their differential equations are coupled. In general, the second approach is more computationally costly than the first one. However, due to its higher accuracy, LTNE approach is deemed more suitable in micro systems [90].

In the LTNE model, the heat flux is split on the basis of the thermal conductivities of the respective phases of the porous material and their corresponding temperature gradients. This technique may be applied in a number of ways. One method of accomplishing this is referred to as Model A [91–94] and has been widely used in literature (see for example [95–98]). At the interface between the porous medium and the channel wall, parts of the wall are in contact with the fluid phase of the porous medium and other parts are in contact with the porous solid phase. Model A determines the share of each phase from the interface heat flux based on the temperature gradient and the effective thermal conductivity of each phase [91,92], as shown in equation (2-8). The use of the effective thermal conductivity of each phase accounts for the differing area of contact between each phase and the interface.

$$q_{interface} = k_{es} \left.\frac{\partial T_s}{\partial y}\right|_{interface} + k_{ef} \left.\frac{\partial T_f}{\partial y}\right|_{interface} \tag{2-8}$$

Where $q_{interface}$ is the heat flux at the interface between the wall and the porous medium, k_{es} and k_{ef} are the effective thermal conductivities of the solid and fluid phases of the porous medium respectively. Likewise, T_s and T_f are the respective temperatures of the solid and fluid phases of the porous medium and y is transverse coordinate.

It is essential to note that Model A assumes that the wall in contact with the porous medium is of zero thickness and is therefore unable to conduct heat. Other variations of this LTNE model have also been examined with a view to taking into account other effects such as variable porosity and thermal dispersion [91]. Extensive examination of these models revealed that, for many cases, Model A can represent the interface condition with the greatest accuracy [91]. Additionally, in many microreactors the transfer of mass and heat are coupled [85], so employing LTNE model can also provide a better prediction of the species concentration within the system. In general, low heat exchanges between the fluid and porous solid phase [99], internal heat generations [93] and short

lengths of flow conduits [100] can cause deviation from LTE and necessitate LTNE analysis. Importantly, almost all these effects are likely to exist in microreactors.

Early analyses of porous microchannels included LTE assumption e.g. [101] and LTNE investigation of microchannels have been only reported in recent years. Buonomo et al. [102] conducted an analytical LTNE study of forced convection in a porous microchannel with a rarefied gas flow. These authors [102] showed that heat transfer increases as Biot number increases and reaches asymptotic values.

A porous filled microchannel configuration has been investigated by Chein and co-workers in a series of numerical studies [103–105]. In these works, the equations governing the transport of momentum, heat and chemical species along with the key reactions for the reforming of methanol were solved simultaneously. The transport of heat in the porous region of the reactor was modelled on the basis of the local thermal equilibrium (LTE) model and the thermal effect of exothermic/endothermic catalytic reactions was represented by a volumetric energy source term [103]. The resultant temperature of the fluid phase and the rate of syngas production were then reported. The main purpose of these works was to understand the combined effects of heat, mass and momentum transfer in the microreactor upon the reforming process. It was concluded that the reactor performance is dominated by the configuration of the porous catalyst [103]. This numerical work was later extended to the analyses of the effects of thermal resistance upon steam reforming of methanol in microreactors [104,105]. Chein et al. [104,105] showed that to optimise the reactor it is essential to carefully minimise the thermal resistances within the system. In a separate work, Chein et al. investigated the influences of microstructure configuration and materials on the conversion rates of a micro-reformer and made a number of design suggestions [106]. These findings clearly demonstrate the significance of accurate prediction of heat transfer rates in the design of microreactors. Although the significance of the temperature fields was well demonstrated [104,106], no detailed heat transfer analysis and Nusselt number (Nu) evaluation were conducted in these investigations. The latter is of primary importance in microreactors as their proper operation is often subject to an efficient exchange of heat with an external heat sink or source [65,107]. Further, the recent advancements in the field of heat convection in partially filled porous conduits have revealed the strong effects of exothermicity on the temperature profiles and heat transfer rates within the system. Importantly, almost all existing studies on transport phenomena in porous microreactors assumed LTE in the porous region [103–106]. However, recent studies on porous channels with exothermic or endothermic processes assert that an accurate prediction of the thermal behaviour of such systems warrants a local thermal non-equilibrium (LTNE) analysis [93,97,98,108].

In their recent theoretical studies, Karimi et al. [109] and Torabi et al. [98,108] considered internal heat sources in partially-filled porous channels with varying configurations. They solved the problem under local thermal non-equilibrium (LTNE) and compared the results with those of the corresponding local thermal equilibrium analyses (LTE). This showed that the introduction of heat

sources in porous conduits could significantly undermine the assumption of local thermal equilibrium. Hence, the temperature profiles and *Nu* calculations under LTE can be highly erroneous and conduction of LTNE analysis is an essential necessity in any accurate heat transfer study of these systems. Most recently, these conclusions were further extended to nanofluid-porous systems with internal heat generations [95,97].

In another recent development, it was shown that the inclusion of thick walls of the conduit in the heat transfer analysis of microchannels results in very pronounced modifications of their thermal behaviour. Ibanez et al. [110] considered the problem of heat and fluid flow in a microchannel with thick walls. Here, constant thermal conductivity for the solid walls was assumed, and analytical expressions for the velocity and temperature fields were derived [110]. Theoretical works of Torabi et al. [86,111] on forced convection in porous microchannels showed that the finite thickness of the channel walls could significantly influence the thermal and entropic behaviours of the system. Most recently, Elliott et al. [100] investigated the thermal behaviour of a porous channel with thick walls subject to asymmetric thermal boundary conditions and internal heat sources. This work considered LTNE condition and showed that the temperature fields and Nusselt number of the system are strongly affected by the thickness of the wall and asymmetry of the boundary conditions [100]. It follows from the works of Torabi et al. [86,111] and Elliot et al. [100] that ignoring the wall thickness in porous channels and microchannels could lead to the introduction of significant errors in the calculated temperature fields and Nusselt number. As stated earlier, such errors may introduce major problems in the design and operation of microreactors. Currently, the extent of wall influences upon the thermal behaviour of the partially filled porous microchannels is still unclear. In particular, there is little comprehension on the effects of exothermicity, local non-equilibrium and thick asymmetric channel walls, while coexistence of these effects is common in microreactors.

Through considering the viscous forces in porous microchannels, Ting et al. [112] conducted an LTNE analysis on a nanofluid filled porous microchannel. This study clearly revealed that neglecting viscous dissipations in porous microchannels could result in significant overestimation of the Nusselt number [112]. The effects of nanofluid viscous dissipations upon heat transfer were also investigated in clear microchannels [113,114] and porous microchannels with internal heat generation within the solid phase [115]. These investigations showed that the inclusion of viscous dissipations is a necessity for the precise prediction of thermal processes in microchannels with liquid and nanofluid flow. The studies of Buonomo et al. [102] and Ting et al. [112–115] neglected the finite thickness of the channel wall. Although such assumption is widely made in the analysis of macro-channels, the validity of neglecting wall thickness in microchannels is less obvious. This is due to the fact that, in microchannels the channel height or diameter is very comparable to the thickness of the wall. Existing analyses in clear microchannels [116] and recent studies on porous microchannels [100,111,117] have rigorously demonstrated the significant influences of thick walls upon the heat transfer in these systems. Nonetheless, inclusion of wall effects on porous microchannels with strong axial advection has, thus far, remained unexplored.

2.4.2 Second law analysis

Similar to that in macroreactors, entropy generation in microreactors is of high significance [66]. Entropy generation minimisation is now employed widely in the design and optimisation of various thermal and thermochemical systems [118,119]. These include porous systems under LTE [120,121] and LTNE [115,122] and have been also recently extended to solid systems [119]. Investigation of the local and total entropy production highlights the sources and locations of irreversibilities, and hence illustrates the necessary design modifications [119]. The second law analyses of forced convection of heat in porous media have shown that compared to hydrodynamic irreversibilities, thermal effects have a relatively larger share of the total irreversibility of the system [119,120,122]. This finding is more pronounced for the systems under LTNE [95,97,98,108]. Expectedly, thermal irreversibilities are very strong in exothermic porous systems and are dominated by the intensity of exothermicity [98,108]. However, the existing works on entropy generation in microreactors are almost entirely limited to micro-combustors (see for example Refs. [123–125]). Notably, currently there is nearly no work on the entropic behaviours of porous micro-reactors. Exceptions to this, are the most recent works of Elliot et al. [117] and Torabi et al. [85], who investigated heat and mass transfer and entropy generation in a catalytic microreactor. Nonetheless, these analyses were one-dimensional and hence had limited applications. Thus, the existence of a gap in the studies of entropy generation in microreactors is evident. It is now well-demonstrated that microreactors are sophisticated thermochemical systems, which can feature non-straightforward entropic behaviours [104,105,126]. Further, recent investigations on porous microchannels have clearly shown the richness of the problem of entropy generation in these systems. Second law analysis of microreactors detects areas for possible performance enhancement [127] by leading to the understanding of the destruction of exergy. Entropy generation minimisation is now employed widely in the design and optimisation of various thermal and thermochemical systems [118,119].

Ideally, entropic analysis of a microreactor should include the irreversibilities by the thermal and viscous effects, mass transfer and chemical reactions. Yet, investigations of entropy generation in highly exothermic reactive flows have indicated that the total irreversibility is dominated by the thermal effects [128]. Therefore, it is expected that in microreactors exothermicity of the reactions and heat transfer characteristics of the system govern the rate of the entropy generation.

Recent works have begun to pave the way for the entropy generation analysis of microchannels and thereby for microreactors [85,117]. The conventional one-dimensional approach to the problem of entropy generation in microchannels was extended to two-dimensional analysis by Ting et al. [115,129] in their investigations of a fully filled porous microchannel. The investigations assumed LTNE and took into account viscous dissipation effect and heat sources within the fluid. In addition, Ting et al. [115,129] theoretically examined entropy generation in microchannels with inserted nanofluid-filled porous media. They took an LTNE approach and conducted a two-dimensional, analytical solutions for the temperature fields and local entropy generation [115,129]. Their results mapped the influences of different mechanisms of entropy generation in a porous microchannel. In particular, they highlighted the significance of hydrodynamic irreversibilities in cases with viscous convection of nanofluids [115]. Other theoretical works on the convection of nanofluids in heat generating/consuming porous channels demonstrated the necessity of considering LTNE for the accurate prediction of irreversibilities [95,97]. Another important factor complicating the irreversibilities of microreactors is the influences of solid thick walls. Recent studies on chemically inert microchannels have revealed the strong effects of the thick walls upon the rate of entropy generation [111,130,131]. This is essentially due to the effects of the solid thick walls upon the thermal fields in the microchannel, which in turn influences the rates of entropy generation [130]. Yet, the entropic influences of the thick walls on thermo-diffusive systems have just started to receive attention [85] and remain far from being well understood. The authors separated the contributions of local entropy generation from different sources and compared the irreversibilities from each source. In keeping with other authors [95,97,100], Ting et al. emphasized the necessity to consider LTNE when there are heat source/sinks in the system.

2.5 Computational fluid dynamics

In addition to investigations using analytical techniques, numerical methods may also be brought to bear in the study of heat and mass transport in microreactors. Limitations imposed by operating on the micro scale, such as determination of heat and mass transfer characteristics inside microchannels, create problems for experiments. Such difficulties are not pertinent to numerical methods, which can then be used to reveal these details and the results obtained may aid in either understanding or design of microsystems [132].

The focus of the investigation to be undertaken using computational fluid dynamics (CFD) is the effect of the microstructure on the mass transfer properties of a catalytic

microchannel. To accomplish this requires the implementation of a chemical mechanism that has been robustly examined and tested against experimental results. Further, this reaction must fulfil the requirement that the reaction can be heterogeneously catalysed. One reaction mechanism that meets these criterion is that of Deutschmann et al. [133]. While this reaction permits the addition of a homogeneous reaction process, such an addition would only serve to mask precisely the effects that are the subject of the study. As such, the conditions under which the model microchannel operates are those that permit only the heterogeneous reaction to take place.

2.5.1 Heterogeneous catalytic microreactors

Micro-structured reactors, or microreactors, have attracted a considerable interest for use in a wide range of technologies from distributed fuel production [59] and methanol steam reforming [60] to process intensification [58] and nanoparticle generation [61]. In addition, development of micro-combustors for the purpose of micro power generation has been examined [62]. Small characteristic lengths in microreactors, as compared to those of macro-reactors, permit significant enhancement of heat and mass transfer [66]. Of particular interest for the purposes of applying heterogeneous catalysts, is the large area to volume ratio which ensures high efficiency of transport processes [134]. Further, the resulting improved controllability of the thermal field within the microreactor allows for increased selectivity as compared to traditional reactors [74,75]. Consequently, microreactors are of interest for chemical synthesis [66,79,135] and are especially suited to highly exothermic and endothermic reactions [55,59,136]. This has led to significant inquiry into the development of micro-combustors for micro power generation This has led to significant efforts for development of micro-combustion and micro fuel processing processes that involve exothermic/endothermic catalytic reactions and micro-reformers for hydrogen and syngas production [62].

Micro-combustion devices fuelled by hydrocarbons are being investigated as the successors to conventional lithium-ion battery used in micro-propulsion [137,138]. This is primarily due to the much higher energy densities attained by hydrocarbon fuels, and indeed hydrogen, as compared to typical rechargeable batteries [137]. Catalytic combustion in such microreactors has several advantages in comparison with its larger scale counterparts. These include low temperature performance and therefore low NO_X production [139,140]. The lower temperature of operation is of significant benefit as it removes some of the restrictions on the material used in manufacturing of micro-combustor [141]. Furthermore, there are

clearly safety advantages in having combustion without flames. This flameless combustion is made possible by two main quenching mechanisms, first being radical (or chemical) and the second being thermal (or physical) quenching [62]. Radical quenching, where radical species, which allow the gas phase reaction to progress, are absorbed at the walls of the reactor where they react to form stable molecules [62,141,142]. Thermal quenching occurs due to heat loss from both the gas phase and the burner walls, due to convection and radiation for example [62,141,142]. Microreactors are susceptible to both of these leading to a marked decrease in gas phase chemistry, contributing to the lack of flames.

In addition to their potentials as portable energy sources, catalytic combustion microreactors show promise in the area of chemical synthesis. One such example, which has received considerable attention, is the catalytic partial oxidation (CPO) of methane to syngas (CO and H_2) [78,143]. This is of great interest as it provides the first step in both conversion to methanol and the Fischer-Tropsch process to produce longer chain alkanes. Often steam reforming methods are employed to produce syngas, however, it has been found that high selectivity for H_2 and CO is obtained via CPO over a Pt (or Rh) catalyst [144]. The cost of these materials is an important contributor to the reactor construction and operation costs [62]. Also, catalyst replacement is a known issue in microreactors [57], which further highlights the importance of improving catalytic activities in this type of reactor. The general relation between catalytic reactions and mass transfer process is well-established [145,146].

A great number of studies, both numerical and experimental, have been carried out investigating oxidation of methane over noble metal catalysts. It is for this reason that the combustion of methane over a platinum catalyst is the reaction of choice for this study. Experimental studies on stagnation point flow has been a key technique for elucidation of reaction kinetic parameters and has been used to determine mechanisms for numerical works [147–150]. The chemical mechanism used in this work is that proposed by Deutschmann et al. [133] which has been extensively studied and validated against experimental results. Experimental results from chemical reactions in microreactors have been obtained and favourable comparisons have been made with the numerical analyses [62,82,83]. Of these studies, the typical geometry has been cylindrical in order to represent a single channel within a catalytic monolith [141,151–153]. Other geometries frequently examined are coated foams [154], sintered spheres [155], wire gauzes [156]. The focus of these studies has not chiefly been concerned with the geometric effects.

A porous material in the form of a ceramic foam was ground to a powder and the loaded with a $LaMnO_3$ perovskite catalyst for the purpose of investigating methane combustion [154]. Tests were performed on a 30 kW pilot plant comparing different burners and catalyst deposition techniques. This technique demonstrated excellent NO_X production of less than 10 parts per million volume [154].

Studies on Al_2O_3 supported nickel catalyst for steam reforming of methane were conducted on 5mm spheres. The effect of addition of hydrogen on the sintering of these spheres was examined experimentally and concluded that sintering was absent in a H_2/N_2 atmosphere [155].

An interesting geometry was examined by de Smet at al. [157,158] who investigated a catalytic platinum gauze to determine the kinetics of carbon monoxide formation in the partial oxidation of methane and oxygen to syngas. In conjunction with experimental techniques, a two-dimensional flat plate reactor model was implemented to obtain the kinetic data. The intrinsic kinetic data of interest to de Smet et al. was that of the heterogeneous catalytic reaction and as such homogeneous gas phase reactions were not included. Quiceno et al. [156] undertook a study of surface chemistries on a three-dimensional flow field round a section of catalytic gauze incorporating the gas phase reaction in addition to the surface catalysis. It was concluded, however, that under the conditions examined the heterogeneous reactions dominated [156].

Not all microreactors are composed of straight cylindrical channels, however. Many feature bends, corners [159–163], porous inserts to improve heat transfer [164], or a myriad of forms of baffle to enhance mixing or prevent jetting [55,62,65,165]. Bluff bodies, baffles and gauzes have been examined with a view to understanding some of the effects that these geometric features have upon reacting flows [156,165]. While the study by Quiceno et al. [156] applied both the heterogeneous and homogeneous reaction schemes to their CFD simulations, only the homogeneous reaction mechanism was considered by Fan et al. in their work on bluff bodies [165]. In their work on homogeneous hydrogen combustion with bluff bodies, Yan et al. [166] observed and measured the reflux area behind the bluff body. This served to entrap more of the premixed gas fuel, thus increasing the residence time in the low velocity reflux region.

The importance of the boundary layer hydrodynamic mass transport on catalytic reactions is known to be significant [167]. This has led to advances in the area of in situ

measurements of catalytic boundary layer gas phase species concentrations [168]. By combining both numerical and non-invasive measurements such as Raman and laser induced fluorescence (LIF) measurements of OH concentration, interactions between homogeneous and heterogeneous processes can be determined [168]. In the area of interaction between thermofluids and catalyst walls four main areas of interaction between catalytic and gas phase reactions have been identified [167]. Firstly, the high heat of reaction of the catalytic process can promote the onset of homogeneous ignition. Secondly, this same ignition may become inhibited by the depletion of reactive species in the boundary layer next to the wall. Thirdly, production of major species can affect the homogeneous ignition, by either inhibiting or promoting it depending on the reaction scheme and species involved. Finally, the reactor walls can act as a sink of radical species, thus inhibiting the homogeneous reaction pathway.

2.6 Objectives

The work presented in this thesis is composed of two parts. The first part being analytical in nature and seeking to address the issues raised by the application of LTNE conditions in microreactors. This will, in short, be composed a parametric study of heat and mass transfer analysis leading into a second law investigation all performed analytically. The second part of this work involves numerical investigation into the effects of microchannel hydrodynamics on catalytic performance. These are outlined as follows.

The preceding review of literature shows that analytical modelling of transport and thermodynamic irreversibilities in porous microchannels have been now extended to LTNE and two-dimensional analyses [115,129]. The studies in reactive systems can be expanded to include homogeneous and heterogeneous reactions and investigation of combined transport of heat and mass and entropy generation. However, exothermic catalytic reactions have, thus far, been excluded from these investigations. This is, in part, due to the mathematical difficulties associated with consideration of heat release on the internal surfaces of a microchannel. More importantly, the lack of an LTNE interface model capable of considering the wall, fluid and porous solid collectively has rendered the thermal analyses of such systems impossible. The aim of this current work is to tackle these challenges through developing an analytical model of heat and mass transfer in a porous, thick-wall microreactor with exothermic catalytic reactions occurring on the internal surfaces of the walls.

The initial analytical investigative step involves first developing a one-dimensional model of a microchannel to examine the effects introduced by asymmetry of geometry in addition to asymmetry of thermal conditions. The effects of this configuration upon the thermal field and entropy generation will be studied. Once this has been completed, the problem configuration will be extended into two dimensions and include mass transfer analysis representative of production via heterogeneous catalysis. Thus, both heat and mass transfer including the Soret effect will be considered. A second law analysis will conclude the investigation of this system. To cover reactive systems in which homogeneous reactions take place, a two-dimensional analytical model featuring heat and mass transfer and including radiation effects will be developed. This will permit the examination of thermal and concentration fields within a reactive microchannel in addition to an exergy analysis. Finally, an existing phenomenological model of porous interface is extended to include the wall effects. This will permit the analytical modelling of an exothermic catalytic reaction upon the wall of the microchannel, whereby heat may flow both into the channel and into the enclosing structure itself.

In the CFD study, the hydrodynamic effects upon catalytic oxidation of methane over bluff bodies and waved surfaces are examined to determine if similar reflux zones to those encountered by Yan et al. [166] can affect heterogeneous catalysis. These geometries are analysed numerically assuming a three-dimensional flow such that any effects due to secondary flow characteristics can be captured. A detailed surface reaction scheme, after Deutschman et al. [153], is used. Gas phase reactions are ignored for the purposes of this study since the reactant mixture is highly diluted ($\phi = 0.35$) and the focus is on the heterogeneous catalytic activity. This is justified by ensuring that the dimensions of the system of interest allow for the quenching conditions mentioned previously to be met.

Chapter 3 Methodology

3.1 Analytical Methodology

At pore level, there are complicated transport phenomena that play vital roles in the macroscopic increase of heat transfer and pressure loss. Typically, heat and momentum analyses are based upon the respective transport equations that result from balance laws, the solutions to which give the required information about velocity and temperature fields. These solutions are obtained through application of the appropriate boundary conditions. In the case of porous media the complexity of the geometry involved precludes general solutions of the velocity and temperature fields from being obtained [169]. This makes analysis at the pore level very complicated and so a representative elementary volume is chosen which includes both the solid and fluid phases of the porous medium and the transport equations are integrated over this region [92]. While this invariably leads to a loss of information at the pore level, in terms of microscopic transport phenomena, the integrated quantities and associated equations do allow for an effective analysis of the porous medium concerned. The use of the technique of volume averaging provides a rigorous tool for investigation of transport phenomena in porous media. This leads to two possible avenues by which the method of volume averaging may be applied. The first, the one-equation model is averaged over a representative volume encompassing both the solid and fluid phases. While the second or two-equation model is averaged over each phase separately which leads to a specific equation for each of the solid and fluid phases [169,170].

These two main approaches are local thermal equilibrium (LTE) and local thermal non-equilibrium (LTNE) for modelling energy transport in porous media [88] and were discussed in Chapter 2. The LTE approach assumes that the solid matrix and the fluid form a homogeneous medium and so they each have identical temperatures [87]. Clearly, however, when a significant temperature difference between the solid phase and the fluid phase is present the LTE assumption breaks down [92,171]. Such conditions may arise which there are large differences in the thermo-physical properties of the fluid and solid phases leading to a significant thermal resistance between the two phases.

The assumptions that the fluid flow is steady, laminar, viscous and incompressible are in place for the studies presented in this work. Processes featuring abrupt reaction zones, separating hot and cold flows, such as those in micro-combustors [123,124] are not considered here. In addition, the porous media concerned in any of the sections is

homogenous, isotropic and fluid saturated. The porous medium is considered to be under LTNE conditions, requiring two coupled energy equations, one for each phase. Further, physical properties such as porosity, specific heat, density and thermal conductivities are invariants and thermal dispersion effects are ignored. Likewise, since the microchannels presented here are horizontal [55], gravitational effects are ignored due to the very small channel height.

Additional assumptions are made depending on the specifics of the configuration under examination in any given chapter. These are stated in the chapter concerned.

3.1.1 Transport of momentum

Under steady state and for a fully hydrodynamically developed flow in a porous medium, Darcy-Brinkman momentum equation governs the hydrodynamics of the system. That is:

$$-\frac{\partial p}{\partial x}+\mu_{eff}\frac{\partial^2 u}{\partial y^2}-\frac{\mu_f}{\kappa}u=0 \tag{3-9}$$

Since one-dimensional flow in the axial direction (x) is assumed, with velocity, u the first term represents the pressure gradient in the flow direction. The following two terms are viscous terms, the first of which is analogous to the Laplacian term in the Navier-Stokes equation, using the effective viscosity, μ_{eff} as a coefficient. This represents to what extent the vorticity generated at the walls enclosing the matrix penetrates into the flow [87]. The second is known as the Darcy term, this latter term features the fluid viscosity, μ_f divided by the permeability, κ and represents the bulk viscous resistance [87,88]. The permeability is just a scalar in this case due to the porous medium concerned being isotropic [87]. For this case involving flow of a clear fluid (designated with the subscript $f2$) the governing equation for momentum within the clear fluid is required in addition to equation (3-9) is defined as:

$$-\frac{\partial p}{\partial x}+\mu_f\frac{\partial^2 u_{f2}}{\partial y^2}=0 \tag{3-10}$$

Once again, the first term represents the pressure gradient in the direction of flow. Here the second term is the diffusive term and together with the first term is the divergence of stress.

3.1.2 Transport of thermal energy

The transport of energy in Chapters 4-6 is modelled based on the assumptions stated above and differences in configurations may require adaptation of the base model. These are described in the following sections.

3.1.2.1 One-dimensional model

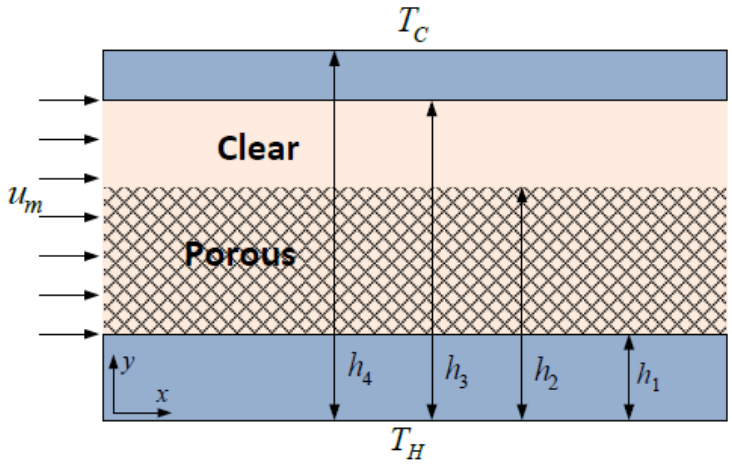

Figure 3-1 Schematic of the model microreactor with thick walls and porous insert

Transport of thermal energy for the components of the system including to the lower wall (1), the fluid ($f2$) and solid (S) phases in the porous region, the clear fluid ($f2$) above the porous region and the upper wall (2), respectively (see Figure 3-1). It should be noted that the clear fluid ($f2$) and the fluid ($f2$) are the same fluid and the nomenclature difference exists only purposes of delineating the regions in which the individual equations (below) are valid. These are expressed by the following equations:

$$k_1 \frac{\partial}{\partial y}\left[\frac{\partial T_1}{\partial y}\right] + \dot{q}_1 = 0 \tag{3-11}$$

$$k_{ef} \frac{\partial^2 T_{f1}}{\partial y^2} + h_{sf} a_{sf}\left(T_s - T_{f1}\right) + s_f = \rho C_p u_{f1} \frac{\partial T_{f1}}{\partial x} \tag{3-12}$$

$$k_{es} \frac{\partial^2 T_s}{\partial y^2} + h_{sf} a_{sf}\left(T_s - T_{f1}\right) + s_s = 0 \tag{3-13}$$

$$k_f \frac{\partial^2 T_{f2}}{\partial y^2} + s_f = \rho C_p u_{f2} \frac{\partial T_{f2}}{\partial x} \tag{3-14}$$

$$k_2 \frac{\partial}{\partial y}\left[\frac{\partial T_2}{\partial y}\right] + \dot{q}_2 = 0 \tag{3-15}$$

Transport of thermal energy in the lower and upper walls is via conduction only and this is represented by the first term in equations (3-11) and (3-15), respectively. The second terms in these equations represents a volumetric heat source. The axial conduction of heat within the walls is not essential and is ignored throughout the analysis. This is justified by noting that experimental investigations [62,77,172] revealed that the axial temperature gradient within the enclosing structure diminishes in thick wall microreactors.

Examination of equation (3-12) reveals that in addition to the conductive term, the first term in this equation, a second term representing the flow of thermal energy between the fluid and solid phases of the porous medium is required [87,91]. Here the specific surface area, a_{sf} and the fluid-to-solid heat transfer coefficient, h_{sf} are taken into account [87,91]. The fluid phase features uniform and steady internal heat generation/consumption, s_f which represents exothermicity/endothermicity of the chemical reactions [103].

It is clear that both the schematic shown in Figure 3-1 and the governing equations utilise both axial and transverse coordinates. In the study presented in Chapter 4, the profile of thermal energy is not dependent upon the axial coordinate. This reduces the aforementioned equations to a one-dimensional form as follows. On the right-hand side of the equation is the advective term, however this becomes vanishingly small when compared to the conduction and internal convection terms. Due to very low fluid velocity, the thermal Peclet number is expected to be quite low ($\mathrm{Pe}_{th} \ll 1$). Under this condition, the axial advection of heat becomes negligible in comparison with the transversal heat transfer by internal heat convection in the porous medium and conduction in the fluid and solid components of the system. This assumption was first introduced and rigorously justified by Mahmud and Fraser [173] and more recently was employed by a large number of authors [86,100,174–176]. Only very low velocities are examined and hence, the advection terms are ignored in the current analysis and the right-hand side of both fluid transport of heat equations is considered zero.

The solid phase also includes internal heat generation, s_s representing absorption of microwave and infrared waves [126,177] for example. Transport of heat in the solid phase is governed by equation (3-13) which also has conductive and interstitial heat transfer terms as the first and second terms.

Finally, the equation for heat transfer in the clear fluid region is defined by equation (3-14) which features only a conductive first term, for the reasons stated above, and a volumetric heat generation/sink term.

3.1.2.2 Two-dimensional model

For the solid walls enclosing the porous microchannel, the governing equations for heat transfer are the same as those above, but without the volumetric heat source terms. That is, equation (3-15) for the upper wall and (3-11) for the lower wall.

The transport of thermal energy within the solid and fluid phases of the microreactor are governed by the followings [115]:

$$k_{ef}\frac{\partial^2 T_f}{\partial y^2} + h_{sf}a_{sf}\left(T_s - T_f\right) + \frac{\mu_f}{\kappa}u^2 + \mu_{eff}\left(\frac{\partial u}{\partial y}\right)^2 = \rho_f C_{p,f} u\frac{\partial T_f}{\partial x} \tag{3-16}$$

$$k_{es}\frac{d^2 T_s}{dy^2} - h_{sf}a_{sf}\left(T_s - T_f\right) = 0 \tag{3-17}$$

The previous discussion justifying that the right-hand side of the energy equations for the fluid flow reducing to zero is based on very low velocity flows. For cases where a greater velocity is present, these terms become significant and so must be considered. These models only feature fully filled porous channels and as such the porous fluid phase is denoted with the subscript, f. Additionally, it has been demonstrated what the omission of viscous dissipation in microchannels can significantly overestimate the thermal performance of the system [112]. To rectify this, equation (3-16) contains terms to account for viscous dissipation in the form of the third and fourth terms. The third term accounts for internal heat generation due to the mechanical power required to push the fluid through the porous medium [112]. Whereas the fourth term arises from frictional heating in the fluid itself [112].

3.1.2.3 Radiation heat transfer

For purposes of investigating the effects of radiation heat transfer, equation (3-13) is modified to include an extra term. Volumetric heat source/sink terms are not included in either the fluid or solid phases in any of the two-dimensional analytic investigations presented in this work.

$$k_{es}\frac{\partial^2 T_s}{\partial y^2} - h_{sf}a_{sf}\left(T_s - T_f\right) - \frac{\partial q_r}{\partial y} = 0 \tag{3-18}$$

The radiation parameter, q_r in equation (3-18) takes the following form:

$$q_r = \frac{-4\,\sigma^*}{3\,\kappa^*}\frac{\partial T_s^4}{\partial y} \tag{3-19}$$

Using the Rosseland approximation [178] the last term of the energy equation for the solid phase of the porous section of the microchannel, equation (3-18), is transformed to:

$$\frac{\partial q_r}{\partial y} = -\frac{16\sigma^* T_0^3}{3\,\kappa^*}\frac{\partial^2 T_s}{\partial y^2} \tag{3-20}$$

where σ^* is the Stefan-Boltzmann constant and $\kappa^*$is the Rosseland mean extinction coefficient.

3.1.2.4 Thermo-physical properties of nanofluids

The effective viscosity for a nanofluid is modelled as a dilute suspension of small rigid spheres in a base fluid is defined by Brinkman [179] as

$$\mu_{nf} = \frac{\mu_f}{(1-\phi)^{2.5}} \tag{3-21}$$

Here ϕ is the volume fraction of the nanoparticles. This equation is an extension of Einstein's equation (valid for concentrations of up to 5%) to incorporate concentrated suspensions [180]. In this study, a nanoparticle concentration of 2% is used. The ratio of the effective thermal conductivity of the nanofluid to the thermal conductivity of the base fluid allows the former to be approximated using the Maxwell-Garnetts model [181]. That is

$$\frac{k_{nf}}{k_f} = \frac{k_p + 2k_f - 2\phi(k_f - k_p)}{k_p + 2k_f + \phi(k_f - k_p)} \tag{3-22}$$

Here the thermal conductivities of the nanofluid particles and the base fluid are represented by k_p and k_f respectively. Whereas the thermal conductivity of the nanofluid taken is k_{nf}, which is dependent on the nanofluid particle volume fraction, ϕ. In addition, the effective density and specific heat are as defined in equations (3-23) and (3-24) respectively [181] in which the same subscripts are used:

$$\rho_{nf} = \rho_f(1 - \phi) + \rho_p\phi \tag{3-23}$$

$$(\rho C_p)_{nf} = (\rho C_p)_f(1 - \phi) + (\rho C_p)_p\phi \tag{3-24}$$

3.1.3 Transport of mass

Mass transfer of chemical species is governed by the following advective-diffusive model, which takes into account contributions from the Soret effect in addition to the Fickian diffusion of species [146]. The second term on the right-hand side of equation (3-25) represents the flow of species along a temperature gradient, or Soret effect. Whereas the first term on the right-hand side represents the diffusion of species according to Fick's law. Diffusion coefficients for Fickian diffusion and thermal diffusion of species represented by D and D_T respectively. These represent the effective values of Fickian and thermal diffusion noting that diffusion coefficients are affected by porous media properties such as porosity and tortuosity rendering the diffusion of species less efficient and thus the effective values tend to be lower than the values in a clear fluid. Taking this into account a value of $D = 10^{-5}\text{cm}^2\text{s}^{-1}$ was chosen as representative [182]. The left-hand side represents the advection of species due to the one-dimensional velocity field within the channel.

$$u\frac{\partial C}{\partial x} = D\frac{\partial^2 C}{\partial y^2} - D_T\frac{\partial^2 T_f}{\partial y^2} \tag{3-25}$$

The negative sign on the right hand side of equation (3-25) arises from the fact that depending upon the relative size of the diffusive molecules and the base fluid, Soret number can be either positive or negative [146]. Here a negative sign in front of a positive D_T presents negative Soret number. It should be noted that the mass diffusion coefficient

presented above is the effective mass diffusion coefficient due to the effect of the porous medium in which it operates.

When homogeneous reactions are considered a mass generation term for the species of interest concentration, is required. Such a term modifies equation (3-25) into the following, where k_r is the generation term.

$$u\frac{\partial C}{\partial x} = D\frac{\partial^2 C}{\partial y^2} - D_T\frac{\partial^2 T_f}{\partial y^2} + k_r \tag{3-26}$$

3.1.4 Nusselt number

The Nusselt number, Nu provides a ratio of the convective to conductive heat transfer taking place across the interface between the walls and the porous fluid phase and is defined in equation (3-27) [145].

$$Nu = \frac{H_w L}{k} \tag{3-27}$$

Here, L is the characteristic length scale which in this study is taken to be the channel height. The thermal conductivity, k is that of the fluid phase of the porous medium and as such is the effective thermal conductivity. The heat transfer coefficient, H_w is defined as [145]:

$$H_w = \frac{q}{\Delta T} \tag{3-28}$$

The temperature difference in the denominator of equation (3-28) is the difference between the temperature on the interface and that of the bulk fluid, here taken to be the mean temperature over a cross-section of the channel.

3.1.5 Sherwood number

In a manner analogous to Nusselt number, Sherwood number provides a measure of the mass transfer taking place at the surface [145]. It is, again, a ratio of the convective mass transport to the diffusive mass transport. Since the reaction taking place on the catalyst surface is of zeroth order, the reaction rate is not dependent upon the concentration of either reactants or products (provided that enough reactant exists to allow for the reaction to

proceed). This permits the mass transfer coefficient, H_m to be calculated according to the relation [145];

$$H_m = \frac{k_R}{C_0 - \overline{C}} \tag{3-29}$$

Similarly, to the temperature difference in equation (3-28), the concentration difference is explicitly defined as the difference between the concentration of species on the wall and the average over the channel. With the mass transfer coefficient thus defined, and using the microchannel height $(h_1 + h_2)$ as the characteristic length scale, the Sherwood number, Sh may now be expressed in the following form [145]:

$$Sh = \frac{(h_1 + h_2)H_m}{D} \tag{3-30}$$

3.1.6 Second law analysis

The exergy analysis in this study can be split into two areas of interest. Firstly, there is the volumetric entropy generation rate which reveals the entropy that is produced in any one region of the system. This permits examination of how the entropy in any one component of the system under investigation compares to the other components. Secondly, there is the total entropy of the system. As the name suggests, this is the entropy generated integrated over the whole system. This technique displays how the entire system responds entropically to any change in one of the parameters describing the system. In both local and total entropy equations, there will be variations defined by the system under investigation. For one-dimensional studies, there will be only the appropriate terms for that case, similarly for the cases involving nanofluids.

3.1.6.1 Local entropy generation

In order to examine the entropy generation of the system, contributions from different sources are considered separately and then as a whole, to yield an understanding as to how each component contributes to the whole. Following the literature [114,129,183], the system has been split into contributions from the walls, the solid porous matrix heat transfer, the fluid heat transfer, the fluid friction component and that of the mass transfer. The volumetric entropy generations for the system are expressed by the equations listed below [85,115,184].

The term, $\dot{S}'''_{1,2}$ accounts for the entropy generation in the walls, with the subscript 1 or 2 defining which wall is being described.

$$\dot{S}'''_{1,2} = \frac{k_{1,2}}{T_{1,2}^2}\left[\left(\frac{\partial T_{1,2}}{\partial x}\right)^2 + \left(\frac{\partial T_{1,2}}{\partial y}\right)^2\right] \tag{3-31}$$

Entropy generation in the solid phase of the porous medium due to heat transfer may be calculated using $\dot{S}'''_S$.

$$\dot{S}'''_S = \frac{k_{es}}{T_S^2}\left[\left(\frac{\partial T_S}{\partial x}\right)^2 + \left(\frac{\partial T_S}{\partial y}\right)^2\right] - \frac{h_{sf}a_{sf}\left(T_S - T_f\right)}{T_S} \tag{3-32}$$

Similarly, $\dot{S}'''_f$ is defined to find the entropy generation rate in the fluid phase.

$$\dot{S}'''_f = \frac{k_{ef}}{T_f^2}\left[\left(\frac{\partial T_f}{\partial x}\right)^2 + \left(\frac{\partial T_f}{\partial y}\right)^2\right] + \frac{h_{sf}a_{sf}\left(T_S - T_f\right)}{T_f} \tag{3-33}$$

The first term on the right-hand side of equations (3-31), (3-32), and (3-33) defines the contribution to the volumetric entropy generation due to the heat transfer from the thermal gradients [115]. Additionally, the contribution due to the interstitial heat transfer is represented by the second term on the right-hand side of equations (3-32) and (3-33) [115]. It is noted that the thermal energy source terms do not explicitly appear in equations. Yet, they indirectly affect the entropy generation through altering the temperature fields [119].

In the porous fluid phase and the clear fluid phase where applicable, the fluid friction irreversibility is accounted for by $\dot{S}'''_{FF}$ [115].

$$\dot{S}'''_{FF} = \frac{\mu_f}{\kappa\, T_f}u^2 + \frac{\mu_{eff}}{T_f}\left(\frac{du}{dy}\right)^2 \tag{3-34}$$

Examination of equation (3-16) reveals that the terms on the right-hand side of equation (3-34) represent the entropy contribution due to viscous dissipation of heat. These terms represent the contributions from their counterparts in equation (3-16).

Irreversibility sources due to the combination of concentration gradients are represented by the first term on the right-hand side of equation (3-35). Whereas those due to

mixed thermal and concentration gradients are found in the second term on the right-hand side of the equation for the diffusive entropy generation, $\dot{S}_{DI}'''$ [184].

$$\dot{S}_{DI}''' = \frac{R\,D}{C}\left[\left(\frac{\partial C}{\partial x}\right)^2 + \left(\frac{\partial C}{\partial y}\right)^2\right] + \frac{R\,D}{T_f}\left[\left(\frac{\partial C}{\partial x}\right)\left(\frac{\partial T_f}{\partial x}\right) + \left(\frac{\partial C}{\partial y}\right)\left(\frac{\partial T_f}{\partial y}\right)\right] \tag{3-35}$$

Here R is the specific gas constant.

3.1.6.2 Total entropy

For the total entropy generation in the microreactor, S_{Tot}, the sum of the parts of volumetric entropy generation in the ranges in which they are valid is integrated over the volume of the channel. The contributions from the walls are then added. The limits of integration in equation (3-36) will be dependent on the configuration under investigation to include the entire region in both the axial and transverse directions. This gives a numerical value for the total entropy for any given configuration, and is obtained using the following equation:

$$S_{Tot} = \int_{-1}^{1}\int_{0}^{1}\sum S_i\,dxdy, \qquad i = 1, s, f, FF, DI, 2. \tag{3-36}$$

3.2 Numerical methodology

Chemical micro-reactors often use microchannels with the diameters of several hundred micrometres [55,62]. Since this characteristic length scale is significantly longer than the molecular mean free path [62], the Knudsen number (the ratio of the mean free path to the characteristic length) is sufficiently small such that continuum theory is still applicable. Having established this important criterion, governing equations need to be determined. The three-dimensional models used in this investigation were developed using the computational fluid dynamics (CFD) software STAR CCM+ (version 12.04.010). A finite-volume method was applied to the governing equations detailed below to develop their numerical solutions. Detailed surface reaction chemistry (see section 3.2.2) mechanisms interface with the CFD aspect of the software to allow study of the interaction between fluid hydrodynamics and surface catalytic activity.

3.2.1 Multi-component gas flow

The governing equations used in the CFD analysis commence with the following. Continuity of mass:

$$\frac{\partial \rho u}{\partial x}+\frac{\partial \rho v}{\partial y}+\frac{\partial \rho w}{\partial z}=0, \tag{3-37}$$

in which ρ is the mass density and x, y, z are the Cartesian coordinates with respective velocity components, u, v, w. Similarly, the conservation of momentum for a Newtonian fluid is written in the following form wherein the dynamic viscosity μ refers to that of the gaseous mixture.

$$\frac{\partial \rho u u}{\partial x}+\frac{\partial \rho u v}{\partial y}+\frac{\partial \rho u w}{\partial z}+\frac{\partial p}{\partial x}-\frac{\partial}{\partial x}\left[2\mu\frac{\partial u}{\partial x}-\frac{2}{3}\mu\left(\frac{\partial u}{\partial x}+\frac{\partial v}{\partial y}+\frac{\partial w}{\partial z}\right)\right] - \frac{\partial}{\partial y}\left[\mu\left(\frac{\partial u}{\partial y}+\frac{\partial v}{\partial x}\right)\right]-\frac{\partial}{\partial z}\left[\mu\left(\frac{\partial u}{\partial z}+\frac{\partial w}{\partial x}\right)\right]=0, \tag{3-38}$$

$$\frac{\partial \rho v u}{\partial x}+\frac{\partial \rho v v}{\partial y}+\frac{\partial \rho v w}{\partial z}+\frac{\partial p}{\partial y}-\frac{\partial}{\partial y}\left[2\mu\frac{\partial v}{\partial y}-\frac{2}{3}\mu\left(\frac{\partial u}{\partial x}+\frac{\partial v}{\partial y}+\frac{\partial w}{\partial z}\right)\right] - \frac{\partial}{\partial z}\left[\mu\left(\frac{\partial v}{\partial z}+\frac{\partial w}{\partial y}\right)\right]-\frac{\partial}{\partial x}\left[\mu\left(\frac{\partial u}{\partial y}+\frac{\partial v}{\partial x}\right)\right]=0, \tag{3-39}$$

$$\frac{\partial \rho w u}{\partial x}+\frac{\partial \rho w v}{\partial y}+\frac{\partial \rho w w}{\partial z}+\frac{\partial p}{\partial z}-\frac{\partial}{\partial z}\left[2\mu\frac{\partial w}{\partial z}-\frac{2}{3}\mu\left(\frac{\partial u}{\partial x}+\frac{\partial v}{\partial y}+\frac{\partial w}{\partial z}\right)\right] - \frac{\partial}{\partial x}\left[\mu\left(\frac{\partial u}{\partial z}+\frac{\partial w}{\partial x}\right)\right]-\frac{\partial}{\partial y}\left[\mu\left(\frac{\partial v}{\partial z}+\frac{\partial w}{\partial y}\right)\right]=0. \tag{3-40}$$

Conservation of species is expressed through a set of partial differential equations using the species mass fraction, Y_i of species, i in the multicomponent mixture and that of species molar production rate, $\hat{R}_i$ (see section 3.2.2).

$$\frac{\partial \rho u Y_i}{\partial x}+\frac{\partial \rho v Y_i}{\partial y}+\frac{\partial \rho w Y_i}{\partial z}=\frac{\partial J_i}{\partial x}+\frac{\partial J_i}{\partial y}+\frac{\partial J_i}{\partial z}+\hat{R}_i. \tag{3-41}$$

Here, $\hat{R}_i$ is the net rate of production of species, i due to surface chemical reactions (see section 3.2.2) and J_i, is the diffusive flux in the direction j determined by Fick's law as follows:

$$J_{i,j} = \rho D_{i,m} \nabla Y_i, \tag{3-42}$$

where $D_{i,m}$ is the molecular diffusivity of species, i.

Energy balance within the model is described using the enthalpy, h, of the multi-component mixture and h_i, is the enthalpy of each species, i.

$$\frac{\partial \rho uh}{\partial x} + \frac{\partial \rho vh}{\partial y} + \frac{\partial \rho wh}{\partial z} \tag{3-43}$$
$$= \frac{\partial}{\partial x}\left(\lambda \frac{\partial T}{\partial x} - \sum_i^{N_g} h_i J_{i,x}\right) + \frac{\partial}{\partial y}\left(\lambda \frac{\partial T}{\partial y} - \sum_i^{N_g} h_i J_{i,y}\right)$$
$$+ \frac{\partial}{\partial z}\left(\lambda \frac{\partial T}{\partial z} - \sum_i^{N_g} h_i J_{i,z}\right) + u\frac{\partial p}{\partial x} + v\frac{\partial p}{\partial y} + w\frac{\partial p}{\partial z} + \sum_i^{N_g} h_i \hat{R}_i$$

The gas density, ρ is calculated using the ideal gas law and the molecular diffusivity, $D_{i,m}$ is determined using kinetic theory. The gas enthalpy is defined as follows.

$$\mathrm{h} = \sum_{\mathrm{i}}^{\mathrm{N_g}} \mathrm{h_i Y_i}\,, \tag{3-44}$$

In which;

$$h_i = h_{i,REF} + \int_{T_{REF}}^{T} C_{p,i}\, dT, \tag{3-45}$$

where $C_{p,i}$ is the specific heat capacity at constant pressure, and T_{REF} is the standard state temperature of species, i.

3.2.2 Surface chemical reactions

The surface chemistry of oxidation of an ultra-lean methane and air mixture is described using a series of elementary chemical reactions using the mean-field approximation [185].

Table 3-1 Surface reaction mechanism after Deutschmann et al [133]. The units of A_r are in mol, cm and s, whereas E_a and ε are given in kJmol^{-1}. Sticking coefficients are indicated with an *.

	Reaction	A_r	β	E_a (kJmol^{-1})	ε_i, μ_i (kJmol^{-1})
1)	H_2 + 2Pt(s) ⇒ 2H(s)	4.60 x 10^{-2}*			$\mu_{Pt(s)} = -1$
2)	2H(s) ⇒ 2Pt(s)+ H_2	3.70 x 10^{21}	0.0	67.4	$\varepsilon_{H(s)} = 6$
3)	H + Pt(s) ⇒ H(s)	1.00*			
4)	O_2 + 2Pt(s) ⇒ 2O(s)	1.80 x 10^{21}	-0.5	0.0	
5)	O_2 + 2Pt(s) ⇒ 2O(s)	2.30 x 10^{-2}*			
6)	2O(s) ⇒ 2Pt(s) + O_2	3.70 x 10^{21}	0.0	213.2	$\varepsilon_{O(s)} = 60$
7)	O + Pt(s) ⇒ O(s)	1.00*			
8)	H_2O + Pt(s) ⇒ H_2O(s)	0.75*			
9)	H_2O(s) ⇒ H_2O +Pt(s)	1.00 x 10^{13}	0.0	40.3	
10)	OH + Pt(s) ⇒ OH(s)	1.00*			
11)	OH(s) ⇒ OH + Pt(s)	1.00 x 10^{13}	0.0	192.8	
12)	O(s) + H(s) ⇔ OH(s) +Pt(s)	3.70 x 10^{21}	0.0	11.5	
13)	H(s) + OH(s) ⇔ H_2O(s) + Pt(s)	3.70 x 10^{21}	0.0	17.4	
14)	OH(s) + OH(s) ⇔ H_2O(s) + O(s)	3.70 x 10^{21}	0.0	48.2	
15)	CO + Pt(s) ⇒ CO(s)	8.40 x 10^{-1}*			$\mu_{Pt(s)} = 1$
16)	CO(s) ⇒ CO + Pt(s)	1.00 x 10^{13}	0.0	125.5	
17)	CO_2(s) ⇒ CO_2 + Pt(s)	1.00 x 10^{13}	0.0	20.5	
18)	CO(s) + O(s) ⇒ CO_2(s) + Pt(s)	3.70 x 10^{21}	0.0	105.0	
19)	CH_4 + 2Pt(s) ⇒ CH_3(s) + Pt(s)	1.00 x 10^{-2}*			$\mu_{Pt(s)} = 0.3$
20)	CH_3(s) + Pt(s) ⇒ CH_2(s) + H(s)	3.70 x 10^{21}	0.0	20.0	
21)	CH_2(s) + Pt(s) ⇒ CH(s) + H(s)	3.70 x 10^{21}	0.0	20.0	
22)	CH(s) + Pt(s) ⇒ C(s) +H(s)	3.70 x 10^{21}	0.0	20.0	
23)	C(s) + O(s) ⇒ CO(s) + Pt(s)	3.70 x 10^{21}	0.0	62.8	
24)	CO(s) + Pt(s) ⇒ C(s) + O(s)	1.00 x 10^{18}	0.0	184.0	

This mechanism is based on that proposed by Deutschmann et al. [133] (see also http://www.detchem.com/mechanisms) and is used here without modification (see Table 3-1) using surface CHEMKIN [186]. The units of A_r are the same as those of the rate constant, thus it is specific to each individual reaction. The concentration is in moles per

cm^3, and the timescale is in seconds thus A_r has units of powers of mol, s, and cm. In the current investigation, the catalytic surface is that of the noble metal, platinum with a surface site density, Γ of 2.72 x 10^{-8} kmol m^{-2} consistent with Ref. [153].

In this surface chemistry model, the gas species mass fractions at the surface are assumed to be the same as their mass fractions at the centre of the cell volume. The ratio of the catalytic area to that of the geometry area is given by the washcoat factor, γ_w. This serves as a measure of surface roughness and in this study is defined as unity, indicating a smooth surface. The gas phase and surface species molar production rates for species, i with surface concentration $[X_i]$ are given by;

$$\hat{R}_i = \sum_{r=1}^{N_{reac}} g_{i,r} k_r \prod_{i=1}^{N_s+N_g+N_b} [X_i]^{\upsilon_{(i,r)}} \tag{3-46}$$

where N_{reac} represents the number of surface reactions, this includes both adsorption and desorption (see Table 3-1 for further details). The stoichiometric coefficients of the products minus that of the reactants for the reaction is denoted by $g_{i,r}$ with the stoichiometric coefficient of the species acting at the rate exponent, $\upsilon_{(i,r)}$. The total number of gas phase species, surface species and bulk species are represented by N_g, N_s and N_b, respectively. The site species concentration $[X_i]$ is defined as:

$$[X_i] = \Theta_i \, \Gamma. \tag{3-47}$$

Reaction rate coefficient, k_r for any given surface reaction, r may be dependent on surface site coverage, Θ_i of species, i in addition to temperature and is given by the modified Arrhenius reaction expression:

$$k_r = A_r T^{\beta_r} exp\left(-\frac{E_a}{RT}\right) \prod_{i=1}^{N_s} 10^{\eta_{ir}} \Theta_i^{\mu_{ir}} exp\left(-\frac{\varepsilon_{ir}\Theta_i}{RT}\right), \tag{3-48}$$

in which the universal gas constant, R, the temperature exponent, β, the activation energy, E_a, and the pre-exponential factor of the reaction, A_r of reaction, r are empirical factors defined by the chemical mechanism. The surface coverage dependence for species, i and reaction, r is considered by the terms, η_{ir}, μ_{ir}, and ε_{ir}, [186] values for which are given in

Table 3-1 for specific reactions to which they apply. The adsorption rate constant for species i is modelled using the Motz-Wise correction rate expression [187].

The surface coverage represents the portion of possible surface sites that are covered by species, i, at any given time. This can be calculated using the surface reaction rates via the relation:

$$\frac{\partial \Theta_i}{\partial t} = \frac{\hat{R}_i}{\Gamma} \qquad \left(i = N_g + 1, \ldots, N_g + N_s\right). \tag{3-49}$$

Clearly, under steady state condition, the variation of surface coverage with time for species, i will be zero. Thus, the system of equations can be solved to generate the values for both the surface coverage and surface mass flux.

3.2.3 Numerical techniques

The conservation equations in the preceding sections were solved using a finite volume method. A second-order upwind discretisation scheme is used on the transport equations. The resulting equations are solved using the SIMPLE algorithm.

The complex chemistry model deals with the chemical reaction scheme and employs a stiff ordinary differential equation solver, Sundials CVODE for the equations dealing with the chemical composition. The CVODE solver evaluates reaction rates and their analytical Jacobian, which are then integrated. An operator splitting algorithm is used to separate the species transport equation from these stiff chemical reaction equations. Since the steady state is used in the numerical simulations presented, an artificial time step is introduced based on convection and diffusion fluxes in a given cell.

Chapter 4 One-dimensional model of heat transfer in microreactors

4.1 Introduction

Microreactors build upon the technological progress in the general fields of microchannels and micro-fluids to accommodate homogenous or heterogonous chemical reactions [65,79]. These devices offer massively increased surface to volume ratio and highly improved transport of heat and mass, which make them attractive for the processes with large heat of reaction [67]. The volume of fluid inside the microreactor is usually very small. However, the fluid velocity in the channel may vary from few centimetres to tens of centimetres per second [76]. This together with the variations in the fluid type renders a wide range of operational parameters (e.g. Reynolds and Peclet numbers) in microreactors [76].

The fluid dynamics and mass transfer behaviours of microreactors have been already subject to significant investigations, see for example [76,77] for reviews of literature. Although there has been some works on the exchanges of heat between the microreactors and surrounding [65], the internal heat transfer aspects of these devices remain largely unexplored. This is surprising as the few existing heat transfer analyses in microreactors have already revealed that the internal heat transfer processes could significantly affect the chemical performance of the reactor [65,78]. Further, recent studies strongly emphasised the importance of microstructure design in the optimal functioning of microreactors [58]. Indeed, any detailed design of microstructure calls for comprehensive thermal analyses of microreactors under varying configuration.

Microreactors often include a collection of microchannels, in which the chemical reactions take place [55,79]. An inherent characteristic of a microchannel is the non-negligible influence of the channel walls on the thermal behaviour of the system [111,188]. Hence, a complete heat transfer analysis of any microchannel system should include heat conduction within the microchannel walls. Besides, microchannels may use porous materials for further enhancement of heat transfer [55,79]. In microreactors, porous inserts are also used to introduce catalysts and increase the rate of mass transfer [80,81]. Typically, these porous inserts are attached to the walls of the channel and may vary in thickness and structural characteristics.

Given these points, the current study aims to provide an analytical view of the first and second law behaviours of a simple, yet representative, model of a microreactor with highly exothermic or endothermic reactions. The focus of the study is on the thermal aspects and hence mass transfer and reactions are ignored, while the effects of the latter are represented by an energy source term. Further, the influences of the absorption of microwaves or infrared waves [177] are represented by another energy source term within the solid phase of the microstructure. The composite system, including a partial porous insert and thick asymmetric walls, is then analysed theoretically through a local non-equilibrium approach.

4.2 Analytical solution

4.2.1 Configuration and assumptions

Figure 4-1 shows a schematic view of the problem under investigation. The fluid (reactants) enters a two-dimensional microchannel confined between parallel slabs of solid walls with different thicknesses and subject to constant but unequal temperatures on the external surfaces. The channel is partially filled by a porous insert attached to the lower wall. The thickness of this insert varies and so does the thickness of the thick walls. The configuration under investigation is therefore geometrically and thermally asymmetric. The existence of porous insert significantly increases the thermal diffusivity of the microchannel.

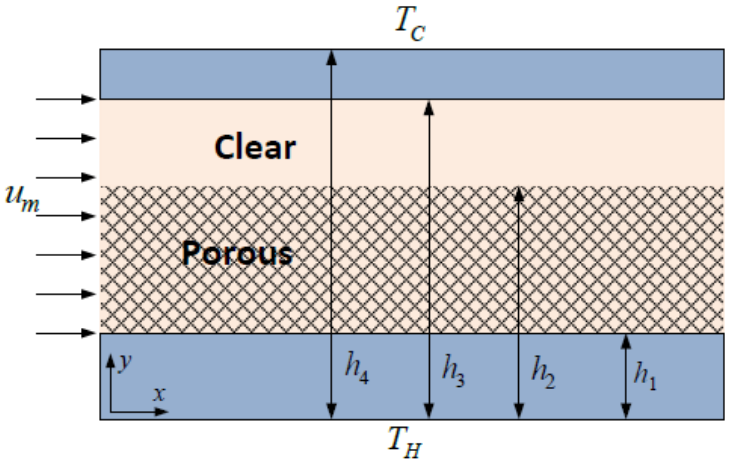

Figure 4-1 Schematic of the model microreactor with thick walls and porous insert

The following assumptions are made throughout the current study.

- The thermal model of microreactor, shown in Figure 4-1, excludes mass transfer and chemical reactions and is exclusively concerned with the hydrodynamic, thermal and entropic behaviours of the system.

- The porous medium is homogenous, isotropic and fluid saturated. The fluid phase features uniform and steady internal heat generation/consumption, which represents exothermicity/endothermicity of the chemical reactions [103]. The solid phase also includes internal heat generation representing absorption of microwave and infrared waves [126,177].

- The fluid flow is steady, laminar, viscous and incompressible, satisfying the no-slip boundary conditions on the wall. Further, thermally and hydrodynamically fully developed conditions hold in both open and porous regions. Furthermore, physical properties such as porosity, specific heat, density and thermal conductivities are invariants and thermal dispersion effects are ignored [189,190].

- Due to the submillimeter transverse dimension of the system, the Rayleigh number and therefore natural convection effects are negligibly small. Further, thermal emissivity is assumed small and radiative heat transfer is ignored.

- Due to very low velocity flow considered in this study, the effects due to fluid friction are assumed sufficiently small that the effects of viscous dissipation are negligible and are therefore ignored.

The current analysis is concerned with those processes, which feature volumetrically almost uniform reactions [103–105]. Processes with abrupt reaction zones, separating hot and cold flows, such as those encountered in micro-combustion [165] are not considered. As a result, the axial conduction of heat within the walls is not essential and is ignored throughout the analysis. This is further justified by noting that experimental investigations [62,77,172] revealed that the axial temperature gradient within the microstructure diminishes in thick wall microreactors. Hence, the axial heat conduction in the configuration shown in Figure 4-1 is insignificant.

4.2.2 Boundary conditions

The separate phases of the system are indicated for their various properties by the subscripts where appropriate. The convention employed herein is that the lower wall uses

subscript (1), the porous solid (S), the porous fluid ($f1$), the clear fluid ($f2$), and the upper wall (2). Where a term is the effective thermal conductivity of the solid porous phase has subscript of (es). Likewise, the term is the effective thermal conductivity of the porous fluid phase has subscript of (ef). Employing Darcy-Brinkman model, the equations for the transport of momentum in the porous and clear regions, respectively, are given by equations (3-9) and (3-10).

Since the flow is one dimensional, the velocity only varies in the axial direction and is independent of the transverse direction in accordance with the previously stated assumptions. As such, the partial derivatives of the velocity field are equivalent to the full derivatives and the partial differential equations become ordinary differential equations. With two second-order ordinary differential equations, four boundary conditions are required for solution. These are:

$$y = h_1: \qquad u_{f1} = 0 \tag{4-50}$$

$$y = h_2: \qquad \mu_{eff}\frac{\partial u_{f1}}{\partial y} = \mu_f \frac{\partial u_{f2}}{\partial y}, \qquad u_{f1} = u_{f2} \tag{4-51}$$

$$y = h_3: \qquad u_{f2} = 0 \tag{4-52}$$

As discussed in Chapter 3, the advection terms on the right hand side of equations thermal energy equations for the fluid flows become vanishingly small when compared to the conduction and internal convection terms. Hence, the advection terms are ignored in the current analysis. This results in the transformation of the governing equations (3-12) and (3-14) into the following:

$$k_{ef}\frac{d^2T_{f1}}{dy^2} + h_{sf}a_{sf}\left(T_s - T_{f1}\right) + s_f = 0 \qquad h_1 \le y < h_2 \tag{4-53}$$

$$k_f\frac{d^2T_{f2}}{dy^2} + s_f = 0 \qquad h_2 \le y < h_3 \tag{4-54}$$

The boundary conditions at the outside limits of the walls are:

$$y = h_4 \qquad T_2 = T_C \tag{4-55}$$

$$y = 0 \qquad T_1 = T_H \tag{4-56}$$

In addition to these, he following conditions representing the interface conditions are required for closure of the system [98,100,108].

$$y = h_1: \quad T_1 = T_s = T_{f1}, \qquad k_1 \left.\frac{dT_1}{dy}\right|_{y=h_1} = k_{ef} \left.\frac{dT_{f1}}{dy}\right|_{y=h_1} + k_{es} \left.\frac{dT_s}{dy}\right|_{y=h_1} \tag{4-57}$$

$$y = h_2: \quad T_{f2} = T_s = T_{f1}, \qquad k_f \left.\frac{dT_{f2}}{dy}\right|_{y=h_2} = k_{ef} \left.\frac{dT_{f1}}{dy}\right|_{y=h_2} + k_{es} \left.\frac{dT_s}{dy}\right|_{y=h_2} \tag{4-58}$$

$$y = h_3: \quad T_2 = T_{f2}, \qquad k_2 \left.\frac{dT_2}{dy}\right|_{y=h_3} = k_{ef} \left.\frac{dT_{f1}}{dy}\right|_{y=h_3} \tag{4-59}$$

4.2.3 Nusselt number

In accordance with the discussion in Chapter 3, the Nusselt number, Nu can be written in the following form [98,108] using the channel width as the characteristic length scale:

$$Nu = \frac{2(h_3 - h_1)q_w}{k_f(T_{f1,w} - T_{f,m})} \tag{4-60}$$

Where;

$$T_{f,m} = \frac{1}{(h_3 - h_1)u_m}\left(\int_{h_1}^{h_2} u_{f1}T_{f1}\, dy + \int_{h_2}^{h_3} u_{f2}T_{f2}\, dy)\right) \tag{4-61}$$

$$u_m = \frac{1}{(h_3 - h_1)}\left(\int_{h_1}^{h_2} u_{f1}\, dy + \int_{h_2}^{h_3} u_{f2}\, dy\right) \tag{4-62}$$

$$q_w = k_1 \left.\frac{dT_1}{dy}\right|_{y=h_1} \tag{4-63}$$

4.2.4 Entropy equations

To complete a second law analysis, the general entropy equations described in Chapter 3 need to be adapted to encompass the specifics of this configuration. The resultant equations for the local entropy rate across all components of the system can be written as follows [98,108,119].

$$\dot{S}_1''' = \frac{k_1}{T_1^2}\left(\frac{dT_1}{dy}\right)^2 \qquad 0 < y < h_1 \qquad (4\text{-}64)$$

$$\dot{S}_{f1}''' = \frac{k_{ef}}{T_{f1}^2}\left(\frac{dT_{f1}}{dy}\right)^2 + \frac{h_{sf}a_{sf}\left(T_S - T_{f1}\right)}{T_S T_{f1}} + \frac{\mu_f}{\kappa\, T_{f1}}{u_{f1}}^2 + \frac{\mu_{eff}}{T_{f1}}\left(\frac{du_{f1}}{dy}\right)^2 \qquad h_1 < y < h_2 \qquad (4\text{-}65)$$

$$\dot{S}_S''' = \frac{k_{es}}{T_S^2}\left(\frac{dT_S}{dy}\right)^2 - \frac{h_{sf}a_{sf}\left(T_S - T_{f1}\right)}{T_S T_{f1}} \qquad h_1 < y < h_2 \qquad (4\text{-}66)$$

$$\dot{S}_{f2}''' = \frac{k_f}{T_{f2}^2}\left(\frac{dT_{f2}}{dy}\right)^2 + \frac{\mu_f}{T_{f2}}\left(\frac{\partial u_{f2}}{\partial y}\right)^2 \qquad h_2 < y < h_3 \qquad (4\text{-}67)$$

$$\dot{S}_2''' = \frac{k_2}{T_2^2}\left(\frac{dT_2}{dy}\right)^2 \qquad h_3 < y < h_4 \qquad (4\text{-}68)$$

4.2.5 Dimensionless equations

The following dimensionless parameters are introduced to enable further physical analysis.

$$\theta_1 = \frac{T_1}{T_C}, \quad \theta_s = \frac{T_s}{T_C}, \quad \theta_{f1} = \frac{T_{f1}}{T_C}, \quad \theta_{f2} = \frac{T_{f2}}{T_C}, \quad \theta_2 = \frac{T_2}{T_C}, \quad \theta_H = \frac{T_H}{T_C}, \qquad (4\text{-}69)$$

$$Y = \frac{y}{h_4},\ Y_1 = \frac{h_1}{h_4}, \quad Y_2 = \frac{h_2}{h_4}, \quad Y_3 = \frac{h_3}{h_4}, \quad Q_1 = \frac{\dot{q}_1 {h_4}^2}{k_1 T_C}, \quad Q_2 = \frac{\dot{q}_2 {h_4}^2}{k_2 T_C},$$

$$\omega_s = \frac{s_s {h_4}^2}{k_{es} T_C}\ ,\ \omega_f = \frac{s_f {h_4}^2}{k_{es} T_C}, \quad U_{f1} = \frac{u_{f1}}{u_r}, \quad U_{f2} = \frac{u_{f2}}{u_r}, \quad u_r = -\frac{h_4^2}{\mu_f}\frac{\partial p}{\partial x},$$

$$k = \frac{k_{es}}{k_{ef}} = \frac{(1-\varepsilon)k_s}{\varepsilon k_f}, \qquad Bi = \frac{h_{sf} a_{sf} {h_4}^2}{k_{es}}, \quad Br = \frac{\mu_f {u_r}^2}{T_C k_{es}}, \quad k_{e1} = \frac{k_{ef}}{k_1},$$

$$k_{e2} = \frac{k_{ef}}{k_2}, \quad Da = \frac{\kappa}{{h_4}^2}$$

Substituting the above parameters into the governing equations (3-9) to (3-11), (3-13), (3-15), (4-53), and (4-54) results in the non-dimensional equations for the transport of momentum and thermal energy. Explicitly, applying parameters from equation (4-69) to the momentum equations (3-9) and (3-10) results in the following dimensionless forms.

$$1 + \frac{1}{\varepsilon}\frac{d^2 U_{f1}}{dY^2} - \frac{U_{f1}}{Da} = 0 \qquad Y_1 < Y \leq Y_2 \qquad (4\text{-}70)$$

$$1 + \frac{d^2 U_{f2}}{dY^2} = 0 \qquad Y_2 < Y \leq Y_3 \qquad (4\text{-}71)$$

The associated boundary conditions, equations (4-50) to (4-52) are likewise transposed to yield the following:

$$Y = Y_1: \qquad U = 0 \qquad (4\text{-}72)$$

$$Y = Y_2: \qquad \frac{1}{\varepsilon}\frac{\partial U_{f1}}{\partial Y} = \frac{\partial U_{f2}}{\partial Y} \qquad U_{f1} = U_{f2} \qquad (4\text{-}73)$$

$$Y = Y_3: \qquad U = 0 \qquad (4\text{-}74)$$

Similarly, the equations for the transport of heat (equations (3-11), (3-13), (3-15), (4-53), and (4-54)) reduce to the following:

$$\frac{d}{dY}\left[\frac{d\theta_1}{dY}\right] + Q_1 = 0 \qquad 0 < Y \leq Y_1 \qquad (4\text{-}75)$$

$$\frac{1}{k}\frac{d^2\theta_{f1}}{dY^2} + Bi\left(\theta_s - \theta_{f1}\right) + \omega_f = 0 \qquad Y_1 < Y \leq Y_2 \qquad (4\text{-}76)$$

$$\frac{d^2\theta_s}{dY^2} - Bi\left(\theta_s - \theta_{f1}\right) + \omega_s = 0 \qquad Y_1 < Y \leq Y_2 \qquad (4\text{-}77)$$

$$\frac{1}{\varepsilon k}\frac{d^2\theta_{f2}}{dY^2} + \omega_f = 0 \qquad Y_2 < Y \leq Y_3 \qquad (4\text{-}78)$$

$$\frac{d}{dY}\left[\frac{d\theta_2}{dY}\right] + Q_2 = 0 \qquad Y_3 < Y \leq 1 \qquad (4\text{-}79)$$

Furthermore, the thermal boundary conditions on the outer edges of the walls, equations (4-55) and (4-56) become:

$$Y = 0: \qquad \theta_1 = \theta_H \qquad (4\text{-}80)$$

$$Y = 1: \qquad \theta_2 = 1 \qquad (4\text{-}81)$$

The thermal interface conditions, equations (4-57) to (4-59) reduce to;

$$Y = Y_1: \quad \theta_1 = \theta_s = \theta_{f1} \quad \left.\frac{d\theta_1}{dY}\right|_{Y=Y_1} = k_{e1}\left.\frac{d\theta_{f1}}{dY}\right|_{Y=Y_1} + k\,k_{e1}\left.\frac{d\theta_s}{dY}\right|_{Y=Y_1} \qquad (4\text{-}82)$$

$$Y = Y_2: \quad \theta_{f1} = \theta_s = \theta_{f2} \quad \left.\frac{d\theta_{f2}}{dY}\right|_{Y=Y_2} = \varepsilon\left.\frac{d\theta_{f1}}{dY}\right|_{Y=Y_2} + k\,\varepsilon\left.\frac{d\theta_s}{dY}\right|_{Y=Y_2} \qquad (4\text{-}83)$$

$$Y = Y_3: \quad \theta_2 = \theta_{f2} \quad \left.\frac{d\theta_2}{dY}\right|_{Y=Y_3} = \frac{k_{e2}}{\varepsilon}\left.\frac{d\theta_{f2}}{dY}\right|_{Y=Y_3} \qquad (4\text{-}84)$$

Utilising the dimensionless parameters in equations (4-69), the dimensionless Nusselt number is given by the following relations.

$$Nu = \frac{2\varepsilon(Y_3 - Y_1)}{k_{e1}(\theta_{f1}(Y_1) - \theta_{f,m})}\left.\frac{d\theta_1}{dY}\right|_{Y=Y_1} \qquad (4\text{-}85)$$

Where,

$$\theta_{f,m} = \frac{1}{(Y_3 - Y_1)U_m}\left(\int_{Y_1}^{Y_2} U_{f1}\theta_{f1}\, dY + \int_{Y_2}^{Y_3} U_{f2}\theta_{f2}\, dY\right) \tag{4-86}$$

$$U_m = \frac{1}{(Y_3 - Y_1)}\left(\int_{Y_1}^{Y_2} U_{f1}\, dY + \int_{Y_2}^{Y_3} U_{f2}\, dY\right) \tag{4-87}$$

$$Q_w = \left.\frac{d\theta_1}{dY}\right|_{Y=Y_1} \tag{4-88}$$

Upon normalisation using the dimensionless variables given in equation (4-69) the dimensionless local volumetric entropy generation rate, N_{Si} (for $i = 1, 2, f1, f2, s$) is given by for each individual phase:

$$N_{S1} = \frac{1}{{\theta_1}^2}\left(\frac{d\theta_1}{dY}\right)^2 \qquad 0 < Y \leq Y_1 \tag{4-89}$$

$$N_{Sf1} = \frac{k_{e1}}{\theta_{f1}^2}\left(\frac{d\theta_{f1}}{dY}\right)^2 + \frac{kk_{e1}Br\left(\theta_s - \theta_{f1}\right)^2}{\theta_s\theta_{f1}} + \frac{kk_{e1}BrU_{f1}^2}{Da\theta_{f1}} + \frac{kk_{e1}Br}{\theta_{f1}}\left(\frac{dU_{f1}}{dY}\right)^2 \qquad Y_1 < Y \leq Y_2 \tag{4-90}$$

$$N_{SS} = \frac{kk_{e1}}{\theta_s^2}\left(\frac{d\theta_s}{dY}\right)^2 + \frac{kk_{e1}Bi\left(\theta_s - \theta_{f1}\right)^2}{\theta_s\theta_{f1}} \qquad Y_1 < Y \leq Y_2 \tag{4-91}$$

$$N_{Sf2} = \frac{k_{e1}}{\varepsilon\theta_{f2}^2}\left(\frac{d\theta_{f2}}{dY}\right)^2 + \frac{kk_{e1}Br}{\theta_{f2}}\left(\frac{dU_{f2}}{dY}\right)^2 \qquad Y_2 < Y \leq Y_3 \tag{4-92}$$

$$N_{S2} = \frac{k_{e1}}{k_{e2}{\theta_2}^2}\left(\frac{d\theta_2}{dY}\right)^2 \qquad Y_3 < Y \leq 1 \tag{4-93}$$

Finally, the dimensionless volumetric averaged entropy generation rate, N_t is defined as

$$N_t = \int_0^1 N_{Si}\, dY. \tag{4-94}$$

4.2.6 Velocity profiles

The normalised velocity equation for the clear fluid region equation (4-71) is readily solved to reveal the following velocity profile,

$$U_{f2} = \frac{-Y^2}{2} + A_1 Y + A_2. \tag{4-95}$$

Nevertheless, equation (4-70) is more complicated, though may be solved using though may be solved using standard techniques for the solution of a second order differential equation. Application of boundary conditions (4-72) to (4-74) allow the determination of the constants. Its analytical solution results in the following velocity profile for the fluid in the porous region:

$$U_{f1} \tag{4-96}$$
$$= \frac{-2(2A_2 - 2Da + 2A_1 Y_2 - Y_2^2)\, cosh\left(\frac{z}{2}(Y - Y_1)\right)}{cosh(2zY_1) - cosh(2zY_2) + sinh(2zY_1) - sinh(2zY_2)}$$
$$+ \frac{cosh\left(\frac{z}{2}(Y + Y_1 - 2Y_2)\right) sinh\left(\frac{z}{2}(Y - Y_1)\right)}{cosh(2zY_1) - cosh(2zY_2) + sinh(2zY_1) - sinh(2zY_2)} \left[\left(cosh\big(z(Y_1 + Y_2)\big) + sinh\big(z(Y_1 + Y_2)\big)\right)\right]$$

Where A_1 and A_2 are constants and $z = \sqrt{\frac{\varepsilon}{Da}}$.

4.2.7 Temperature profiles

Equations (4-76) and (4-77) may be decoupled by increasing the order of derivatives to form a new set of differential equations in a manner that each equation contains only one dependent variable, either θ_s or θ_{f1}. This gives rise to the following decoupled equations for the solid and fluid phases, respectively.

$$\theta_s''''(Y) - Bi(k+1)\theta_s''(Y) - Bik\big(\omega_f + \omega_s\big) = 0 \tag{4-97}$$

$$\theta_{f1}''''(Y) - Bi(k+1)\theta_{f1}''(Y) - Bik\big(\omega_f + \omega_s\big) = 0 \tag{4-98}$$

Since these equations are fourth order in θ_s and θ_{f1}, two more boundary conditions for each of θ_s and θ_{f1} are required for the closure of the system. The first of each of these is obtained by evaluating the second order derivative terms of equations (4-76) and (4-77) at $Y = Y_2$ and applying the conditions of equation (4-83) to yield:

$$\theta_{f1}''(Y_2) = -k\omega_f, \qquad \theta_s''(Y_2) = -\omega_s. \tag{4-99}$$

Obtaining the remaining conditions requires taking the derivative of equations (4-76) and (4-77) with respect to Y and evaluating them at $Y = Y_2$. After some algebraic manipulations, the following equations result to complete the closure of the system:

$$\theta_{f1}'''(Y_2) = -Bik\left(\theta_s'(Y_2)(1+k) - \frac{1}{\varepsilon}\theta_{f2}'(Y_2)\right) \tag{4-100}$$

$$\theta_s'''(Y_2) = Bi\left(\theta_s'(Y_2)(1+k) - \frac{1}{\varepsilon}\theta_{f2}'(Y_2)\right) \tag{4-101}$$

The system of equations (4-75), (4-78), (4-79), (4-97) and (4-98) can now be solved analytically. The resulting general solutions for the temperature distributions in the lower solid wall, the porous solid phase, the fluid inside porous phase, the clear fluid and the upper solid wall are, respectively, governed by:

$$\theta_1(Y) = \frac{1}{2}(-Q_1Y^2 + 2\theta_H + 2B_1Y) \tag{4-102}$$

$$\theta_s(Y) = -\frac{k(\omega_f + \omega_s)Y^2}{2(1+k)} + \frac{e^{\alpha Y}B_2}{\alpha^2} + \frac{e^{-\alpha Y}B_3}{\alpha^2} + B_4 + B_5Y \tag{4-103}$$

$$\theta_{f1}(Y) = -\frac{k(\omega_f + \omega_s)Y^2}{2(1+k)} + \frac{e^{\alpha Y}B_6}{\alpha^2} + \frac{e^{-\alpha Y}B_7}{\alpha^2} + B_8 + B_9Y \tag{4-104}$$

$$\theta_{f2}(Y) = -\frac{1}{2}k\omega_f\varepsilon Y^2 + B_{10} + 2B_{11}Y \tag{4-105}$$

$$\theta_2(Y) = \frac{1}{2}(-Q_2Y^2 + Y(2 + Q_2 - 2B_{12}) + 2B_{12}) \tag{4-106}$$

where B_1 to B_{12} are constants and $\alpha = \sqrt{Bi(k+1)}$.

In order to find the particular solutions to the above equations, the boundary and interface conditions (equations (4-80) to (4-84), (4-99) to (4-101)) need to be used. The algebraic manipulations required to elucidate the coefficients for equations (4-102) to (4-106) are rather substantial. To handle this, Wolfram Mathematica was employed to solve the expressions analytically and deliver the constants listed above. These constants are particularly involved and very lengthy whilst simultaneously not particularly enlightening and therefor are not shown here.

4.2.8 LTE Temperature solution

In order to obtain the LTE equations governing the temperature distribution of the system in the porous region, it is first necessary to add equations (4-76) and (4-77). This results in;

$$\frac{1}{k}\theta_{f1}'' + \theta_s'' + \omega_f + \omega_s = 0. \tag{4-107}$$

Local thermal equilibrium condition implies the temperature of the solid and fluid phases of the porous medium are equal. Thus, $\theta_s = \theta_{f1} = \theta_p$, where θ_p is the temperature function of the porous medium under LTE condition. This permits expressing the one-equation model as

$$\left(\frac{1}{k} + 1\right)\theta_P'' + \omega_f + \omega_s = 0. \tag{4-108}$$

Equation (4-108) is subject to the following boundary conditions

$$\theta_1(Y_1) = \theta_P(Y_1), \qquad \theta_{f2}(Y_2) = \theta_P(Y_2), \tag{4-109}$$

$$\theta_{f2}'(Y_2) = (\varepsilon + \varepsilon k)\theta_P'(Y_2), \qquad \theta_1'(Y_1) = (k_{e1} + \mathrm{k}k_{e1})\theta_P'(Y_1). \tag{4-110}$$

Rearranging and integrating equation (4-108) and the system of equations (4-75), (4-78), (4-79) and applying boundary conditions (4-109) and (4-110) yields the LTE temperature distribution, which reads

$$\theta_P(Y) = -\frac{k(\omega_f + \omega_s)Y^2}{2(1+k)} + C_{1P}Y + C_{2P}, \tag{4-111}$$

where $C_{1P}$and C_{2P} are constants. They are not shown here in expanded form as they are substantial and the included details do not serve to further illuminate.

4.3 Validation

It is well established that by increasing the internal heat exchanges within the porous insert the temperature difference between the solid and fluid phases diminishes [89,109]. Thus, under this condition, the system is brought towards local thermal equilibrium. The Biot number (Bi) is a measure of internal heat exchanges in the porous medium and therefore at high Biot numbers the LTE and LTNE solutions presented in Sections 4.2.7 and 4.2.8 should approach each other. This validation method has been employed previously in the analyses of similar problems, e.g. [100], and can be also used in the current theoretical work. Figure 4-2a shows the solid phase temperature profile across the system derived through LTNE calculations at $Bi = 100$ and compare those with their corresponding values calculated under LTE assumption. A similar comparison is made in Figure 4-2b for the LTE and LTNE models to calculate the Nusselt number. Different values of the surface temperature ratio have been considered in these figures. The excellent agreements between the two approaches observed in Figure 4-23a and b confirm the validity of the mathematical solutions of Section 4.2.

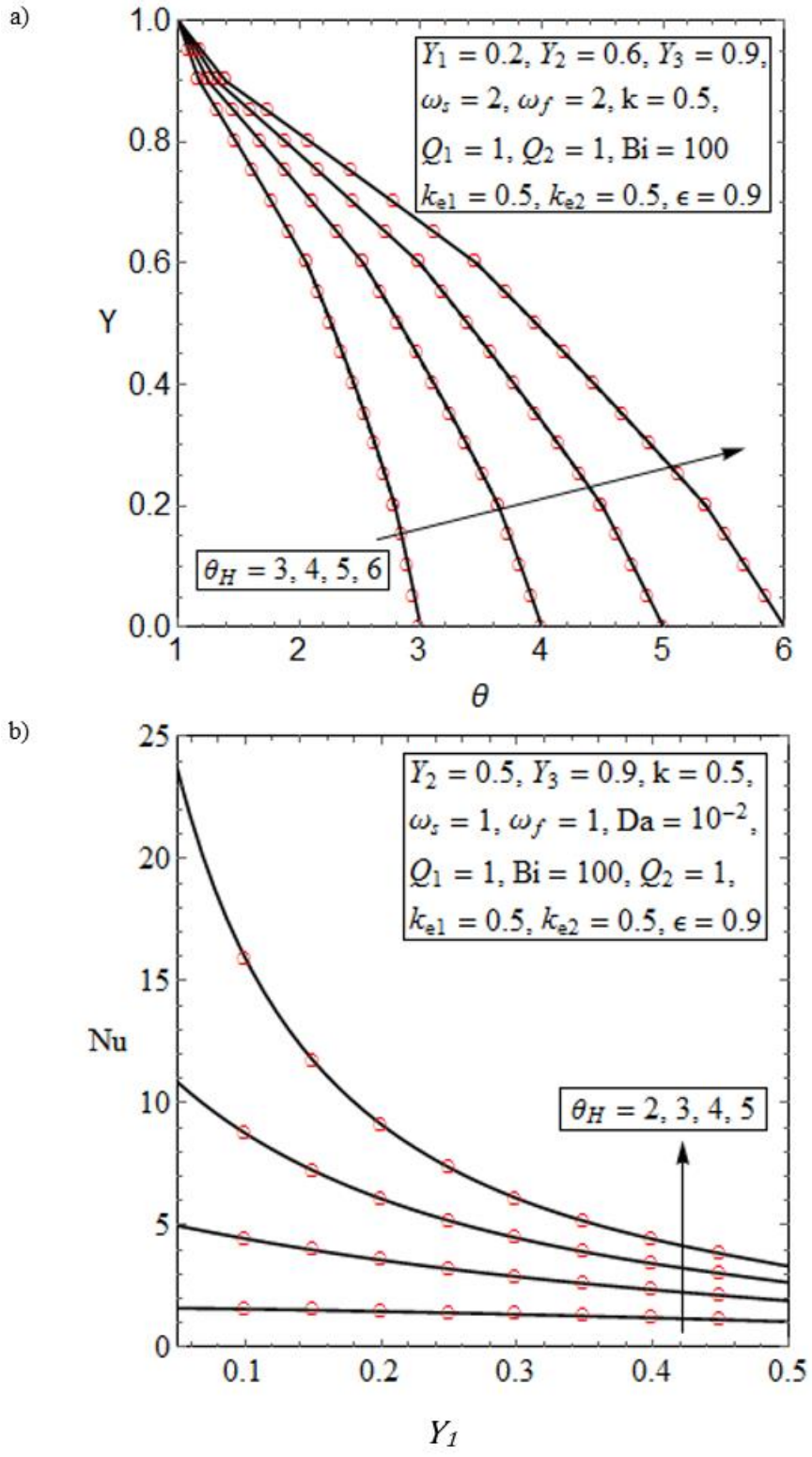

Figure 4-2 a) - Temperature distribution showing LTNE solution as solid black line and LTE solution as red dots for various values of the lower wall temperature, $\boldsymbol{\theta_H}$ and b) - Variation in Nusselt number versus varying lower wall thickness, with the LTNE solution as the solid black line and the LTE solution as the red dots for various values of the lower wall temperature, $\boldsymbol{\theta_H}$.

4.4 Temperature distributions

The problem under investigation is applied to four main test cases on the basis of the exothermicity source terms. Table 4-1 summarises these cases. Case 1 includes a source term in the solid phase of the porous medium and no exothermicity in the fluid. This case is a representation of the processes enhanced by external radiation of microwaves or other sources of electromagnetic waves [126,177]. Examining the definition of ω_s it can be seen that with T_C = 30ºC, h_4 = 1mm, and a k_{es} of order of magnitude 1-10 then a solid phase heat source term, s_S would be of order of magnitude approximately 100 kW/m^3. This is easily accomplished with either the aforementioned mechanisms or a radioactive source. In Case 2, heat is generated within the fluid phase, which represents a large group of exothermic or endothermic chemical reactions [2]. The definition of ω_f is identical to that of ω_s with the exception that a fluid phase source term is involved instead of a solid phase one. As such any chemical reaction with an enthalpy of reaction of the order of 10-100 kJmol^{-1} would be sufficient. Consider, for example, a one molar aqueous solution would contain about 1000 moles of solute in one cubic metre. In Case 3, both solid and fluid phases include thermal energy source terms. Case 4, however, is a model of a microchannel flow without any thermochemical activity. This provides a basic test case for comparison with the other three cases. In all of the temperature and local entropy generation plots provided in this investigation, the solid line is the specification of the system for the solid phase in that point, and the dashed line is the specification of the system for the fluid phase. In the porous medium of the microchannel, as LTNE model has been used, both solid and dashed lines are seen.

Table 4-1 Summary of the internal heat generations in the investigated test cases.

	ω_s	ω_f
Case 1	2	0
Case 2	0	2
Case 3	2	2
Case 4	0	0

Further, throughout the proceeding discussions the thickness of different components of the system are specified indirectly through determining the values of the three parameters h_1, h_2 and h_3 (see Figure 4-1). The default values for the parameters within this study are detailed in Table 4-2. These values will be used for all figures unless otherwise stated. The hydrodynamics of configuration shown in Figure 4-1 has been previously analysed by Torabi et al. [191]. In short, the velocity distribution includes zero velocity on the walls and smooth transition from channel flow to that in the porous insert. Further discussion about the hydrodynamics of the problem can be found in Refs. [191,192] and is not repeated here.

Table 4-2 Dimensionless parameters and the associated default values

Dimensionless Parameter		Default Value
Symbol	Name	
Bi	Biot Number	0.5
Br	Brinkman number	10
Da	Darcy Number	10^{-3}
k	Porous thermal conductivity ratio	2
k_{e1}	Lower wall thermal conductivity ratio	0.1
k_{e2}	Upper wall thermal conductivity ratio	0.1
Q_1	Volumetric heat source in lower wall	1
Q_2	Volumetric heat source in upper wall	1
Y_1	Lower wall thickness	0.2
Y_2	Porous insert thickness	0.5
Y_3	Upper wall thickness	0.8
ϵ	Porosity	0.9
θ_H	Lower wall temperature	3

Geometrical configuration of the microchannel is expected to strongly affect the temperature distributions within the system. Figure 4-3 to Figure 4-8 investigate the extent of these effects through varying the thicknesses of the lower wall (Figure 4-3 and Figure 4-4), the porous insert (Figure 4-5 and Figure 4-6) and the upper wall (Figure 4-7 and Figure 4-8).

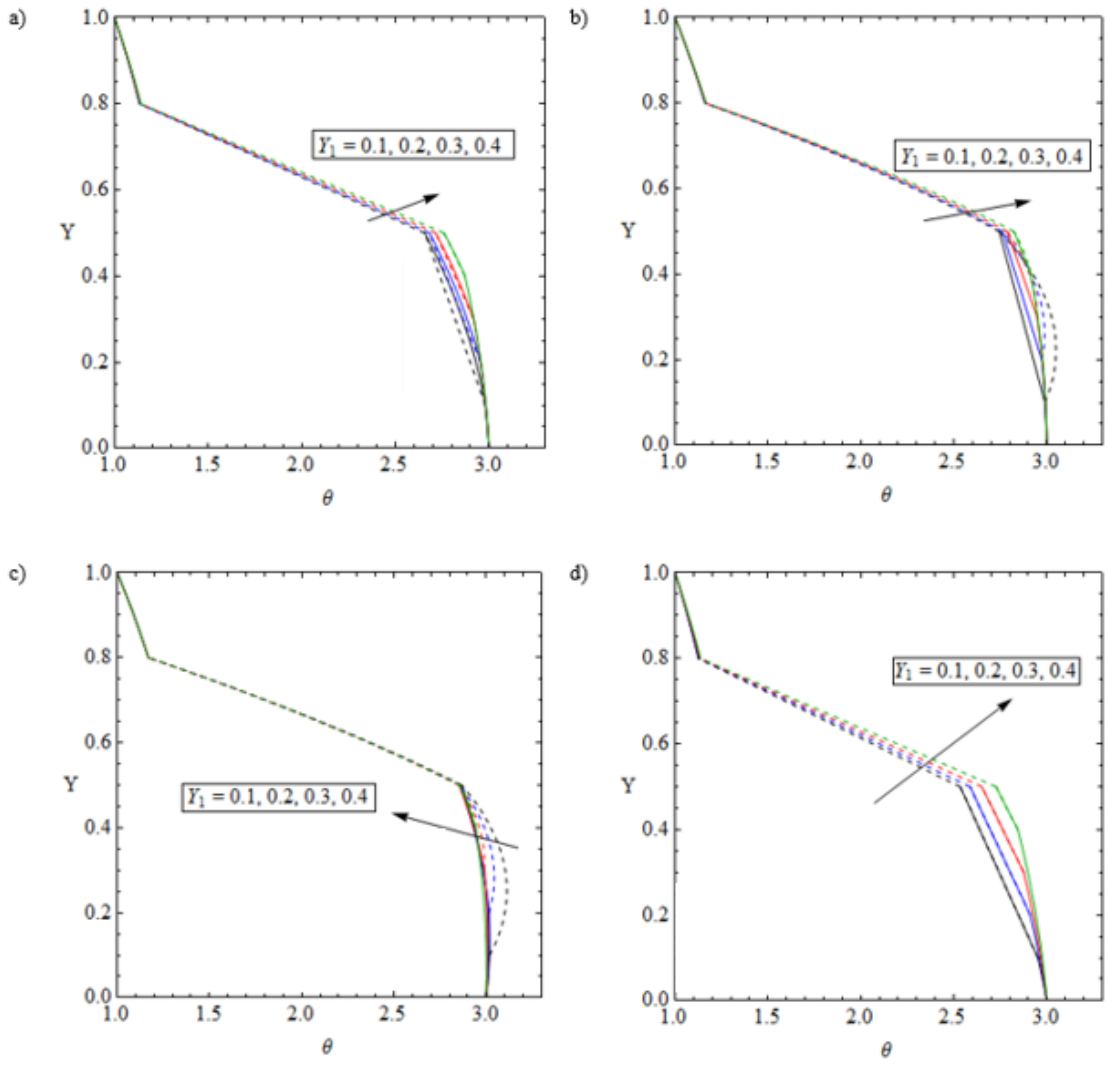

Figure 4-3 Temperature distribution with various values of the lower wall thickness number, $\boldsymbol{Y_1}$ for a) Case 1, b) Case 2, c) Case 3, and d) Case 4. Dashed line represent fluid phase, solid lines represent solid phase.

These figures show the profile of the non-dimensional solid and fluid temperatures across the system under the four test cases specified in Table 4-1 and a similar set of other parameters. The temperature profiles of the entire system have been shown in Figure 4-3, Figure 4-5, and Figure 4-7 . For clarity Figure 4-4 , Figure 4-6 , and Figure 4-8 are focused on the porous region.

Figure 4-3 d to Figure 4-8 d clearly show that for Case 4 with no exothermicity, the temperature profile features a simple behaviour under all investigated configurational variations. This includes a linear temperature distribution in all components of the system, which is a manifestation of classical conductive systems. Further, the fluid and solid temperature difference always remains negligible implying the domination of LTE in this particular case. Due to the fluid flow being extremely slow, and only conductive heat transfer occurring as described in Chapter 3, the linear conductive thermal field is observed.

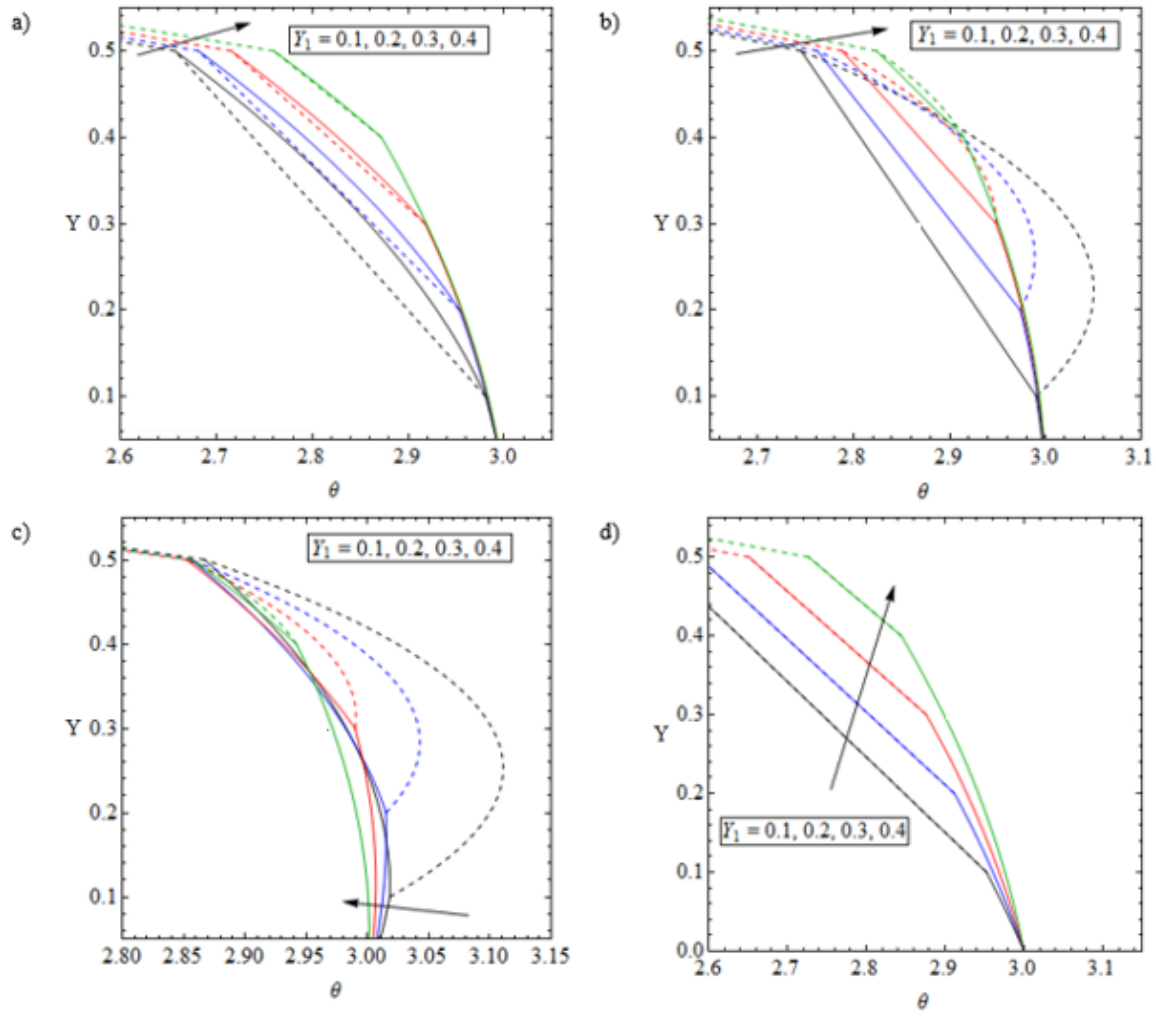

Figure 4-4 Temperature distribution with various values of the lower wall thickness number, $\boldsymbol{Y_1}$ focus on the porous region for a) Case 1, b) Case 2, c) Case 3, and d) Case 4. Dashed line represent fluid phase, solid lines represent solid phase.

However, the situation is significantly altered by the introduction of exothermicity in test Cases 1-3. Addition of internal heat generation to the solid phase of the porous insert, in Case 1, makes this phase hotter than the adjacent fluid phase.

This behaviour can be equally seen in part a) of Figure 4-3 to Figure 4-8 . Increasing the lower wall thickness in Figure 4-3 a and Figure 4-4 a reduces the temperature difference between the solid and fluid phases and therefore the system approaches local equilibrium state. As the lower wall thickness increases, the thickness of the porous insert decreases and so the quantity of heat generated by the volumetric source in the solid phase likewise decreases. This leads to the observed effect in Figure 4-5 a and Figure 4-6 a whereby the temperature difference between the solid and fluid phases decreases with increasing lower wall thickness.

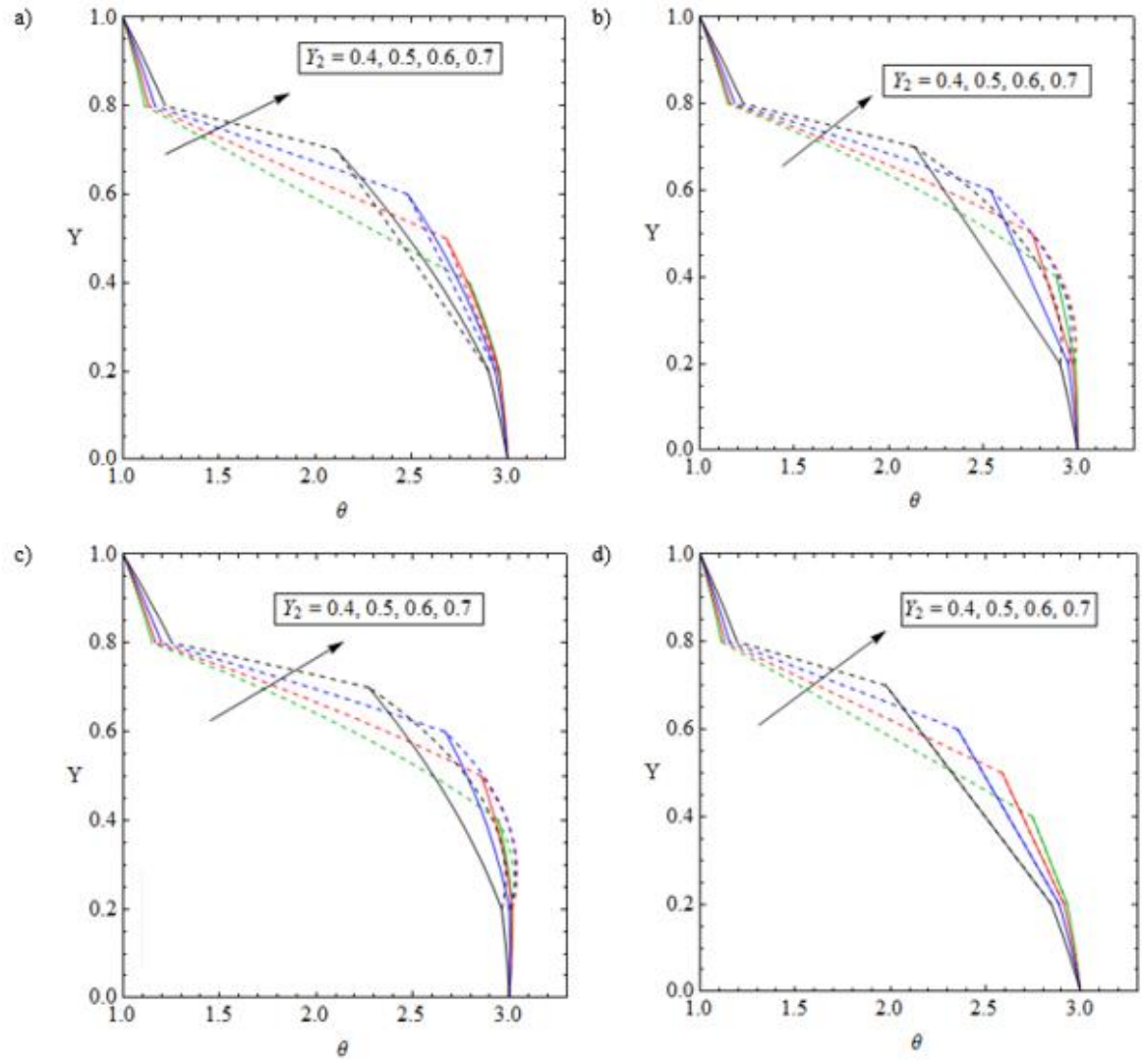

Figure 4-5 Temperature distribution with various values of the Porous insert thickness number, $\boldsymbol{Y_2}$ for a) Case 1, b) Case 2, c) Case 3, and d) Case 4. Dashed line represent fluid phase, solid lines represent solid phase.

Similarly decreasing the thickness of porous insert in Figure 4-5 a and Figure 4-6 a has the same effect, the corresponding reduction of volumetric heat source reduces the degree to which the temperature is augmented in the solid phase as compared to the fluid phase.

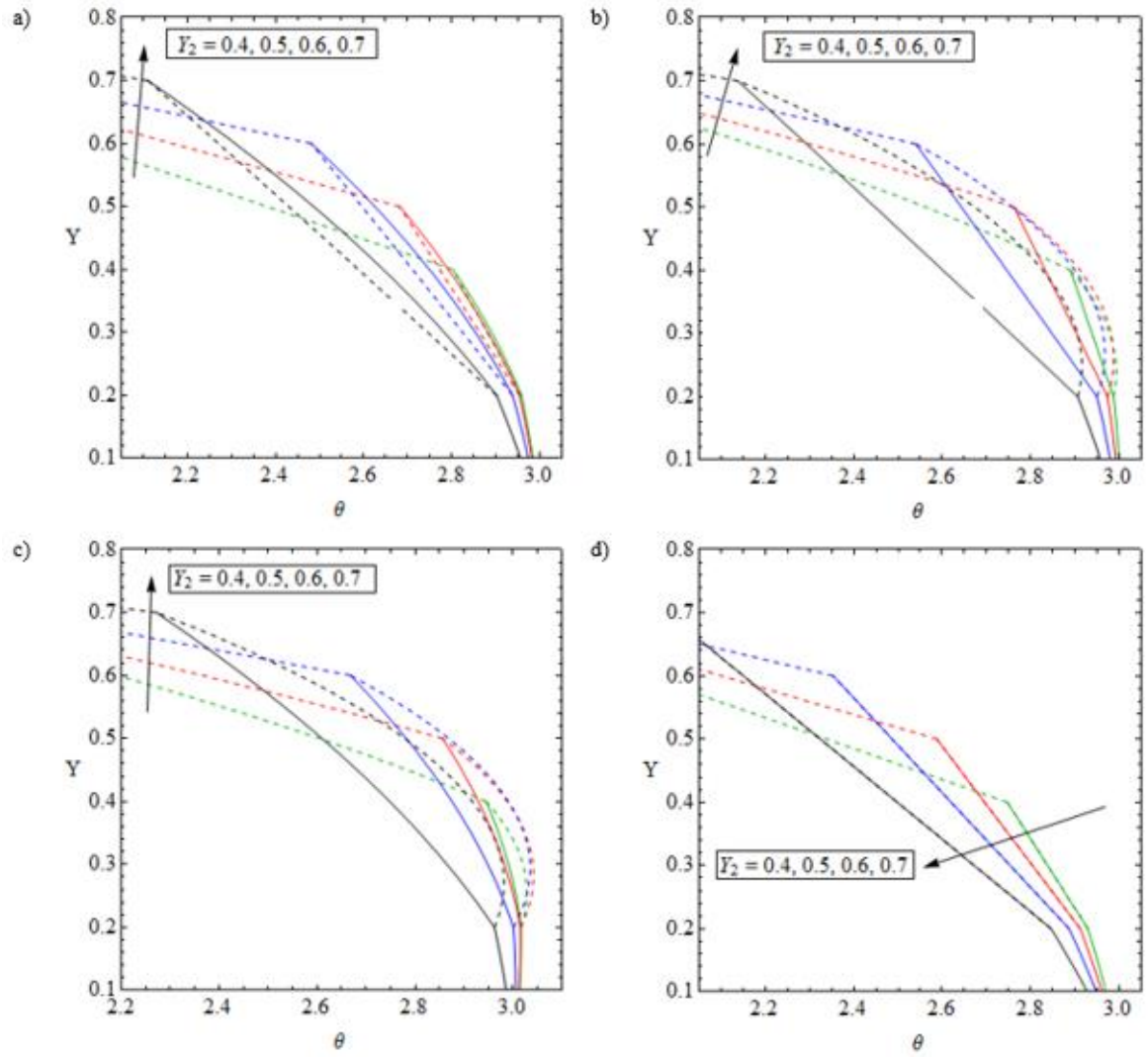

Figure 4-6 Temperature distribution with various values of the porous insert thickness number, $\boldsymbol{Y_2}$ focussing on the porous insert for a) Case 1, b) Case 2, c) Case 3, and d) Case 4. Dashed line represent fluid phase, solid lines represent solid phase.

The same applies to Figure 4-5 a and Figure 4-6 a, in which as the thickness of the porous insert increases and the total volume of the microchannel is occupied by the porous material LTNE becomes more dominant.

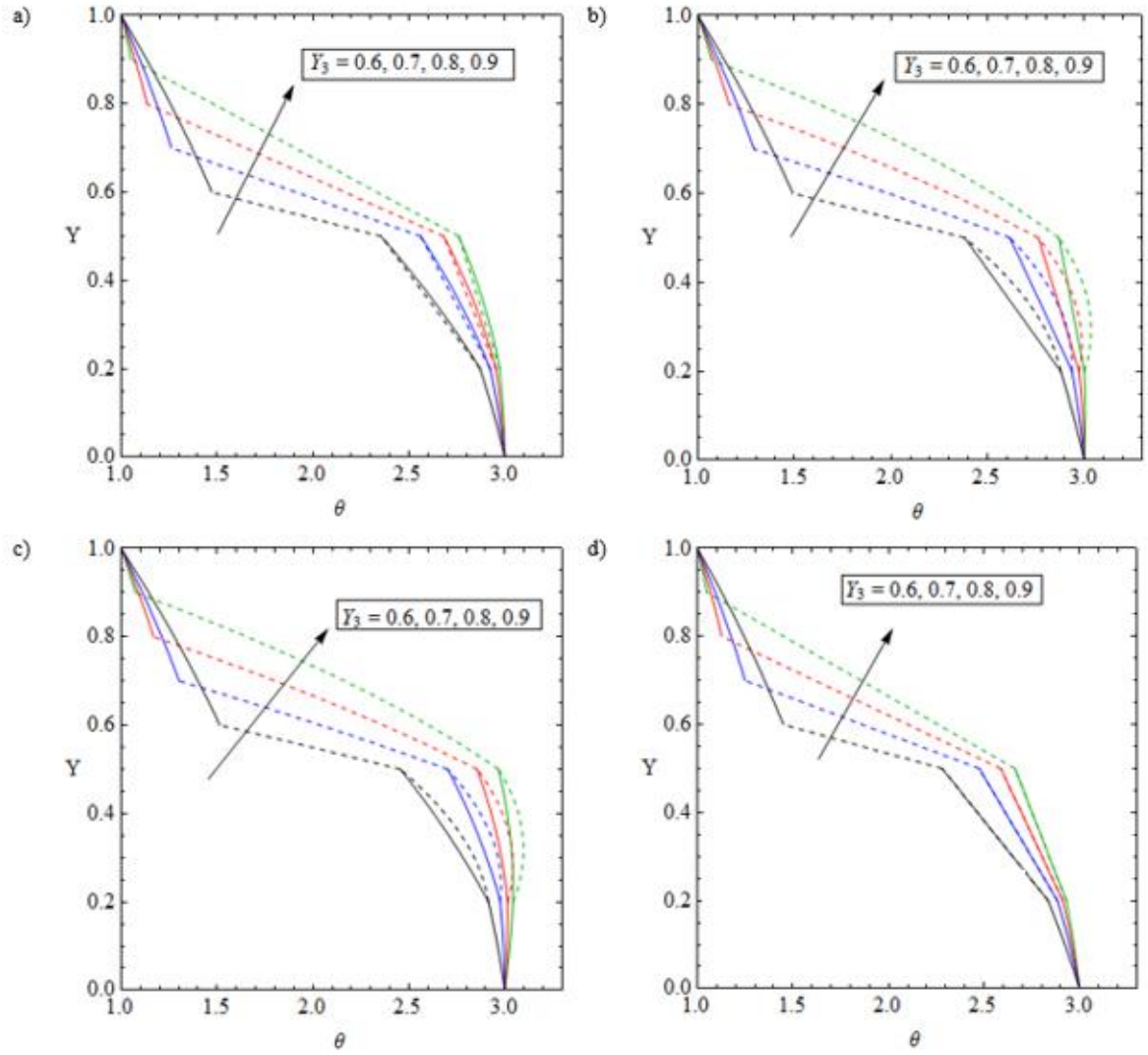

Figure 4-7 Temperature distribution with various values of the upper wall thickness number, $\boldsymbol{Y_3}$ for a) Case 1, b) Case 2, c) Case 3, and d) Case 4. Dashed line represent fluid phase, solid lines represent solid phase.

However, although still existing, this trend is less pronounced in Figure 4-7 a and Figure 4-8 a, corresponding to the changes in the thickness of the upper wall. Here the difference between solid and fluid temperatures remains roughly constant as does the porous insert thickness. The increase in the upper wall thickness has the effect of significantly reducing the temperature at the interface between the porous insert and the clear fluid. This is likely due to the significantly larger thermal conductivity of the upper wall as compared that of the clear fluid. Thus the boundary between the clear fluid and the upper wall is at a decreases temperature for a thicker upper wall. So there is a corresponding decrease in temperature at the interface between the clear fluid and the porous medium since for a thick walled system, there is very little on the way of clear fluid available to mitigate this reduced temperature.

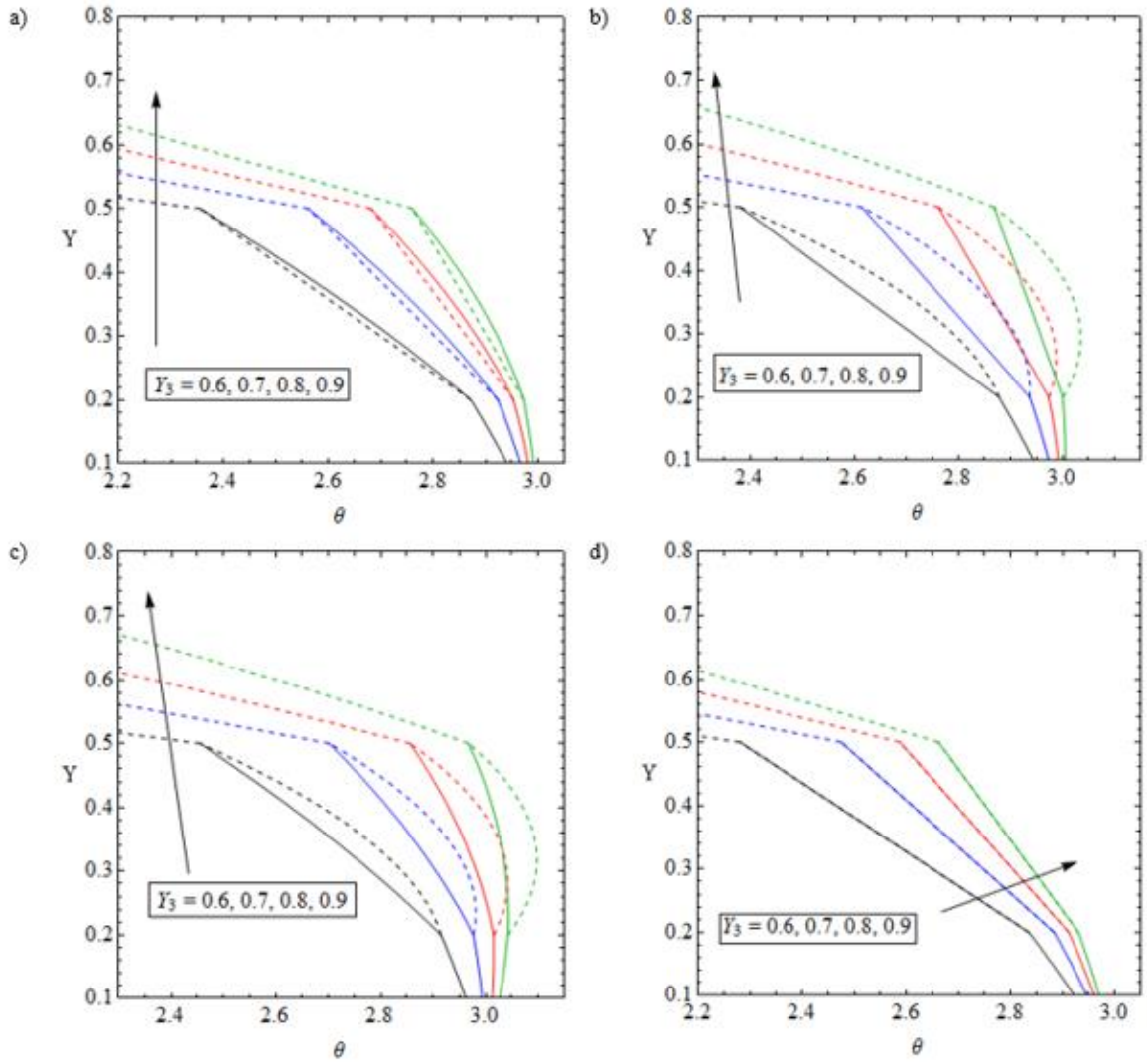

Figure 4-8 Temperature distribution with various values of the upper wall thickness number, $\boldsymbol{Y_3}$ focus on the porous insert for a) Case 1, b) Case 2, c) Case 3, and d) Case 4. Dashed line represent fluid phase, solid lines represent solid phase.

Moving to Case 2, investigated in part b of Figure 4-3 to Figure 4-8 , results in a substantial temperature difference in the porous region, which persists under all configurational variations. Compared with Case 1, temperature difference between the two phases in the porous medium of the system in case 2, has greatly increased (see Figure 4-4 b, Figure 4-6 b and Figure 4-8 b). In all of the investigated cases, having nine-fold more fluid phase within the porous insert compared to that of the solid phase, i.e. $\varepsilon = 0.9$, may be an important reason for the major quantitative differences between the temperature fields within the porous medium of cases 1 and 2. Additionally, the heat source term also increases the temperature in the clear fluid region in Case 2. In Case 1 when the source term is only in the solid phase, the added heating (as compared to Case 4) is only in the porous insert. This effect serves to increase the temperature of the boundary layer between the porous insert and

the clear fluid. However, as intuitively can be perceived, the inclusion of the source term in the solid phase of the porous media, i.e. Case 1, increases the temperature of the solid phase compared to that of the fluid phase. Similarly, the fluid phase temperature of the porous medium in case 2 is higher than the temperature of the solid phase. In a qualitative agreement with that discussed for Case 1, increasing the thicknesses of the lower wall and the porous insert tends to reduce the temperature difference between the two phases in the porous part of the system. This behaviour is almost repeated in Figure 4-3 c to Figure 4-8 c, in which equal exothermicity applies to the solid and fluid phases (Case 3). Once again, it must be considered that due to the default porosity value, there is considerably less heat source in the solid phase and as such it is at a lower temperature. This is compounded by the fluid phase having a lower thermal conductivity (than the solid or walls). There is some degree of interstitial heat transfer, but this is limited by the Biot number value chosen, preventing there from being homogeneous temperature distribution. Additionally, the heat produced within the clear fluid section of the channel again increases the temperature on the boundary between the clear fluid and the porous insert. Coupled with the presence of heat sources throughout the channel, this leads to temperatures within the porous insert exceeding that of the hot wall. The local equilibrium trend observed here is generally in keeping with that discussed in partially-filled porous channels with exothermicity [98,108]. Nevertheless, inclusion of the thick walls in the present problem makes the thermal behaviour of system more complicated. For instance, Figure 4-3 and Figure 4-4 imply that variations in the thickness of the lower walls do not affect the temperature of the upper wall. Yet, modifying the thickness of the porous layer (Figure 4-5 and Figure 4-6) and that of the upper wall (Figure 4-7 and Figure 4-8) can change the temperature of the entire system noticeably.

The preceding analysis indicates that the strength of internal heat generations is an important parameter influencing the thermal characteristics of the system. This is further investigated in Figure 4-9 a to Figure 4-9 d through varying the thermal energy source terms within the fluid and solid phases for two different values of porosity. The range of this variation includes negative values of the source terms, which refers to endothermic chemical reactions (such as those encountered in reforming processes [103]). Figure 4-9 a and Figure 4-9 b show that variation in the internal heat sources within the fluid phase can majorly modify the temperature profiles across the system. Further, the temperature difference between the fluid and solid phases in the porous region is strongly affected by this parameter [98,108]. Larger values of internal heat generation in the fluid temperature signify the temperature difference and push the system towards LTNE.

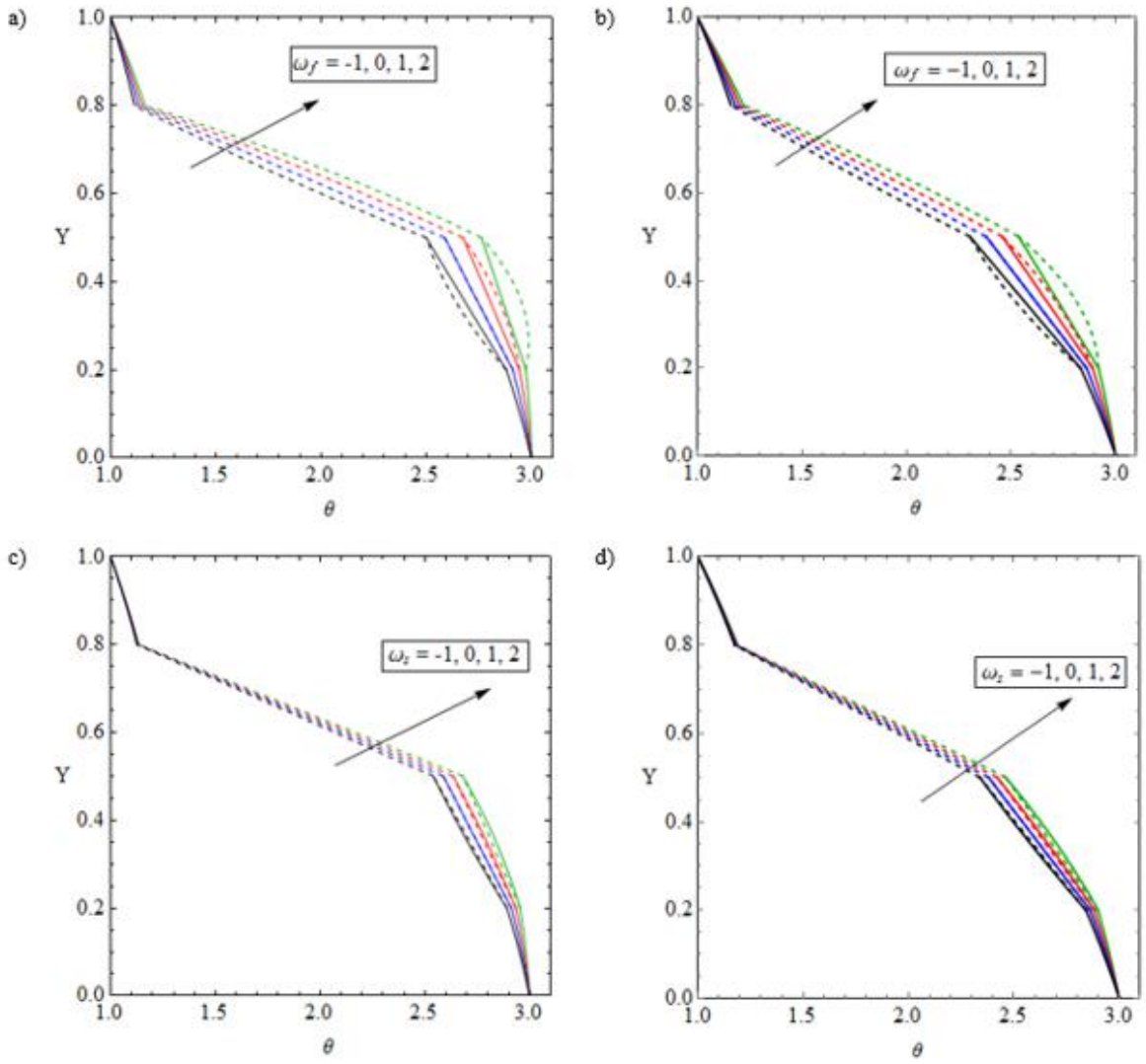

Figure 4-9 Temperature distribution with different values of exothermicity and endothermicity a) in the porous fluid phase, $\boldsymbol{\omega_f}$ for porosity, $\boldsymbol{\varepsilon = 0.9}$,b) in the porous fluid phase, $\boldsymbol{\omega_f}$ for porosity, $\boldsymbol{\varepsilon = 0.5}$, c) in the porous solid phase, $\boldsymbol{\omega_s}$ for porosity, $\boldsymbol{\varepsilon = 0.9}$, and d) in the porous solid phase, $\boldsymbol{\omega_s}$ for porosity, $\boldsymbol{\varepsilon = 0.5}$. Dashed line represent fluid phase, solid lines represent solid phase.

These arguments equally apply to Figure 4-9 c and Figure 4-9 d, in which internal heat generation is limited to the solid phase of the porous medium. As an important difference, however, heat generation in the solid phase appears to be less capable of disturbing the local thermal equilibrium of the system. The cause of this for the case where porosity, $\varepsilon = 0.9$ is again chiefly down to the fact that a volumetric heat source in the solid phase will be considerably lower in heat output than that in the fluid phase due to the significant difference in volume of each material. However, when the porosity, $\varepsilon = 0.5$ then there are equal amounts in the solid and fluid phases and yet with the source term in the fluid phase, the system tends to depart further from the LTE condition and towards LTNE. This may be due to the difference in thermal conductivity between the solid and fluid phases since in Figure 4-9 a value of $k = 2$ is used. To clarify the effect that thermal conductivity has,

Figure 4-10 shows how the temperature field varies with thermal conductivity ratio (with porosity, $\varepsilon = 0.5$) for Case 3. As can be seen, for $k = 0.5$ (where the fluid phase has greater thermal conductivity), the temperature difference between the phases is similar to that observed for $k = 2$. Additionally, when the effective thermal conductivities are equal, LTE conditions are observed. This helps explain why the solid phase appears less able to cause deviation from LTE conditions in Figure 4-9 b compared to Figure 4-9 d.

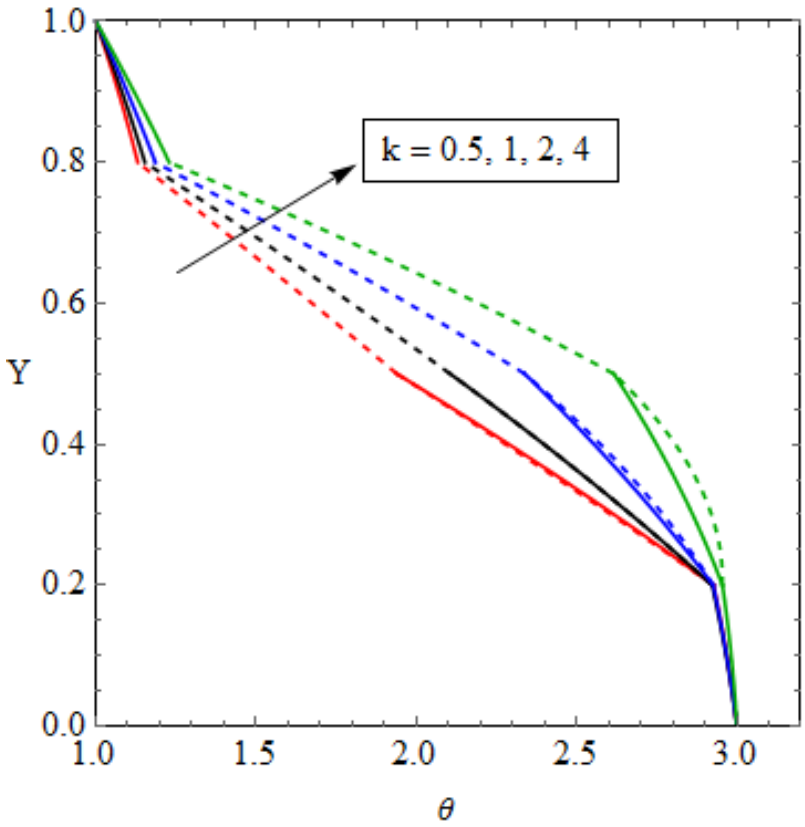

Figure 4-10 Temperature distribution for Case 3 with $\varepsilon = 0.5$ for various values of k. Dashed line represent fluid phase, solid lines represent solid phase.

4.5 Nusselt number

Section 4.4 showed that the geometrical configuration of the microreactor can significantly affect the temperature distributions. This implies that the rates of heat transfer and therefore the Nusselt number would change by varying the system configuration. Figure 4-11 to Figure 4-13 illustrate such modifications of Nusselt number. Figure 4-11 depicts the values of Nusselt number, for the four cases of Table 4-1. In this figure, the Nusselt number has been calculated for a few different values of porosity. A comparison of Figure 4-11 a-d reveals that variation in the exothermicity in Cases 1-4 causes significant qualitative and quantitative changes in the behaviour of the Nusselt number. In the basic case with no exothermicity (Case 4 shown in Figure 4-11 d and Figure 4-12 d), the behaviour of the

Nusselt number is monotonic with respect to increase in the thickness of the lower wall and increasing porosity of the porous insert. In Figure 4-11 d, the Nusselt number has a value between 4 and 5 for the thin wall system and its magnitude decreases sharply by thickening the lower wall. Introduction of exothermicity in Figure 4-11 a-c results in a general decrease in the numerical value of the Nusselt number. This observation is consistent with the fact that for Cases 1 to 3 the average temperature across the channel, shown in Figure 4-3 and Figure 4-4 , is higher than that of Case 4.

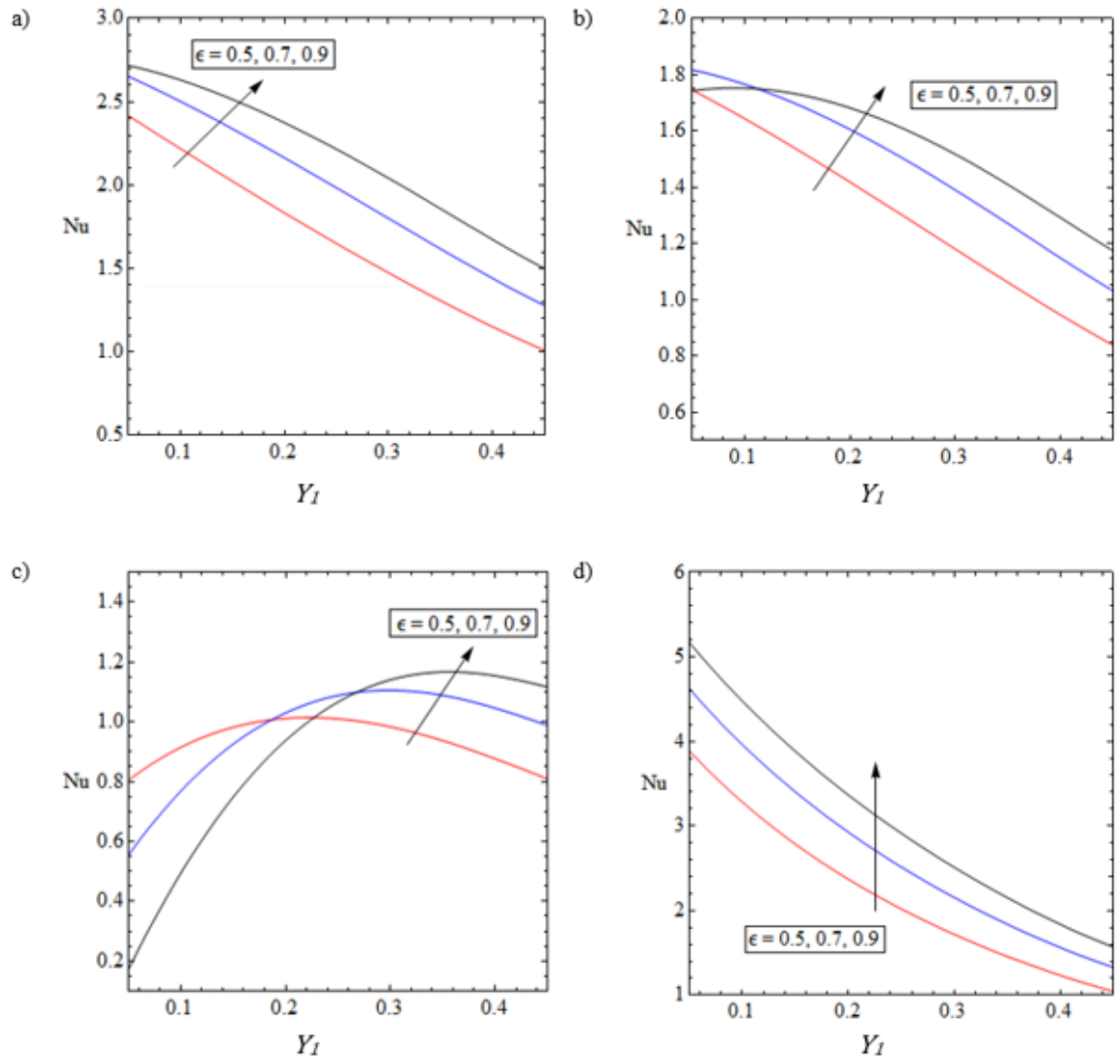

Figure 4-11 Variation in Nusselt number versus the lower wall thickness, $\boldsymbol{Y_1}$, for different values of porosity for a) Case 1, b) Case 2, c) Case 3, and d) Case 4.

Lower heat transfer coefficients in the internally heat generating cases leads to higher temperatures in the system and therefore larger heat transfer potentials. Comparison to the thermal fields shown in Figure 4-4 c shows that for thin lower walls (and thereby thicker porous inserts) yields higher temperatures, which fall as Y_1 increases. As such there is an observed increase in Nusselt number in Figure 4-11 c until a Y_1 value between 3 and 4 is

obtained, it is in this transitional zone that there ceases to be a significant temperature increase in Figure 4-4 c. At this point there is a larger temperature difference between the bulk flow and the lower wall surface leading to lower heat transfer coefficients and a corresponding decrease in Nusselt number. Further, Figure 4-11 b and c show that in Cases 2 and 3 there exist optimal values of the lower wall thickness, which render the maximum Nusselt number. Figure 4-11 c indicates that the optimal thickness increases with increasing the porosity. It follows that in microreactors with exothermic fluids the thickness of the wall can play a significant role in heat transfer characteristics of the system. For example, as it can be clearly seen from Figure 4-11 b, for $\varepsilon = 0.9$, the Nusselt number is maximised when the lower wall thickness is close to $Y_1 = 0.15$.This is particularly important as the current analysis shows that introduction of exothermicity in the fluid can generally bring down the Nusselt number in comparison with the corresponding system with no exothermicity. Hence, selecting the right wall thickness becomes an essential task in the thermal design of microreactors with highly exothermic reactions.

It is, generally, known that the thickness of the porous insert in the partially-filled conduits is an essential parameter dominating the rate of heat transfer [86,100]. Figure 4-12 shows that thick wall microchannels with exothermic chemical reactions can further substantiate the role of porous insert thickness. In Figure 4-12 a (Case 1), starting from a relatively thin porous insert ($Y_2 = 0.2$) and increasing the thickness of the porous layer can strongly influence the value of the Nusselt number. This is more pronounced at higher values of porosity. Figure 4-12 a shows that for small thicknesses of the porous insert, first there is a Nusselt number decreasing trend, which continues till a minimum value is reached. For very thin porous inserts there is fluid that is at extremely low velocity adjacent to the channel wall which inhibits the heat transfer from the wall. It acts in a manner which is not unlike that of a thickened laminar boundary layer which inhibits forced convection. As the porous insert thickens, so this layer thickens and further reduces the Nusselt number. However, once the layer reaches approximately $Y_2 = 0.5$ the flow within the porous layer begins to increase until the channel becomes fully filled and slug flow is achieved [193]. Slug flow is known to enhance the Nusselt number significantly and as such there is a rapid increase in Nusselt number as the channel approaches a fully filled porous state [193].

The exact value of this minimum Nusselt number depends upon the configurational parameters such as porosity. Nonetheless, Figure 4-12 a indicates that while making the insert more porous can generally increase the Nusselt number, the location of the minimum point remains more and less insensitive to this parameter. Figure 4-12 b shows that addition

of exothermicity to the fluid (Case 2) alters the situation noticeably. Here, for the small thicknesses of the porous insert Nusselt number is almost independent of the porosity. The Nusselt number is sensitive to the bulk temperature of the flow and addition of porous solid (which for Case 2 does not release heat) causes the bulk flow to exhibit comparatively lower temperatures since it replaces fluid containing exothermicity. Clearly for greater thickness and lower porosity a greater volume of heat sources are being replaced by this solid and so for thick inserts lower porosity decrease bulk temperature and thus enhances the heat transfer coefficient leading to higher Nusselt numbers. For very thin porous inserts, there is very little in the way of heated fluid being replaced and so porosity has only a limited effect on the bulk flow temperature. This leads to the Nusselt number being almost constant for very thin porous inserts as shown in Figure 4-12 b.

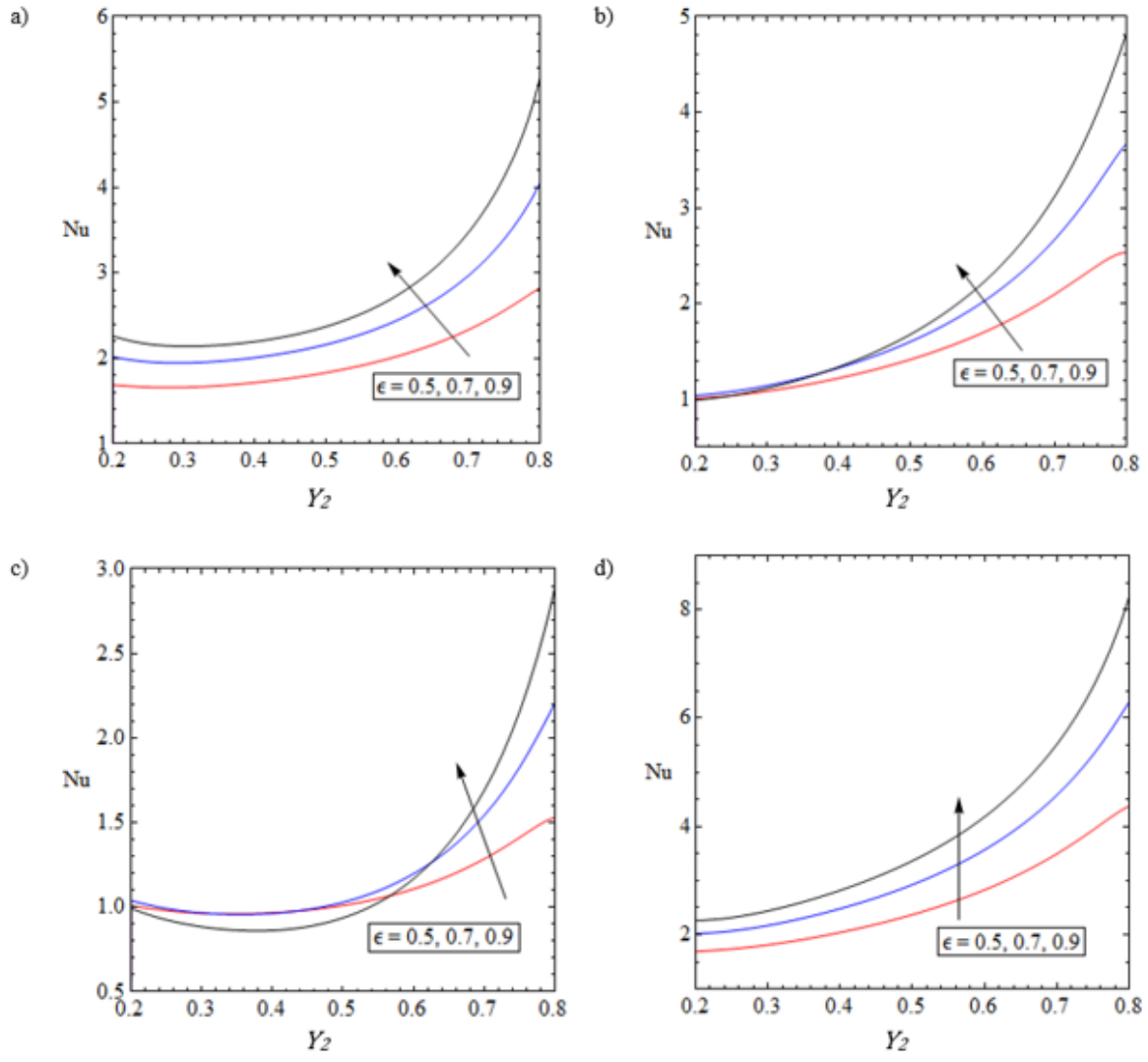

Figure 4-12 Variation in Nusselt number versus the porous insert thickness, $\boldsymbol{Y_2}$, for different values of porosity for a) Case 1, b) Case 2, c) Case 3, and d) Case 4.

Further increase in the thickness of the porous insert results in increasing the value of Nusselt number, while the rate of increase appears to be greater at higher porosities. Considering exothermicity in both solid and fluid (Case 3 shown in Figure 4-12 c) complicates the behaviour of the Nusselt number. Similar to that discussed for Case 1 (Figure 4-12 a) increasing the thickness of the porous insert in Case 3 first results in the reduction of the Nusselt number and development of minima in Figure 4-12 c. This is particularly noticeable for the highest value of porosity. Once again, the locations of these minima are not strongly affected by the changes in porosity. Further thickening the porous insert significantly increases the value of Nusselt number. Nonetheless, comparing to Figure 4-12 a and b for a given thickness of the porous insert the numerical value of the Nusselt number in Figure 4-12 c is considerably lower. Removing all sources of exothermicity in Figure 4-12 d (Case 4) greatly simplifies the problem. Here, for all investigated porosities, the Nusselt number increases monotonically with increases in the thickness of the porous insert. Importantly, the numerical values of the Nusselt number in Figure 4-12 d are always higher than all other cases, revealing the interfering role of exothermicity in the heat convection process. These significant modifications through addition of exothermicity clearly reflect the importance of considering the exothermic terms under an LTNE framework.

Figure 4-13 illustrates the effects of changes in the thickness of the upper wall of Figure 4-1 on the Nusselt number. The general trend observed in this figure reflects that of Figure 4-11 , in which the value of the Nusselt number is often correlated with the porosity and wall thickness. However, unlike the lower wall effects shown in Figure 4-11 , thickening of the upper wall results in a monotonic increase of the Nusselt number. An exception to this is case 3 (Figure 4-13 c), in which, at the highest investigated porosity, the Nusselt number variation versus the wall thickness features a maximum point.

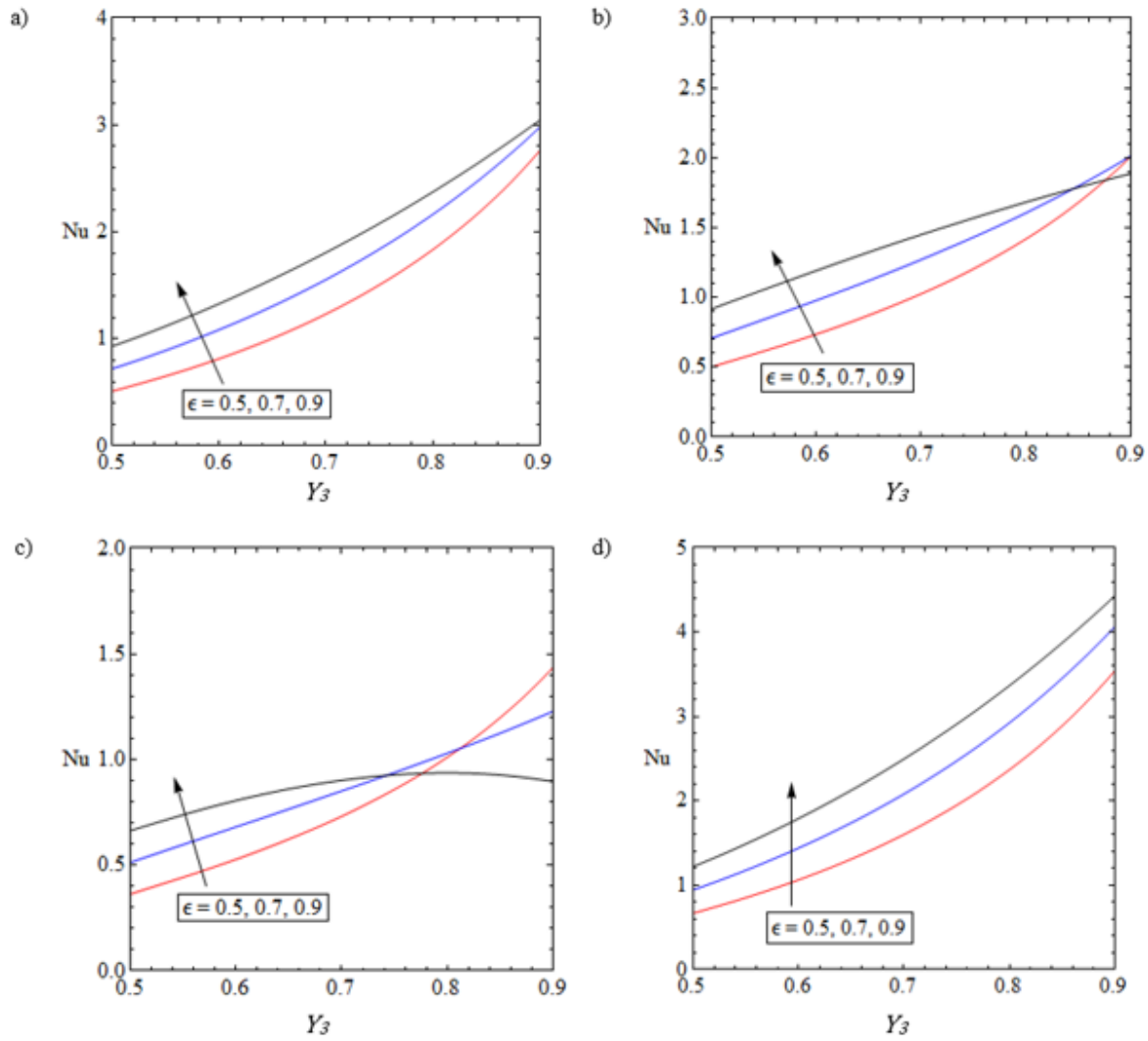

Figure 4-13 Variation in Nusselt number versus the upper wall thickness, $\boldsymbol{Y_3}$, for different values of porosity for a) Case 1, b) Case 2, c) Case 3, and d) Case 4.

Figure 4-11 to Figure 4-13 clearly show that in the absence of internal heat generation the heat transfer behaviour of the microchannel shown in Figure 4-1 is fairly simple. However, inclusion of exothermicity in the system can introduce major complexities. As such, the changes of the Nusselt number with respect to change in the thickness of the system components is not monotonic anymore and can feature extremum points. Further, the existence of exothermic sources in the microchannel can signify the sensitivity of the heat transfer processes to the porosity of the porous insert and cause a general reduction in the value of the Nusselt number. Clearly, these findings have direct consequences upon the design and operation of microreactors.

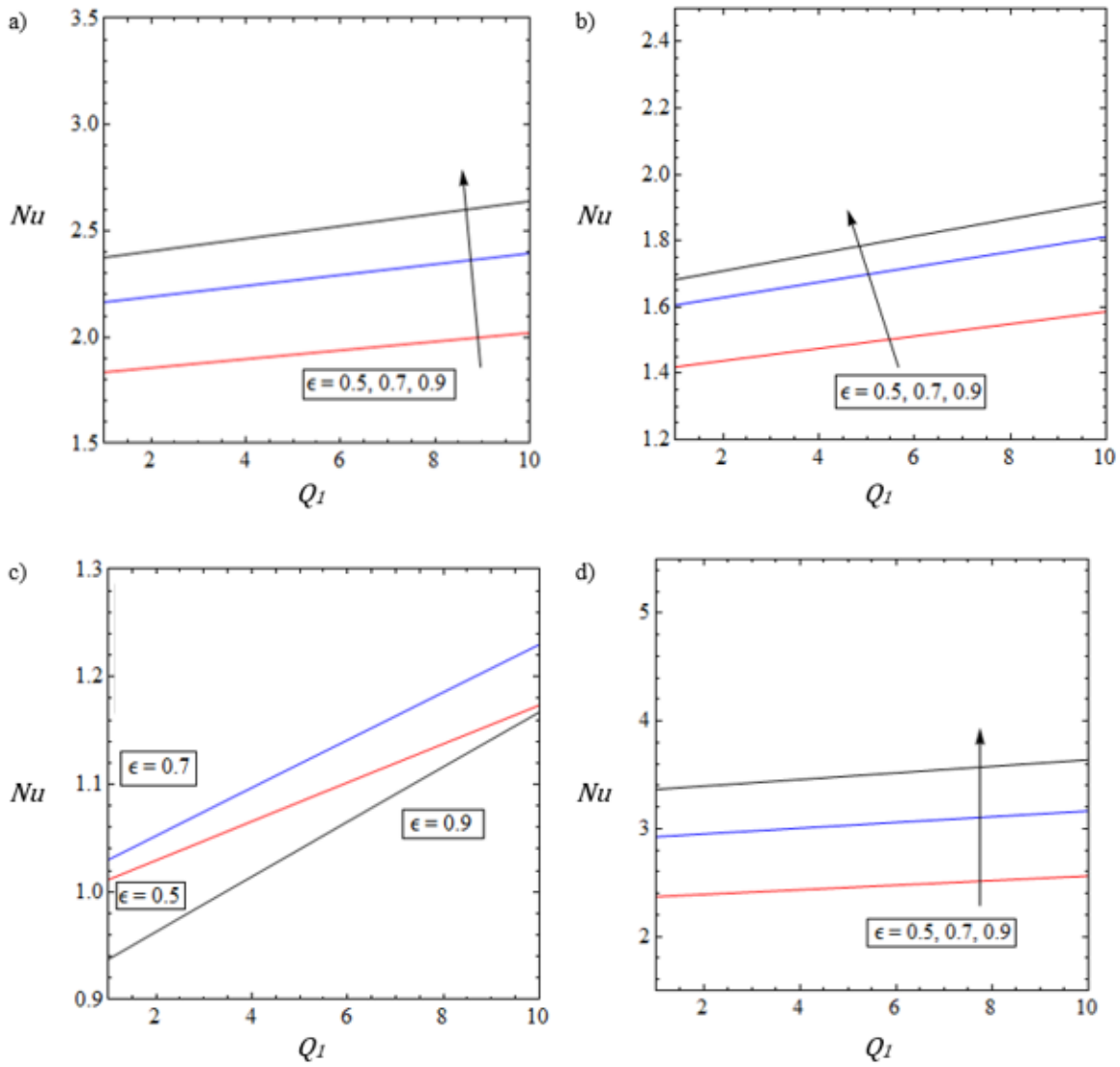

Figure 4-14 Variation in Nusselt number versus thermal generation in the lower wall, $\boldsymbol{Q_1}$, for different values of porosity for a) Case 1, b) Case 2, c) Case 3, and d) Case 4.

The microchannel configuration under investigation (Figure 4-1) can include internal heat generations within the thick walls of the system. As discussed earlier, this is a manifestation of the absorption of microwaves or infrared waves by the solid structure of the microreactor. Figure 4-14 demonstrates the variations of the Nusselt number due to the changes in the internal heat generation within the lower wall. The existence of a general positive correlation between the Nusselt number and wall internal heat generation is clear in this figure. In keeping with the results shown in other figures, high values of porosity in Figure 4-14 produce larger Nusselt numbers.

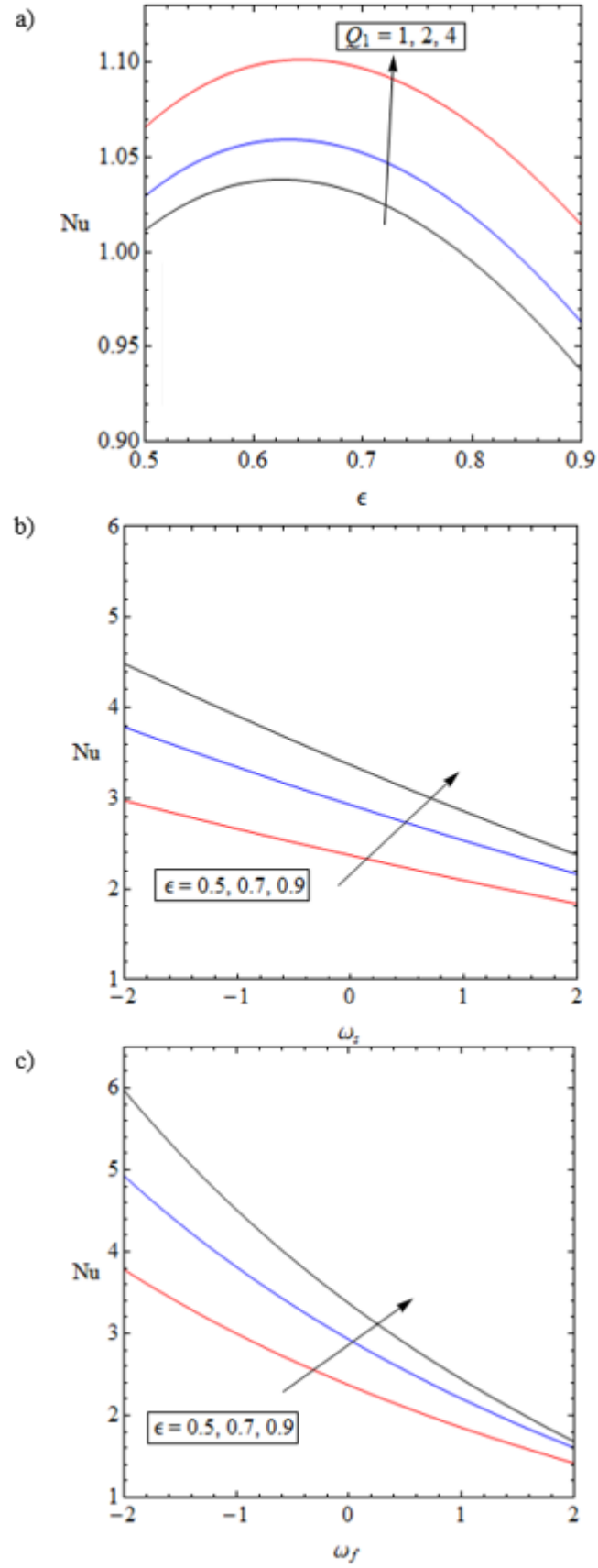

Figure 4-15 Variation in Nusselt number versus a) porosity, $\boldsymbol{\varepsilon}$, for different values of heat generation in the lower wall, Q_1 for Case 3, b) heat source/sink in the porous solid phase, $\boldsymbol{\omega_s}$, for different values of porosity, and c) heat source/sink in the fluid phase, $\boldsymbol{\omega_f}$, for varying values of porosity.

The relation between the Nusselt number and the porosity of the porous layer is further investigated in Figure 4-15 a. This figure shows changes of the Nusselt number against porosity for varying values of the lower wall internal heat generation. Evidently, Figure 4-15 a features an extremum behaviour and reflects initial increase of the Nusselt number with increasing the porosity followed by a sudden drop. Interestingly, variation of the intensity of heat generation in the wall appears to have a relatively small effect on the optimal porosity and the maximum Nusselt number. The reason for this may be connected to the effect of porous insert thickness upon Nusselt number. Consider that the increase in porosity increases the volume of fluid present in the porous insert; this fluid has very low velocity, but nonetheless has some velocity. Obviously, the solid does not. This causes an increase in Nusselt number initially by virtue of the effect the velocity field has upon the mean temperature. This is expressed mathematically in equation (4-86). However, the increase in porosity would also lead to a continued increase of low thermal conductivity fluid creating a similar effect to the thickened laminar fluid boundary layer previously discussed. These effects counteract one another until a maximum is reached at the point where they balance out. This point would not be expected to change significantly with Q_1 value since it related predominantly to the amount of fluid phase present and as such, the maximum position does not vary greatly in Figure 4-15 a. Eventually the still fluid effect take precedence and the Nusselt number begins to drop. It is further worthy of note at this point that the graph has a base Y_2 value of 0.5 and thus is of relatively low thickness.

This brings about the explanation for the feature seen in Figure 4-14c, whereby the porosity changes from 0.5 to 0.9 and yet the value of the Nusselt number is not significantly different for $Q_1 = 10$. As the proposed explanation above describes, once the porosity passes the maximum value at about a porosity of 0.65, the associated Nusselt number decreases. It was suggested that this is due to the thin porous layer creating a still fluid region (as compared to the free fluid zone) and thus inhibiting the Nusselt number. The reason for the similarity in Nusselt Number for the these porosity values at $Q_1 = 10$ may simply be due to the still fluid effect drops the Nusselt number from its maximum to a lesser extent as Q_1 increases. This can be seen in Figure 4-15a where the difference between Nusselt number values at porosity of 0.5 and porosity 0.9 is less for $Q_1 = 4$ than for $Q_1 = 1$. The reason behind this would likely be due to the increased wall temperature associated with the increase in heat source within the wall. This would serve to mitigate the effect of the Nusselt number drop associated with the still fluid effect described previously.

The effects of exothermicity and endothermicity within the fluid and porous solid phase upon the Nusselt number are investigated in Figure 4-15 b and c. It is clear from these figures that reduction of the endothermicity and increases in the exothermicity in either of the fluid and porous solid phase results in decreasing the Nusselt number. For a similar range of internal heat generation in Figure 4-15 b and c, the Nusselt number drop in Figure 4-15 b is more significant. This implies that compared to that of porous solid, the fluid exothermicity/endothermicity has a stronger effect upon the Nusselt number. Further, Figure 4-15 b and c both show that as the magnitude of exothermicity increases the influences of porosity on the value of Nusselt number decreases. This trend is particularly clear in Figure 4-15 c. A comparison between Figure 4-15 b and c further reveals that the numerical value of Nusselt number varies significantly by shifting the internal heat source from the fluid to the solid phase. This is yet another factor emphasising the importance of considering LTNE approach in the thermal analysis of microreactors.

4.6 Entropy generation

4.6.1 Local entropy generation

The effects of configurational variations on the local generation of entropy across the microchannel has been analysed in Figure 4-16 to Figure 4-18 . Figure 4-16 shows the modification of local entropy generation caused by the changes in the thickness of the porous layer. The four cases of Table 4-1 have been investigated in this figure. As a general trend in Figure 4-16 , it is observed that for all cases the generation of entropy increases by thickening the porous layer. This increase can be seen in all components of the system (the solid walls, solid and fluid phase within the porous region and the fluid phase in the clear region).

In the upper wall, it can be seen from the temperature field show in Figure 4-5 that in all cases the temperature is greater for greater thicknesses of porous insert. This increased temperature is the cause of the increased entropy generation in the upper wall. This is also the case for the clear fluid, however, the entropy values in this zone are considerably greater than those in the upper wall. This implies that there is an additional mechanism at work. This comes from the contribution due to the velocity, which exhibits a sharp increase from the wall at zero velocity to the mid-point of the clear fluid region. This velocity gradient generates a significant quantity of entropy to the system. For greater porous insert thickness, there is a narrower clear fluid region and so a corresponding increase in fluid velocity and gradient. This gives rise to the observed increase in local entropy generation in the clear fluid region. Within the porous region (both solid and fluid) the increase in porous thickness means there is simply more porous material and so any contribution to entropy generation is increased. Additionally, for both the porous insert (both solid and fluid) and the lower wall, the temperature gradient ($\frac{d\theta}{dY}$) is greater for thicker porous inserts and as such the entropy generation is correspondingly greater.

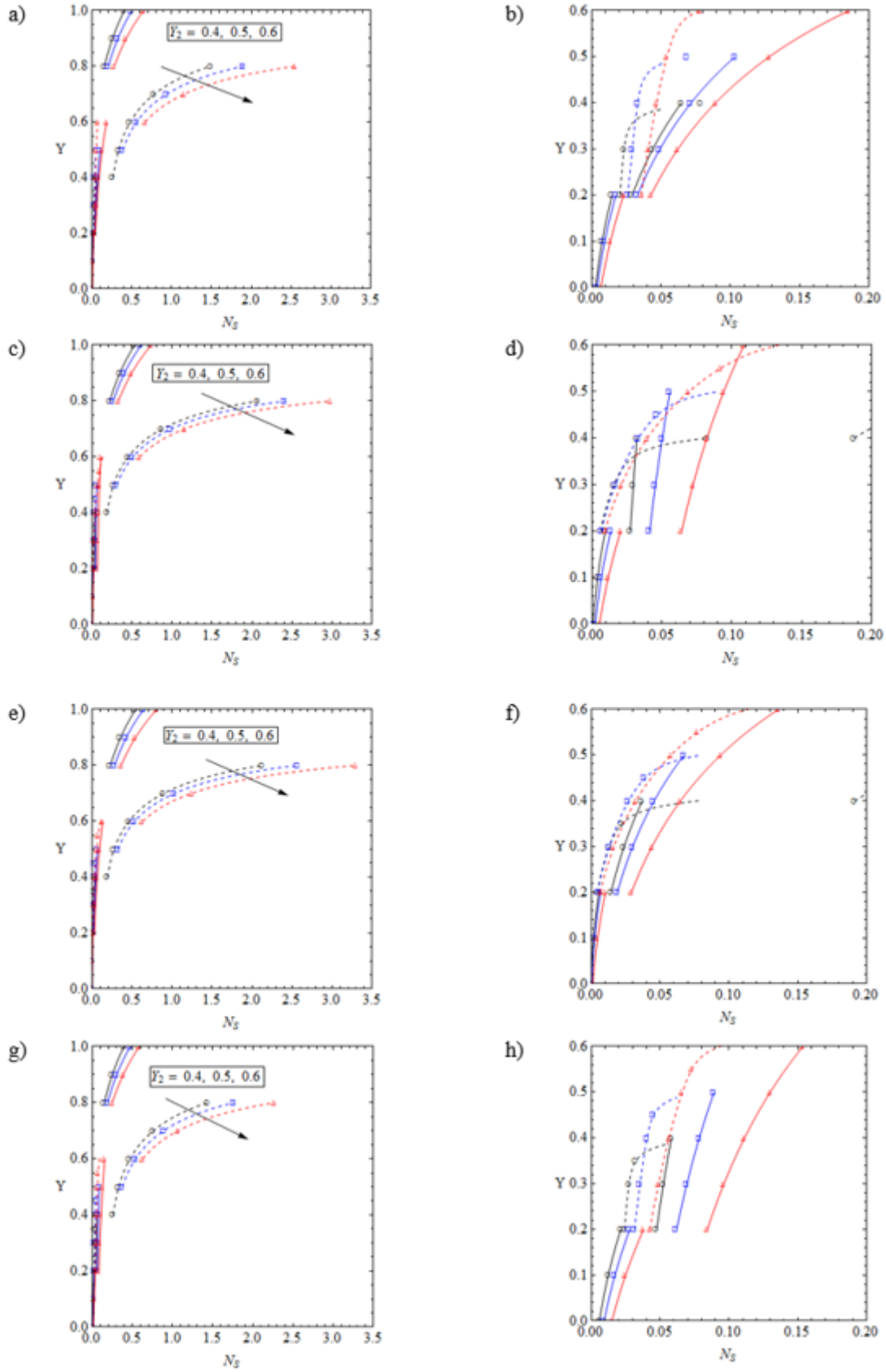

Figure 4-16 Local entropy generation distribution with various values of the porous insert thickness, $\boldsymbol{Y_2}$. Full graphs on left and graphs focussing on porous region on the right for a, b) - Case 1, c, d) - Case 2, e, f) - Case 3, g & h - Case 4. Dashed line represent fluid phase, solid lines represent solid phase.

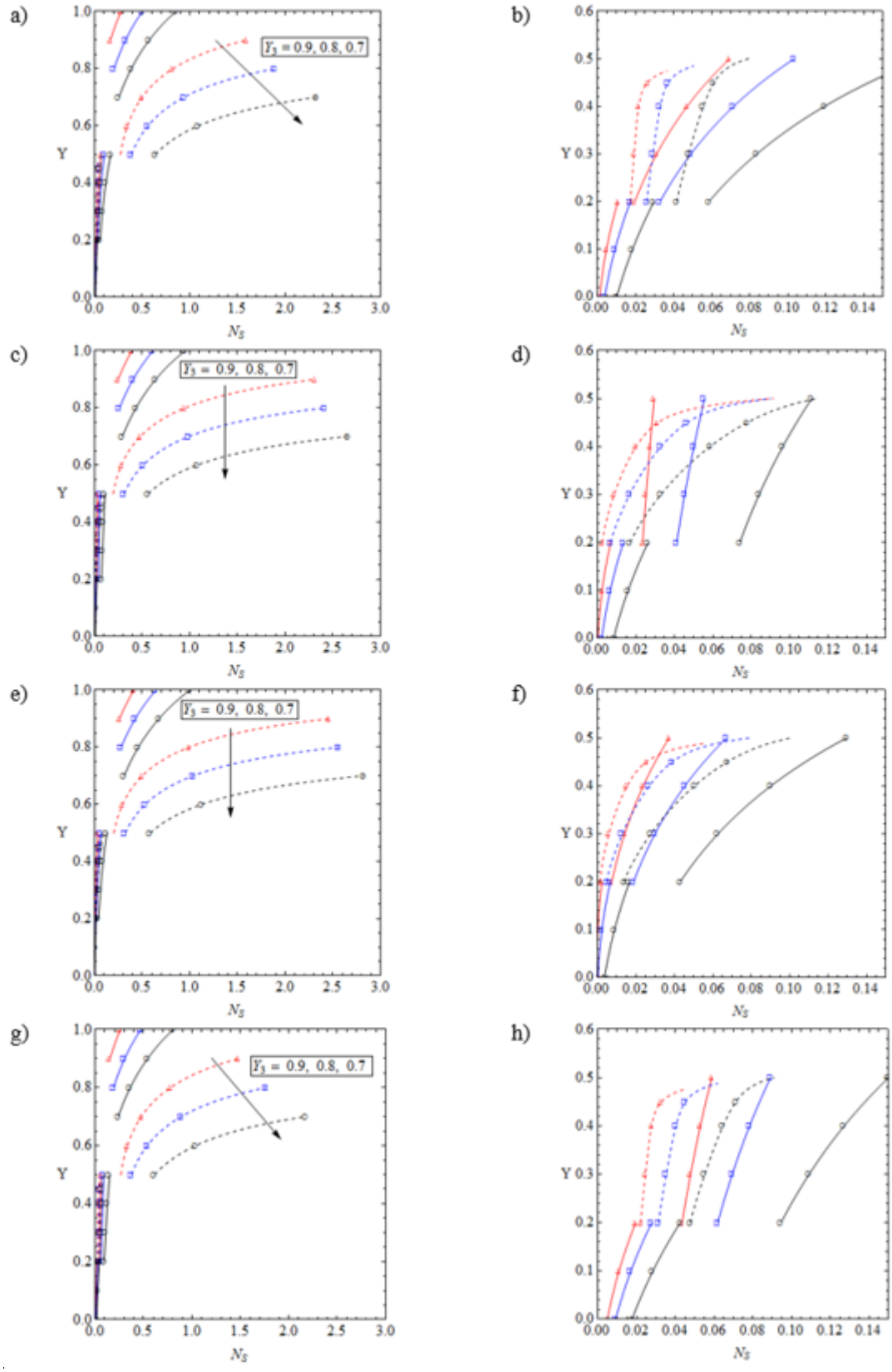

Figure 4-17 Local entropy generation distribution with various values of the upper wall thickness, Y_3 . Full graphs on left and graphs focussing on porous region on the right for a, b) - Case 1, c, d) - Case 2, e, f) - Case 3, g & h - Case 4. Dashed line represent fluid phase, solid lines represent solid phase.

Nonetheless, it appears that the fluid in the clear region and the solid upper wall are most affected by the variations in the thickness of the porous layer. Comparing to Case 1, the extent of these changes seem to be slightly larger in Cases 2 and 3, while Case 1 features the lowest local entropy generation. This is consistent with the observations made in similar configurations with zero wall thickness [98,108] and hence, is not further discussed. As stated earlier, the finite thickness of the microchannel walls is a distinctive feature in the thermal analysis of microreactors. The effects of variations in this parameter upon the local entropy generation have been depicted in Figure 4-17 . This figure shows that, for all cases under investigation, altering the thickness of the upper wall of the microchannel, which is directly related to that of the clear section of the microchannel, noticeably affects the local entropy generation. It is clear from this figure that increasing the thickness of the upper wall of the channel signifies the local generation of entropy. This may be partially due to the fact that the thermal conductivity of the wall is much higher than that of the fluid material, and therefore increasing the thickness of the upper wall increases the rate of heat transfer, and consequently the local entropy generation rate is enhanced. Similar to that discussed in Figure 4-16 , the extent of this increase is minimal in Case 1 (Figure 4-17 g) and maximum in Case 3 (Figure 4-17 e). However, the situation is different in the porous region, in which Case 2 shows the minimum local entropy generation (Figure 4-17 d) and Cases 1 and 4 (Figure 4-17 b and h) are the most irreversible Cases.

The thermal asymmetry due to the exposure of the system to two different temperatures at the outer most boundaries is expected to be a strong source of irreversibility. This thermal asymmetry is very common in microreactors and particularly can be found in reforming applications, in which sustaining the process is often subject to asymmetric transfer of heat [62,194]. Figure 4-18 shows how changes in the ratio of the outer surface temperatures, θ_H, affects the local generation of entropy. According to this figure, entropy generation can be intensified by an order of magnitude with a modest change in θ_H between 1.5 and 5. Importantly, Figure 4-18 indicates that variations in θ_H can strongly affect the generation of entropy within the clear region of the microchannel and the upper wall. The existence of exothermic sources in the system (Cases 1-3 shown in Figure 4-18 a,c and e) appear to magnify this irreversibility.

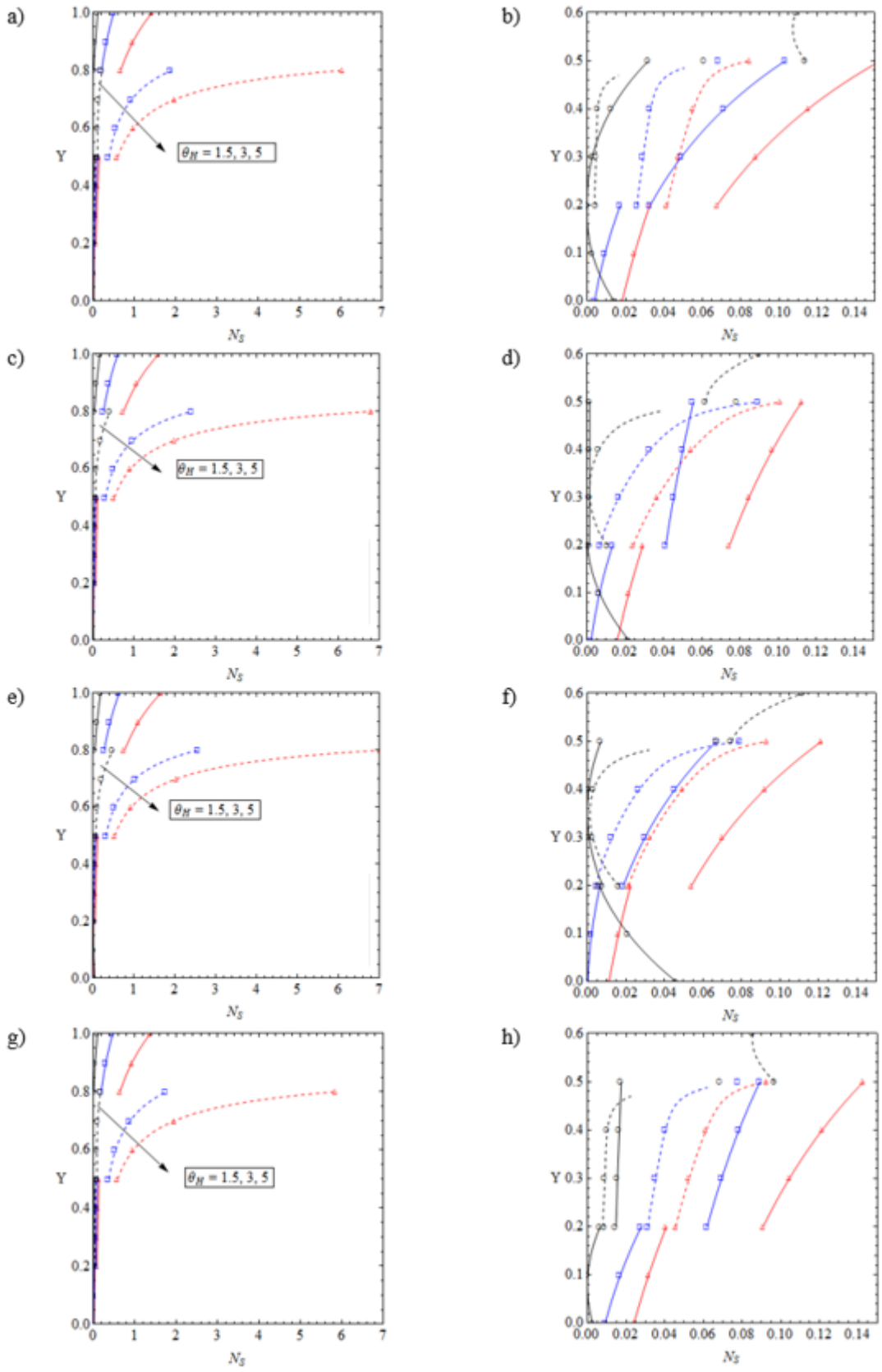

Figure 4-18 Local entropy generation distribution with various values of the lower wall temperature, $\boldsymbol{\theta_H}$. Full graphs on left and graphs focussing on porous region on the right for a, b) - Case 1, c, d) - Case 2, e, f) - Case 3, g & h - Case 4. Dashed line represent fluid phase, solid lines represent solid phase.

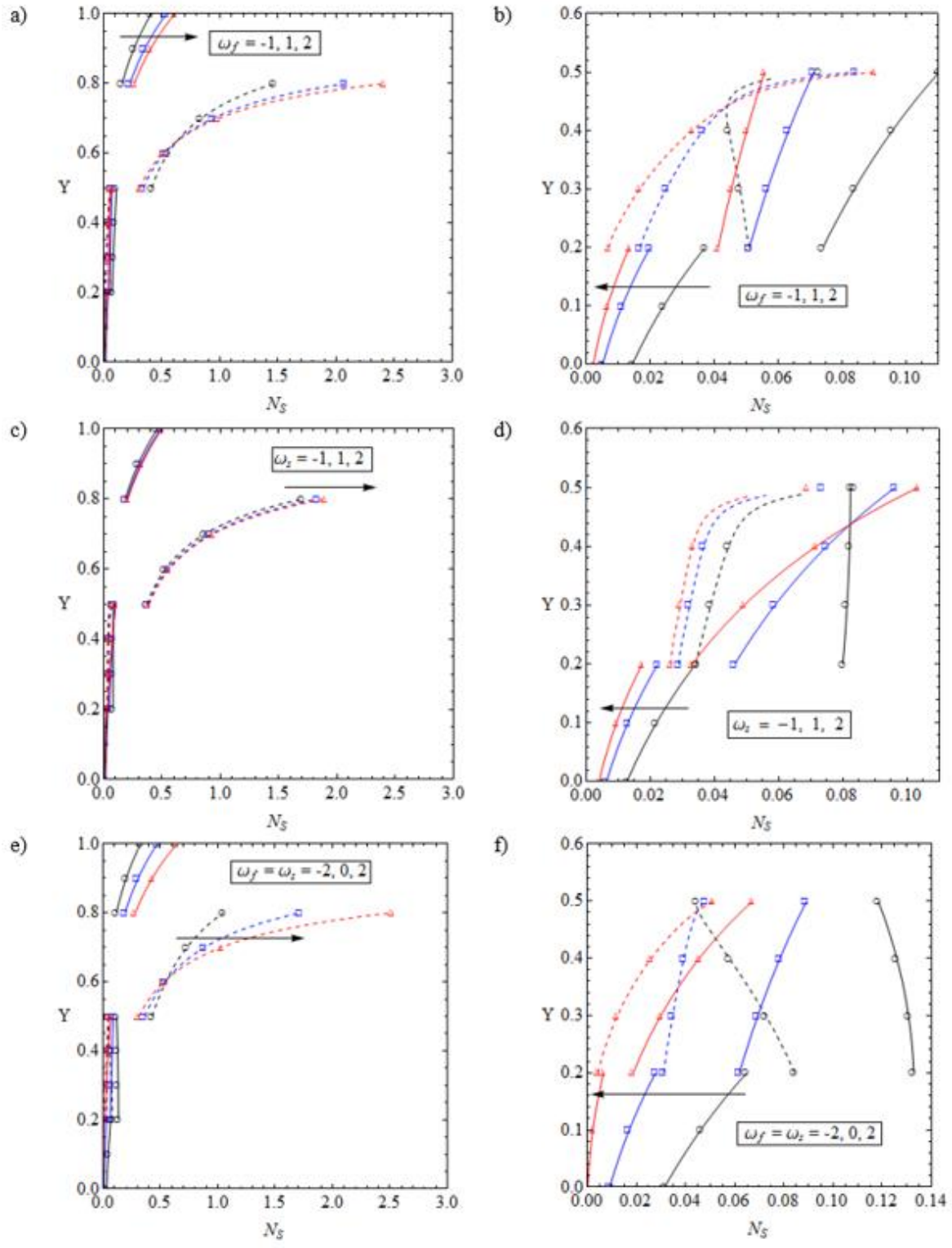

Figure 4-19 a & b - Local entropy generation distribution for different values of $\boldsymbol{\omega_f}$ and no heat source/sink in the solid porous phase. c & d - Local entropy distribution for different values of $\boldsymbol{\omega_s}$ and no heat source/sink in the fluid phase. e & f - Local entropy distribution for different values of $\boldsymbol{\omega_f}$ and $\boldsymbol{\omega_s}$. Full graphs on left and graphs focussing on porous region on the right. Dashed line represent fluid phase, solid lines represent solid phase.

Given that in reality microreactors used for reforming can be exposed to catalytic combustion on one side and room temperature on other side, the value of θ_H is expected to be between 3 and 4 [62]. Figure 4-18 shows that at these values of θ_H the irreversibility caused by the thermal asymmetry of the system is quite significant and should be certainly included in any second law analysis of the microreactor.

Intuitively, the exothermicity of microreactor, represented by the internal heat generations within the solid and fluid phases, could be a major source of entropy production. Figure 4-19 implies that although the general notion of generation of entropy by exothermicity/endothermicity is correct, this factor is not as significant as other investigated parameters. Figure 4-19 e shows that, compared to a case with no internal heat generation, addition of relatively strong thermal energy source terms ($\omega_f = \omega_s = 2, -2$) alters the local entropy generation by less than 40%. A similar behaviour is observed in Figure 4-19 a and c, in which internal heat generation is respectively limited to the fluid and porous solid phase. This figure, further, shows that variation in the internal energy generation within the fluid and solid phases leads to a common intersection of entropy generation curves in the clear fluid region. This bifurcation behaviour is a characteristic of fluid conduits with internal heat generations and has been recently studied in Refs. [98,108]. The common intersections are also present inside the porous region, (Figure 4-19 b, d and f). They occur in the fluid phase for cases with internal heat generations in the fluid only (Figure 4-19 b) and equal thermal energy source term in the solid and fluid (Figure 4-19 f), and within the solid region when heat is exclusively generated inside the porous solid (Figure 4-19 d).

4.6.2 Total entropy generation

Integration of the local entropy generation over the entire volume of the system (as in equation (4-94)) results in the calculation of the total entropy generation. Although not shown here, a parametric study of the total entropy generation revealed that for all investigated cases in Table 4-1 increasing the porosity of the porous insert results in a considerable reduction of the total entropy. This appears to be true for all variations in the system geometrical configurations and also changes in the thermal asymmetry of the system. This may be due to the increase in solid phase which has higher thermal conductivity than the fluid phase it is replacing. This could serve to permit more efficient heat transfer between the hot and cold walls, thus reducing the thermal gradients and thereby the total entropy. The results discussed in sections 4.3 and 4.4 showed that the thickness of the upper wall is an important parameter influencing the temperature profiles and Nusselt number.

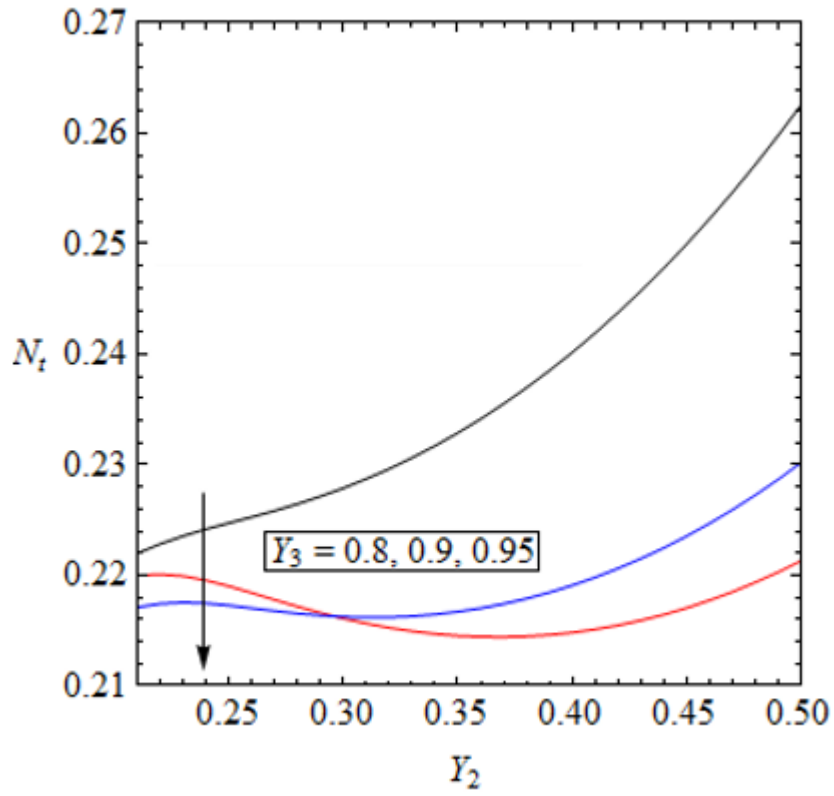

Figure 4-20 Total entropy versus porous insert thickness, $\boldsymbol{Y_2}$ for various values of the upper wall thickness, $\boldsymbol{Y_3}$.

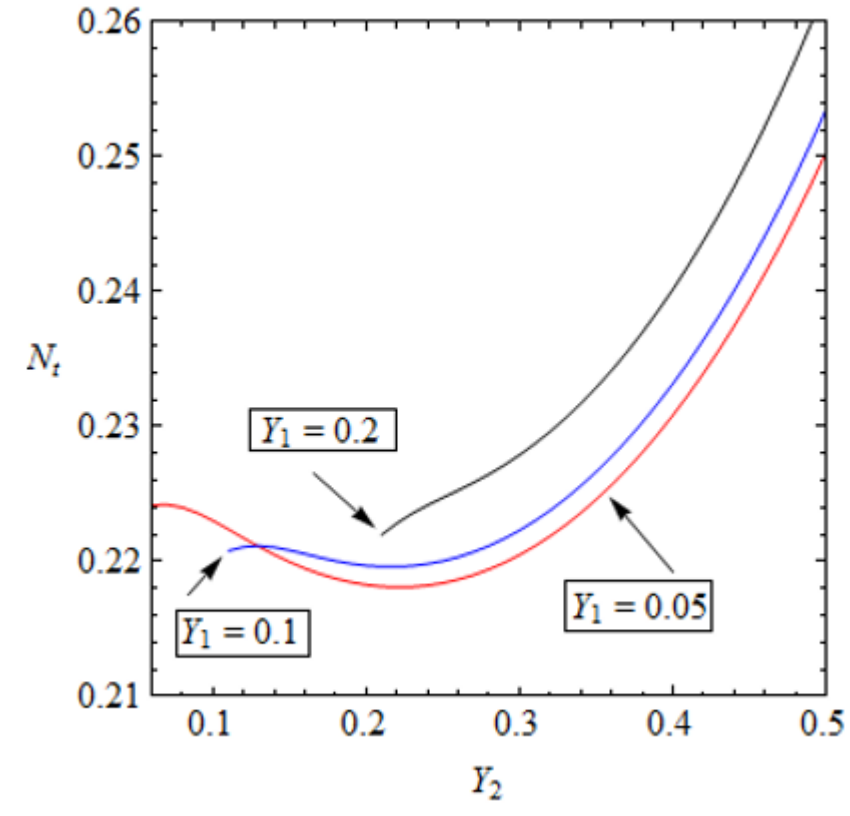

Figure 4-21 Total entropy versus porous insert thickness, $\boldsymbol{Y_2}$ for various values of the lower wall thickness, $\boldsymbol{Y_1}$

It was, further, shown in section 4.5.1 that the wall thickness strongly affects the local generation of entropy. In Figure 4-20 the total entropy production, N_t, has been plotted against the thickness of the porous layer, Y_2 (for constant value of Y_1). In this figure the variations of N_t versus Y_2 has been demonstrated for different values of the upper wall thickness (Y_3). This figure indicates that for a relatively thick upper wall ($Y_3 = 0.9$) there are two extremum points for the variations of the total entropy generation with the porous layer thickness. The first extremum point is a local maximum and occurs at thin porous thicknesses. As the porous layer grows in thickness a second extremum point appears in the form of a local minimum. Further increase in the thickness of the porous insert results in a monotonic growth in the total entropy generation. Alteration of the system configuration towards very thick upper walls ($Y_3 = 0.95$) shifts the location of the minimum point towards higher thicknesses of the porous insert. A qualitatively similar behaviour is observed in Figure 4-21 , in which N_t has been plotted versus Y_2 for different values of the lower wall thickness. Interestingly, however, smaller values of the lower wall thickness in Figure 4-21 have similar effects as high thicknesses of the upper wall in Figure 4-20 .

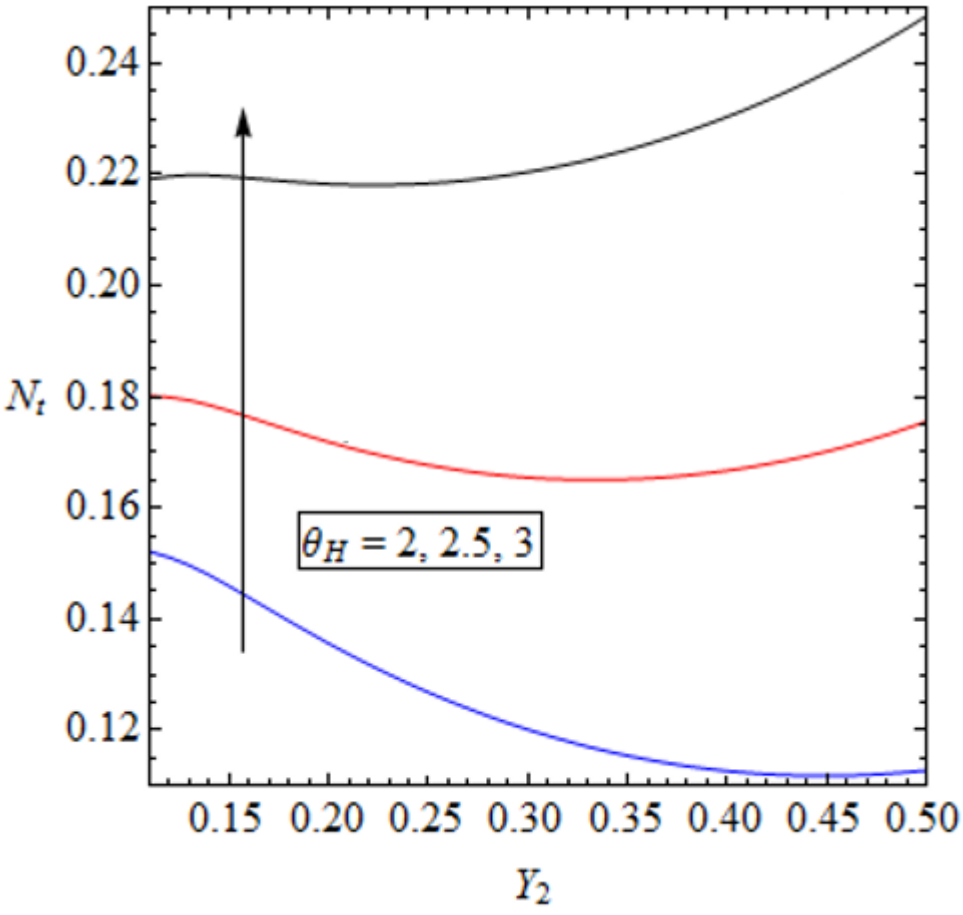

Figure 4-22 Total entropy versus the porous insert thickness, $\boldsymbol{Y_2}$, for different values of the lower wall temperature, $\boldsymbol{\theta_H}$.

It was observed in Sections 4.4 and 4.5.1 that the thermal asymmetry of the system has very strong effect upon the temperature fields, heat transfer and local entropy generation of the microreactor. Figure 4-22 shows that the pronounced influences of this parameter are readily extended to the total entropy generation. This figure depicts the variation of the total entropy versus thickness of the porous layer for three different values of the outer surfaces temperature ratio, θ_H. The existence of a minimum entropy point is evident in Figure 4-22 , in which for larger values of θ_H the minimum entropy occurs at smaller thicknesses of the porous insert. This behaviour can have direct consequences on the exergetic design of the microreactor. It implies that for any value of θ_H there is an optimal thickness of the porous insert, which results in the minimisation of the total entropy generation in the system.

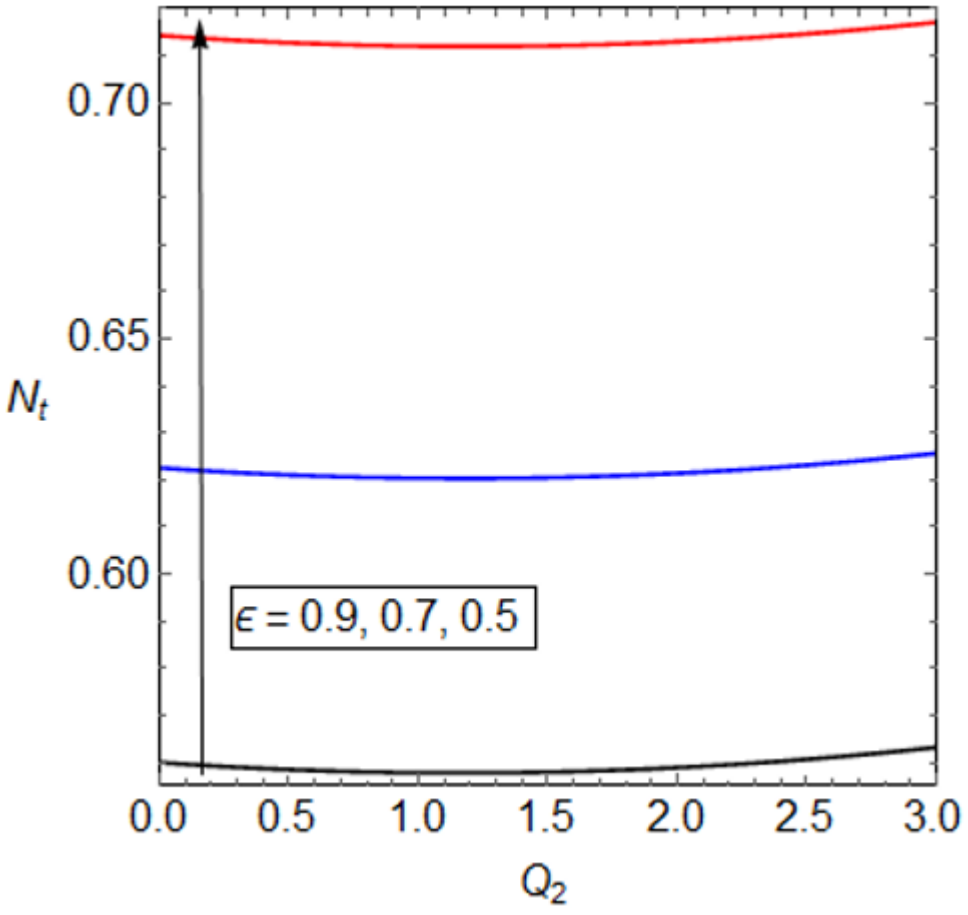

Figure 4-23 Total entropy versus heat source/sink in the upper wall, $\boldsymbol{Q_2}$ for different values of porosity under conditions of a heat sink in the fluid phase and walls of thickness 0.1.

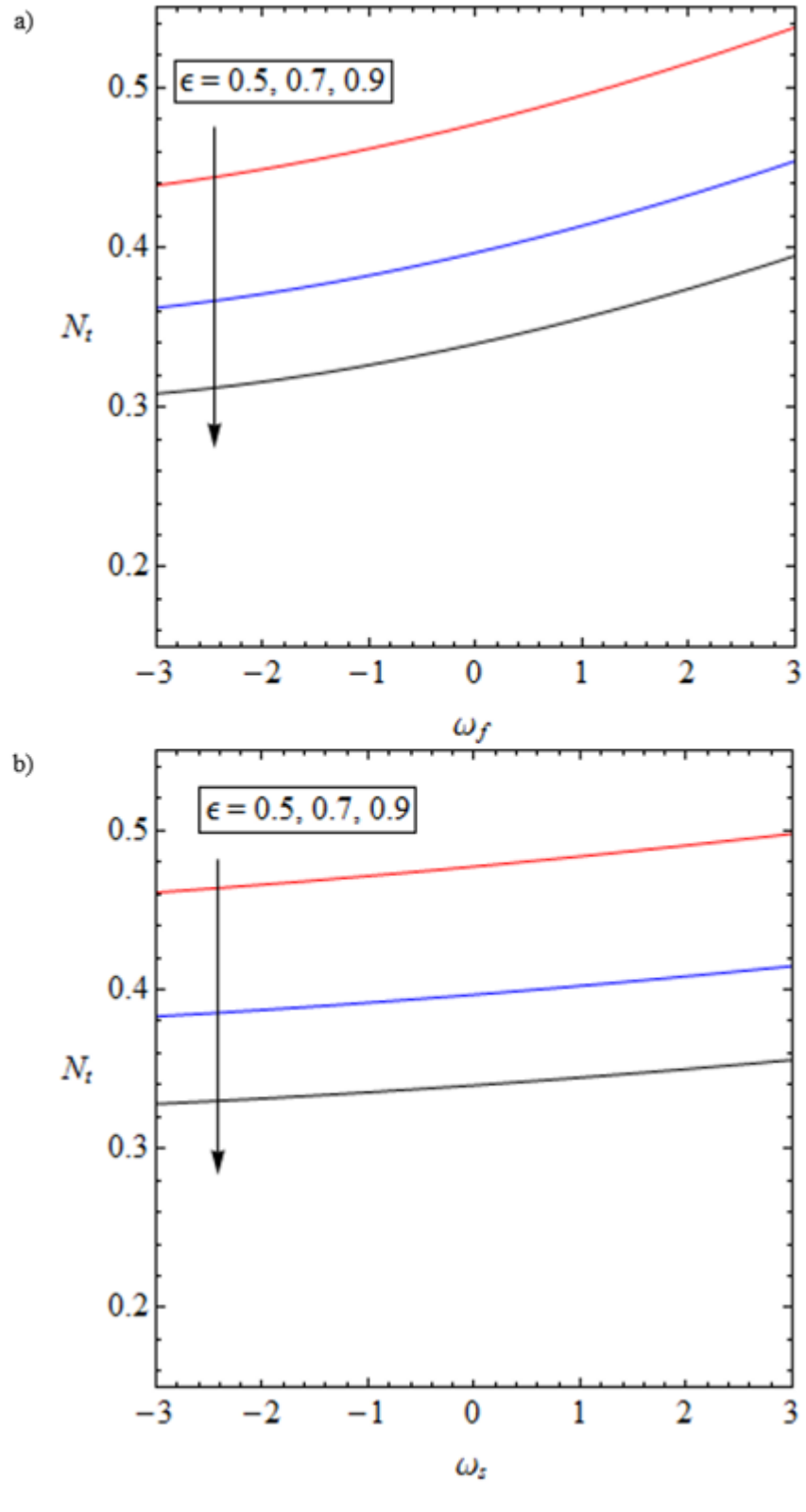

Figure 4-24 a) Total entropy versus heat source/sink in the fluid regions, $\boldsymbol{\omega_f}$, for varying values of porosity and b) Total entropy versus heat source/sink in the porous solid medium, $\boldsymbol{\omega_s}$ for varying values of porosity.

Figure 4-23 illustrates the effects of internal heat generation inside the wall on the total entropy generation. In this figure, the total entropy has been plotted for different values of porosity. Although changes of the total entropy generation with the increases in the wall

internal heat generation are relatively small, there exist a minimum point in each graph of Figure 4-23 . Further, the numerical value of entropy production appears to be strongly dependent on the porosity and takes a higher value at lower porosities. However, the optimal non-dimensional heat generation in the wall is almost insensitive to the porosity. This is such that for all investigated porosities the optimal internal heat generation in the upper wall is around $Q_2 = 1.2$. Finally, Figure 4-24 shows the existence of a monotonic relation between the total entropy generation and rates of exothermicity and endothermicity within the fluid and porous solid. Heat consumption (endothermicity) results in lowering the total entropy production. A comparison between Figure 4-24 a and b indicates that internal heat generation/consumption in the fluid is a stronger irreversible agent. In keeping with the previous discussions, these figures show that the increases in porosity decrease the total entropy production.

4.7 Conclusions

A thermal model was established for microreactors accommodating highly exothermic/endothermic reactions. This includes a thick wall, asymmetric microchannel partially filled with a porous material subject to constant but unequal temperatures at the outermost surfaces. The heat of reactions and absorption of microwaves and infrared waves were represented by volumetrically uniform, energy source terms. The porous region was assumed under local thermal non-equilibrium. It was argued that in such system the irreversibility is dominated by the thermal effects and hence mass transfer and chemical irreversibilities were ignored. In the limit of low thermal Peclet number, analytical solutions were developed for the conjugate heat transfer problem as well as the local and total entropy generations. A comprehensive parametric study was subsequently conducted.

Introduction of the heat of reaction and internal heat generations can significantly perturb the system from LTE condition. The extent of this deviation depends on the configuration of the microreactor. In particular, the thickness of the porous insert was found to be a dominating factor. This finding substantiates the necessity of applying LTNE in the thermal analysis of microreactors.

It was shown that the variations in the thicknesses of the walls and porous insert in the microreactor can majorly modify the Nusselt number. This is such by varying these parameters extremum points appear in the Nusselt number graphs, indicating the existence of optimum configurations. Nusselt number appeared to be inversely correlated with the

internal heat generations, whilst demonstrating a positive correlation with the porosity of the insert.

Changes in the wall and porous layer thickness led to the formation of minimum total entropy generation points. Thermal asymmetry of the system appeared to be an important source of irreversibility and its variation could minimise the total entropy production.

These points clearly reflect the significant role of the microstructure in shaping the thermal and entropic behaviour of microreactors. It further shows that to achieve an optimal design, thermal characteristics of the system such as thermal boundary conditions and internal heat generation should be considered in conjunction of the configurational specification of the system.

Chapter 5 Two-dimensional model of heat and mass transfer in porous microreactors

5.1 Introduction

The analysis of mass transfer in microreactors usually involves solution of a diffusion-advection equations on the basis of a simple Fickian mass diffusion [126,195,196]. Microreactors have been identified as suitable for coupled heat and mass transfer processes due to Soret effect [66], which is of importance in catalytic reactions [197]. However, so far, Soret effect has received very limited attention in microreactor and microchannel investigations. Habib-Matin and Pop investigated heat and mass transfer in a porous microchannel with catalytic internal surfaces [198]. These authors considered a simple one-dimensional diffusion of mass through a concentration diffusion mechanism as well as a thermodiffusion (Soret) effect. They derived analytical solutions for the LTE temperature and concentration fields in an axisymmetric configuration with zero wall thickness [198]. The general problem of thermodiffusion in porous media has been analysed in a relatively small number of investigations, e.g. [199–201]. However, analysis of thermodiffusion effects under LTNE and for more realistic thick wall microreactors is yet to be conducted.

Similar to that in macro-reactors, entropy generation in microreactors is of high significance [66]. Surprisingly, however, the existing works on entropy generation in microreactors are almost entirely limited to micro-combustors [123–125]. Notably, currently there is nearly no work on the entropic behaviours of porous micro-reactors. Exceptions to this, are the most recent works of Elliot et al. [117] and Torabi et al. [85], who investigated heat and mass transfer and entropy generation in a catalytic microreactor. Nonetheless, these analyses were one-dimensional and hence had limited applications. Thus, the existence of a gap in the studies of entropy generation in microreactors is evident. This shortcoming requires immediate attention as it is now well-demonstrated that microreactors are sophisticated thermochemical systems, which can feature non-straightforward entropic behaviours [104,105,126]. Further, recent investigations on porous microchannels have clearly shown the richness of the problem of entropy generation in these systems. As such, Ting et al. [115,129] theoretically examined entropy generation in microchannels with inserted nanofluid-filled porous media. They took an LTNE approach and conducted a two-dimensional, analytical solutions for the temperature fields and local entropy generation [115,129]. Their results mapped the influences of different mechanisms of entropy generation in a porous microchannel. In particular, they highlighted the significance of

hydrodynamic irreversibilities in cases with viscous convection of nanofluids [115]. Other theoretical works on the convection of nanofluids in heat generating/consuming porous channels demonstrated the necessity of considering LTNE for the accurate prediction of irreversibilities [95,97]. Another important factor complicating the irreversibilities of microreactors is the influences of solid thick walls. Recent studies on chemically inert microchannels have revealed the strong effects of the thick walls upon the rate of entropy generation [111,130,131]. This is essentially due to the effects of the solid thick walls upon the thermal fields in the microchannel, which in turn influences the rates of entropy generation [130]. Yet, the entropic influences of the thick walls on thermo-diffusive systems have just started to receive attention [85] and remain far from being well understood.

This reveals a number of important points about the current state of transport and entropy generation analyses in microreactors. First, porous microreactors have not been sufficiently analysed from an LTNE view even though the importance of such analysis is now well-demonstrated [93,97,98,100,108]. Second, there exists a major shortage of studies on the details of internal heat transfer in microreactors. In particular, the three-way interactions amongst the fluid phase, porous solid phase and microstructure of the reactor require further investigations. Third, the subject of thermo-diffusion in microreactors has received very limited attention. This topic is of high relevance to catalytic reactions and hence its inclusion in microreactor analysis is a crucial necessity. Finally, so far, the research on irreversibilities of microreactors has been exclusively focused on non-porous micro-combustors, e.g. [124,125]. Extension of these investigations to porous and particularly porous-catalytic microreactors is yet to be accomplished. Given these, the current study aims to establish a deeper understanding of the transport phenomena and irreversibilities, and their interactions with the microstructure in catalytic microreactors. Such understanding will be vital for the design and optimisation of practical microreactors.

To further these aims two cases are examined. Firstly, Case 1 investigates a heterogeneously catalysed reaction, with the catalyst on the walls of the enclosing structure (see Figure 5-1). Secondly, Case 2 explores the situation where the reaction within the microreactor channel is homogeneous in nature (see Figure 5-15).

5.2 Case 1-Catalytic reactor

5.2.1 Configuration and assumptions

Figure 5-1 illustrates the schematics of the problem under investigation. The microreactor consists of a single microchannel fully filled by porous materials. The system includes a microstructure consisting of two thick walls subject to unequal thermal fluxes and a catalytic coating covers the internal surface of the microchannel. A nanofluid flow enters the reactor from the left side.

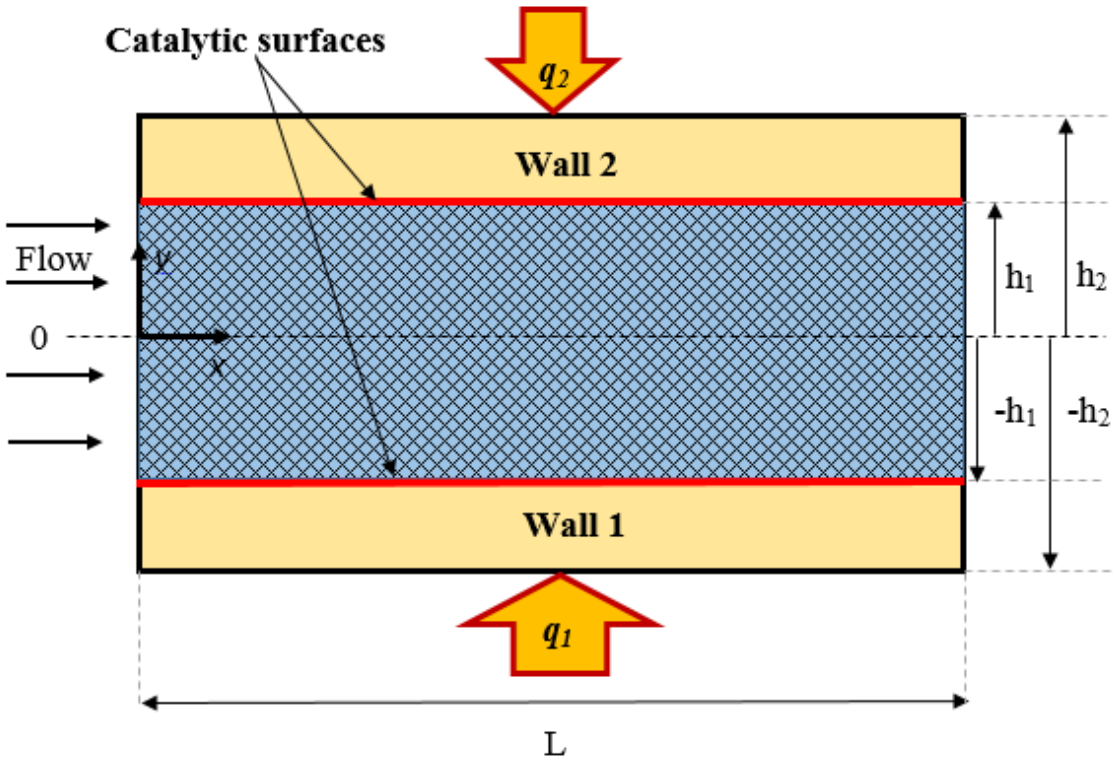

Figure 5-1 Schematics of the microreactor under investigation.

The following assumptions are made through the current analysis.

- The chemical reactions in the model microreactors shown in Figure 5-1 are limited to a zeroth-order reversible, catalytic reaction. Also, in keeping with the previous theoretical analysis of catalytic reactions in microchannels [103,104,198], the catalyst is assumed to be located on the internal surfaces of the channel.

- The effects of temperature variations on the catalytic reaction are ignored [198].

- The porous medium is homogenous, isotropic and fluid saturated and is under LTNE. Further, gravitational effects and radiative heat transfer are ignored.

- The nanofluid flow is steady and laminar satisfying the no-slip boundary conditions on the wall. Further, thermally and hydrodynamically fully developed conditions hold in the entire channel and there exist a no-slip boundary condition on the internal surface of the channel.

- Though nanofluids are known to exhibit shear-thinning behaviour, the nanofluid presented herein is assumed to behave as a Newtonian fluid. This is justified by the use of a 2% nanoparticle concentration, which is considerably below the limit of 13% up to which nanofluids may behave in a Newtonian manner[202].

- Physical properties such as porosity, specific heat, density, coefficient of thermal diffusion of mass and thermal conductivities are invariants. Following the literature dispersion of scalars (Temperature and Concentration) is ignored [183,184,198,203].

- The nanoparticles are uniformly distributed throughout the fluid forming a homogenous phase.

- Processes featuring abrupt reaction zones, separating hot and cold flows, such as those in micro-combustors [123,124] are not considered here. As a result, the axial conduction of heat within the walls is insignificant and is neglected throughout the analysis. This is further justified by noting that experimental studies [77] have already shown that the axial temperature gradient within the microstructure diminishes in thick wall microreactors.

It should be noted that the existence of nanofluid is not central to the current analysis. Nanofluids are considered for the sake of completeness of the study and their practical relevance to the subject of nanoparticle generation in microreactors [204].

5.2.2 Analytical solution

For the convenience of the reader, the governing equations described in Chapter 3 are presented again here. The separate phases of the system are indicated for their various properties by the subscripts where appropriate. The convention employed herein is that the lower wall uses subscript (1), the porous solid (S), the nanofluid (nf), and the upper wall

(2). Where a term is the effective thermal conductivity of the solid porous phase has subscript of (es). Likewise, the term is the effective thermal conductivity of the nanofluid phase has subscript of (enf).

5.2.2.1 Boundary conditions

The Darcy-Brinkman model of transport of momentum governs the hydrodynamics of the system, equation (3-9). It is important to emphasise that the value of Reynolds number used in this study (default value of $Re = 150$) permits the use of the Darcy-Brinkman equations since this Reynolds number is calculated using a characteristic length scale of the channel height. That is to say, this is not a pore scale analysis, but uses volume-averaged parameters. Consider a channel of height 800 micrometres, with pores of diameter of 4 micrometres. For the Darcy-Brinkman equation to be valid, the pore scale Reynolds number should be less than one. This would yield a Reynolds number of less than 200. Thus the use of the default value of $Re = 150$ would be consistent with the use of the Darcy-Brinkman equation in this case.

The transport of thermal energy within the solid and fluid phases of the microreactor are governed by the followings [115,205].

$$k_2 \frac{\partial}{\partial y}\left[\frac{\partial T_2}{\partial y}\right] = 0 \qquad h_1 < y \leq h_2 \qquad (5\text{-}112)$$

$$k_{enf}\frac{\partial^2 T_{nf}}{\partial y^2} + h_{sf}a_{sf}\left(T_s - T_{nf}\right) + \frac{\mu_{nf}}{\kappa}u^2 + \mu_{eff}\left(\frac{\partial u}{\partial y}\right)^2 = \rho_{nf}C_{p,nf}u\frac{\partial T_{nf}}{\partial x} \qquad -h_1 \leq y < h_1 \qquad (5\text{-}113)$$

$$k_{es}\frac{\partial^2 T_s}{\partial y^2} - h_{sf}a_{sf}\left(T_s - T_{nf}\right) = 0 \qquad -h_1 \leq y < h_1 \qquad (5\text{-}114)$$

$$k_1 \frac{\partial}{\partial y}\left[\frac{\partial T_1}{\partial y}\right] = 0 \qquad -h_2 \leq y < -h_1 \qquad (5\text{-}115)$$

Chapter 3 (Section 3.1.2.4) discussed how the thermophysical properties of nanofluid are calculated from those of the base fluid and nanoparticles. It is emphasised that heat generation by viscous dissipation has been included in equation (5-113) [115].

Mass transfer of chemical species is governed by the following advective-diffusive model, which takes into account contributions from the Soret effect in addition to the Fickian diffusion of species [146]. Since no specific reaction is modelled by this study, in order to prevent loss of generality, a value of $D = 10^{-5}\text{cm}^2\text{s}^{-1}$ was chosen as representative [182]. This value could be varied to give rise to different values of Soret number in the parametric study.

$$u\frac{\partial C}{\partial x} = D\frac{\partial^2 C}{\partial y^2} - D_T\frac{\partial^2 T_{nf}}{\partial y^2} \qquad -h_1 \le y < h_1 \qquad (5\text{-}116)$$

The momentum transport equations are subject to the no slip and symmetry boundary conditions:

$$y = h_1: \qquad u_{nf} = 0 \qquad (5\text{-}117)$$

$$y = 0: \qquad \frac{du_{nf}}{dy} = 0 \qquad (5\text{-}118)$$

The heat transport equations are subject to the following boundary conditions [115,205]:

$$y = h_2: \qquad k_2\frac{\partial T_2}{\partial y}\bigg|_{y=h_2} = q_2'' \qquad (5\text{-}119)$$

$$y = h_1: \qquad q_2'' = k_{enf}\frac{\partial T_{nf}}{\partial y}\bigg|_{y=h_1} + k_{es}\frac{\partial T_s}{\partial y}\bigg|_{y=h_1} \qquad T_2 = T_{nf} = T_s = T_{w2} \qquad (5\text{-}120)$$

$$y = -h_1: \qquad q_1'' = -k_{enf}\frac{\partial T_{nf}}{\partial y}\bigg|_{y=-h_1} - k_{es}\frac{\partial T_s}{\partial y}\bigg|_{y=-h_1} \qquad T_1 = T_{nf} = T_s = T_{w1} \qquad (5\text{-}121)$$

$$y = -h_2: \qquad k_1\frac{\partial T_1}{\partial y}\bigg|_{y=-h_2} = -q_1'' \qquad (5\text{-}122)$$

Here T_{w1} and T_{w2} are the temperatures on the interface between the porous medium and wall1 and wall2 respectively. The reference point, by which the temperatures within the system are compared, is the inlet on the lower wall, which is T_{w1} at $x = 0$ which will be considered as zero. To obtain meaningful results, a reference concentration value at a specific point should also be defined. Since the reference for the temperature field was

defined at the inlet on the lower wall, the reference concentration at this point is set to C_0 and the following concentration boundary conditions are written.

$$y = -h_1: \qquad C = C_0 \tag{5-123}$$

$$y = 0: \qquad D\frac{\partial C}{\partial y} = D_T\frac{\partial T_{nf}}{\partial y} \tag{5-124}$$

The boundary condition shown in equation (5-24) denotes the concentration flux across the centreline of the channel. Under equal heat flux conditions, the symmetry condition is applicable with no net flow of mass across the centreline. Applying an asymmetric heat flux would have no effect on a channel in which there was no Soret (or Dufour) effect and the symmetry condition would still hold. However, once the Soret effect is taken into account, then a mass flux due to the flow of mass along the thermal gradient exists. Since under asymmetric thermal conditions such a temperature gradient would exist across the centreline of the channel, then there would be a mass flux due to the thermal diffusion of mass. This is the physical interpretation of equation (5-24). This boundary condition may also be derived mathematically, as shown in Section 5.2.2.7.

5.2.2.2 Nusselt number

The heat transfer coefficients at the bottom and top walls of the channel are defined as;

$$H_{w1} = \frac{q_1''}{T_{w1} - \bar{T}_{nf}}, \tag{5-125}$$

$$H_{w2} = \frac{q_2''}{T_{w2} - \bar{T}_{nf}}. \tag{5-126}$$

Where;

$$\bar{T}_{nf} = \frac{1}{2\bar{u}h_1}\int_{-h_1}^{h_1} uT_{nf}\,dy. \tag{5-127}$$

Thus, Nusselt number based on the channel height h_1 is expressed as follows,

$$Nu_{w1} = \frac{2H_{w1}h_1}{k_{enf}} \tag{5-128}$$

$$Nu_{w2} = \frac{2H_{w2}h_1}{k_{enf}} \tag{5-129}$$

5.2.2.3 Entropy equations

The volumetric entropy generation for the system are expressed by equations (3-31) to (3-35) as shown in Chapter 3 [85,115,205]. Note that the fluid subscript, f are now replaced with nanofluid subscript, nf for consistency of this Chapter.

In equations (3-31) to (3-35), entropy generation terms have been split into contributions from different sources of irreversibility. The terms $\dot{S}_1'''$ and $\dot{S}_2'''$ account for the entropy generation in the lower and upper thick walls respectively. Entropy generation in the solid phase of the porous medium due to heat transfer is accounted by $\dot{S}_s'''$, similarly $\dot{S}_{nf}'''$ accounts for the entropy generation rate in the nanofluid phase. The contribution made by the irreversibility due to flow friction is calculated as $\dot{S}_{FF}'''$. The term $\dot{S}_{DI}'''$ is the entropy generation caused by the combination of concentration gradients and also that by mixed thermal and concentration gradients.

5.2.2.4 Dimensionless equations

Next, the following dimensionless parameters are introduced to enable further physical analysis.

$$\theta_i = \frac{2\left(T_i - T_{w,in}\right)k_{es}}{(q_1'' + q_2'')h_2}, \qquad \gamma = \frac{k_R h_1}{D}, \qquad Da = \frac{\kappa}{h_2^2},$$
$$u_r = -\frac{h_2^2}{\mu_f}\frac{\partial p_{nf}}{\partial x}, \qquad Y = \frac{y}{h_2}, X = \frac{x}{L}, \qquad Y_1 = \frac{h_1}{h_2},$$
$$Bi = \frac{h_{sf}a_{sf}{h_2}^2}{k_{es}}, \qquad M = \frac{\mu_{eff}}{\mu_{nf}}, \qquad k_{e1} = \frac{k_1}{k_{es}},$$
$$Br' = \frac{2\mu_{eff}\bar{u}^2}{(q_1'' + q_2'')h_2}, \qquad Q = \frac{q_2''}{(q_1'' + q_2'')}, \qquad k_{e2} = \frac{k_2}{k_{es}}, \tag{5-130}$$
$$Sr = \frac{(q_1'' + q_2'')h_1 D_T}{2C_0 k_{nf} D}, \qquad S = \frac{1}{\sqrt{MDa}}, \qquad Pe = \frac{\bar{u}h_1}{D},$$

$$k = \frac{k_{enf}}{k_{es}} = \frac{\varepsilon k_{nf}}{(1-\varepsilon)k_s}, \qquad \xi = \frac{h_2}{L}, \qquad \Phi = \frac{C}{C_0},$$

$$Re = \frac{2h_2\rho_{nf}\bar{u}}{\mu_{eff}}, \qquad Pr = \frac{C_{p,nf}\mu_{eff}}{k_{enf}}, \qquad U = \frac{u}{u_r}.$$

$$\omega = \frac{(q_1'' + q_2'')h_2}{2k_{es}T_{w,in}} \qquad N_i = \frac{\dot{S}_i'''h_2^2}{k_{es}}, \qquad \varphi = \frac{RDC_0}{k_{es}}$$

Where the dimensionless temperature follows the labelling convention; $i = 1,\ s,\ nf, 2$. Similarly the dimensionless entropy generation, N_i follows the labelling convention $i = 1, s, nf, FF, DI, 2$.

5.2.2.5 Velocity profiles

Equation (3-9) can be non-dimensionalised using the parameters defined in equations (5-130), resulting in

$$M\frac{d^2U}{dY^2} - \frac{U}{Da} + 1 = 0 \qquad -Y_1 \le Y < Y_1 \qquad (5\text{-}131)$$

Similarly, the no slip boundary condition and the condition due to the axial symmetry at $Y = 0$, can also be expressed in non-dimensional form as

$$U(\pm Y_1) = 0, \qquad U'(0) = 0. \qquad (5\text{-}132)$$

The solution of equation (5-131) then may be expressed by

$$U = Da\left(1 - \frac{cosh(SY)}{cosh(SY_1)}\right). \qquad -Y_1 \le Y < Y_1 \qquad (5\text{-}133)$$

From this equation, and the boundary conditions given in equation (5-132) the dimensionless average velocity across the channel can be calculated as

$$\bar{U} = Da\left(1 - \frac{tanh(SY_1)}{SY_1}\right). \qquad (5\text{-}134)$$

By combining equations (5-133) and (5-134) the following ratios are defined

$$u/\bar{u} = U/\bar{U} = \frac{SY_1(cosh(SY_1) - cosh(SY))}{SY_1\, cosh(SY_1) - sinh(SY_1)}. \tag{5-135}$$

5.2.2.6 Temperature profiles

Due to the assumption of fully developed flow and by incorporating the assumptions summarised in Section 5.2.1, the following conditions hold [115],

$$\frac{\partial T_{nf}}{\partial x} = \frac{d\bar{T}_{nf}}{dx} = \frac{\partial T_s}{\partial x} = \frac{d\bar{T}_s}{dx} = \frac{dT_{w1}}{dx} = \frac{dT_{w2}}{dx} = \Omega = constant. \tag{5-136}$$

Thus, the following form of solution is sought for the temperature equations:

$$T_i(x, y) = f_i(y) + \Omega x \qquad i = 1, 2, s, nf, \tag{5-137}$$

where $f_i(y)$ is a function to be determined by solving equations (5-112) to (5-115) in association with the given boundary conditions. In order to solve the transports of thermal energy in the porous medium, first it is necessary to add equation (5-113) to (5-114) and then integrate the resultant equation over the cross-section of the channel. Substituting in the heat flux boundary conditions from equations (5-121 to 5-120) and (5-121) yields

$$q_1'' + q_2'' + \frac{\mu_{nf}}{\kappa}\int_{-h_1}^{h_1} u^2\, dy \;+\; \mu_{eff}\int_{-h_1}^{h_1}\left(\frac{\partial u}{\partial y}\right)^2 dy = \rho_{nf} C_{p,nf}\int_{-h_1}^{h_1} u\frac{\partial T_{nf}}{\partial x}\, dy. \tag{5-138}$$

Rearranging equation (5-135) allows substitution for u in equation (5-138). Applying the non-dimensional parameters, defined in equations (5-130), facilitates the integration process to obtain

$$\frac{d\bar{T}_{nf}}{dx} = \frac{1}{2\rho_{nf} C_{p,nf}\bar{u}h_1 h_2}\left[h_2 q_1'' + h_2 q_2'' + \frac{2\mu_{eff}S^3\bar{u}^2 Y_1^2 cosh(SY_1)}{SY_1\, cosh\ (SY_1) - sinh(SY_1)}\right] = \Omega \tag{5-139}$$

Where the mean bulk temperature is given by equation (5-127). Utilising the non-dimensional parameters of equations (5-130) and the rearranged form of equation (5-135) together with equation (5-139) lead to the non-dimensional forms of equations (5-112) to (5-115). The constant coefficients are defined explicitly in Appendix A, section 1.

$$k_{e2}\theta_2'' = 0 \qquad\qquad Y_1 < Y \leq 1 \tag{5-140}$$

$$k\theta_{nf}'' + Bi\left(\theta_s - \theta_{nf}\right) + D_2\, cosh(2SY) + D_3\, cosh(SY) + D_4 = 0 \qquad -Y_1 \le Y < Y_1 \qquad (5\text{-}141)$$

$$\theta_s'' - Bi\left(\theta_s - \theta_{nf}\right) = 0 \qquad -Y_1 \le Y < Y_1 \qquad (5\text{-}142)$$

$$k_{e1}\theta_1'' = 0 \qquad -1 \le Y < -Y_1 \qquad (5\text{-}143)$$

Algebraic manipulation of equations (5-141) and (5-142), yields

$$k\theta_{nf}'''' - Bi(1+k)\theta_{nf}'' + (4S^2 - Bi)D_2\, cosh\,(2SY) + (S^2 - Bi)D_3\, cosh\,(SY) - BiD_4 = 0 \qquad (5\text{-}144)$$

$$k\theta_s'''' - Bi(1+k)\theta_s'' - Bi(D_2\, cosh\ (2SY) + D_3\, cosh\ (SY) + D_4) = 0 \qquad (5\text{-}145)$$

Equations (5-120) and (5-121) along with equations (5-141) and (5-142) allow for the calculation of the 8 boundary conditions of the two fourth order differential equations, (5-144) and (5-145). These equations are, however, linked to equations (5-140) and (5-143), which then require further four boundary conditions in order for a solution to be obtained. Equations (5-119) to (5-122) provide the necessary extra boundary conditions. These give the following 12 boundary conditions required for the closure of the system:

Table 5-1 Boundary conditions for temperature equations

$\theta_{nf}(-Y_1) = \theta_s(-Y_1) = 0,$	$\theta_{nf}(Y_1) = \theta_s(Y_1) = \theta_{w2},$
$\theta_s''(-Y_1) = \theta_s''(Y_1) = 0,$	
$\theta_1(-Y_1) = 0,$	$k_{e1}\theta_1'(1) = 2(1-Q),$
$\theta_2(Y_1) = \theta_{w2},$	$k_{e2}\theta_2'(1) = 2Q.$
$\theta_{nf}''(-Y_1) = \theta_{nf}''(Y_1) = -\frac{1}{k}(D_2 \cosh(2SY) + D_3 \cosh(SY) + D_4),$	

Applying the boundary conditions given in Table 5-1 allows the analytical solutions of the system of equations (5-140), (5-143), (5-144) and (5-145) to be found. The resultant closed-form dimensionless temperature profiles in the transversal direction are:

$$\theta_2(Y) = E_1 + E_2 Y \qquad Y_1 < Y \le 1 \qquad (5\text{-}146)$$

$$\theta_{nf}(Y) = E_3\, cosh(2SY) + E_4\, cosh(SY) + E_5\, cosh(\alpha Y) + E_6 Y^2 + E_7 Y + E_8 \qquad -Y_1 \le Y < Y_1 \qquad (5\text{-}147)$$

$$\theta_s(Y) = E_9\, cosh(2SY) + E_{10}\, cosh(SY) + E_{11}\, cosh(\alpha Y) + E_6 Y^2 + E_7 Y + E_{12} \qquad -Y_1 \le Y < Y_1 \qquad (5\text{-}148)$$

$$\theta_1(Y) = E_{13} + E_{14} Y \qquad -1 \le Y < -Y_1 \qquad (5\text{-}149)$$

in which

$$\alpha = \sqrt{Bi(1 + k^{-1})}. \qquad (5\text{-}150)$$

Through substitution of the dimensionless axial and transverse temperature profiles into equation (5-137) the final two-dimensional temperature profiles become

$$\theta_2(X,Y) = \frac{2\,X\,[1 + Br' D_1\, S^2 Y_1\, cosh(SY_1)]}{Re\, Pr\, k\, Y_1 \xi} + E_1 + E_2 Y \qquad Y_1 < Y \le 1 \qquad (5\text{-}151)$$

$$\theta_{nf}(X,Y) = \frac{2\,X\,[1 + Br' D_1\, S^2 Y_1\, cosh(SY_1)]}{Re\, Pr\, k\, Y_1 \xi} + E_3\, cosh(2SY) + E_4\, cosh(SY) + E_5\, cosh(\alpha Y) + E_6 Y^2 + E_7 Y + E_8 \qquad -Y_1 \le Y < Y_1 \qquad (5\text{-}152)$$

$$\theta_s(X,Y) = \frac{2\,X\,[1 + Br' D_1\, S^2 Y_1\, cosh(SY_1)]}{Re\, Pr\, k\, Y_1 \xi} + E_9\, cosh(2SY) + E_{10}\, cosh(SY) + E_{11}\, cosh(\alpha Y) + E_6 Y^2 + E_7 Y + E_{12} \qquad -Y_1 \le Y < Y_1 \qquad (5\text{-}153)$$

$$\theta_1(X,Y) = \frac{2\,X\,[1 + Br' D_1\, S^2 Y_1\, cosh(SY_1)]}{Re\, Pr\, k\, Y_1 \xi} + E_{13} + E_{14} Y \qquad -1 \le Y < Y_1 \qquad (5\text{-}154)$$

where the expressions for coefficients $E_1 - E_{14}$ are provided in Appendix A section1.

To further the analysis of the thermal conditions within the microchannel, the Nusselt number for the upper and lower walls must also be rendered dimensionless. This yields:

$$Nu_{w1} = \frac{4(Q-1)Y_1}{k\bar{\theta}_{nf}} \tag{5-155}$$

$$Nu_{w2} = \frac{4QY_1}{k(\theta_{w2} - \bar{\theta}_{nf})} \tag{5-156}$$

The dimensionless bulk mean temperature of the nanofluid, $\bar{\theta}_{nf}$ may be found by determining a dimensionless form of equation (5-127) and then integrating over the channel.

$$\bar{\theta}_{nf} = \frac{D_1}{2\,Y_1}\int_{-Y_1}^{Y_1} \theta_{nf}[cosh(SY_1) - cosh(SY)]\,dY. \tag{5-157}$$

Since the top wall temperature is not known in advance, it is necessary to find the equation by which it is defined. This may be accomplished by using the dimensionless form of the boundary condition in equation (5-120), which defines q_2'':

$$\theta_s'(Y_1) + k\theta_{nf}'(Y_1) = 2Q. \tag{5-158}$$

Substituting from equations (5-144) and (5-145) and some algebraic manipulations lead to

$$\theta_{w2} = \frac{Y_1[4QS + 2D_4SY_1 + 2D_3\,sinh(SY_1) + D_2\,sinh(2SY_1)]}{S(k+1)} \tag{5-159}$$

5.2.2.7 Concentration profiles

Seeking a solution to the governing equation of mass transfer of the form:

$$C(x,y) = g(y) + h(x). \tag{5-160}$$

A control volume over a section of the channel with the length dx is considered and the thickness in the z direction is chosen to be 1. Application of the Taylor series expansion on a species balance written for this control volume leads to the following equation,

$$\left[\int_0^{h_1} u.C\ dy\right] + K_R dx - \left[\int_0^{h_1} u.C\ dy + \frac{\partial}{\partial x}\left(\int_0^{h_1} u.C\ dy\right)dx\right] = 0. \tag{5-161}$$

Gathering terms and applying Leibniz rule leads to:

$$\int_0^{h_1} u\frac{\partial C}{\partial x}dy = k_R. \tag{5-162}$$

The velocity profile is symmetric over the channel and so the half channel may be used, thus the mean velocity across the half channel is given by:

$$\bar{u} = \frac{1}{h_1}\int_0^{h_1} u\ dy. \tag{5-163}$$

Noting that the desired form of the solution means that $\frac{\partial C}{\partial x}$ does not rely on y and utilising equation (5-163) results in:

$$\frac{\partial C}{\partial x} = \frac{k_R}{h_1\bar{u}}. \tag{5-164}$$

Assigning C_0 as the initial concentration, the solution of equation (5-164) takes the form of

$$C(x) = \frac{k_R x}{h_1\bar{u}}. \tag{5-165}$$

Using the dimensionless parameters defined in equations (5-130), the equation (5-165) can be non-dimensionalised in the following form,

$$\Phi(X) = \frac{\gamma X}{Pe\ Y_1 \xi} \tag{5-166}$$

Substitution of equation (5-164) into equation (5-116) gives

$$\frac{u\ k_R}{h_1\bar{u}} = D\frac{\partial^2 C}{\partial y^2} - D_T\frac{\partial^2 T_{nf}}{\partial y^2} \tag{5-167}$$

The mathematical derivation of the boundary condition equation (5-124) is best demonstrated at this point. Substitution of equation (5-135) into the above equation give:

$$\left(\frac{(cosh(SY_1) - \cosh(SY))}{SY_1\, cosh(SY_1) - \sinh(SY_1)}\right)\frac{SY_1 k_R}{h_1} = D\frac{\partial^2 C}{\partial y^2} - D_T\frac{\partial^2 T_{nf}}{\partial y^2} \tag{5-168}$$

Integrating the above equation with respect to y gives (noting that $Y = \frac{y}{h_2}$):

$$\left(\frac{cosh(SY_1)y - (\frac{h_2}{S})\sinh(SY))}{SY_1\, cosh(SY_1) - \sinh(SY_1)}\right)\frac{SY_1 k_R}{h_1} = D\frac{\partial C}{\partial y} - D_T\frac{\partial T_{nf}}{\partial y} + fn(x) \tag{5-169}$$

Where $fn(x)$ is an arbitrary function of x. The desired boundary condition is at $y = 0$ so this becomes:

$$D\frac{\partial C}{\partial y} = D_T\frac{\partial T_{nf}}{\partial y} + fn(x) \tag{5-170}$$

This is the boundary condition, but clearly $fn(x)$ needs to be defined. Consider, this boundary condition must be able to permit the model to function under both asymmetric and symmetric thermal boundary conditions. Under symmetric boundary conditions, where the temperature gradient is zero, this equation must reduce to:

$$D\frac{\partial C}{\partial y} = 0 \tag{5-171}$$

This may only be achieved if $fn(x)$ is the zero function. Armed with this knowledge, the resulting boundary condition is that stated in equation (5-124).

By employing the dimensionless parameters of equation (5-164) and the velocity ratio of equation (5-135) allows equation (5-167) to be non-dimensionalised and rearranged in the form of

$$\Phi''(Y) = \frac{Sr\, k}{Y_1\varepsilon}\theta''_{nf}(Y) + \frac{\gamma D_1(cosh(SY_1) - cosh(SY))}{Y_1^2}. \tag{5-172}$$

Since $\theta''_{nf}(Y)$ may be determined from equation (5-152) only the boundary conditions equations (5-123) and (5-124) require to be non-dimensionalised. These are expressed by,

$$\Phi(-Y_1) = 1 \tag{5-173}$$

$$\Phi'(0) = \frac{Sr\ k}{Y_1 \varepsilon}\theta'_{nf}(0). \tag{5-174}$$

Through applying equations (5-173) and (5-174), equation (5-172) can be solved analytically to obtain the dimensionless concentration profile in the transverse direction. This reads

$$\Phi(Y) = F_1 + F_2 Y + F_3 Y^2 + F_4\, cosh(2SY) + F_5\, cosh(SY) + F_6\, cosh(\alpha Y). \tag{5-175}$$

Finally, substituting (5-175) and (5-166) into (5-160) gives the dimensionless concentration profiles in the axial and transverse directions,

$$\Phi(X,Y) = e\frac{\gamma X}{Pe\ Y_1 \xi} + F_1 + F_2 Y + F_3 Y^2 + F_4\, cosh(2SY) + F_5\, cosh(SY) + F_6\, cosh(\alpha Y). \tag{5-176}$$

Analytical expressions for $F_1 - F_6$ are lengthy and rather cumbersome and thus are not provided explicitly.

5.2.2.8 Entropy profiles

The resultant non-dimensionalised versions of by equations (3-31) to (3-35) are:

$$N_1 = \frac{k_{e1}\omega^2}{(\omega\theta_1 + 1)^2}\left[\xi^2\left(\frac{\partial\theta_1}{\partial X}\right)^2 + \left(\frac{\partial\theta_1}{\partial Y}\right)^2\right] \tag{5-177}$$

$$N_s = \frac{\omega^2}{(\omega\theta_s + 1)^2}\left[\xi^2\left(\frac{\partial\theta_s}{\partial X}\right)^2 + \left(\frac{\partial\theta_s}{\partial Y}\right)^2\right] - \frac{Bi\omega\left(\theta_s - \theta_{nf}\right)}{(\omega\theta_s + 1)} \tag{5-178}$$

$$N_{nf} = \frac{k\ \omega^2}{\left(\omega\theta_{nf} + 1\right)^2}\left[\xi^2\left(\frac{\partial\theta_{nf}}{\partial X}\right)^2 + \left(\frac{\partial\theta_{nf}}{\partial Y}\right)^2\right] + \frac{Bi\omega\left(\theta_s - \theta_{nf}\right)}{\left(\omega\theta_{nf} + 1\right)} \tag{5-179}$$

$$N_{FF} = \frac{D_2\omega}{\left(\omega\theta_{nf} + 1\right)}\left[cosh^2(SY_1) - 2\, cosh(SY)\, cosh(SY_1) + cosh(2SY)\right] \tag{5-180}$$

$$N_{DI} = \frac{\varphi}{\Phi}\left[\xi^2\left(\frac{\partial \Phi}{\partial X}\right)^2 + \left(\frac{\partial \Phi}{\partial Y}\right)^2\right] + \frac{\varphi\omega}{\left(\omega\theta_{nf}+1\right)}\left[\xi^2\left(\frac{\partial \Phi}{\partial X}\right)\left(\frac{\partial \theta_{nf}}{\partial X}\right) + \left(\frac{\partial \Phi}{\partial Y}\right)\left(\frac{\partial \theta_{nf}}{\partial Y}\right)\right] \quad (5\text{-}181)$$

$$N_2 = \frac{k_{e2}\omega^2}{(\omega\theta_2+1)^2}\left[\left(\frac{\partial \theta_2}{\partial X}\right)^2 + \left(\frac{\partial \theta_2}{\partial Y}\right)^2\right] \quad (5\text{-}182)$$

To facilitate the study of entropy generation and compare the contributions from different sources of irreversibility, the equations for the nanofluid and the solid phases of the porous medium are broken down. This provides the following equations for the irreversibility of heat transfer in the system.

$$N_{s,ht} = \frac{\omega^2}{(\omega\theta_s+1)^2}\left[\xi^2\left(\frac{\partial \theta_s}{\partial X}\right)^2 + \left(\frac{\partial \theta_s}{\partial Y}\right)^2\right], \quad (5\text{-}183)$$

$$N_{nf,ht} = \frac{k\,\omega^2}{\left(\omega\theta_{nf}+1\right)^2}\left[\xi^2\left(\frac{\partial \theta_{nf}}{\partial X}\right)^2 + \left(\frac{\partial \theta_{nf}}{\partial Y}\right)^2\right]. \quad (5\text{-}184)$$

By adding the remaining components of equations (5-178) and (5-179) the interstitial volumetric entropy generation term can be expressed by,

$$N_{int} = \frac{Bi\;\omega^2\left(\theta_{nf}-\theta_s\right)^2}{(\omega\theta_s+1)\left(\omega\theta_{nf}+1\right)}. \quad (5\text{-}185)$$

The volumetric entropy generations for the porous insert, N_{pm} is simply the sum of the equations that are applicable to the porous medium. This is a function defining the entropy generation for the combined processes of heat transfer, viscous dissipation, and concentration gradients for any given points (X, Y).

$$N_{pm} = N_{s,ht} + N_{nf,ht} + N_{int} + N_{FF} + N_{DI}. \quad (5\text{-}186)$$

For the total entropy generation in the microreactor, N_{Tot}, the sum of the parts of volumetric entropy generation in the ranges in which they are valid is integrated over the volume of the channel. The contributions from the walls are then added. This gives a

numerical value for the total entropy for any given configuration, and is obtained using the following equation

$$N_{Tot} = \int_{-1}^{1}\int_{0}^{1}\sum N_i \, dXdY, \qquad i = 1, s, nf, FF, DI, 2. \tag{5-187}$$

5.2.3 Validation

To validate the mathematical model developed in Section 5.2.2, it is demonstrated here that when the wall thickness tends to zero, the temperature fields reduce to that presented by Ting et al. [115] with no internal heat generation term. For details, see Appendix B section 1.1.

5.2.4 Discussion

The problem solved in Section 5.2.2 features a large number of dimensionless parameters. To conduct quantitative analyses default values are assigned to them in Table 5-2.

Table 5-2 Default values of dimensionless parameters used in figures.

Dimensionless parameter	Dimensionless parameter name	Default value
ϕ	Nanoparticle concentration	2%
Bi	Biot Number	1
Br'	Modified Brinkman number	0.01 0.00001 (Entropy analysis)
γ	Damköhler number	1
Da	Darcy number	0.1
Pe	Peclet number	10
Pr	Prandtl number	5
Re	Reynolds number	150
Sr	Soret number	0.7
ε	Porosity	0.95
k	Thermal conductivity ratio	0.05
k_{e1}	Dimensionless Wall1 thermal conductivity	0.5
k_{e2}	Dimensionless Wall1 thermal conductivity	0.5
Q	Heat flux ratio	0.75
ω	Dimensionless heat flux	0.001
φ	Irreversibility distribution ratio	0.01
Y_1	Channel thickness	0.8
ξ	Aspect ratio of channel	0.05

5.2.4.1 Temperature fields

Figure 5-2 to 5 show contours of the dimensionless temperatures plotted for the entire duct. The non-dimensional temperature fields of the nanofluid and porous solid phases are shown and the figures do not include the temperature distributions inside the solid walls. It should be noted that the dimensionless temperature defined in equations (5-130) is based on the reference of the wall temperature at the inlet of the duct. Hence, both negative and positive dimensionless temperatures may exist throughout the duct. Figure 5-2 depicts the variation of the solid and nanofluid temperature fields for different values of thermal conductivity of the lower wall. Other parameters are provided in Table 5-1. The asymmetric behaviour of the dimensionless temperature fields is evident in this figure. This is primarily due to the imbalance in the thermal loads applied to the top and bottom external surfaces of the system.

It is also due to the variations in the thermal conductivity of the lower wall, which changes the thermal resistance of this wall and hence can contribute with the asymmetry of the temperature profiles. Figure 5-2a and Figure 5-2b show that there exists a considerable temperature difference between the wall and the nanofluid at the inlet of the duct. This is depicted by a relatively large negative dimensionless temperature at the entrance of the microchannel. Continuous heating results in increase of the solid and nanofluid temperatures, which in turn pushes the dimensionless temperatures towards zero and positive values. When the values of thermal conductivity of the lower wall increase, the sign change in the dimensionless temperatures occurs earlier along the duct.

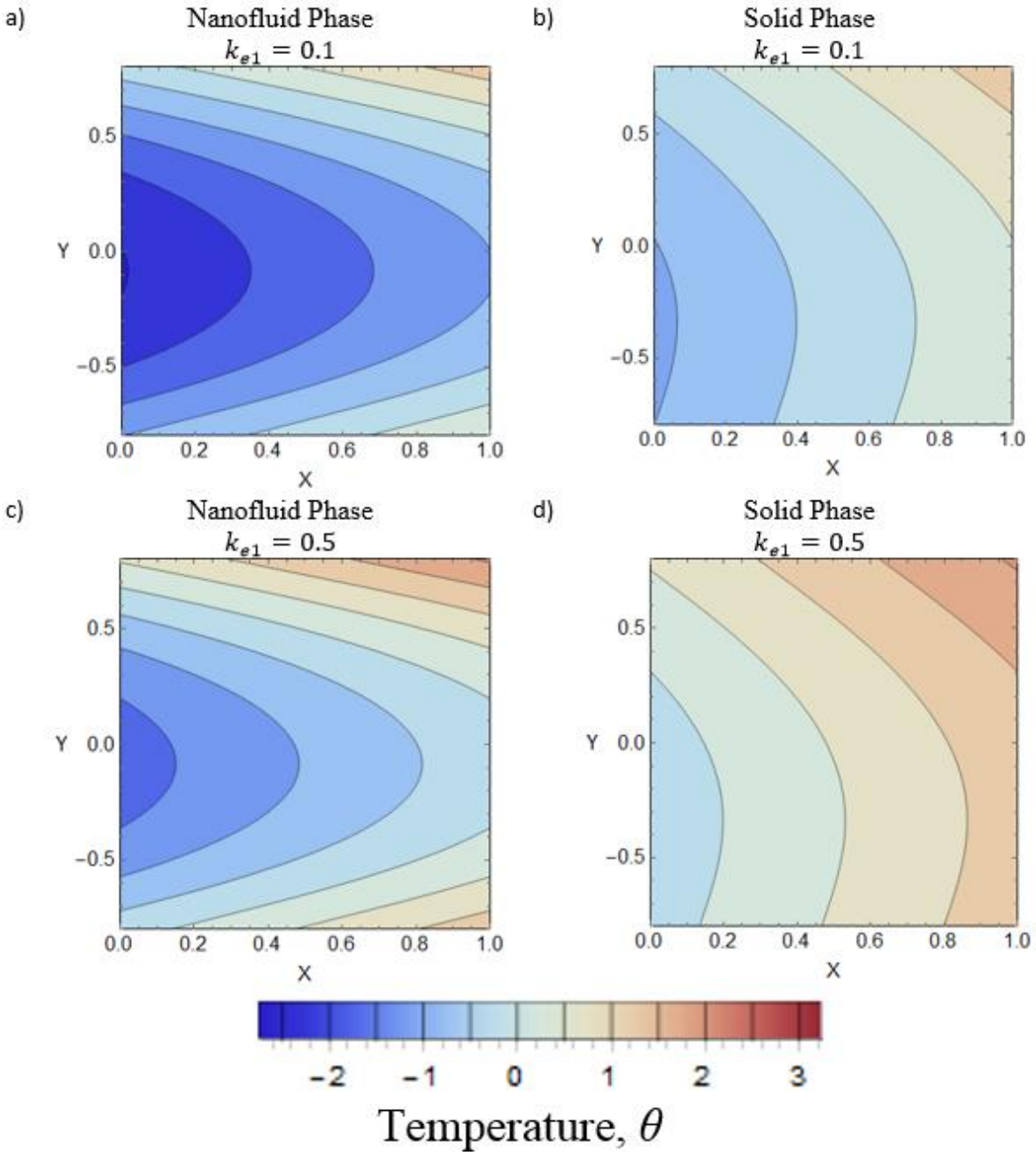

Figure 5-2 Temperature contours for varying lower wall thermal conductivity, $\boldsymbol{k_{e1}}$.

Figure 5-2c and Figure 5-2d show that as the thermal conductivities of the wall increases a larger fraction of the duct volume features small values of dimensionless temperatures. This behaviour implies that the temperature differences between the solid and fluid phases at the inlet of the duct are lower at higher thermal conductivities of the wall. This is to explained by the enhancing of the thermal conductivity of the wall reducing its thermal resistance and this results in lowering the required temperature differences for the transfer of the imposed thermal load to the nanofluid. Figure 5-2 also reflects the significant difference between the temperature fields in the nanofluid and porous solid phase. Such difference highlights the importance of the undertaken LTNE approach.

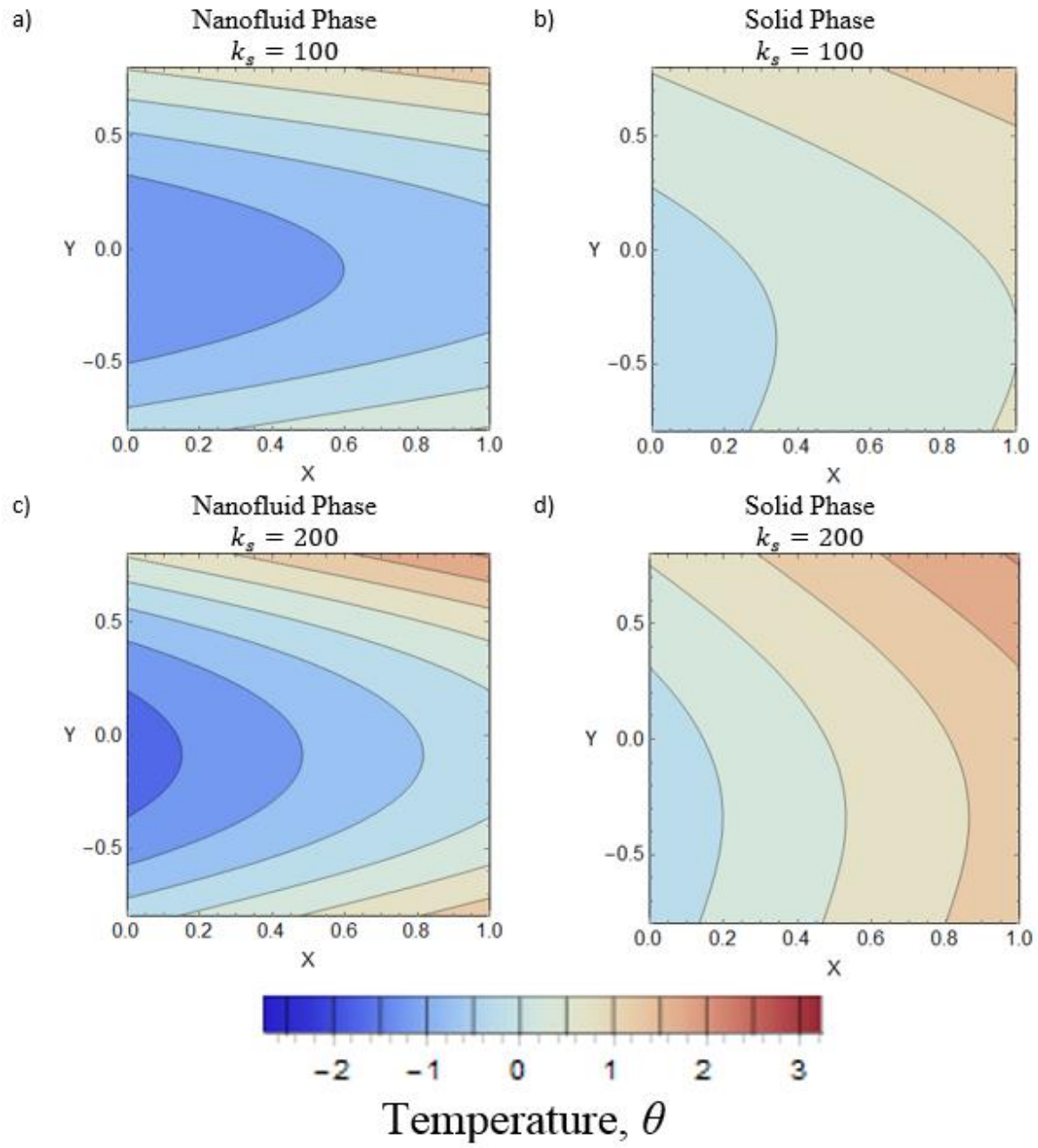

Figure 5-3 Temperature contours for varying thermal conductivity of the porous solid, $\boldsymbol{k_s}$

Figure 5-3 shows the contours of the dimensionless temperatures for different values of the porous solid conductivity. It is clear in this figure that for low conductivity values of the porous solid (Figure 5-3a and Figure 5-3b) the change of dimensionless temperature through the pipe is minimal. By increasing the thermal conductivity of the porous solid, the nanofluid and solid phases both experience more extensive variations in their non-dimensional temperatures. In the case of the porous solid this is due to the increase in its thermal conductivity permitting more efficient heat transfer in both axial and transverse directions. The fluid phase is affected by the increase in temperature of the solid phase via interstitial heat transfer and as a result also experiences increased temperature variations.

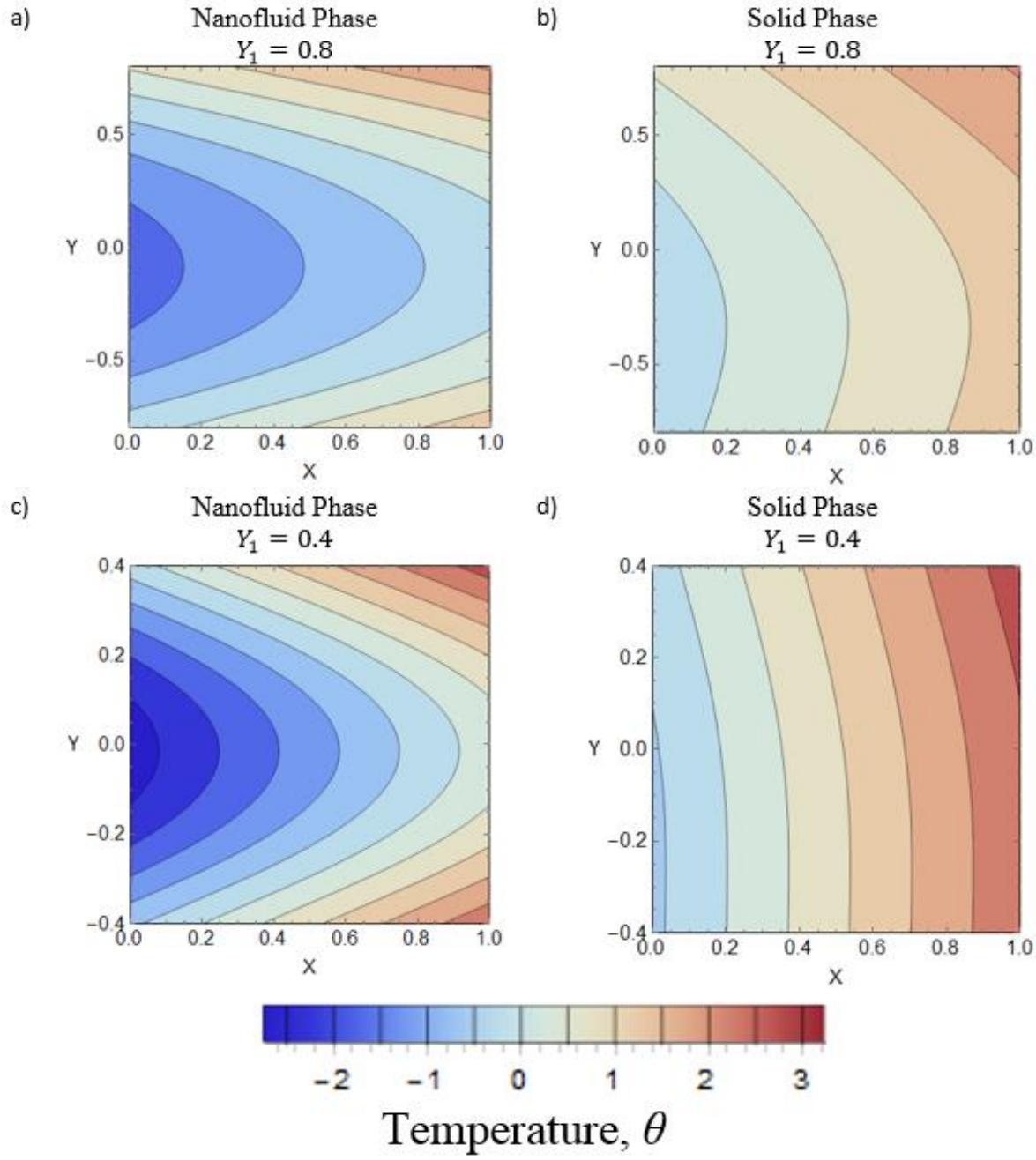

Figure 5-4 Temperature contours for varying wall thickness, $\boldsymbol{Y_1}$

Figure 5-4 illustrates the influences of the wall thickness upon the dimensionless temperature fields. It is evident from this figure that by thickening the wall (decreasing the value of $\boldsymbol{Y_1}$) the variations in the dimensionless temperatures are intensified. This could be readily verified by comparing Figure 5-4a and Figure 5-4c or Figure 5-4b and Figure 5-4d. In particular, for the thicker walls the solid and nanofluid phases experience greater temperature differences. This result is consistent with the physical intuition, which requires larger temperature differences for thicker and more resistive walls. It is also in keeping with the recent results in Refs. [85,117,205], which reported one-dimensional analyses of heat transfer in microreactors. Here there is the same thermal load entering a narrower channel, as such, there is less material to absorb the heat and higher temperatures are achieved.

Additionally, the Reynolds number remains constant for both configurations and since the channel height has decreased, there must be a corresponding increase in velocity. This is why the temperatures entering the channel at the centre are lower for the thicker walled channel. Most importantly, the behaviour observed in Figure 5-4 is of practical significance in the design of microreactors as it clearly shows the major effects of wall thicknesses on the temperature fields inside the reactor. Such effects are often negligible in macro-reactors.

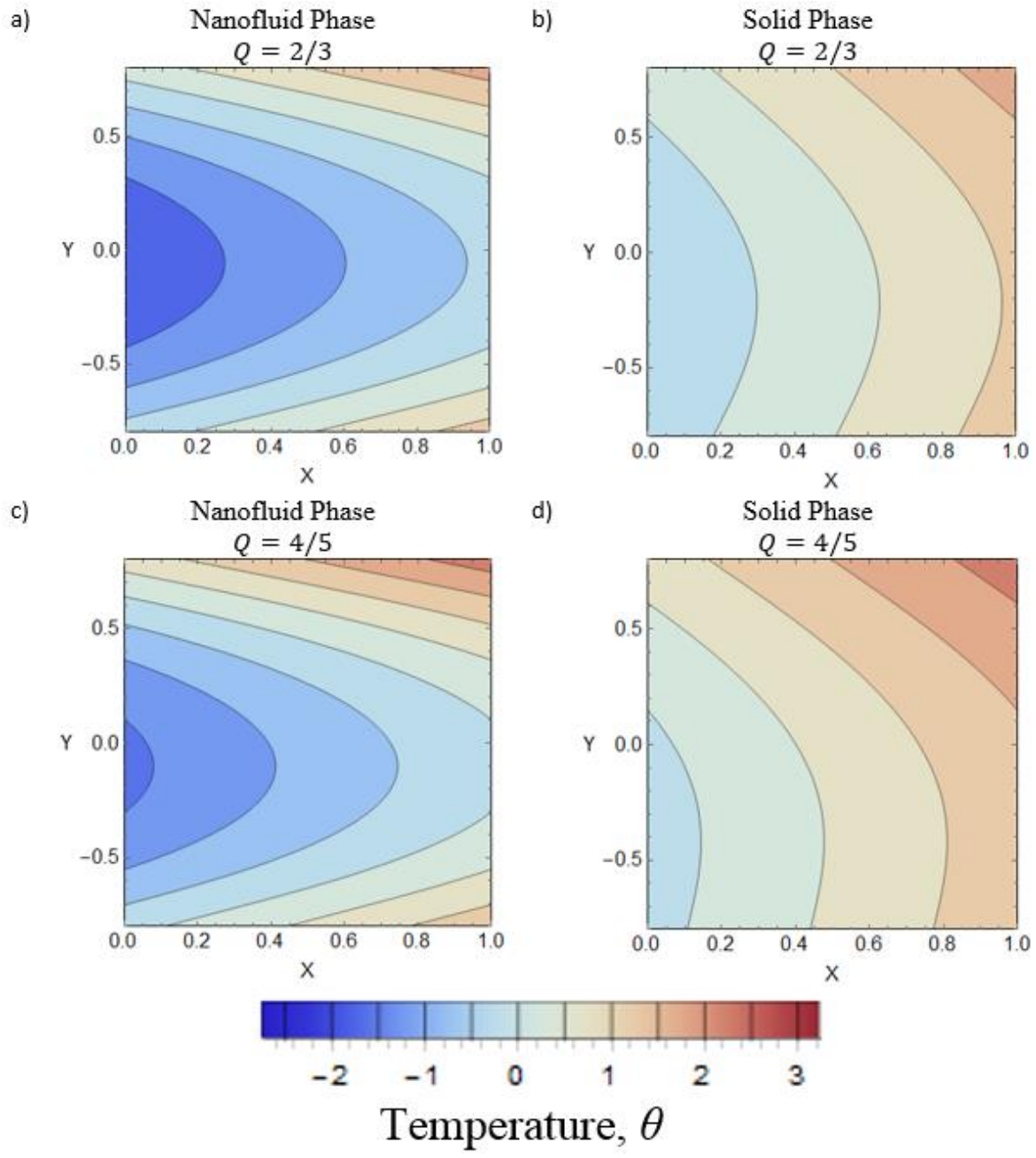

Figure 5-5 Temperature contours for varying heat flux ratio, $\boldsymbol{Q}$

Nonetheless, the similarity of channel diameter and wall thickness in microsystems imparts a pronounced effect on the thermal behaviour of these systems. The effects of strengthening the imbalance in the exposed thermal fluxes are investigated in Figure 5-5.

This figure shows that, magnifying the heat flux (q_2'') on the upper wall increases the asymmetry of the temperature fields. It also shows that the temperature gradients near the upper wall have increased to enable transversal transfer of stronger heat loads to the nanofluid and solid phases. Of interest is that there is a general increase in overall temperature as the heat flux conditions in the channel become increasingly asymmetric. This may be due to the disparity between the asymmetric thermal conditions and the symmetric flow field. This leading to a lower quantity of cold fluid entering at the centre of the channel, which in turn will affect the overall temperature of the channel.

It should be recalled that in practice, temperature is amongst the most essential characteristics of any chemical system. The results presented in this subsection showed that the configuration of the microstructure, as well as the thermophysical properties of the porous solid can majorly affect the thermal behaviour of the microreactor.

5.2.4.2 Nusselt number

Figure 5-6 shows the variations of Nusselt number on the upper and lower internal walls of the channel against the changes in the lower wall thickness. As a general trend, this figure shows that the numerical value of Nusselt number increases significantly by reducing the thickness of the lower wall. This is a clear manifestation of the significant role of the microstructure in the thermal behaviour of microsystems and has been also emphasised in other recent studies [205]. Figure 5-6a depicts the sensitivity of Nusselt number to the thermal conductivity of the porous solid. Increases in the value of thermal conductivity of the solid phase of the porous medium results in enhancement of the Nusselt number. The effects of thermal load imbalance (Q defined in equation (5-130)) on the Nusselt number have been investigated in Figure 5-6b. According to this figure as the value of Q approaches unity, the Nusselt number increases. The effects of permeability of the porous medium on the rate of heat transfer have been shown in Figure 5-6c. In keeping with the findings of other investigations [108], this figure shows that the Nusselt number increases at lower values of Darcy number. As permeability decreases, the magnitude of the mean temperature also decreases as it is intrinsically connected to the associated reduction in velocity (see equation 5-127). This lower magnitude of mean temperature in turn causes an increase in Nusselt number (see equation 5-155) through its enhancement of the heat transfer coefficient. Figure 5-6d shows the response of Nusselt number to changes in the volumetric concentration of nanoparticles. A modest improvement is observed in Nusselt number by

increases in the volumetric concentration of nanoparticles. This is in total agreements with the findings of the recent studies of forced convection of nanofluids in porous media [95,97].

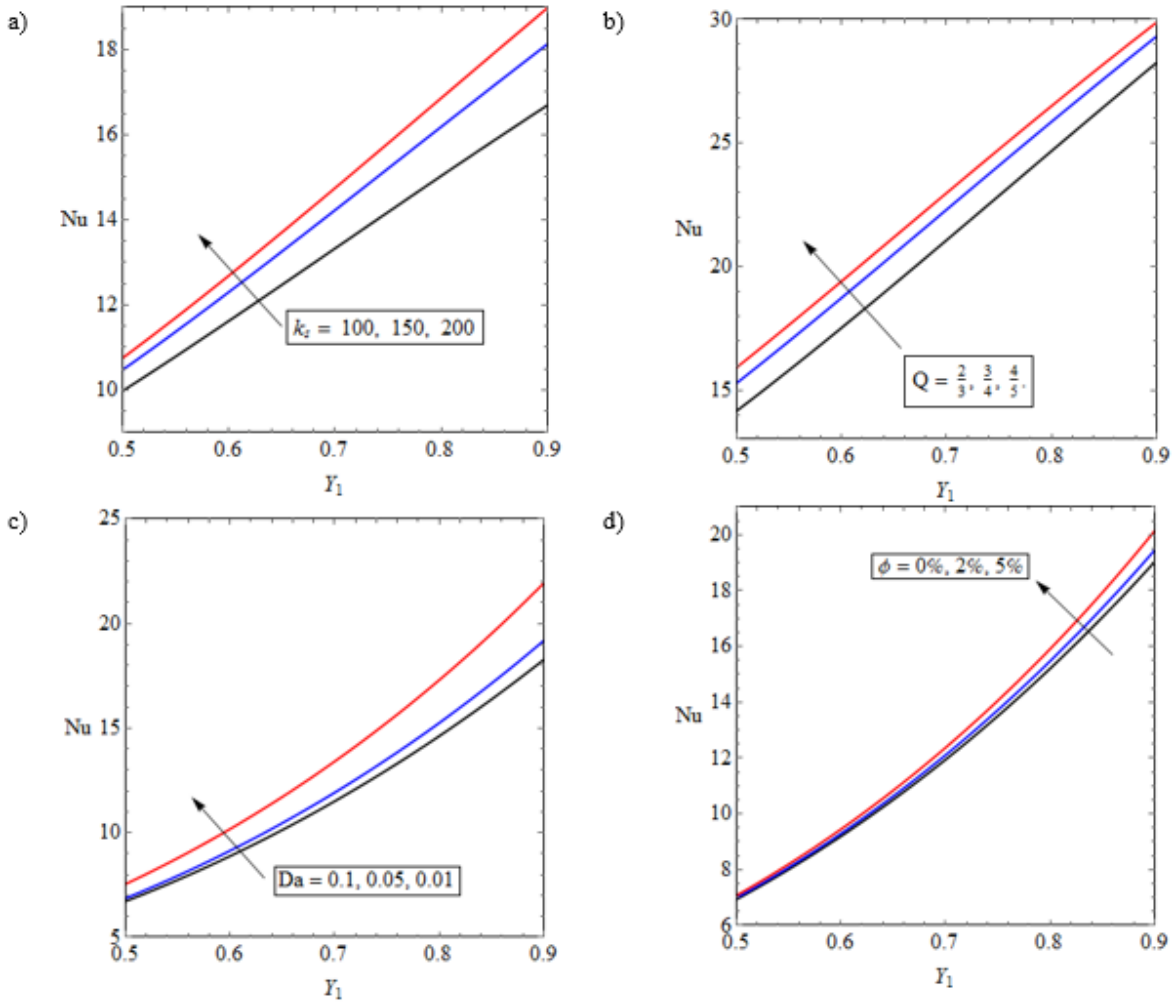

Figure 5-6 Nusselt number versus the lower wall thickness, $\boldsymbol{Y_1}$ a) on the upper wall and for different values of thermal conductivity of the porous medium, $\boldsymbol{k_s}$ (W/m.K) b) on the upper wall and different values of Q, c) on the lower wall and different values of Darcy number, d) on the lower wall and different volumetric concentration of nanoparticles.

5.2.4.3 Concentration fields

Figure 5-7 and Figure 5-8 show the concentration contours throughout the entire channel (part a) and also for a selected segment (parts b, c and d). These figures clearly demonstrate the axial increase of the concentration due to catalytic activities and the subsequent advection of species by the flow. Figure 5-7 illustrates the effects of increase in Damköhler number on the concentration field. Parts b, c and d of this figure indicate that the axial gradient of the concentration field is enhanced as the numerical value of Damköhler number increases. This is to be expected, as Damköhler number correlates with the reaction rate on the surface of catalyst and hence it is a measure of chemical activity of the system.

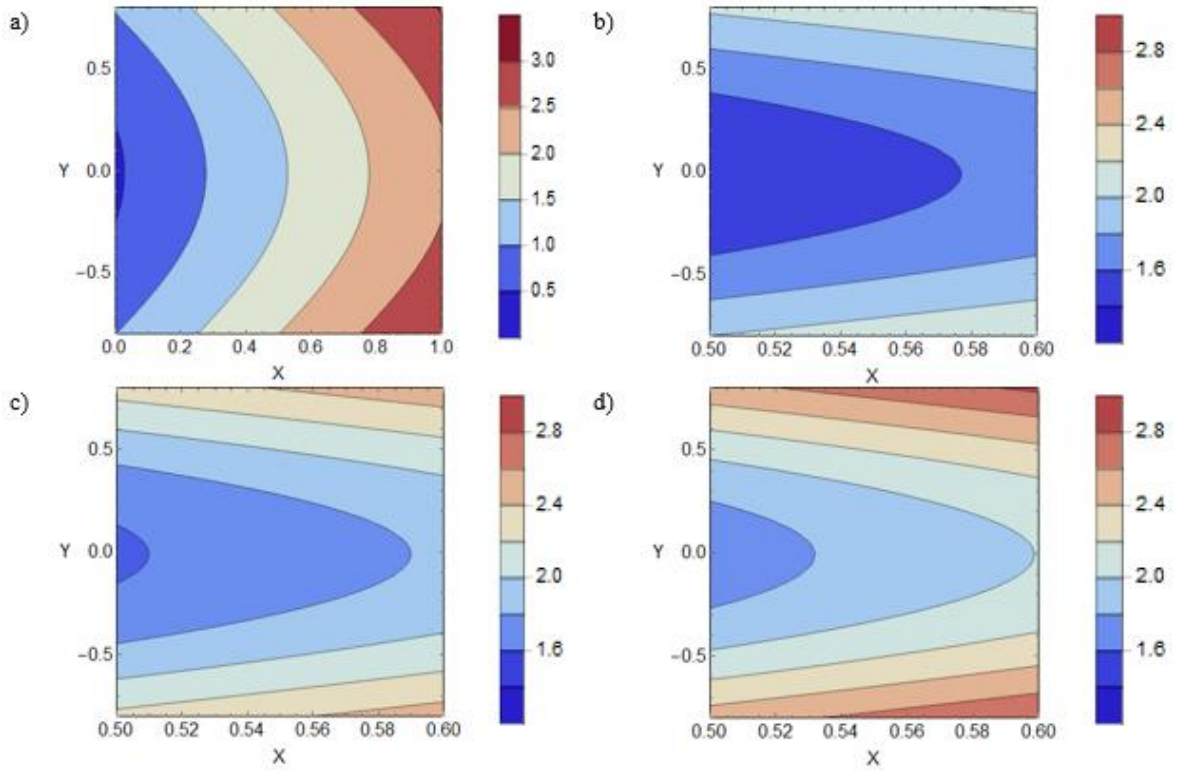

Figure 5-7 Concentration contours for varying Damköhler number, $\boldsymbol{\gamma}$, a) the full channel for $\boldsymbol{\gamma = 0.8}$, b) mid-section of the channel, for $\boldsymbol{\gamma = 0.8}$, c) mid-section for $\boldsymbol{\gamma = 1.0}$, and d) mid-section for $\boldsymbol{\gamma = 1.2}$.

Figure 5-7 also shows that by increasing Damköhler number the transversal gradient of concentration increases. This can be verified by comparing the variations of concentration from the lower or upper wall to the central axis of the channel in Figure 5-7b, Figure 5-7c and Figure 5-7d. Similar behaviours are observed in Figure 5-8, which depicts the response of the concentration field to the changes in Soret number. A notable feature of Figure 5-7 and Figure 5-8 is the symmetricity of the concentration contours. The transport of mass is coupled to that of heat through Soret effect (see equation (5-116)) and Figure 5-2 to Figure 5-5 showed the highly asymmetric character of the temperature contours. It may be expected, then, that the distribution of concentration contours should be also asymmetric. However, it is important to note that only the second derivative of temperature appears in equation (5-116). This tends to smear out the asymmetry of the temperature and results in mostly symmetric concentration contours shown in Figure 5-7 and Figure 5-8.

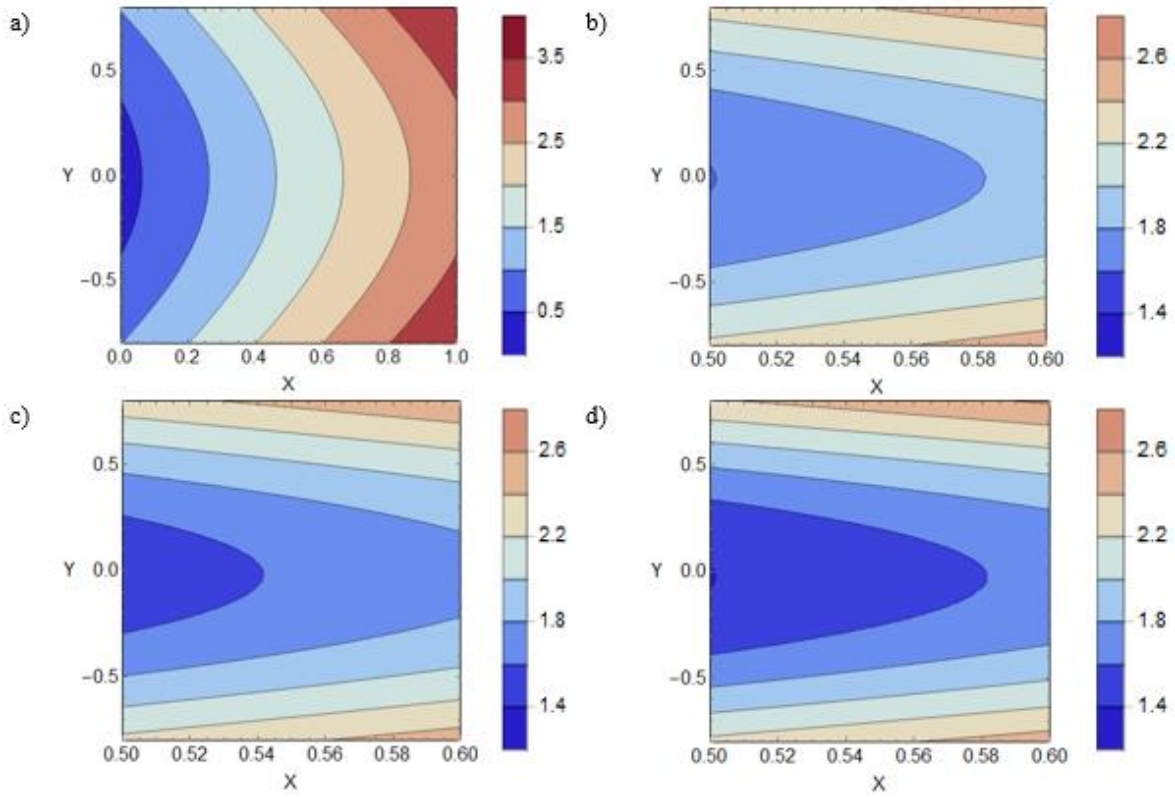

Figure 5-8 Concentration contours for varying Soret number, $\boldsymbol{Sr}$, a) the full channel for $\boldsymbol{Sr = 0.5}$, b) mid-section of channel, for $\boldsymbol{Sr = 0.5}$, c) mid-section for $\boldsymbol{Sr = 0.7}$, and d) mid-section for $\boldsymbol{Sr = 0.9}$.

5.2.4.4 Local entropy generation

A detailed study of local entropy generation is presented in Figure 5-9 to Figure 5-12. Each figure includes 6 sub-figures demonstrating different terms in equation (5-186). This division is on the basis of the work of Ting et al. [115] and extends that to mass transferring flows by including N_{DI} term. It should be stated that in these figures, only the microchannel has been considered and the irreversibilities of the two solid walls have been excluded. Figure 5-9 shows the contours of local entropy generation for the default conditions set in Table 5-2. In this figure, the asymmetric behaviour of entropy generation by intra-phase heat transfer in solid and nanofluid phase is in keeping with those observed in temperature contours presented in Figure 5-2 to Figure 5-5. Interestingly, however, the irreversibility associated with the interphase heat transfer between the porous solid and nanofluid is more symmetric, which indicates that the interphase heat transfer is largely unaffected by the asymmetry of the problem.

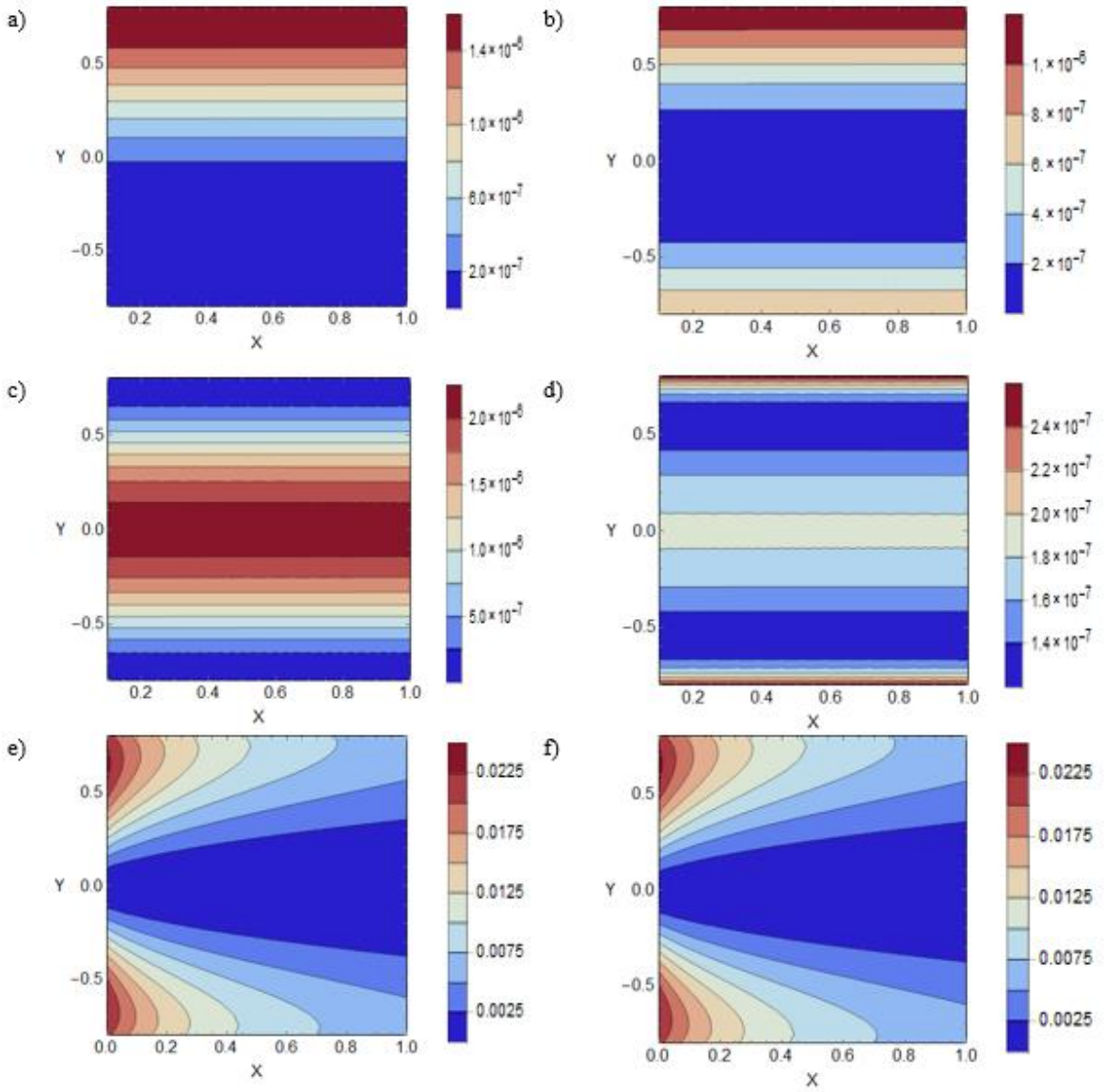

Figure 5-9 Entropy contours for the base configuration (Table 5-2) a)$\boldsymbol{N_{s,ht}}$, b) $\boldsymbol{N_{nf,ht}}$, c) $\boldsymbol{N_{int}}$, d)$\boldsymbol{N_{FF}}$, e) $\boldsymbol{N_{DI}}$ and f) $\boldsymbol{N_{pm}}$.

Figure 5-9d shows the local entropy generation by the hydrodynamic irreversibilities. The highly irreversible regions in the vicinity of the walls and around the centreline of the channel are quite noticeable in this figure. The former is because of the enhanced viscous effects in the near wall region, while the latter is due to the higher velocity of the fluid around the centreline of the microchannel. It is noted that a very similar behaviour of hydrodynamic irreversibility was reported by Ting et al. [115] with the same order of magnitude as that shown in Figure 5-9d. It should be emphasised here that the inclusion of viscous dissipation terms in heat transport equation has a major influence on the magnitude of this source of irreversibility. Exclusion of this effect often renders the entropy generation by fluid flow rather negligible in comparison with the irreversibility of heat transfer [130]. However, Figure 5-9 shows that hydrodynamic and heat transfer irreversibilities in nanofluid phase are of the same order of magnitude and therefore of comparable significance. This conclusion

was also made by Ting et al. [115]. Figure 5-9e shows the contours of local entropy generation by mass transfer. There are two distinctive features in this figure. First, the general configurations of the contours are different to those of other sub-figures and are correlated with the diffusive-advective nature of mass transfer from the catalytic surfaces. Second, the magnitude of mass transfer irreversibility appears to be much larger than other sources of irreversibility. As a result, the overall local irreversibility is entirely dominated by entropy generation through mass transfer.

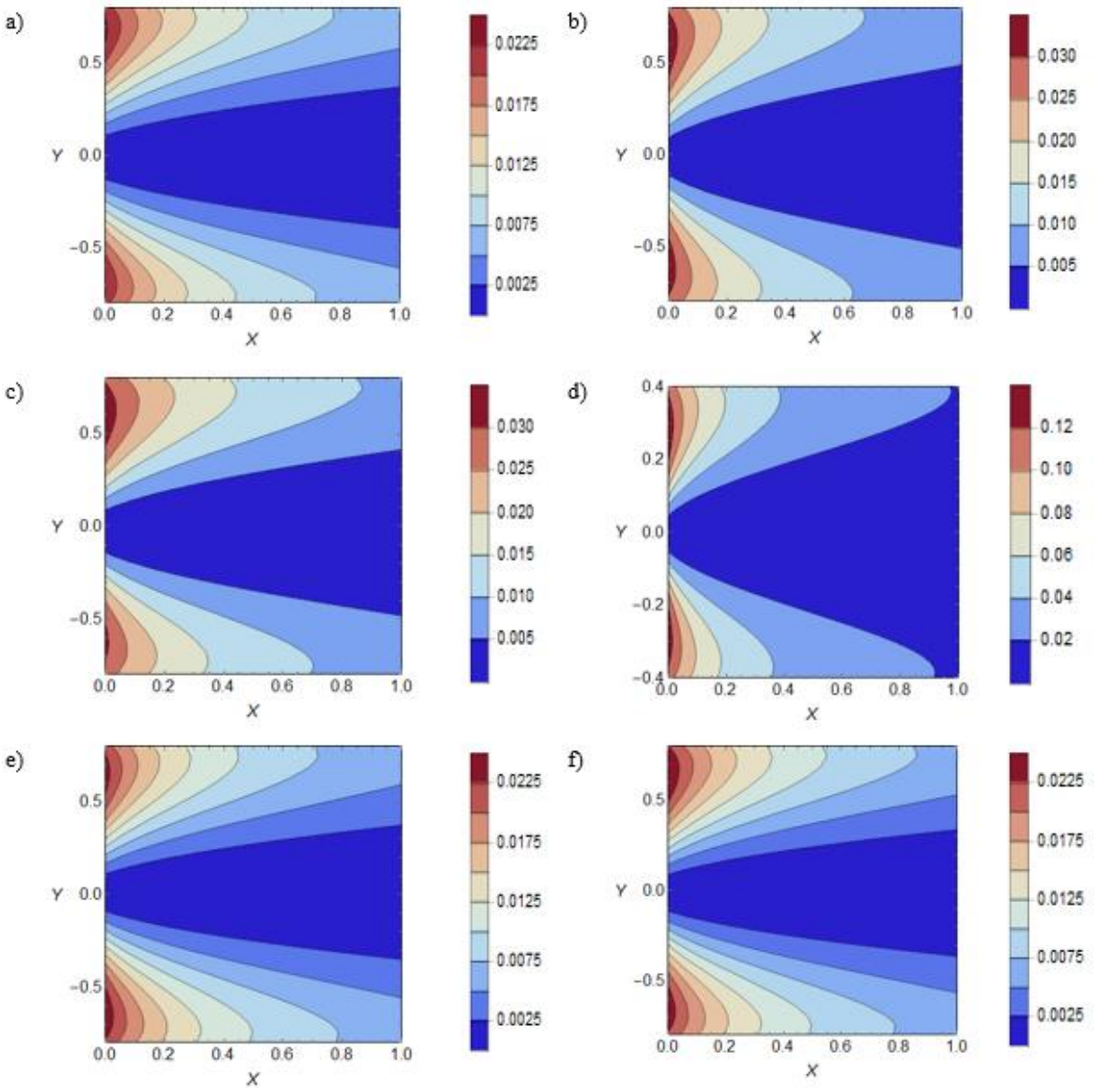

Figure 5-10 Contours of local entropy generation by mass transfer, $\boldsymbol{N_{DI}}$, a) D$\boldsymbol{a = 0.05}$, b) $\boldsymbol{\gamma = 1.2}$, c) $\boldsymbol{k = 0.2}$, d) $\boldsymbol{Y_1 = 0.4}$, e) $\boldsymbol{Q = 0.2}$, f) $\boldsymbol{Sr = 0.9}$.

Although not shown in here, an extensive parametric study revealed that the dominance of mass transfer irreversibility prevails for a large part of the parametric space. For this reason, Figure 5-10 only includes the contours of local entropy generation by mass transfer. Figure 5-10a depicts the effects of decreasing the permeability of the medium

compared to the default value of Darcy number in Table 5-2. A comparison between this figure and Figure 5-9e indicates that the resultant flow modification has affected the distribution of local entropy generation. This is to be anticipated as mass transfer is highly influenced by advection and therefore changes in the flow affect the irreversibility of mass transfer. Specifically of interest is an increase in the range of the fluid friction component (not shown here), the decrease in permeability caused the minimum volumetric entropy contribution to be equivalent to that of the entropy in the centre-line of the base case (Figure 5-9d). For the lower permeability, the centreline entropy was greater than the maximum entropy achieved due to fluid friction in the base case. By way of comparison, the maximum fluid friction contribution of the $Da = 0.05$ case exceeded that of the base case by some 50%. The decrease in permeability would require a greater force to extrude the fluid through the pores and as such cause a significant increase in fluid friction and via this mechanism and increase in temperature. This could account for the increase in entropy contribution observed for the fluid friction component. In terms of the N_{DI} contribution displayed in Figure 5-10a, however, the contribution is so small as to make very little difference as compared to that of the concentration field.

The effect of increasing Damköhler number has been considered in Figure 5-10b. In agreement with the arguments made about Figure 5-7 and Figure 5-8, magnifying Damköhler number intensifies the mass transfer rate and hence increases the associated irreversibility. Increasing the thermal conductivity ratio in Figure 5-10c leads to an interesting effect. Here the transversal gradient of the local entropy generation has increased in comparison to that in Figure 5-9e. However, the axial gradient of the local entropy generation shows a considerable decline with respect to the base case. This is particularly the case for areas between the walls and the centreline of the microchannel. An important behaviour is observed in Figure 5-10d, wherein the thickness of the wall has been doubled in comparison with the default value in Table 5-2. It is noted that the local entropy generation in this sub-figure is one order of magnitude larger than any other sub-figure in Figure 5-10. Once again, this reflects the significance of the wall thickness or microstructure configuration in the thermal and entropic responses of the microreactors. Figure 5-10e and Figure 5-10f show the influences of imbalance in the imposed heat flux (Q) and Soret number, respectively. It appears that both Q and Soret number have minimal effects on the local entropy generation.

The preceding discussion may imply that in the current problem the mass transfer irreversibilities are always the most significant source of entropy generation. However, this

will be an incorrect generalisation and there exist situations in which entropy generation by mass transfer is very much comparable with other sources of irreversibility. Figure 5-11 and Figure 5-12 illustrate two examples of such situations. In Figure 5-11, the microchannel has been exposed to a high thermal load represented by a significant increase in ω compared to the default values. This has led to a major boost in the heat transfer irreversibility, shown in Figure 5-11a, Figure 5-11b and Figure 5-11c, which has subsequently intensified the entropy generation by fluid flow, shown in Figure 5-11d. Yet, entropy generation by mass transfer remains within the same order of magnitude as the default case (Figure 5-9).

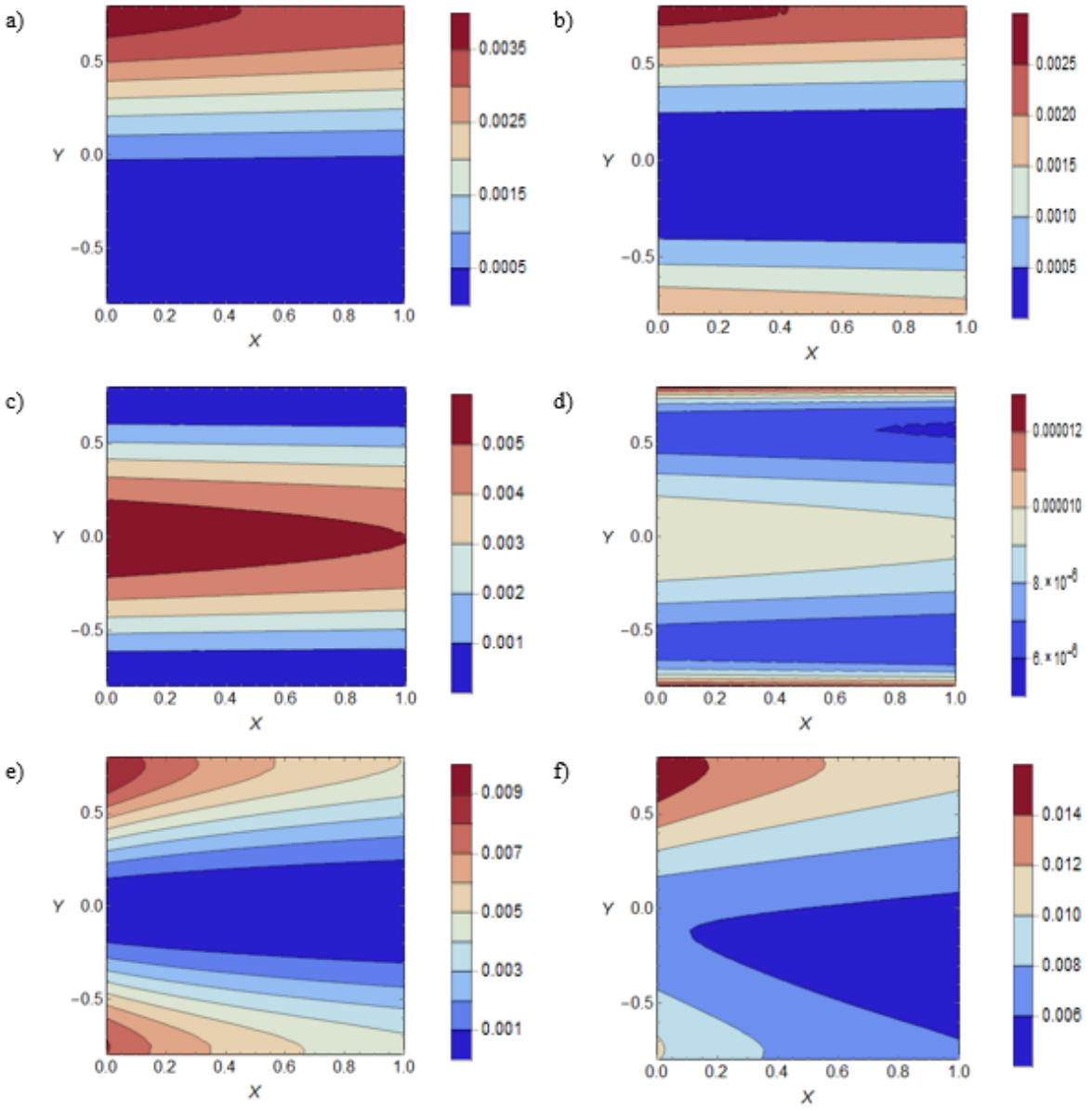

Figure 5-11 Entropy contours for heat flux, $\boldsymbol{\omega = 0.05}$, a) $\boldsymbol{N_{s,ht}}$, b) $\boldsymbol{N_{nf,ht}}$, c) $\boldsymbol{N_{int}}$, d) $\boldsymbol{N_{FF}}$, e) $\boldsymbol{N_{DI}}$ and f) $\boldsymbol{N_{pm}}$.

Consequently, the overall local entropy generation, shown in Figure 5-11f, is no longer dominated by the irreversibility of mass transfer. In fact, in this case the additive

effect of entropy generations by heat transfer is the most significant source of entropy generation. Figure 5-12 illustrate a particular case with zero Soret number. Part e of this figure shows that by excluding the thermal diffusion of mass the numerical value of entropy generation by mass transfer declines by about three orders of magnitude. As a result, in Figure 5-12 entropy generation by heat and mass transfer are of the same order of magnitude. This clearly shows the essential role of coupled heat and mass transfer in entropy generation and identifies the Soret effect as a major contributor to the total irreversibility encountered in the microreactor.

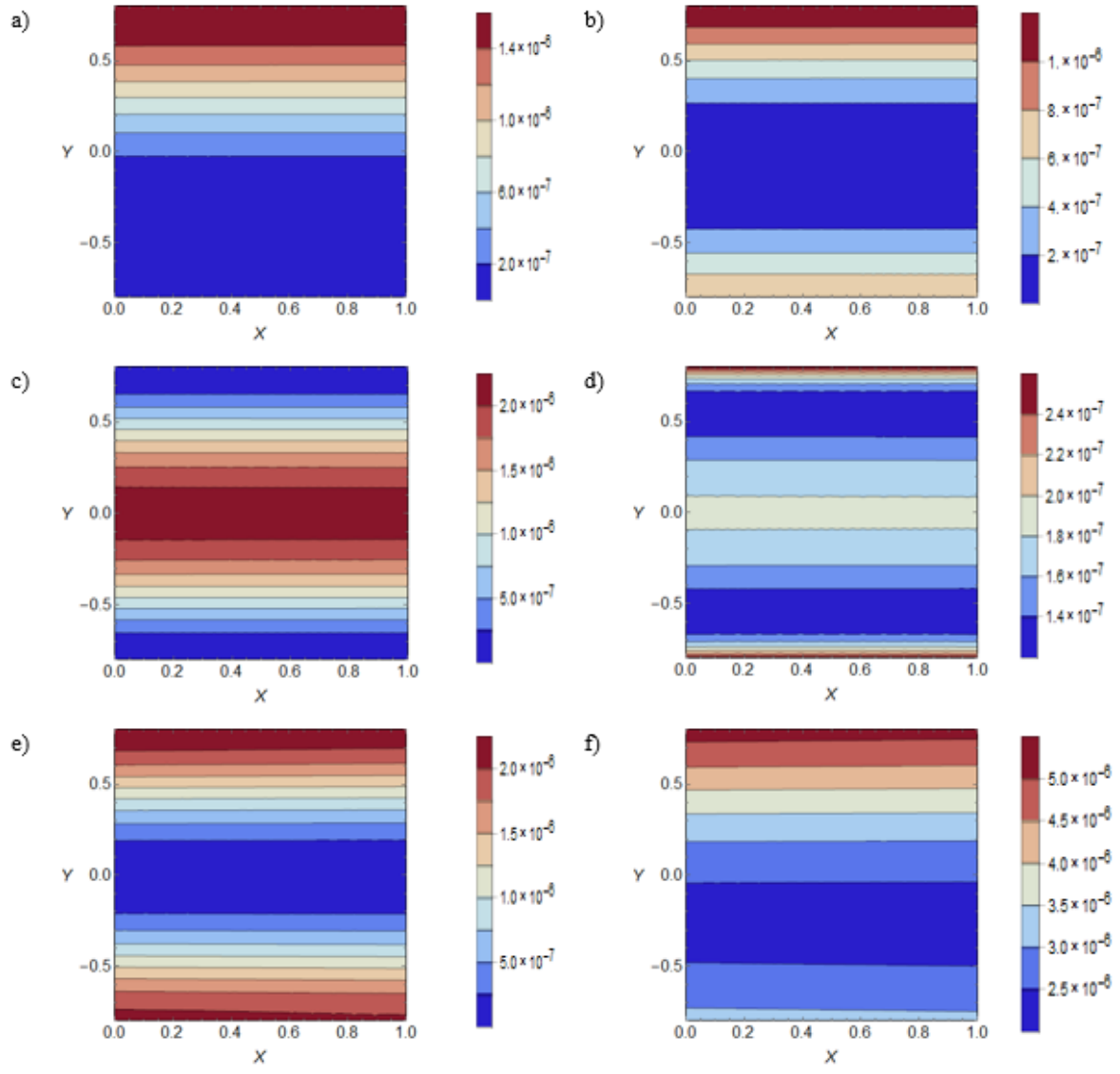

Figure 5-12 Entropy contours for Damköhler number, $\boldsymbol{\gamma = 0.1}$ with $\boldsymbol{Sr = 0}$ for; a) $\boldsymbol{N_{s,ht}}$, b) $\boldsymbol{N_{nf,ht}}$, c) $\boldsymbol{N_{int}}$, d) $\boldsymbol{N_{FF}}$, e) $\boldsymbol{N_{DI}}$ and f) $\boldsymbol{N_{pm}}$.

5.2.4.5 Total entropy generation

The total entropy generation within the system is the sum of the five different sources of irreversibility within the microchannel plus entropy generation in the solid walls, see equation (5-187). The total entropy generation is a measure of irreversibility of the whole system and is therefore of obvious practical significance. Figure 5-13 and Figure 5-14 depict the variations of the total entropy generation within the system against a number of parameters. Figure 5-13 illustrates the effects of Soret number on the total generation of entropy. In Figure 5-13a, the total entropy generation has been plotted against the dimensionless heat flux and for different values of Soret number. This figure shows a positive correlation between the total entropy generation and the non-dimensional heat flux. It also indicates that for all values of non-dimensional heat flux, magnification of Soret number intensifies the total generation of entropy. A similar trend is observed in Figure 5-13b in which total entropy increases with increasing the thermal conductivity ratio and Soret number.

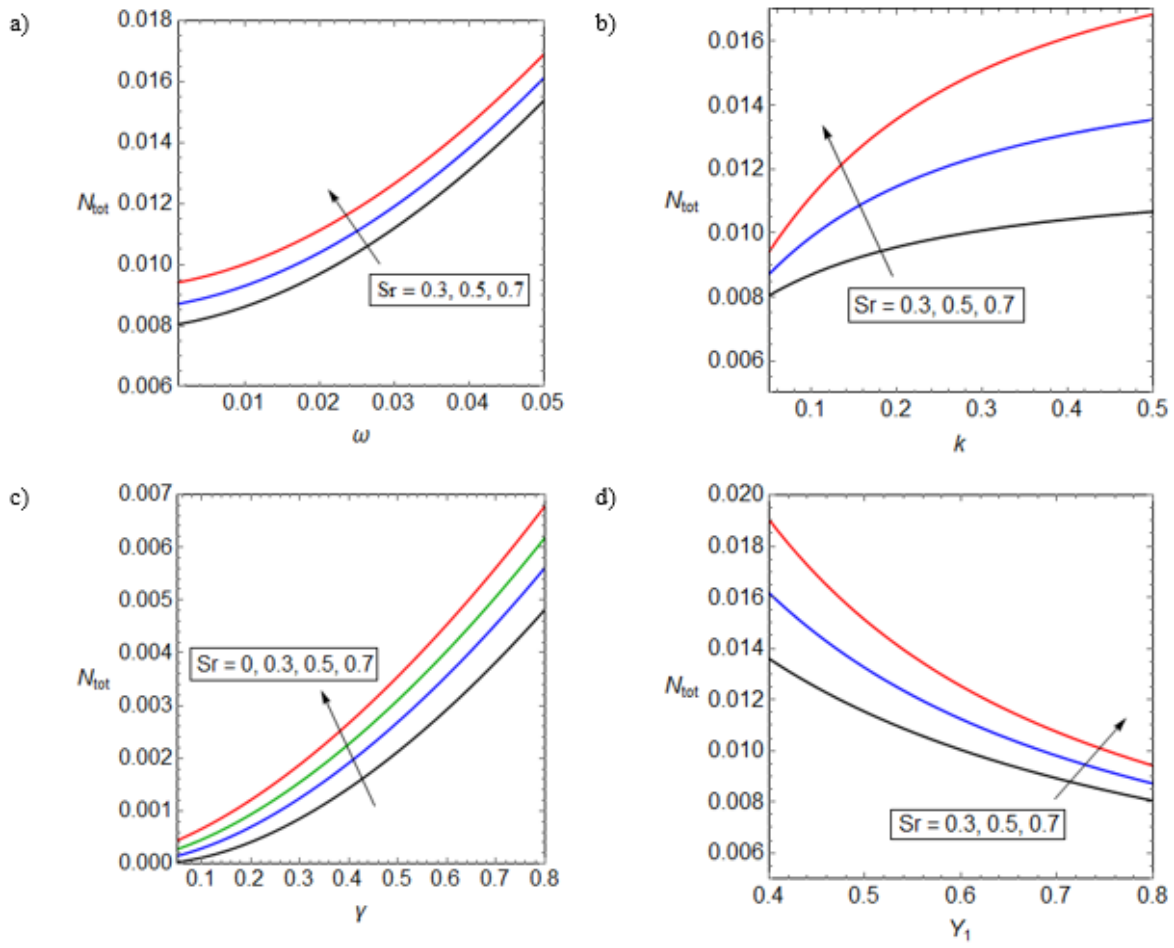

Figure 5-13 Total Entropy generation for different values of Soret number, $\boldsymbol{Sr}$ against varying a) dimensionless heat flux, $\boldsymbol{\omega}$ b) thermal conductivity ratio, $\boldsymbol{k}$ c) Damköhler number, $\boldsymbol{\gamma}$ and d) dimensionless thickness of the lower wall, $\boldsymbol{Y_1}$.

Figure 5-13c reveals the interactions between the irreversibilities of the two mechanisms of mass transfer. This figure shows the total entropy generation in a range of Damköhler number and for a few discrete values of Soret number. For Soret number of zero, and thus no thermal diffusion of mass, the total entropy generation increases monotonically with Damköhler number. Introducing a finite Soret number results in increasing the total generation of entropy. Nonetheless, the monotonic trend in increasing the total entropy through increasing Damköhler number remain unchanged. Figure 5-13d indicates that the total entropy generation within the system is significantly affected by the variations in the thickness of the microchannel walls. It should be clarified here that based upon the definitions provided in equation (5-130), increasing Y_1 implies a decrease in the thickness of the microchannel. Thus, Figure 5-13d indicates that through increasing the thickness of the wall the total irreversibility of the system is intensified quite significantly. Once again, Soret number acts in favour of magnifying the total entropy generation.

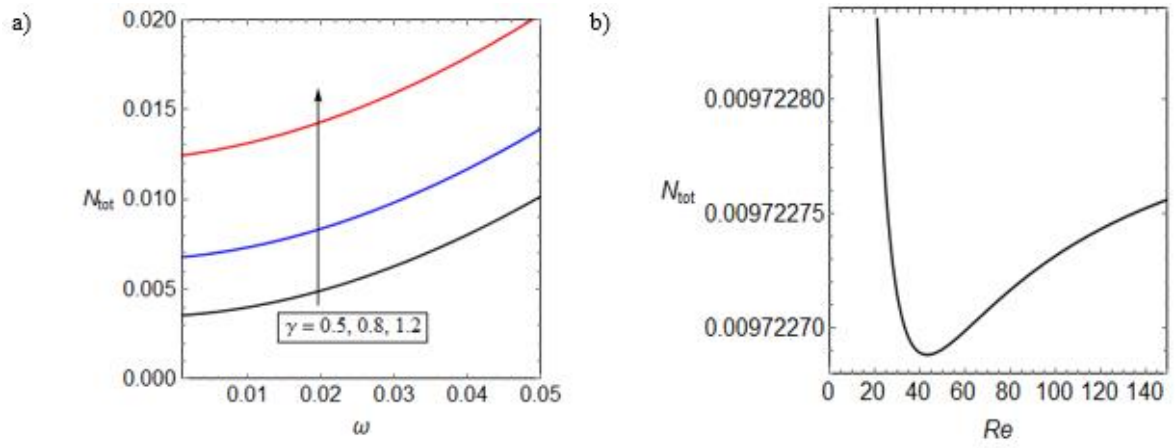

Figure 5-14 Total Entropy vs a) dimensionless heat flux, $\boldsymbol{\omega}$ and b) Reynolds number, $\boldsymbol{Re}$.

Figure 5-14 shows the variations of total entropy generation with non-dimensional heat flux groups of ω and Re. Figure 5-14a demonstrates the strong correlation between the total entropy generation and the dimensionless heat flux. This figure also indicates that for any fixed value of ω, the total entropy increases significantly by magnifying the value of Damköhler number. Figure 5-14b shows that the changes of total entropy generation with the Reynolds number (defined in equation (5-130)) can include an extremum point. This figure clearly shows the dual effects of Reynolds number upon the total irreversibility of the system. For very small values of Reynolds number, the entropy generation is large. This is because of the fact that under small flow rates the forced convection mechanism is highly suppressed and therefore the system in Figure 5-1 builds up in temperature and becomes highly irreversible. Increasing the flow rate permits the convection of heat to occur and so brings down temperature and hence the total irreversibility falls sharply and leads to the

formation of a local minimum point. Any increase of Reynolds number beyond this point slightly increases the total irreversibility as the hydrodynamic irreversibilities start to become noticeable. With the heat now being advected away, large temperature gradients between the walls and the channel centre-line can develop which affect the concentration gradients via the Soret effect and thus there is a corresponding increase in total entropy. The minimum observed in Figure 5-14b represents the point at which these two mechanisms balance each other out.

The sensitivity of the results to certain parameters are listed qualitatively in Table 5-3. Overall, the parameter to which the results were most sensitive was the thermal conductivity ratio, k. This parameter had a large effect on every study conducted. Similarly, the thermal conductivity ratio for the walls and also the porous solid thermal conductivity were found to have strong effects on the temperature field. The Damköhler number and Soret numbers had a lesser, but significant effect on the concentration field and thereby on the local and total entropy generation. Entropy generation was found to be susceptible to the dimensionless heat flux value, especially when this value was raised such that the concentration field was no longer the dominant factor in entropy generation. All other parameters had only minor effect on these fields.

Table 5-3 Dimensionless Parameter sensitivity.

Dimensionless parameter	Dimensionless parameter name	Sensitivity
ϕ	Nanoparticle concentration	Small
Bi	Biot Number	Moderate
Br'	Modified Brinkman number	Small
γ	Damköhler number	Highly sensitive
Da	Darcy number	Moderate
Pe	Peclet number	Moderate
Pr	Prandtl number	Moderate
Re	Reynolds number	Moderate (except at very low values)
Sr	Soret number	Highly sensitive
ε	Porosity	Moderate
k	Thermal conductivity ratio	Very highly sensitive
k_{e1}	Dimensionless Wall1 thermal conductivity	Moderate
k_{e2}	Dimensionless Wall1 thermal conductivity	Moderate
Q	Heat flux ratio	Sensitive
ω	Dimensionless heat flux	Highly sensitive
φ	Irreversibility distribution ratio	Sensitive
Y_1	Channel thickness	Sensitive
ξ	Aspect ratio of channel	Small

5.3 Case 2-Homogeneous reactor

For the homogeneous microreactor, a zeroth order reaction was chosen. Zeroth order kinetic behaviour is prevalent in biological systems such as enzyme-catalysed reactions [206]. A catalytic surface may also cause reactions to exhibit zero order kinetics [206] due to limited availability of active sites. This is not, however, only a feature of large catalytic surfaces (such as channel wall catalysts) but is also the case when the catalyst is a small particle (as is the case in a slurry) [207]. With such systems in mind, the kinetics chosen for this study are zeroth order.

There is now significant evidence showing that the solid body of micro-structured reactors should be included in the thermal analyses of these systems. Further, accurate performance prediction of microreactors with highly exothermic reactions is subject to conduction of comprehensive thermal analyses which take into account thermal radiation. However, theoretical examinations of radiative effects in porous microreactors are scarce. To fill these gaps, the present work puts forward a two-dimensional investigation on the influences of thermal radiation upon heat and mass transfer, and entropic behaviour of porous microreactors with thick walls.

5.3.1 Configuration and assumptions

Figure 5-15 shows the porous microreactor under investigation with thick walls and symmetric heat flux thermal boundary condition. It is assumed that the process in the microreactor can include high temperature reactions. Thus, the internal radiation plays an important role in the overall heat transfer process. For the purposes of the following analysis, Rosseland approximation has been used to model the thermal radiation. As LTNE model is adopted in this investigation, internal convective heat exchanges between the fluid and solid phases of the porous medium have been also considered in the mathematical model. The thicknesses of the solid walls of the reactor are incorporated in the model and the mass diffusion has been coupled with temperature field of the fluid through assuming a finite Soret number [85]. The other assumptions include steady, laminar, fully developed and incompressible fluid flow. Homogeneity of the properties of the materials, existence of no sharp reaction zones, absence of gravitational effects [205] [117], and reversibility of the homogenous chemical reaction are also assumed. In the current investigation, the heat of reaction may appear as a constant source term in the energy equation of the fluid phase.

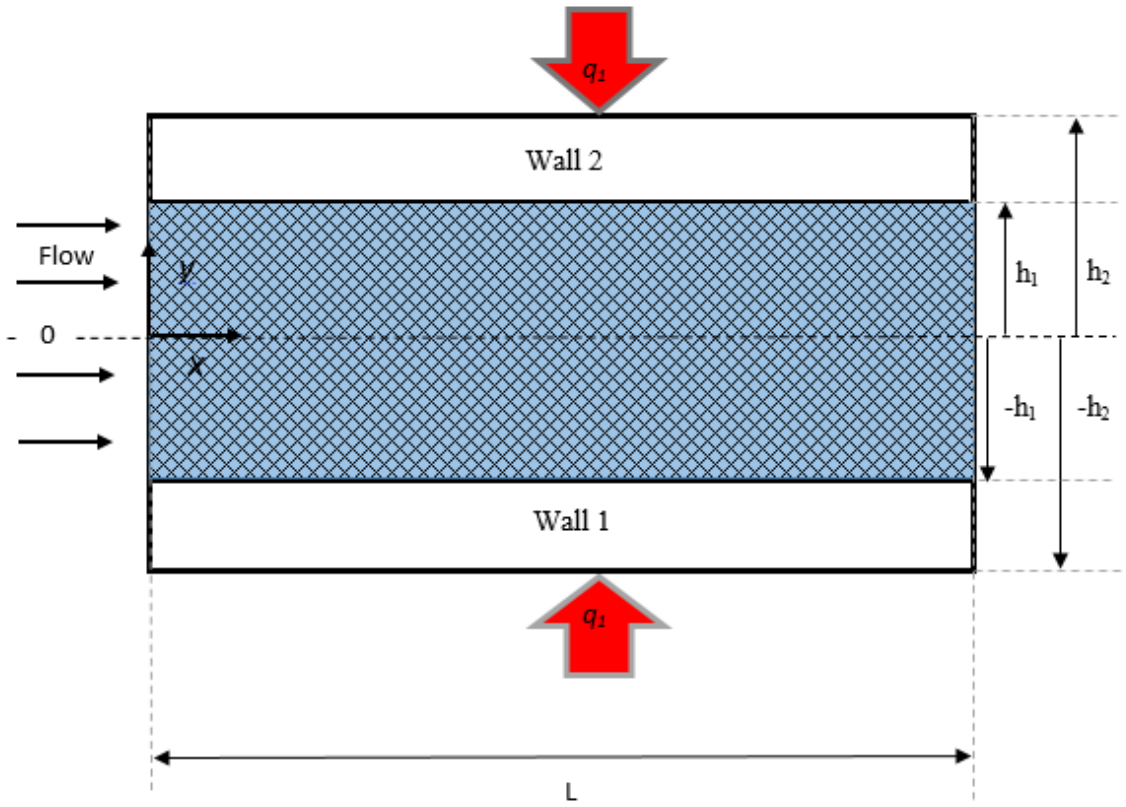

Figure 5-15 Schematic view of the investigated microreactor

Nonetheless, this has been extensively studied in a number of previous investigations [205][117] [93][100][97] and hence it is not further considered in the current work. Thus for the purposes of this study heat of reaction has not been included. Further, in the followings the fluid phase is assumed to be a nanofluid. This is not an essential element of the analysis and can be readily removed by setting the volume fraction of nanoparticles to zero. Though nanofluids are known to exhibit shear-thinning behaviour, the nanofluid presented herein is assumed to behave as a Newtonian fluid. This is justified by the use of a 2% nanoparticle concentration, which is considerably below the limit of 13% up to which nanofluids may behave in a Newtonian manner[202]. Nonetheless, it has been added to the analysis to make it applicable to the microreactors that involve nanoparticles [61][208].

5.3.2 Analytical solution

The naming convention described in Section 5.2.2 is adopted in the following analysis with the one minor change. Due to the symmetric nature of the system, only the top half of the system is modelled. The lower half simply being the mirror image. Many of the governing equations and boundary conditions from Section 5.2 are unchanged and so are not repeated in this section.

5.3.2.1 Boundary conditions

The Darcy-Brinkman model of transport of momentum describes the hydrodynamics of the flow in microreactor, equation (3-9), remains unchanged. The velocity boundary conditions shown in equations (5-117) and (5-118) remain relevant to this study.

The differential energy equations for the solid walls of the microreactor and the fluid phases of the porous section of the system are expressed by equations (5-115) and (5-113) respectively. The porous solid phase is governed by the energy equation:

$$k_{es}\frac{\partial^2 T_s}{\partial y^2} - h_{sf}a_{sf}\left(T_s - T_{nf}\right) - \frac{\partial q_r}{\partial y} = 0 \qquad 0 \le y < h_1 \qquad (5\text{-}188)$$

As described in chapter 3, the Rosseland approximation is used for the radiative term. The radiative heat flux from the solid phase of the porous medium is caused by the solid phase having the ability to lose (or absorb) heat through radiation. In the current model, the fluid is assumed to be transparent to radiation, which is readily justifiable by considering the fact that most fluids are optically highly transparent [178]. Of course, that is not to say that the fluid phase is unaffected by the radiative heat loss form the solid phase, merely that the effect is indirect. The radiation parameter in equation (5-188) takes the form:

$$q_r = \frac{-4\,\sigma^*}{3\,\kappa^*}\frac{\partial T_s^4}{\partial y} \qquad (5\text{-}189)$$

Where under the Rosseland approximation, the radiation term in equation (5-188) becomes

$$\frac{\partial q_r}{\partial y} = -\frac{16\sigma^* T_0^3}{3\,\kappa^*}\frac{\partial^2 T_s}{\partial y^2}. \qquad (5\text{-}190)$$

The following advection-diffusion-reaction model for a zeroth order, homogenous, temperature indifferent chemical reaction governs the production and transport of chemical species in the reactor. The model takes into account the contributions from the Soret effect in addition to the Fickian diffusion of species [146]. It is recalled that in the current problem the terms in energy transport equation are generally much larger than those in mass transport equation. As a result, the relatively small contribution of Dufour effect with the energy balance has been ignored. However, the influence of Soret effect upon mass transport equation remains noticeable and therefore it has been taken into account. This argument has

been already made in a number of previous investigations, see for example [209][200][210][198].

$$u\frac{\partial C}{\partial x} = D\frac{\partial^2 C}{\partial y^2} - D_T\frac{\partial^2 T_{nf}}{\partial y^2} + k_r \qquad 0 \le y < h_1 \qquad (5\text{-}191)$$

The equal temperature boundary conditions of equation (5-121) and remain in force in this study, recalling that the system is symmetric. The heat flux boundary conditions to be adopted are as follows:

$$y = h_2: \qquad k_1\frac{\partial T_1}{\partial y}\Big|_{y=h_2} = q_1'' \qquad (5\text{-}192)$$

$$y = h_1: \qquad q_1'' = k_{enf}\frac{\partial T_{nf}}{\partial y}\Big|_{y=h_1} + (k_{es} + \frac{16\sigma^*}{3\,\kappa^*})\frac{\partial T_s}{\partial y}\Big|_{y=h_1} \qquad (5\text{-}193)$$

$$y = 0: \qquad \frac{\partial T_{nf}}{\partial y}\Big|_{y=0} = \frac{\partial T_s}{\partial y}\Big|_{y=0} = 0 \qquad (5\text{-}194)$$

For a zeroth order chemical reaction, the imposed conditions for the concentration of chemical species are the following.

$$y = h_1: \qquad C = C_0 \qquad (5\text{-}195)$$

$$y = 0: \qquad D\frac{\partial C}{\partial y} = D_T\frac{\partial T_{nf}}{\partial y} \qquad (5\text{-}196)$$

5.3.2.2 Nusselt number

To calculate the Nusselt number on the microchannel wall, the heat transfer coefficient should firstly be evaluated. The heat transfer coefficient at the top wall of the microchannel is defined as:

$$H_w = \frac{q_1''}{T_w - \bar{T}_{nf}} \qquad (5\text{-}197)$$

Where the bulk mean temperature is again defined by equation (5-127). Thus, Nusselt number using length scale of the channel height $2h_1$ is expressed by

$$Nu_w = \frac{2H_w h_1}{k_{enf}} \tag{5-198}$$

5.3.2.3 Entropy equations

Entropy generation is still covered in this investigation by the volumetric entropy generation equations (3-31) to (3-35) as shown in Chapter 3 [85,115,205]. Note that the fluid subscript, f are now replaced with nanofluid subscript, nf for consistency of this Chapter.

5.3.2.4 Dimensionless equations

In addition to the dimensionless parameters presented in equations (5-130), several further parameters are required or altered. These are as follows:

$$Br' = \frac{\mu_{eff}\bar{u}^2}{q_1'' h_2}, \qquad Sr = \frac{q_1'' h_1 D_T}{C_0 k_{nf} D},$$
$$\theta_i = \frac{(T_i - T_{w,in})k_{es}}{q_1'' h_2}, \qquad \gamma = \frac{k_R h_1^2}{D C_0}, \tag{5-199}$$
$$\omega = \frac{q_1'' h_2}{2k_{es} T_{w,in}}, \qquad Rd = \frac{16\,\sigma^*}{3\,\kappa^* k_{es}}.$$

5.3.2.5 Velocity profiles

Both the governing equation and the boundary conditions for the momentum equation remains the same as that provided in Section 5.2.2.1. The velocity profile is defined by equation (5-133), the mean velocity by equation (5-134) and the velocity ratio by equation (5-135).

5.3.2.6 Temperature profiles

Due to the assumption of fully developed the following conditions hold [115],

$$\frac{\partial T_{nf}}{\partial x} = \frac{d\bar{T}_{nf}}{dx} = \frac{\partial T_s}{\partial x} = \frac{d\bar{T}_s}{dx} = \frac{dT_w}{dx} = \frac{dT_1}{dx} = \Omega_R = constant. \tag{5-200}$$

This allows for the following form of the solution to be sought for the temperature field,

$$T_i(x,y) = f_i(y) + \Omega_R x \qquad i = 1, s, nf \tag{5-201}$$

where $f_i(y)$ is a function to be determined by solving equations (5-112), (5-113), and (5-188) in association with the given boundary conditions. In order to solve the transports of thermal energy in the porous medium, first it is necessary to add equations (5-113) and (5-188) and then integrate the resultant equation over the cross-section of the microchannel. Substituting in the heat flux boundary condition from equations (5-193) and (5-194) yields,

$$q_1'' + \frac{\mu_{nf}}{\kappa}\int_0^{h_1} u^2\,dy + \mu_{eff}\int_0^{h_1}\left(\frac{du}{dy}\right)^2 dy = \rho_{nf}C_{p,nf}\int_0^{h_1} u\frac{\partial T_{nf}}{\partial x}\,dy \tag{5-202}$$

Rearranging equation (5-135) allows for the substitution for u into equation (5-202). Applying the non-dimensional parameters, as defined in equations (5-130) and (5-199), facilitates the integration process and reveals:

$$\frac{d\bar{T}_{nf}}{dx} = \frac{1}{\rho_{nf}C_{p,nf}\bar{u}h_1h_2}\left[h_2q_1'' + \frac{\mu_{eff}S^3\bar{u}^2Y_1^2cosh(SY_1)}{SY_1\,cosh\,(SY_1) - sinh(SY_1)}\right] = \Omega_R \tag{5-203}$$

Utilising the non-dimensional parameters of equations (5-130) and (5-199), the rearranged form of equation (5-135) together with equation (5-203) lead to the non-dimensional forms of equations (5-112), (5-113) and (5-188). The constant coefficients are defined explicitly in Section 5.2.4.

$$k_{e1}\theta_1'' = 0 \qquad Y_1 < Y \le 1 \tag{5-204}$$

$$k\theta_{nf}'' + Bi\left(\theta_s - \theta_{nf}\right) + D_2\,cosh(2SY) + D_3\,cosh(SY) + D_4 = 0 \qquad 0 \le Y < Y_1 \tag{5-205}$$

$$(1+Rd)\theta_s'' - Bi\left(\theta_s - \theta_{nf}\right) = 0 \qquad 0 \le Y < Y_1 \tag{5-206}$$

Through an algebraic manipulation of equations (5-205) and (5-206), the following relations are developed.

$$k(1+Rd)\theta_{nf}'''' - Bi(1+k+Rd)\theta_{nf}'' + (4S^2(1+Rd) - Bi)D_2\,cosh\,(2SY) + (S^2(1+Rd) - Bi)D_3\,cosh\,(SY) - BiD_4 = 0, \tag{5-207}$$

$$k(1+Rd)\theta_s'''' - Bi(1+k+Rd)\theta_s'' - Bi(D_2\,cosh\,(2SY) + D_3\,cosh\,(SY) + D_4) = 0. \tag{5-208}$$

These provide decoupled solid and fluid energy equations in the porous medium. Particular solutions of equations (5-204), (5-207) and (5-208) require 10 boundary conditions as given in Table 5-4.

Table 5-4 Dimensionless temperature boundary condition

$\theta_{nf}(Y_1) = \theta_s(Y_1) = 0$	$\theta_1(Y_1) = 0$
$\theta_s''(Y_1) = 0$	$\theta_{nf}''(Y_1) = -\frac{1}{k}(D_2 \cosh(2SY) + D_3 \cosh(SY) + D_4)$
$\theta_{nf}'(0) = 0$	$k_{e1}\theta_1'(1) = 1$
$\theta_s'(0) = 0$	$\theta_{nf}'''(0) = \theta_s'''(0) = 0$

Applying the boundary conditions given in Table 5-1 allows the analytical solutions of the system of equations (5-204), (5-207) and (5-208) to be found. The resulting closed-form dimensionless temperature profiles in the transverse direction are:

$$\theta_1(Y) = E_1 + E_2 Y \qquad Y_1 < Y \leq 1 \qquad (5\text{-}209)$$

$$\theta_{nf}(Y) = E_3\, cosh(2SY) + E_4\, cosh(SY) + E_5\, cosh(\alpha Y) + E_6 Y^2 + E_7 Y + E_8 \qquad 0 \leq Y < Y_1 \qquad (5\text{-}210)$$

$$\theta_s(Y) = E_9\, cosh(2SY) + E_{10}\, cosh(SY) + E_{11}\, cosh(\alpha Y) + E_6 Y^2 + E_7 Y + E_{12} \qquad 0 \leq Y < Y_1 \qquad (5\text{-}211)$$

in which $\alpha = \sqrt{\frac{Bi(1+k+Rd)}{k(1+Rd)}}$.

The explicit form of the constant parameters are given in Appendix A, section 1.2, the choice of using the letter, E for the coefficients was to permit ease of comparison for validation purposes (Appendix B section 1.2). Through substitution of the dimensionless axial and transverse temperature profiles into equation (5-201), and incorporating equation (5-203) the two-dimensional temperature fields can be obtained. These are given by the following expressions.

$$\theta_1(X,Y) = \frac{2\,X\,[1 + Br' D_1\,S^2\,cosh(SY_1)]}{Re\,Pr\,k\,Y_1\xi} + E_1 + E_2 Y \qquad Y_1 < Y \leq 1 \qquad (5\text{-}212)$$

$$\theta_{nf}(X,Y) = \frac{2\,X\,[1 + Br' D_1\,S^2\,cosh(SY_1)]}{Re\,Pr\,k\,Y_1\xi} + E_3\,cosh(2SY) + E_4\,cosh(SY) + E_5\,cosh(\alpha Y) + E_6 Y^2 + E_7 Y + E_8 \qquad 0 \leq Y < Y_1 \qquad (5\text{-}213)$$

$$\theta_s(X,Y) = \frac{2\,X\,[1 + Br' D_1\,S^2\,cosh(SY_1)]}{Re\,Pr\,k\,Y_1\xi} + E_9\,cosh(2SY) + E_{10}\,cosh(SY) + E_{11}\,cosh(\alpha Y) + E_6 Y^2 + E_7 Y + E_{12} \qquad 0 \leq Y < Y_1 \qquad (5\text{-}214)$$

The Nusselt number for the walls must also be rendered dimensionless, which results in;

$$Nu_w = \frac{-\,2\,Y_1}{k\bar{\theta}_{nf}}. \qquad (5\text{-}215)$$

5.3.2.7 Concentration profiles

Seeking a solution to the governing equation of mass transfer of the form:

$$C(x,y) = g(y) + h(x) \qquad (5\text{-}216)$$

To evaluate the concentration profile first a control volume over a section of the microchannel should be considered. By doing so and applying a mass balance to this and using the steps outlined in Section 5.2.2.7 the following equation is obtained,

$$\bar{u}\frac{\partial C}{\partial x} = k_r. \qquad (5\text{-}217)$$

Assigning C_0 as the initial concentration, the solution of this equation takes the form of

$$C(x) = \frac{k_r\,x}{\bar{u}}. \qquad (5\text{-}218)$$

Using the dimensionless parameters defined in equations (5-130) and (5-199), equation (5-219) can be non-dimensionalised in the following form.

$$\Phi(X) = \frac{\gamma\, X}{Pe\; Y_1 \xi}. \tag{5-219}$$

Substituting equation (5-217) into equation (5-191) gives:

$$u\; \frac{k_r}{\bar{u}} = D\frac{\partial^2 C}{\partial y^2} - D_T \frac{\partial^2 T_{nf}}{\partial y^2} + k_r. \tag{5-220}$$

By employing the dimensionless parameters from equations (5-130) and (5-199), permits equation (5-220) is first non-dimensionalised and then rearranged in the form of,

$$\Phi''(Y) - (\frac{u}{\bar{u}} - 1)\frac{\gamma}{Y_1^2} = \frac{Sr\; k}{Y_1 \varepsilon}\theta''_{nf}(Y). \tag{5-221}$$

Since $\theta''_{nf}(Y)$ is determined from equation (5-213) only the boundary conditions given by equations (5-195) and (5-196) need non-dimensionalisation. These are expressed by,

$$\Phi'(0) = 0 \qquad\qquad \Phi(Y_1) = 1. \tag{5-222}$$

Through applying these boundary conditions, equation (5-221) can be solved analytically to obtain the dimensionless concentration profile in the transverse direction. This reads

$$\Phi(Y) = F_1\, cosh(2SY) + F_2\, cosh(SY) + F_3\, cosh(\alpha Y) + F_4 Y^2 + F_5. \tag{5-223}$$

Finally, substituting equations (5-219) and (5-223) into equation (5-216) gives the dimensionless, two-dimensional concentration field:

$$\Phi(X,Y) = \frac{\gamma\, X}{Pe\; Y_1 \xi} + F_1\, cosh(2SY) + F_2\, cosh(SY) + F_3\, cosh(\alpha Y) + F_4 Y^2 + F_5. \tag{5-224}$$

Appendix A section 1.2 provides analytical expressions for the constants appearing in the above equations.

5.3.2.8 Entropy profiles

The entropy equations (5-177) to (5-186) defined in section 5.2.2.8 are still the relevant non-dimensional forms of the local entropy generation equations and their use is continued in this study.

To calculate the total entropy generation, the sum of the parts of volumetric entropy generation is integrated over the volume of the microchannel with the inclusion of contributions from the walls. This yields a numerical value for the total entropy and is obtained by the following equation:

$$N_{Tot} = 2\int_0^1 \int_0^1 \sum N_i \, dXdY, \qquad i = 1, s, nf, FF, DI. \tag{5-225}$$

5.3.3 Validation

To validate the mathematical model developed in Sections 5.3, it is demonstrated that when the wall thickness and thermal radiation tend to zero, the analytical form of the temperature fields reduce to those presented by Ting et al. [115] with no internal heat generation term. For details, see Appendix B, Section 1.2.

5.3.4 Discussion

The problem solved in Section 5.3.2 features a large number of dimensionless parameters. To conduct quantitative analyses default values are assigned to them in Table 5-5.

Table 5-5 List of base parameters values used in the production of all graphs except where otherwise stated.

Dimensionless Parameter	Dimensionless parameter name	Default Value
Bi	Biot number	1
Br'	Modified Brinkman number	0.01
γ	Damköhler number	1
Da	Darcy number	0.1
Pe	Peclet number	10
Pr	Prandtl number	5
Re	Reynolds number	150
Sr	Soret number	0.7
ϵ	Porosity	0.95
k	Thermal conductivity ratio	0.05
k_{e1}	Dimensionless Wall1 thermal conductivity	0.5
ω	Dimensionless heat flux	0.001
φ	Irreversibility distribution ratio	0.01
Y_1	Channel thickness	0.8
ξ	Aspect ratio of channel	0.05
Rd	Radiation parameter	2

5.3.4.1 Temperature distributions

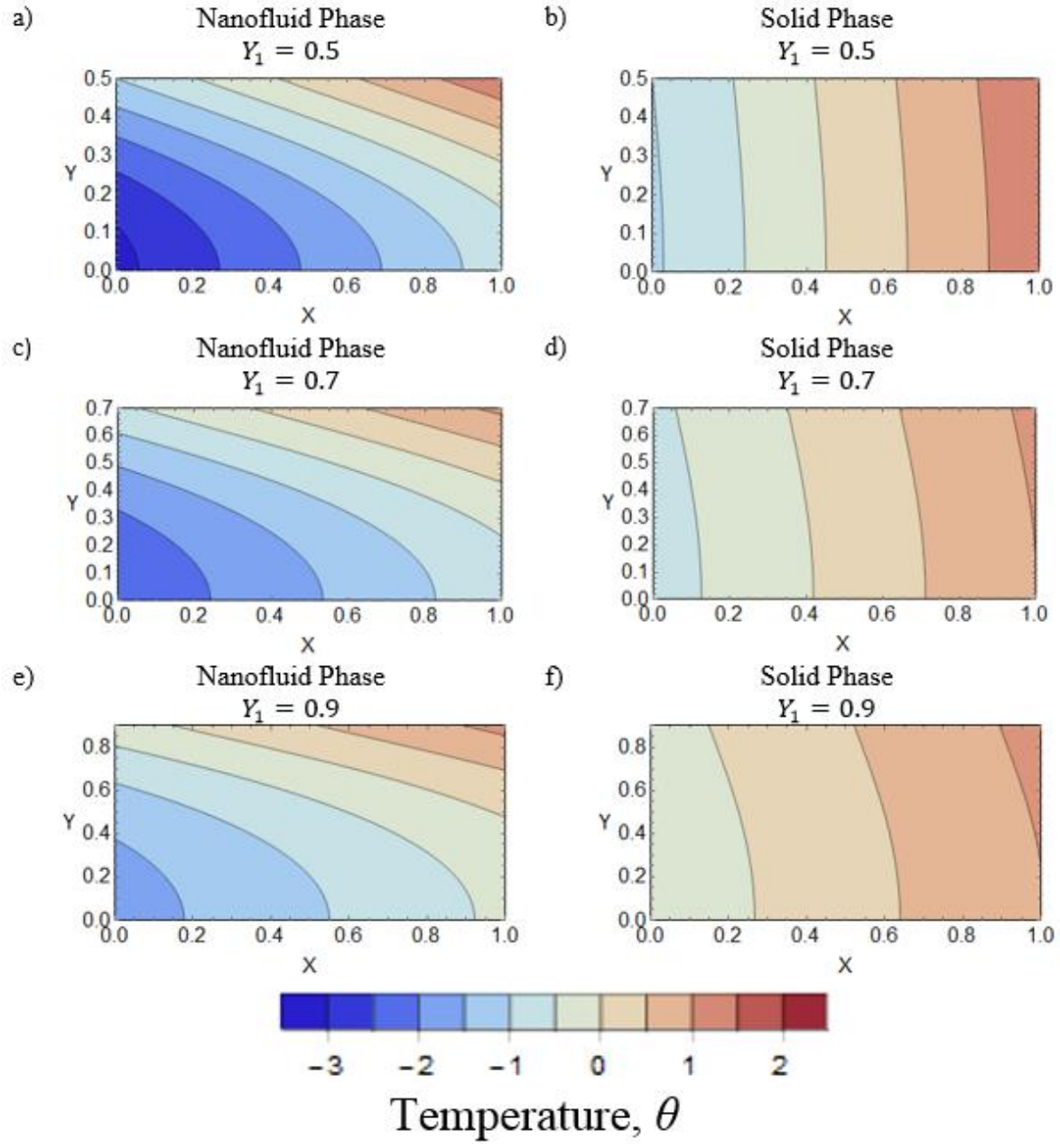

Figure 5-16 Dimensionless temperature contours for varying wall thickness, $\boldsymbol{Y_1}$ for nanofluid and porous solid phases.

Figure 5-16 shows the effects of widening the porous microchannel on the dimensionless temperature contours of the nanofluid (left column) and porous solid (right column) phases. It should be noted that in this figure, and also in other figures of this section, the walls have been excluded and only the interior part of the microchannel is depicted. As Figure 5-15 indicates, increasing the non-dimensional parameter $Y_1 = \frac{h_1}{h_2}$ leads to decreasing the wall thickness and hence widening the microchannel. It is also recalled that here the dimensionless temperature has been defined on the basis of the inlet wall temperature (see equation (5-199)). Therefore, the numerical value of the temperature can vary from a

negative quantity to a positive value. The internal heat generation due to nanofluid friction and the heat flux boundary condition imposed on the walls are the reasons for increasing the temperature to a positive value. Figure 5-16 shows that variations in the width of the microchannel impart significant effects upon the temperature fields. For instance, a comparison between Figure 5-16a and Figure 5-16c shows that for a fixed point inside the microchannel increasing Y_1 results in decreasing the absolute value of the dimensionless temperature of nanofluid. The same trend is observed in the non-dimensional temperature of the porous solid shown in Figure 5-16b, Figure 5-16d and Figure 5-16f. This behaviour can be explained physically. The wall acts as a thermal resistance against the transfer of heat from the external surface of the reactor. It follows that in the current isoflux system, decreasing the wall thickness reduces the required temperature difference for the transfer of a fixed heat flux. By comparing the left and right columns in Figure 5-16, it is also seen that decreasing the wall thickness of the microchannel reduces the temperature difference between the solid and nanofluid phases. This is an important observation and implies that utilisation of LTNE model is an essential necessity in thick wall microchannels. It is further in keeping with the earlier one dimensional findings of Chapter 4 and extends those to the current two-dimensional configuration. Furthermore, it is clear in Figure 5-16 that the solid and nanofluid temperatures increase along the microchannel due to the internal heat generation resulting from nanofluid friction and absorption of external heat flux.

Figure 5-17 demonstrates the impact of thermal conductivity ratio, *k*, on the temperature of nanofluid and porous solid phases when the values of other thermophysical parameters are kept constant. This figure shows that as the thermal conductivity ratio increases, the magnitude of the dimensionless temperature contours in both porous solid and nanofluid phases decreases. This behaviour has been also reported in the previous investigations of forced convection of nanofluids in porous media [95,97]. It can be attributed to the fact that increasing the thermal conductivity of nanofluid enables the nanofluid phase of the system to absorb more heat from the solid component of the porous medium. Nevertheless, Figure 5-17 does not imply that increasing the thermal conductivity ratio can majorly affect the temperature difference between the solid and fluid phases temperature.

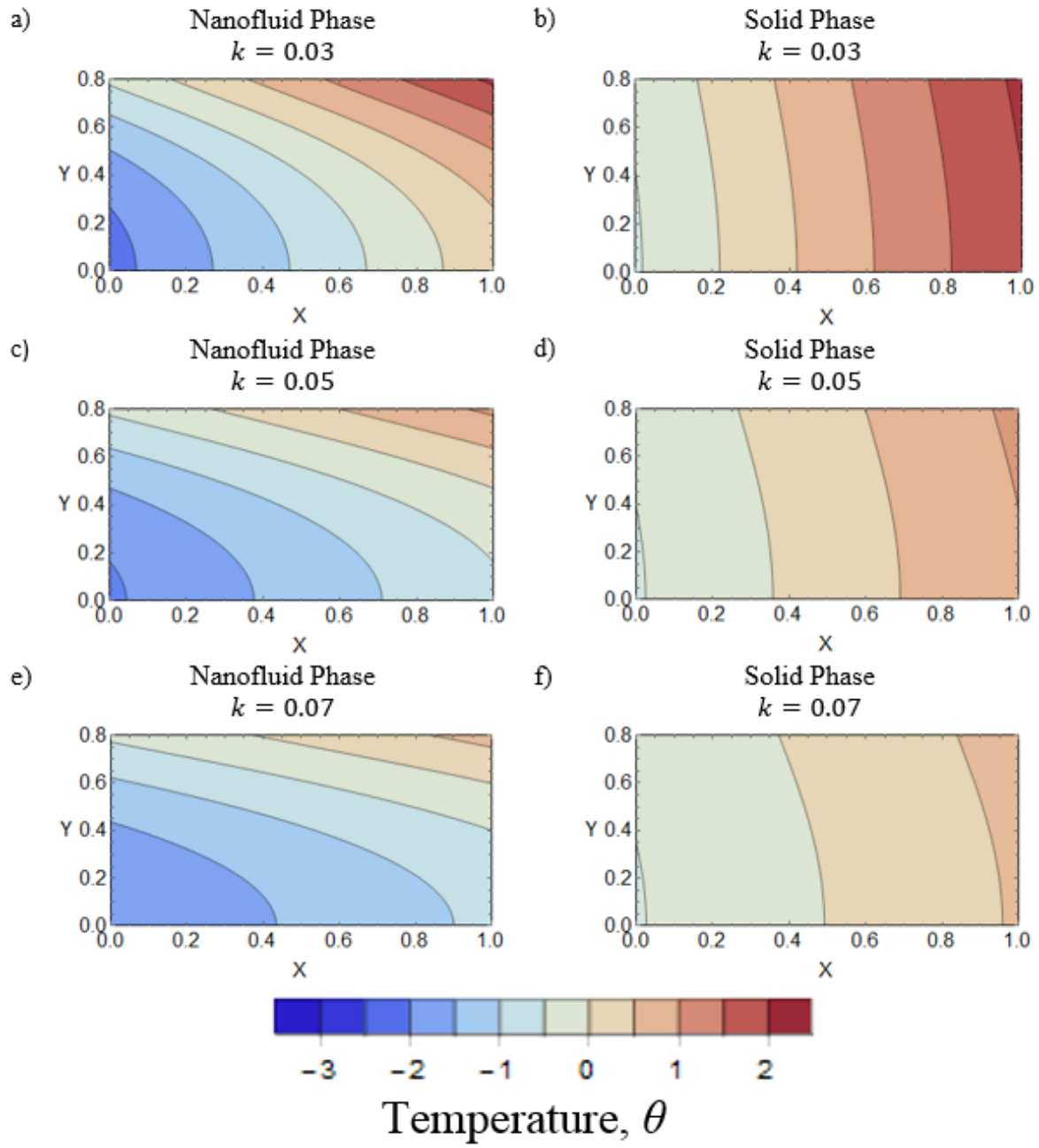

Figure 5-17 Dimensionless temperature contours for varying thermal conductivity, ***k***, for nanofluid and porous solid phases.

The effects of radiation parameter on the temperature contours in the solid and nanofluid phases have been shown in Figure 5-18. Figure 5-18a and Figure 5-18b correspond to the microchannel without radiation effect and Figure 5-18e and Figure 5-18f represent a case with $Rd = 2$. It is seen that augmenting the radiation parameter, increases the heat absorption by the solid phase of the porous medium from the walls. Hence, the temperature of the solid phase increases, while the temperature of the nanofluid phase decreases.

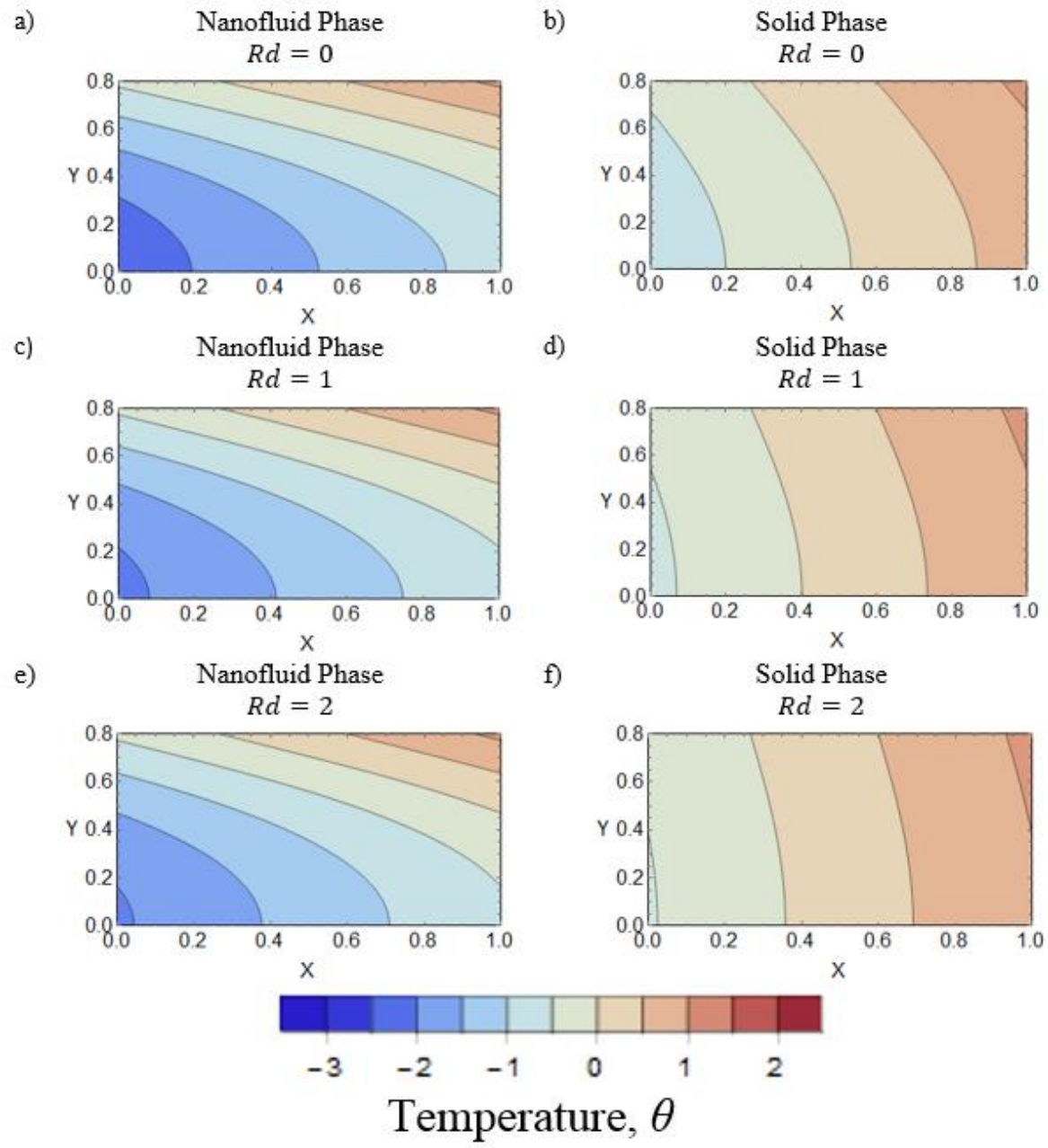

Figure 5-18 Dimensionless temperature contours for varying radiation parameter, $\boldsymbol{Rd}$, for nanofluid and porous solid phases.

5.3.4.2 Nusselt number

Figure 5-19 illustrates the effects of radiation parameter and wall thickness of the microchannel on the Nusselt number. As shown in Figure 5-18, increasing the radiation parameter reduces the temperature of the nanofluid, and hence increases the ability of the nanofluid to convect the heat from the surface of the wall. Therefore increasing the radiation parameter magnifies the Nusselt number as depicted in Figure 5-19a. However, Figure 5-19b indicates that when the dimensionless wall thickness of the microchannel is more than 0.5, increasing the radiation parameter has only a marginal effect on the value of Nusselt number. Both Figure 5-19a and Figure 5-19b show that decreasing the wall thickness increases the

Nusselt number. As already shown in Figure 5-16, this is due to the fact that through reducing the wall thickness the nanofluid dimensionless temperature within the microchannel decreases.

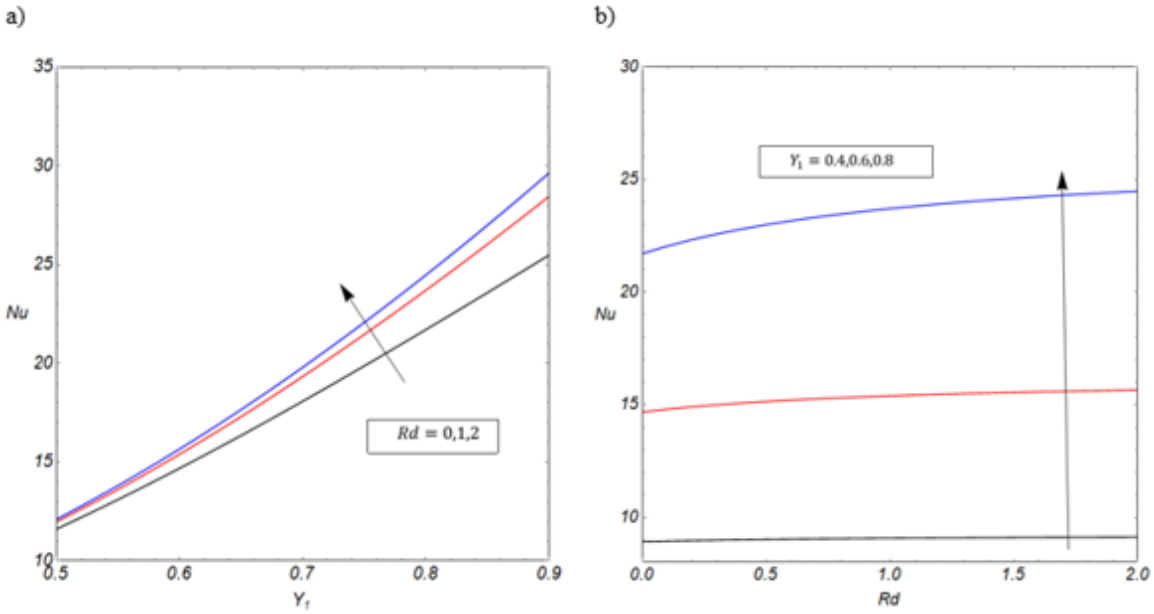

Figure 5-19 Variation of Nusselt number with a) the wall thickness and b) radiation parameter.

5.3.4.3 Concentration field

Figure 5-20 and Figure 5-21 illustrate the effects of Damköhler number and wall thickness on the concentration field within the porous section of the microchannel. Figure 5-20 shows the dimensionless concentration contours for the entire length of the microchannel (Figure 5-20a) and for the second half of the microchannel with different values of Damköhler numbers (Figure 5-20b, c, d). A comparison between Figure 5-20b and Figure 5-20d reveals that decreasing the value of Damköhler number smoothens the concentration field and makes it more uniform. This is to be expected and is because of the fact that Damköhler number is directly related to the chemical reaction rate. Hence, decreasing Damköhler number represents weakening of the homogenous reaction and production of the species.

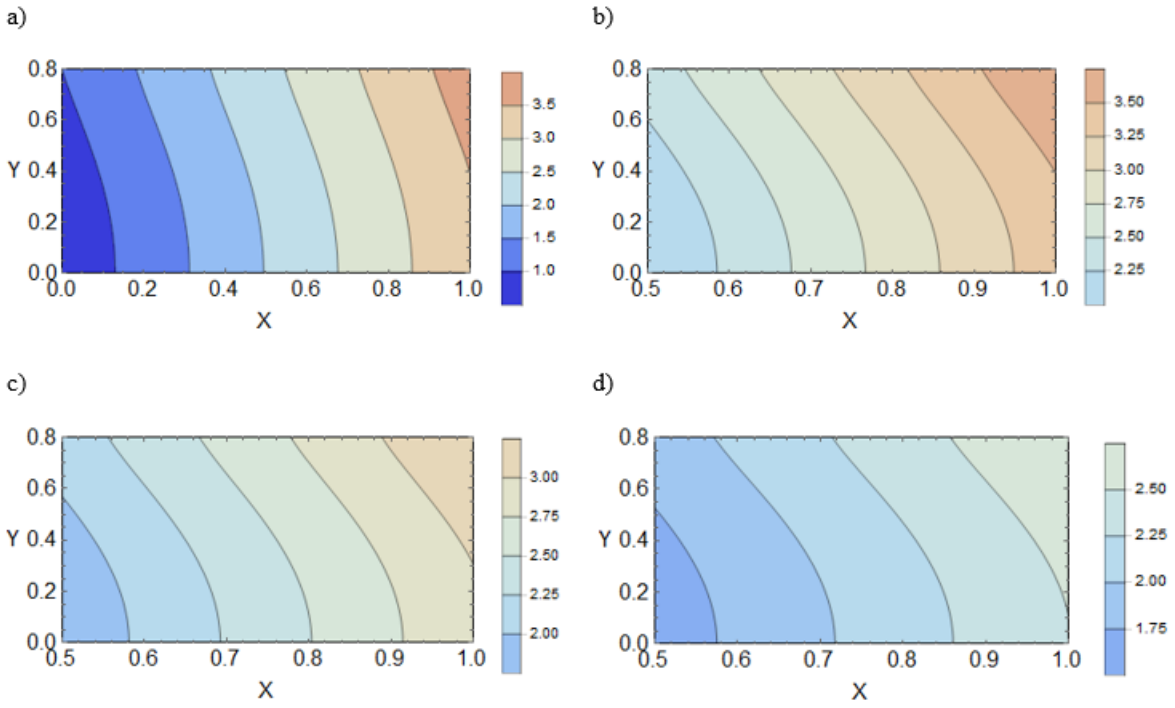

Figure 5-20 Dimensionless concentration contours for varying Damköhler number,$\boldsymbol{\gamma}$, a) showing the full microchannel for $= \mathbf{1.1}$, b) mid-section of microchannel for $\boldsymbol{\gamma} = \mathbf{1.1}$, c) mid-section for $\boldsymbol{\gamma} = \mathbf{0.9}$, and d) mid-section for $\boldsymbol{\gamma} = \mathbf{0.7}$.

Figure 5-21 shows the effects of wall thickness on the concentration distribution. Examination of Figure 5-21b to Figure 5-21d confirms that decreasing the wall thickness of the microreactor reduces the numerical values of the dimensionless concentration contours. As already discussed, reducing the wall thickness of the microchannel decreases the temperature of the nanofluid phase and subsequently affects the concentration field through thermal diffusion effect. Although not shown here the impact of radiation parameter on the concentration field is quite marginal. Radiation affects the temperature field to some extent but only the second derivative of temperature appears in the mass transfer equation (equation (5-221)). This supresses out the effects of thermal radiation and renders the concentration field rather indifferent to variation in radiation parameter.

Figure 5-20 and Figure 5-21 further show that due to the axial advection and production, the species are washed away from the entrance of the channel. Thus, in moving from the entrance of the microreactor towards the exit plane, the dimensionless concentration is constantly increasing. Further, the concentration of species appears to be higher in the vicinity of the walls of microreactor compared to that on the centreline. As the nanofluid temperature near the wall is always higher than the temperature around the centre of the microchannel, the thermo-diffusion effects generate the observed transversal gradient in the species field.

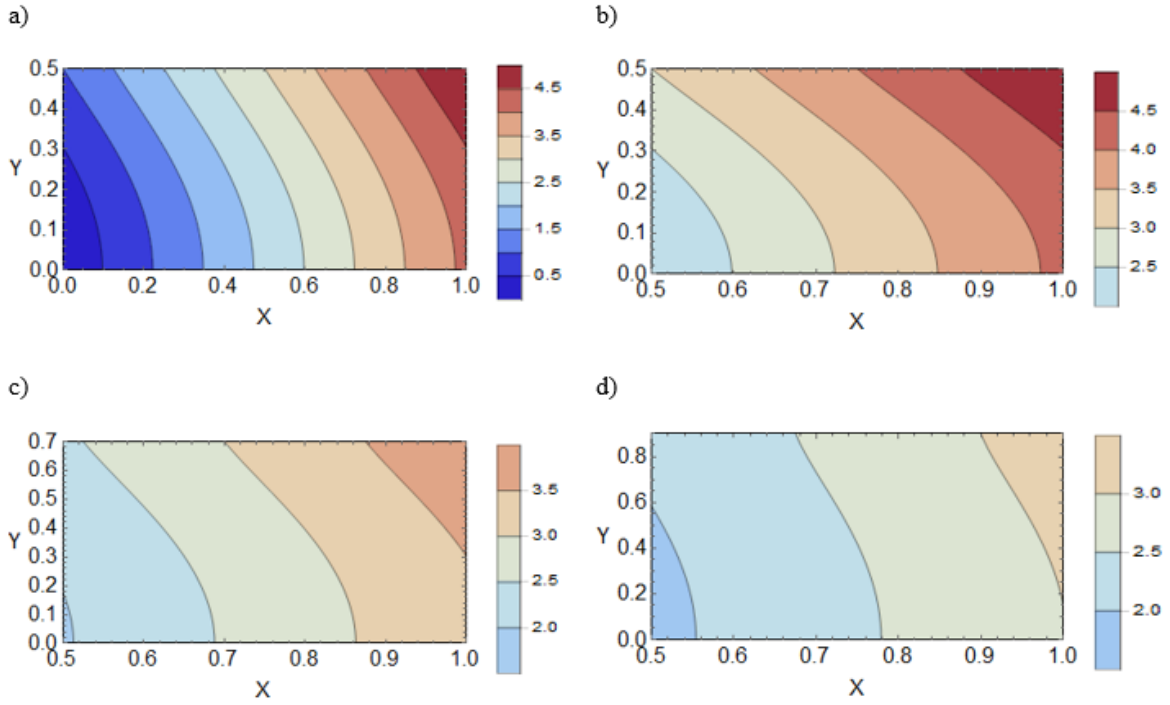

Figure 5-21 Dimensionless concentration contours for varying wall thickness, $\boldsymbol{Y_1}$, a) showing the full microchannel for $\boldsymbol{Y_1 = 0.5}$, b) mi-section of microchannel, for $\boldsymbol{Y_1 = 0.5}$, c) mid-section for $\boldsymbol{Y_1 = 0.7}$ and d) mid-section for $\boldsymbol{Y_1 = 0.9}$.

5.3.4.4 Local entropy generation

In all of the local entropy generation illustrations in this section, the contributions from different sources of irreversibility are shown in subfigure a) to e), and the overall local entropy generation is plotted in sub-figure f). Figure 5-22 shows the local entropy generation for the porous section of the microreactor calculated for the default values given in Table 5-5. This provides a basis to compare the effects of different parameters. Through a simple comparison between the different sources of irreversibility, it is clear that the diffusive irreversibility is the main source of entropy generation and is followed by that of nanofluid friction. It is also observed that the solid and nanofluid entropy generation rates are smaller around the centre of the microreactor. However, the inter-phase volumetric entropy generation rate is larger at the centreline. Figure 5-22d further indicates that by moving transversally from the walls of the reactor towards the centreline, the local entropy generation by nanofluid friction first decreases. It then reaches a minimum value and again hits a high value at the centre of the microreactor, for reasons discussed in Section 5.2.3.4.

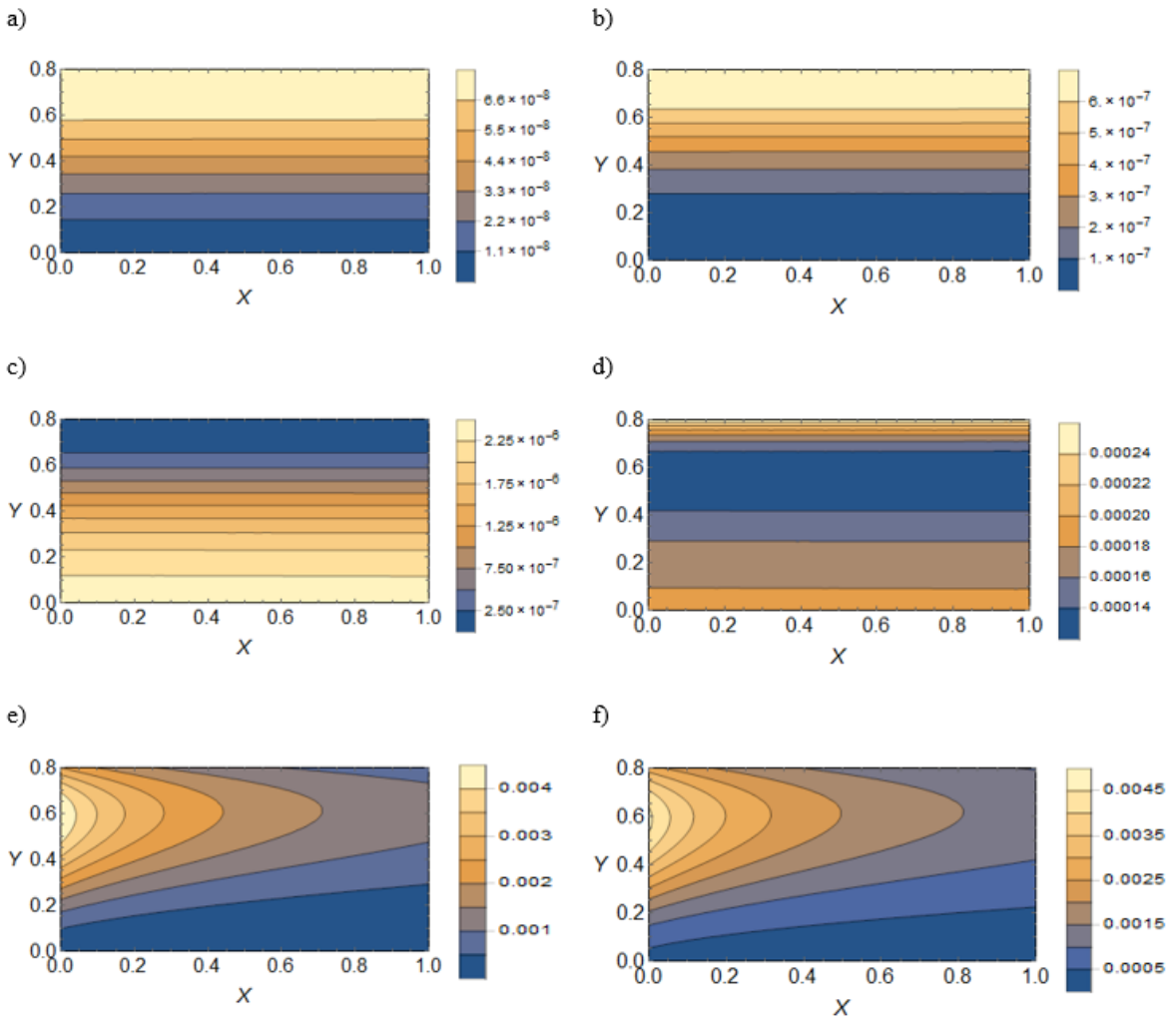

Figure 5-22 Local entropy generation contours for the base configuration showing a)$\boldsymbol{N_{s,ht}}$, b) $\boldsymbol{N_{f,ht}}$, c)$\boldsymbol{N_{int}}$, d)$\boldsymbol{N_{FF}}$, e)$\boldsymbol{N_{DI}}$ and f)$\boldsymbol{N_{pm}}$.

The entropic effects of Soret and Damköhler numbers are further analysed in Figure 5-23. In this figure, the values of Soret and Damköhler number were reduced to 0.01 and 0.3 respectively, which represent a significant reduction in comparison to their default values shown in Table 5-5 and used in Figure 5-22. A comparison between Figure 5-22e and Figure 5-23a reveals that by decreasing the numerical value of Soret number from 0.7 to 0.01 the mass transfer irreversibility decreases by about 40%. Yet, reduction of Damköhler number from 1 (in Figure 5-22e) to 0.3 (in Figure 5-23c) results in 75% reduction in the mass transfer irreversibility. A very similar reduction in overall entropy generation can be seen in Figure 5-23b and Figure 5-23d in comparison with Figure 5-22f. As already discussed this is due to the fact that irreversibility of the process is dominated by the entropy generation through mass transfer. Figure 5-23 clearly shows that while both Soret and Damköhler number are rather influential in determining the irreversibility of the process, Damköhler number seems to be of higher significance.

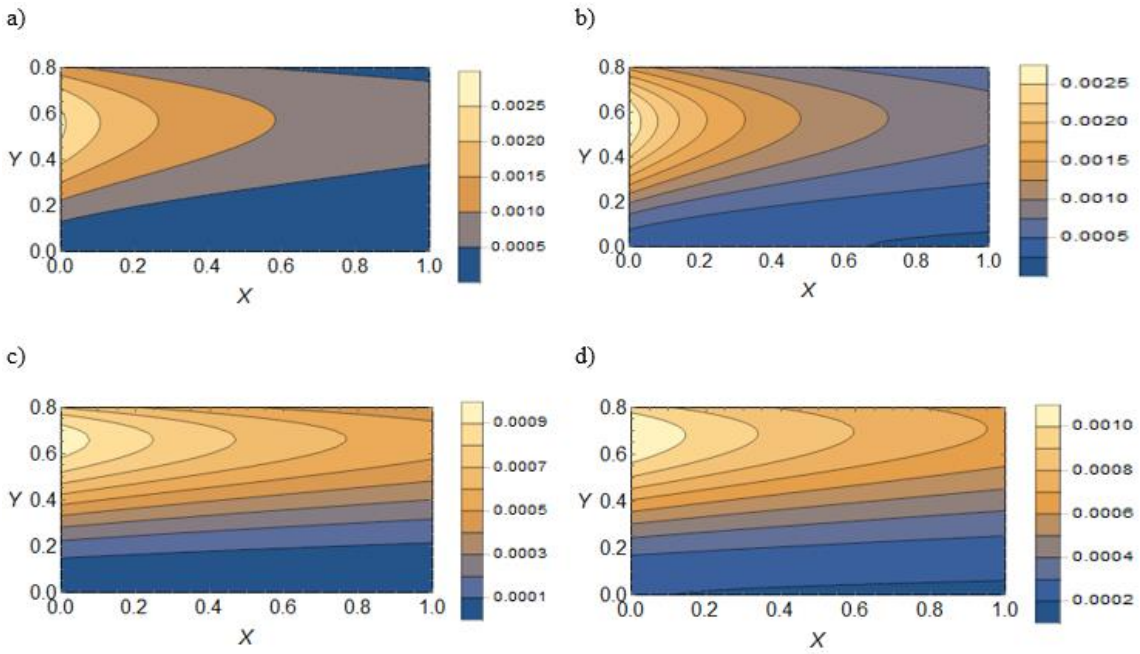

Figure 5-23 The effects of Soret and Damköhler numbers on the local entropy generation, top row: $\boldsymbol{Sr = 0.01}$, a)$\boldsymbol{N_{DI}}$ and b)$\boldsymbol{N_{pm}}$, **bottom row**: $\boldsymbol{\gamma = 0.3}$, c)$\boldsymbol{N_{DI}}$ and d)$\boldsymbol{N_{pm}}$.

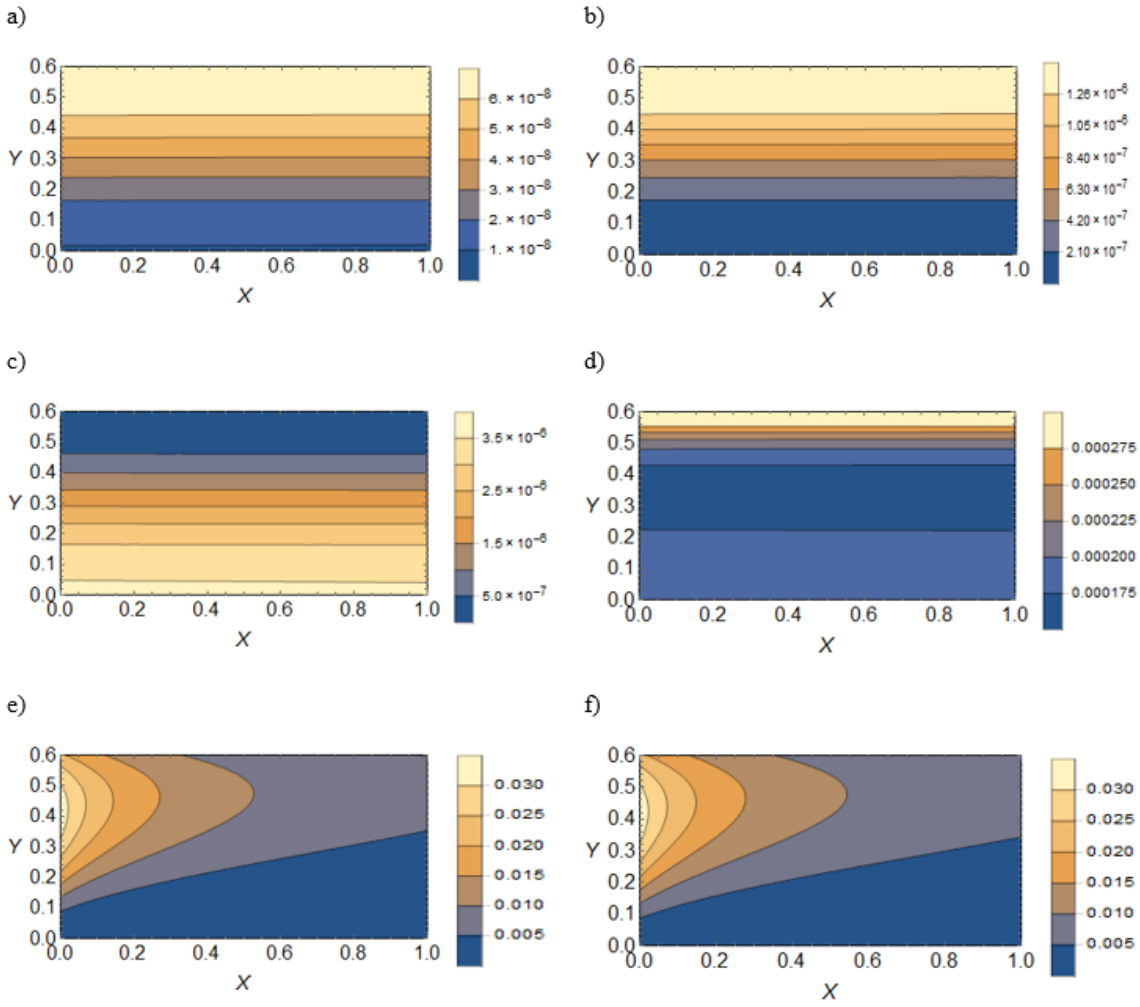

Figure 5-24 Local entropy generation contours for the wall thickness of $\boldsymbol{Y_1 = 0.6}$, showing a)$\boldsymbol{N_{s,ht}}$, b) $\boldsymbol{N_{f,ht}}$, c)$\boldsymbol{N_{int}}$, d)$\boldsymbol{N_{FF}}$, e)$\boldsymbol{N_{DI}}$ and f)$\boldsymbol{N_{pm}}$.

Figure 5-24 depicts the effects of varying the wall thickness on the local entropy generation rates. This figure shows that increasing the thickness of the wall through changing the value of Y_1 from 0.8 to 0.6 has a marginal effect on the nanofluid friction part of the entropy generation. However, it drastically increases the entropy generation by mass transfer. Comparing the values of overall entropy generation rates in Figure 5-22 and Figure 5-24 shows that increasing the thickness of the microchannel wall by two times, has increased the entropy generation rate by almost tenfold. This is a very important result and clearly demonstrates the significance of wall thickness in the level of irreversibility encountered within the microreactor.

5.3.4.5 Total entropy generation

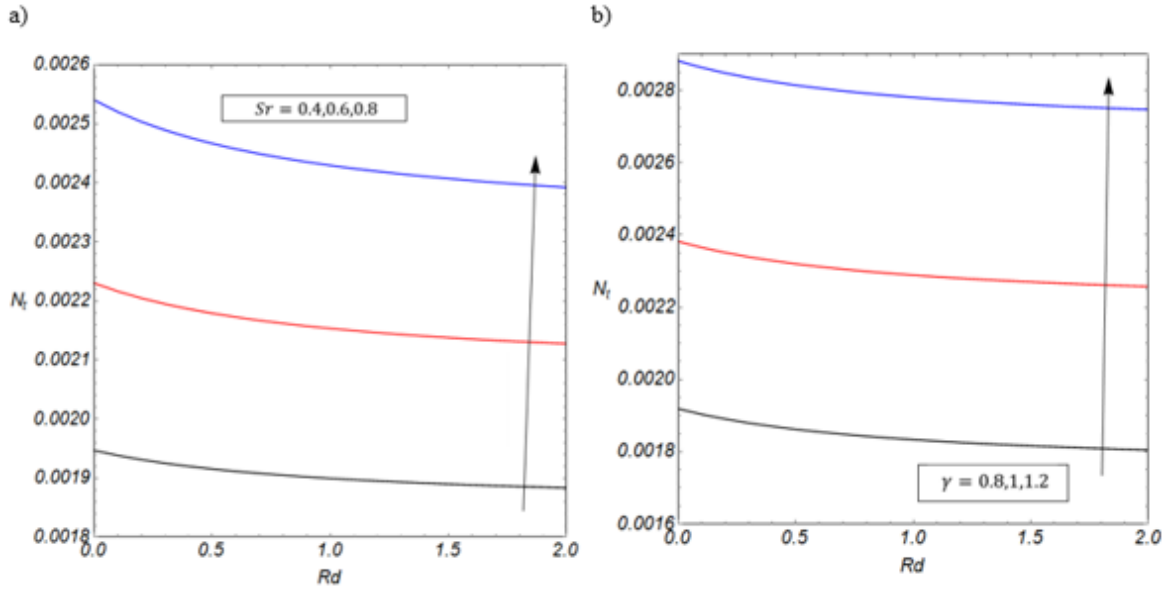

Figure 5-25 Total Entropy generation graphs for varying radiation parameter, $\boldsymbol{Rd}$, with various values of a) Soret number, $\boldsymbol{Sr}$ and b) Damköhler number, $\boldsymbol{\gamma}$.

Figure 5-25 illustrates variations of the total entropy generation rate versus radiation parameter, and Soret and Damköhler numbers. This figure shows that, as expected, increasing either of Soret or Damköhler number would increase the total entropy generation within the microreactor. It also shows that increasing the radiation parameter leads to the reduction of the total entropy generated in the system. Strengthening the thermal radiation intensifies the internal heat exchanges between the components of the reactor and hence leads to smaller temperature gradients. This tends to suppress the thermal and mass transfer irreversibilities and therefore reduces the total entropy generation of the reactor. Figure 5-25 further shows an interesting relation between the radiation parameter and total entropy in which initial increases of radiation parameter from zero result in noticeable reduction in the total entropy. However, further increase in the radiation parameter causes only minor

decreases of the total entropy. From the local entropy study presented in the previous section, it can be seen that the entropy contribution from concentration dominates the system. As mentioned above this reduces the heat transfer and to a lesser extent the mass transfer gradients. This is a limited effect however since once the temperature gradient is sufficiently low, there will be insignificant mass flow due to the Soret effect and further increase in radiation parameter will not greatly decrease the gradient. This result is a lessening effect of increased radiation parameter past a certain value. Additionally, an increase in Soret number would imply a greater levelling of thermal gradient to counteract and this would lead to an associated increase in the range over which the total entropy is affected by thermal radiation. In fact, this is indeed what is observed in Figure 5-25a.

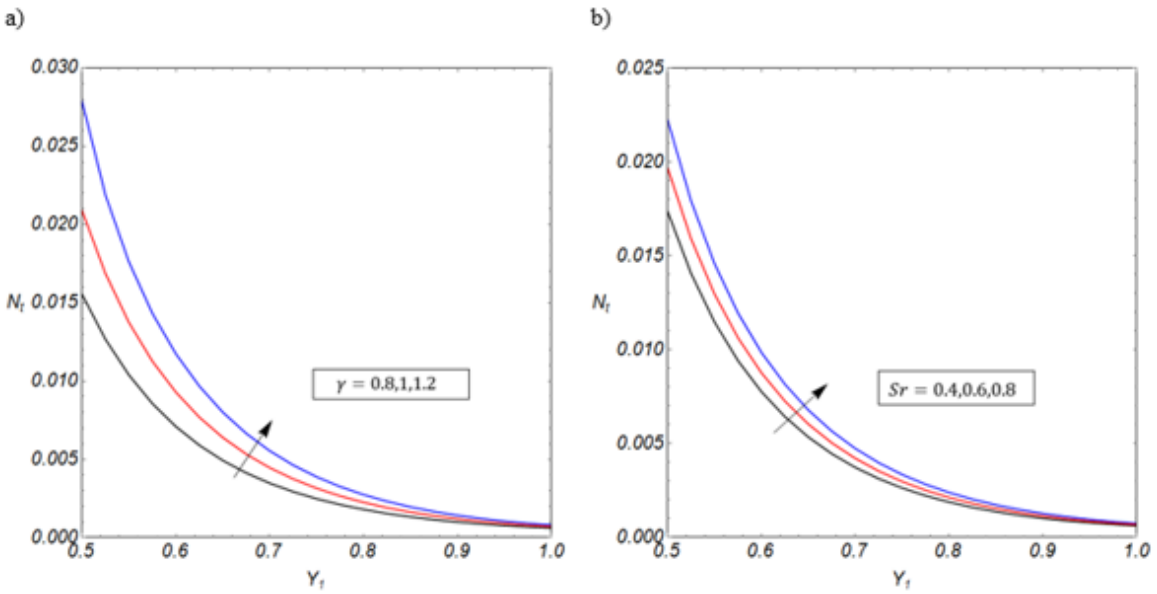

Figure 5-26 Total Entropy graphs for varying wall thickness, $\boldsymbol{Y_1}$ with different values of a) Damköhler number, $\boldsymbol{\gamma}$ and b) Soret number, $\boldsymbol{Sr}$.

The combined effects of wall thickness and Soret and Damköhler numbers upon the total entropy generation are illustrated by Figure 5-26. This figure clearly shows that regardless of the values of Soret and Damköhler numbers reducing the wall thickness (i.e., increasing Y_1) causes substantial decreases in the total irreversibility of the system. Figure 5-26 further shows that such reduction features a highly nonlinear relation with Y_1. It is also clear that total entropy generation in thick wall microreactor is majorly dependent upon the Damköhler number and is affected by Soret number to a lesser extent. For instance, at $Y_1 = 0.5$ by increasing the value of Damköhler number from 0.8 to 1.2, the value of the total entropy generation grows for nearly 80%. However, this influence decreases sharply as the wall becomes thinner.

5.4 Conclusions

Two porous microreactors were modelled featuring two-dimensional convection of heat together with the conjugate heat transfer in the walls were tackled analytically. This included the internal generation of heat through viscous dissipation of flow kinetic energy. Further, a two-dimensional advection-diffusion-reaction model with zeroth order chemical reaction was employed to represent the production and transfer of the chemical species. This was coupled to the transport of heat through thermal diffusion of mass. The resultant coupled heat and mass transfer problem was solved analytically. The analysis of the porous medium was under LTNE conditions and also considered the thermal diffusion of mass and viscous dissipation of momentum. The calculated temperature and concentration fields were then used to predict the local entropy generation within the microreactor. Further, the Nusselt number on the internal surfaces of the microchannel and the total entropy generation within the entire system were calculated. The results were presented in the form of contour plots of temperature, concentration and local entropy generation fields. These visualised the transversal diffusion of heat and mass and the simultaneous advection of them in the investigated microsystem.

In the first, (Case 1) porous material filled the microreactor and the solid thick walls were taken into account to represent the microstructure of the reactor. Catalytic surfaces and exposed to uneven thermal fluxes was representative of heterogeneous reaction processes.

A second porous microreactor (Case 2) accommodating a homogenous chemical reaction and again featuring thick walls was investigated. The axisymmetric system was subject to thermal load in the form of constant heat flux incorporating radiative heat transfer. While there is a long list of parameters that can affect the temperature fields, the wall thicknesses of the microstructure were found most influential in altering the temperatures of the nanofluid and porous solid phases. The Nusselt number on the upper and lower internal walls were shown to be strongly dependent upon the thickness of the walls. In general, increasing the wall thickness results in significant reduction of Nusselt number. This finding was consistent in both Case 1 and Case 2, indicating that irrespective of whether a reaction is catalysed homogeneously of heterogeneously, the thickness of the enclosing structure has an important role to play in thermal management.

In Case 2, increasing the radiation parameter, increases the solid phase temperature and decreases the nanofluid phase temperature. This causes a decrease in the total entropy generation of the microreactor. Additionally, as the dimensionless temperature of the

nanofluid decreases by increasing the radiation parameter, the nanofluid gains more power to wash away heat from the surface of the walls and hence the Nusselt number increases.

In both Case 1 and Case 2, for most combination of parameters, the irreversibility of mass transfer and in particular that of Soret effect is the dominant sources of entropy generation within the microreactor. However, this is not the case for elevated values of imposed heat flux, which result in magnification of thermal irreversibility. Although, depending on the numerical values of other parameters, the nanofluid friction part of the entropy generation can be of comparable significance. Additionally, increasing the Damköhler and Soret numbers intensifies the concentration of species, and magnifies the mass transfer component of the entropy generation rate.

The total entropy appears to be strongly dependent upon the wall thickness and is also affected by the moderate values of radiation parameter in Case 2. Whereas in Case 1, total entropy generation within the system was found to be monotonically increasing with the thermal conductivity ratio and the wall thickness. Minimisation of the total entropy generation may be sought by varying the value of Reynolds number for Case 1. Similarly in Case1 and Case 2, Soret and Damköhler numbers were shown to be very influential in increasing the total entropy generation inside the microreactor.

These points are of clear relevance to the design of more efficient microreactors. Further, the analytical models presented in this work can be used for validation of the future numerical simulations of microreactors.

Chapter 6 Influences of exothermic catalytic reactions upon transport in porous microreactors- A novel porous-solid interface model

6.1 Introduction

Chapter 2 detailed the concept of LTNE conditions and discussed the interface condition known in the literature as Model A. It is essential to note that Model A assumes that the wall in contact with the porous medium is of zero thickness and is therefore unable to conduct heat. Other variations of this LTNE model have also been examined with a view to taking into account other effects such as variable porosity and thermal dispersion [91]. Extensive examination of these models revealed that, for many cases, Model A can represent the interface condition with the greatest accuracy [91]. Additionally, in many microreactors the transfer of mass and heat are coupled [85], so employing LTNE model can also provide a better prediction of the species concentration within the system.

Analytical modelling of transport and thermodynamic irreversibilities in porous microchannels have been now extended to LTNE and two-dimensional analyses (see Chapter 5). The studies in reactive systems have included homogeneous and heterogeneous reactions and investigated combined transport of heat and mass and entropy generation. However, exothermic catalytic reactions have been excluded from these investigations. This is, in part, due to the mathematical difficulties associated with consideration of heat release on the internal surfaces of microreactors. More importantly, the lack of an LTNE interface model capable of considering the wall, fluid and porous solid collectively has rendered the thermal analyses of such systems impossible. The current work tackles these challenges through developing an analytical model of heat and mass transfer in a porous, thick-wall microreactor with exothermic catalytic reactions occurring on the internal surfaces of the walls. Towards this aim, an existing phenomenological model of porous interface is extended to include the wall effects.

6.2 Configuration and assumptions

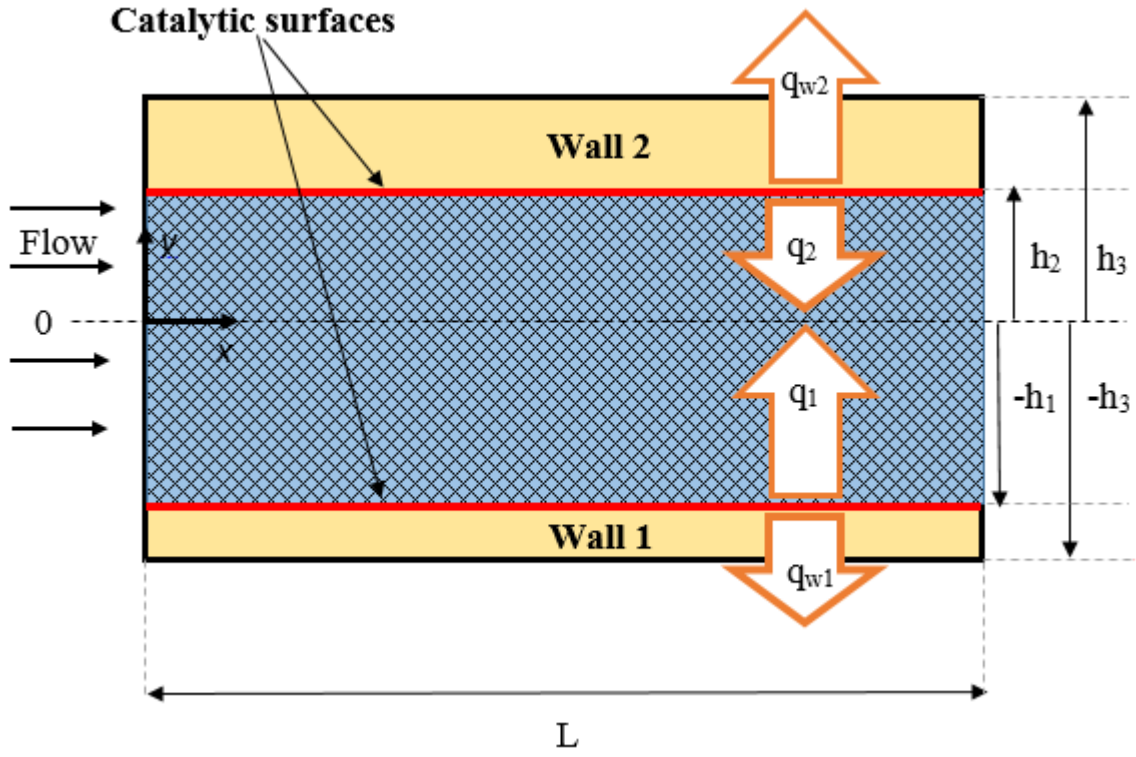

Figure 6-1 Schematic view of the microreactor under investigation.

Figure 6-1 shows schematically the system under investigation including two dissimilar thick walls, the internal surface of which coated with catalysts enhancing exothermic reactions. The heat generated by this reaction imposes a constant heat flux, which is applied to the wall (to which the catalyst is adhered), also to the porous medium. The following assumptions are made.

- The chemical reactions are limited to a zeroth-order reversible, catalytic reaction. Also, in keeping with the previous theoretical analysis of catalytic reactions in microchannels [103,104,198], the catalyst is assumed to be located on the internal surfaces of the microchannel.

- The effects of temperature variations on the catalytic reaction are ignored [198].

- The problem is generally asymmetric and thus the microchannel wall thicknesses and the heat releases on the catalytic surfaces can be uneven.

- The porous medium is homogenous, isotropic and fluid saturated and is under LTNE. Further, gravitational effects and radiative heat transfer are ignored.

- The fluid flow is steady and laminar satisfying the no-slip boundary conditions on the wall. Also, thermally and hydrodynamically fully developed conditions hold over the entire microchannel.

- Physical properties such as porosity, specific heat, density and thermal conductivities are invariants and thermal dispersion effects are ignored.

- The reaction is not diffusion controlled such that diffusive flux of species produced on the surface of the catalyst is at least equal to the rate of species production.

Processes featuring abrupt reaction zones, separating hot and cold flows, such as those in micro-combustors [123,124] are not considered here. As a result, the axial conduction of heat within the walls is insignificant and is neglected throughout the analysis [77]. This is further justified by noting that experimental studies [77] have already shown that the axial temperature gradient within the microstructure diminishes in thick wall microreactors.

6.3 Analytical solution

For the convenience of the reader, the governing equations described in Chapter 3 are presented again here. The separate phases of the system are indicated for their various properties by the subscripts where appropriate. The convention employed herein is that the lower wall uses subscript (1), the porous solid (S), the fluid (f), and the upper wall (2). Where a term is the effective thermal conductivity of the solid porous phase has subscript of (es). Likewise, the term is the effective thermal conductivity of the nanofluid phase has subscript of (ef).

6.3.1 Boundary conditions

Under steady state and for a fully hydrodynamically developed flow, Darcy-Brinkman momentum equation governs the hydrodynamics of the system. That is

$$-\frac{\partial p}{\partial x}+\mu_{eff}\frac{d^2u}{dy^2}-\frac{\mu_f}{\kappa}u=0 \qquad -h_1 \le y < h_2 \qquad (6\text{-}226)$$

The local thermal non-equilibrium condition assumed for energy equation within the solid and fluid phases of the porous media are expressed by the followings [115,205], while viscous dissipation effects are included.

$$k_2 \frac{\partial}{\partial y}\left[\frac{\partial T_2}{\partial y}\right] = 0 \qquad h_2 < y \leq h_3 \qquad (6\text{-}227)$$

$$k_{ef}\frac{\partial^2 T_f}{\partial y^2} + h_{sf}a_{sf}\left(T_s - T_f\right) + \frac{\mu_f}{\kappa}u^2 + \mu_{eff}\left(\frac{du}{dy}\right)^2 = \rho_f C_{p,f} u \frac{\partial T_f}{\partial x} \qquad -h_1 \leq y < h_2 \qquad (6\text{-}228)$$

$$k_{es}\frac{\partial^2 T_s}{\partial y^2} - h_{sf}a_{sf}\left(T_s - T_f\right) = 0 \qquad -h_1 \leq y < h_2 \qquad (6\text{-}229)$$

$$k_1 \frac{\partial}{\partial y}\left[\frac{\partial T_1}{\partial y}\right] = 0 \qquad -h_3 \leq y < -h_1 \qquad (6\text{-}230)$$

Using the following advective-diffusive model, transfer of chemical species by taking into account transport due to the Soret effect as well as diffusion of species due to Fick's Law [146] can be described.

$$u\frac{\partial C}{\partial x} = D\frac{\partial^2 C}{\partial y^2} - D_T\frac{\partial^2 T_f}{\partial y^2} \qquad (6\text{-}231)$$

The no-slip boundary conditions on the microchannel walls are:

$$y = h_2: \qquad u = 0 \qquad (6\text{-}232)$$

$$y = -h_1: \qquad u = 0 \qquad (6\text{-}233)$$

The equations of heat transfer throughout the microchannel are subject to the following boundary conditions [115,205]:

$$y = h_3: \qquad k_2\frac{\partial T_2}{\partial y}\Big|_{y=h_3} = -q''_{w2} \qquad (6\text{-}234)$$

$$y = h_2: \qquad q''_c = k_{ef}\frac{\partial T_f}{\partial y}\Big|_{y=h_2} + k_{es}\frac{\partial T_s}{\partial y}\Big|_{y=h_2} - k_2\frac{\partial T_2}{\partial y}\Big|_{y=h_2} \qquad (6\text{-}235)$$

$$y = -h_1: \qquad q_c'' = -k_{ef}\left.\frac{\partial T_f}{\partial y}\right|_{y=-h_1} - k_{es}\left.\frac{\partial T_s}{\partial y}\right|_{y=-h_1} + k_1\left.\frac{\partial T_1}{\partial y}\right|_{y=-h_1} \tag{6-236}$$

$$y = -h_3: \qquad k_1\left.\frac{\partial T_1}{\partial y}\right|_{y=-h_3} = q_{w1}'' \tag{6-237}$$

Equations (6-235) and (6-236) are extensions of the well-known Model A of Vafai and his co-workers [91,94]. Model A assumes that the split of heat flux on the interface of the porous insert occurs on the basis of the thermal conductivity and transversal temperature gradients of the solid and fluid phases. Thus, a logical extension of this model, for the configuration shown in Figure 6-1, is to add the product of wall thermal conductivity and vertical temperature gradient to those of fluid and porous solid. This permits the total heat flux output of the catalyst, $q_{c,}''$ to be split into its respective heat fluxes into the wall and porous medium. The validity of this extension will be demonstrated later. In addition to the above heat flux boundary conditions, the equality of temperature at the interfaces between the porous medium and the enclosing structure applies the following boundary conditions to the energy equations:

$$y = h_2: \qquad T_2 = T_f = T_s \tag{6-238}$$

$$y = -h_1: \qquad T_1 = T_f = T_s \tag{6-239}$$

The boundary conditions associated with the mass transfer equation (6-231) are given in the following expressions. The reference value, C_0 is the concentration on the lower wall at the entrance to the considered section of the microchannel. This leads to the second imposed condition:

$$y = \frac{y_2 - y_1}{2}: \qquad D\frac{\partial C}{\partial y} = D_T\frac{\partial T_f}{\partial y} \tag{6-240}$$

$$C(0, -h_1): \qquad C = C_0 \tag{6-241}$$

6.3.2 Nusselt number

The heat transfer coefficients at the bottom and top walls of the microchannel are defined as [145]:

$$H_{w1} = \frac{q_1''}{T_{w1} - \bar{T}_f}, \tag{6-242}$$

$$H_{w2} = \frac{q_2''}{T_{w2} - \bar{T}_f}. \tag{6-243}$$

Where the bulk mean temperature of the fluid is given by:

$$\bar{T}_f = \frac{1}{\bar{u}(h_1 + h_2)} \int_{-h_1}^{h_2} u T_f \, dy. \tag{6-244}$$

Thus, Nusselt number utilising the microchannel height $(h_1 + h_2)$ as the characteristic height may be expressed as follows:

$$Nu_{w1} = \frac{H_{w1}(h_1 + h_2)}{k_{ef}} \tag{6-245}$$

$$Nu_{w2} = \frac{H_{w2}(h_1 + h_2)}{k_{ef}}. \tag{6-246}$$

6.3.3 Sherwood Number

Since the reaction taking place at the catalyst surface is of zeroth order, the reaction rate is not dependent upon the concentration of either reactants or products (provided that sufficient reactant exists to allow for the reaction to proceed). This permits the mass transfer coefficient, H_m to be calculated according to the relation [145];

$$H_m = \frac{k_R}{C_0 - \bar{C}}. \tag{6-247}$$

With the mass transfer coefficient thus defined, and using the microchannel height $(h_1 + h_2)$ as the characteristic length scale, the Sherwood number may now be expressed in the following form;

$$Sh = \frac{(h_1 + h_2)H_m}{D} \tag{6-248}$$

Where the mean bulk concentration, $\overline{C}$ is calculated in an analogous manner to equation (6-244).

6.3.4 Entropy Equations

The volumetric entropy generation for the system are expressed by equations (3-31) to (3-35) as shown in Chapter 3 [85,115,205]. In equations (3-31) to (3-35), entropy generation terms represent contributions from different sources of irreversibility. The terms $\dot{S}_1'''$ and $\dot{S}_2'''$ account for the entropy generation in the lower and upper thick walls, respectively. Entropy generation in the solid phase of the porous medium due to heat transfer may be calculated using $\dot{S}_S'''$. Similarly, $\dot{S}_f'''$ is used to find the entropy generation rate in the fluid phase. Fluid friction irreversibility is accounted for by $\dot{S}_{FF}'''$. Irreversibility sources due to the combination of concentration gradients and also those due to mixed thermal and concentration gradients are found using the equation for $\dot{S}_{DI}'''$.

6.3.5 Dimensionless equations

In order to solve the governing equations, it is necessary to render them dimensionless. This is accomplished by defining a series of dimensionless parameters.

The parameters listed in Table 6-1 are introduced to enable further physical analysis. In Table 6-1 the temperature follows the labelling convention $i = 1,2,s,f$. Similarly, the dimensionless entropy generation, N_i follows the labelling convention $i = 1,s,nf,FF,DI,2$.

Table 6-1 Definition of Dimensionless parameters

$\theta_i = \frac{(T_i - T_{w,in})k_{es}}{(q_1'' + q_2'')h_3}$,	$u_r = -\frac{h_3^2}{\mu_f}\frac{\partial p_f}{\partial x}$,	$Bi = \frac{h_{sf}a_{sf}{h_3}^2}{k_{es}}$,
$Y = \frac{y}{h_3}$,	$Da = \frac{\kappa}{h_3^2}$,	$Br' = \frac{\mu_{eff}\bar{u}^2}{(q_1'' + q_2'')h_3}$,
$Y_1 = \frac{h_1}{h_3}$,	$M = \frac{\mu_{eff}}{\mu_f}$,	$k_{e1} = \frac{k_1}{k_{es}}$,
$Y_2 = \frac{h_2}{h_3}$,	$S = \frac{1}{\sqrt{MDa}}$,	$k_{e2} = \frac{k_2}{k_{es}}$,
$\xi = \frac{h_3}{L}$,	$Pr = \frac{C_{p,f}\mu_{eff}}{k_{ef}}$,	$\Phi = \frac{C}{C_0}$,
$U = \frac{u}{u_r}$,	$Pe = \frac{\bar{u}(h_1 + h_2)}{D}$,	$Q_{w1} = \frac{q_{w1}''}{(q_1'' + q_2'')}$,
$X = \frac{x}{L}$,	$q_1'' = q_c'' - q_{w1}''$,	$q_2'' = q_c'' - q_{w2}''$,
$\gamma = \frac{k_R(h_1 + h_2)}{DC_0}$,	$Q = \frac{q_2''}{(q_1'' + q_2'')}$,	$Sr = \frac{(q_1'' + q_2'')(h_1 + h_2)D_T}{C_0 k_f D}$,
$Re = \frac{h_3\rho_f\bar{u}}{\mu_{eff}}$,	$Q_{w2} = \frac{q_{w2}''}{(q_1'' + q_2'')}$,	$k = \frac{k_{ef}}{k_{es}} = \frac{\varepsilon k_f}{(1-\varepsilon)k_s}$,
$N_i = \frac{\dot{S}_i''' h_3^2}{k_{es}}$,	$\varphi = \frac{RDC_0}{k_{es}}$,	$\omega = \frac{(q_1'' + q_2'')h_3}{2k_{es}T_{w,in}}$,

6.3.6 Velocity profiles

Equation (3-9) can be non-dimensionalised using the parameters defined in Table 6-1, resulting in

$$M\frac{d^2U}{dY^2} - \frac{U}{Da} + 1 = 0. \qquad -Y_1 \le Y < Y_2 \qquad (6\text{-}249)$$

It is common practice to assume that $\mu_{eff} = \mu_f$ as this has been shown to yield acceptable results [211]. This leads to $M = 1$ and thus shape factor of the porous medium, $S = \frac{1}{\sqrt{Da}}$. Similarly, the no-slip boundary condition expressed in non-dimensional form is:

$$U(Y_2) = U(-Y_1) = 0, \qquad (6\text{-}250)$$

The solution of equation (6-249) yields:

$$U(Y) = A_1\, cosh(SY) + A_2\, sinh(SY) + Da \qquad -Y_1 \leq Y < Y_2 \qquad (6\text{-}251)$$

Using equation (6-251) and integration over the channel, the average dimensionless velocity across the microchannel is found to be:

$$\overline{U} = \frac{DaS(Y_1 + Y_2) + A_1(sinh(SY_1) + sinh(SY_2)) + A_2(cosh(SY_2) - cosh(SY_1))}{S(Y_1 + Y_2)} \qquad (6\text{-}252)$$

By combining equations (6-251) and (6-252) the following ratios are defined;

$$u/\overline{u} = U/\overline{U} = \frac{SY_1(cosh(SY_1) - cosh(SY))}{SY_1\, cosh(SY_1) - sinh(SY_1)}. \qquad (6\text{-}253)$$

The constants A_1 to A_3 along with all other constants used henceforth are defined explicitly in Appendix A, Section 2.

6.3.7 Temperature profiles

Due to the assumption of fully developed flow and by considering the assumptions summarised in Section 6.2, the following conditions hold [115],

$$\frac{\partial \mathrm{T_f}}{\partial \mathrm{x}} = \frac{\mathrm{d}\overline{\mathrm{T}}_\mathrm{f}}{\mathrm{dx}} = \frac{\partial \mathrm{T_s}}{\partial \mathrm{x}} = \frac{\mathrm{d}\overline{\mathrm{T}}_\mathrm{s}}{\mathrm{dx}} = \frac{\mathrm{dT_{w1}}}{\mathrm{dx}} = \frac{\mathrm{dT_{w2}}}{\mathrm{dx}} = \Omega = \text{constant.} \qquad (6\text{-}254)$$

This permits seeking a solution for the temperature equations of the form:

$$T_i(x, y) = f_i(y) + \Omega x \qquad i = 1, 2, s, f, \qquad (6\text{-}255)$$

where $f_i(y)$ is a function to be determined by solving equations (6-227) to (6-230) and applying the boundary conditions detailed in equations (6-234) to (6-237). Determination of solutions to the transports of thermal energy equations within the porous microchannel requires the addition of equations (6-228) to (6-229) in the first instance. The resulting equation is then integrated over the cross-section of the asymmetric microchannel. Substituting into the heat flux boundary conditions from equations (6-235) and (6-236) and utilising the heat flux relationships stated in Table 6-1 gives rise to;

$$q_1'' + q_2'' + \frac{\mu_{nf}}{\kappa}\int_{-h_1}^{h_2} u^2\,dy \;+\; \mu_{eff}\int_{-h_1}^{h_2}\left(\frac{du}{dy}\right)^2 dy = \rho_f C_{p,f}\int_{-h_1}^{h_2} u\frac{\partial T_f}{\partial x}dy. \tag{6-256}$$

Rearranging equation (6-253) allows substitution for u in equation (6-256). Conversion to non-dimensional parameters as defined in Table 6-1 simplifies integration, which yields:

$$\frac{d\bar{T}_f}{dx} = \frac{\left[2h_3(q_1'' + q_2'') + \mu_{eff}\bar{u}^2 A_4\right]}{(\rho_f C_{p,f})\bar{u}(h_1 + h_2)h_3} = \Omega, \tag{6-257}$$

Where the bulk mean temperature of the fluid is given by equation (6-244). The axial temperature distribution may now be determined by applying equation (6-254) to equation (5-139) followed by non-dimensionalising the resulting differential equation. Solving the resultant equation such that the solution satisfies equation (6-255) yields:

$$\theta_i(X) = \frac{X\,[1 + Br' A_4]}{Re\,Pr\,k\,(Y_1 + Y_2)\xi} \qquad i = 1, 2, s, f \tag{6-258}$$

Non-dimensional forms of equations (6-227) to (6-230) are obtained through algebraic manipulation and by substitution of the parameters listed in Table 6-1 and application of equations (5-139) and (6-254) to give:

$$k_{e2}\theta_2'' = 0 \qquad Y_2 < Y \le 1 \tag{6-259}$$

$$k\theta_f'' + Bi\left(\theta_s - \theta_f\right) + B_1\,cosh(2SY) + B_2\,sinh(2SY) + B_3\,cosh(SY) + B_4\,sinh(SY) + B_5 = 0 \qquad -Y_1 \le Y < Y_2 \tag{6-260}$$

$$\theta_s'' - Bi\left(\theta_s - \theta_f\right) = 0 \qquad -Y_1 \le Y < Y_2 \tag{6-261}$$

$$k_{e1}\theta_1'' = 0 \qquad -1 \le Y < -Y_1 \tag{6-262}$$

Differentiation of equations (6-260) and (6-261), allows for the decoupling of these equations resulting in:

$$k\theta_f'''' - \alpha^2\theta_f'' + (4S^2 - Bi)B_1\, cosh\,(2SY) + (4S^2 - Bi)B_2\, sinh(2SY) + (S^2 - Bi)B_3\, cosh\,(SY) + (S^2 - Bi)B_4\, sinh(SY) - BiB_5 = 0, \quad (6\text{-}263)$$

$$k\theta_s'''' - \alpha^2\theta_s'' - Bi[B_1\, cosh(2SY) + B_2\, sinh(2SY) + B_3\, cosh(SY) + B_4\, sinh(SY) + B_5] = 0, \quad (6\text{-}264)$$

where $\alpha = \sqrt{Bi(1 + k^{-1})}$.

Once equations (6-234) to (6-239) have been rendered dimensionless, then along with equations (6-260) and (6-261), the eight boundary conditions of the two fourth order differential equations (6-263) and (6-264) can be defined.

Table 6-2 Boundary conditions for temperature equations

$\theta_f(-Y_1) = \theta_s(-Y_1) = 0$	$\theta_f(Y_2) = \theta_s(Y_2) = \theta_{w2}$
$\theta_f''(-Y_1) = -\frac{1}{k}[B_1 \cosh(2SY_1) - B_2 \sinh(2SY_1) + B_3 \cosh(SY_1) - B_4 \sinh(SY_1) + B_5]$	
$\theta_s''(-Y_1) = 0$	$\theta_s''(Y_2) = 0$
$\theta_2(Y_2) = \theta_{w2}$	$k_{e2}\theta_2'(1) = -Q_{w2}$
$\theta_1(-Y_1) = 0$	$k_{e1}\theta_1'(-1) = Q_{w1}$
$\theta_f''(Y_2) = -\frac{1}{k}[B_1 \cosh(2SY_2) + B_2 \sinh(2SY_2) + B_3 \cosh(SY_2) + B_4 \sinh(SY_2) + B_5]$	

Four boundary conditions are further required in order to solve (6-259) and (6-262), which are themselves linked to equations (6-263) and (6-264) by the virtue of thermal relationships in the system under investigation. Equations (6-234) to (6-239) provide the necessary extra boundary conditions. This concludes the twelve boundary conditions required for the closure of the system, which are presented in Table 6-2.

Applying the boundary conditions given by Table 6-2 allows the analytical solutions of the system of equations (6-259), (6-262), (6-263), and (6-264) to be found. The resulting closed-form dimensionless temperature formulations in the axial direction are:

$$\theta_2(Y) = C_1 + C_2 Y \qquad Y_2 < Y \leq 1 \qquad (6\text{-}265)$$

$$\begin{aligned}\theta_s(Y) = {} & C_3\, cosh(2SY) + C_4\, cosh(SY) + C_5\, cosh(\alpha Y) \\ & + C_6\, sinh(2SY) + C_7\, sinh(SY) \\ & + C_8\, sinh(\alpha Y) + C_9 Y^2 + C_{10} Y + C_{11}\end{aligned} \qquad -Y_1 \leq Y < Y_2 \qquad (6\text{-}266)$$

$$\begin{aligned}\theta_f(Y) = {} & C_{12}\, cosh(2SY) + C_{13}\, cosh(SY) + C_{14}\, cosh(\alpha Y) \\ & + C_{15}\, sinh(2SY) + C_{16}\, sinh(SY) \\ & + C_{17}\, sinh(\alpha Y) + C_{18} Y^2 + C_{19} Y + C_{20}\end{aligned} \qquad -Y_1 \leq Y < Y_2 \qquad (6\text{-}267)$$

$$\theta_1(Y) = C_{21} + C_{22} Y \qquad -1 \leq Y < -Y_1 \qquad (6\text{-}268)$$

Substitution of equations (6-258) and (6-265) to (6-268) into equation (6-255) reveals the final temperature profiles as:

$$\theta_2(X,Y) = \frac{X\,[1 + Br' A_4]}{Re\, Pr\, k\, (Y_1 + Y_2)\xi} + C_1 + C_2 Y \qquad Y_2 < Y \leq 1 \qquad (6\text{-}269)$$

$$\begin{aligned}\theta_s(X,Y) = {} & \frac{X\,[1 + Br' A_4]}{Re\, Pr\, k\, (Y_1 + Y_2)\xi} + C_3\, cosh(2SY) \\ & + C_4\, cosh(SY) + C_5\, cosh(\alpha Y) \\ & + C_6\, sinh(2SY) + C_7\, sinh(SY) \\ & + C_8\, sinh(\alpha Y) + C_9 Y^2 + C_{10} Y + C_{11}\end{aligned} \qquad -Y_1 \leq Y < Y_2 \qquad (6\text{-}270)$$

$$\begin{aligned}\theta_f(X,Y) = {} & \frac{X\,[1 + Br' A_4]}{Re\, Pr\, k\, (Y_1 + Y_2)\xi} + C_{12}\, cosh(2SY) \\ & + C_{13}\, cosh(SY) + C_{14}\, cosh(\alpha Y) \\ & + C_{15}\, sinh(2SY) + C_{16}\, sinh(SY) \\ & + C_{17}\, sinh(\alpha Y) + C_{18} Y^2 + C_{19} Y + C_{20}\end{aligned} \qquad -Y_1 \leq Y < Y_2 \qquad (6\text{-}271)$$

$$\theta_1(X,Y) = \frac{X\,[1 + Br' A_4]}{Re\,Pr\,k\,(Y_1 + Y_2)\xi} + C_{21} + C_{22}Y \qquad -1 \le Y < -Y_1 \qquad (6\text{-}272)$$

To continue the analysis of the thermal conditions within the microchannel, the Nusselt number for the upper and lower walls be couched in non-dimensional terms. This leads to;

$$Nu_{w1} = \frac{(Q-1)(Y_1 + Y_2)}{k\overline{\theta_f}} \qquad (6\text{-}273)$$

$$Nu_{w2} = \frac{Q(Y_1 + Y_2)}{k(\theta_{w2} - \overline{\theta_f})}. \qquad (6\text{-}274)$$

The dimensionless bulk mean temperature of the fluid, $\bar{\theta}_f$ may be found by first rendering dimensionless, equation (6-244) and then integrating over the microchannel. This yields;

$$\overline{\theta_f} = \frac{A_3}{(Y_1 + Y_2)} \int_{-Y_1}^{Y_2} \theta_f [A_1\, cosh(SY) + A_2\, sinh(SY) + Da]\, dY. \qquad (6\text{-}275)$$

6.3.8 Concentration profiles

Next, the governing equation for mass transfer, equation (6-231), is non-dimensionalised and analytically solved using the boundary conditions given in equations (6-240) and (6-241). Considering a control volume over a section of the microchannel with the length dx is and thickness in the z direction of one and applying a Taylor series expansion to a mass balance to this leads to the following equation,

$$\bar{u}\frac{\partial C}{\partial x} = \frac{2k_R}{(h_1 + h_2)}. \qquad (6\text{-}276)$$

Assigning C_0 as the initial concentration upon the lower wall at the entrance of the microchannel as an arbitrary initial starting point in the axial direction, the solution of equation (6-276) is

$$C(x) = C_0 \frac{2k_R x}{(h_1 + h_2)\bar{u}}. \tag{6-277}$$

Thus, the concentration profile in the axial direction is independent of the profile in the transverse direction and hence, the form of solution for the mass transfer profile is similar to that of the temperature profile:

$$C(x, y) = g(y) + h(x). \tag{6-278}$$

Using the dimensionless parameters defined in Table 6-1, equation (5-165) can be rendered dimensionless to give the following:

$$\Phi(X) = \frac{2\gamma X}{\xi(Y_1 + Y_2)Pe}. \tag{6-279}$$

Substitution of equation (6-276) into equation (6-231) gives

$$\frac{2k_R u}{(h_1 + h_2)\bar{u}} = D\frac{\partial^2 C}{\partial y^2} - D_T \frac{\partial^2 T_f}{\partial y^2}. \tag{6-280}$$

Equation (6-280) can now be non-dimensionalised and rearranged into a form that may be readily solved as detailed below,

$$\Phi''(Y) = \frac{2\gamma A_3(A_1\, cosh(SY) + A_2\, sinh(SY) + Da)}{(Y_1 + Y_2)^2} + \frac{Sr\ k}{\varepsilon(Y_1 + Y_2)}\theta_f''(Y). \tag{6-281}$$

Since $\theta_f''(Y)$ may be determined from equation (6-267) only the boundary conditions (6-240) and (6-241) require expressing in dimensionless form. The results are as follows;

$$\Phi(-Y_1) = 1 \tag{6-282}$$

$$\Phi'\left(\frac{Y_2 - Y_1}{2}\right) = \frac{Sr\ k}{\varepsilon(Y_1 + Y_2)}\theta'\left(\frac{Y_2 - Y_1}{2}\right) \tag{6-283}$$

Utilisation of the boundary conditions defined by equations (6-282) and (6-283) facilitate the particular solution to equation (6-281) to be found analytically. This results in

$$\Phi(Y) = D_1\, cosh(2SY) + D_2\, cosh(SY) + D_3\, cosh(\alpha Y) + D_4\, sinh(2SY) + D_5\, sinh(SY) + D_6\, sinh(\alpha Y) + D_7 Y^2 + D_8 Y + D_9. \quad (6\text{-}284)$$

Finally, substituting equations (5-166) and (5-175) and into equation (6-278) gives the dimensionless concentration profiles in the axial and transverse directions,

$$\Phi(X,Y) = \frac{2\gamma X}{\xi(Y_1 + Y_2)Pe} + D_1\, cosh(2SY) + D_2\, cosh(SY) + D_3\, cosh(\alpha Y) + D_4\, sinh(2SY) + D_5\, sinh(SY) + D_6\, sinh(\alpha Y) + D_7 Y^2 + D_8 Y + D_9. \quad (6\text{-}285)$$

All that remains with regards to development of concentration related analytical solutions is to non-dimensionalise the equation for the Sherwood number. This results in:

$$Sh = \frac{\gamma}{D\left(1 - \overline{\Phi}\right)}, \quad (6\text{-}286)$$

The dimensionless bulk concentration, $\overline{\Phi}$ is found in an analogous manner to that of equation (5-157),

$$\overline{\Phi} = \frac{A_3}{(Y_1 + Y_2)} \int_{-Y_1}^{Y_2} \Phi[A_1\, cosh(SY) + A_2\, sinh(SY) + Da]\, dY. \quad (6\text{-}287)$$

6.3.9 Entropy profiles

The non-dimensionalised versions of equations (3-31) to (3-35) are presented as

$$N_2 = \frac{k_{e2}\omega^2}{(\omega\theta_2 + 1)^2}\left[\xi^2\left(\frac{\partial\theta_2}{\partial X}\right)^2 + \left(\frac{\partial\theta_2}{\partial Y}\right)^2\right] \quad (6\text{-}288)$$

$$N_s = \frac{\omega^2}{(\omega\theta_s + 1)^2}\left[\xi^2\left(\frac{\partial\theta_s}{\partial X}\right)^2 + \left(\frac{\partial\theta_s}{\partial Y}\right)^2\right] - \frac{Bi\omega\left(\theta_s - \theta_f\right)}{(\omega\theta_s + 1)} \quad (6\text{-}289)$$

$$N_f = \frac{k\,\omega^2}{\left(\omega\theta_f + 1\right)^2}\left[\xi^2\left(\frac{\partial\theta_f}{\partial X}\right)^2 + \left(\frac{\partial\theta_f}{\partial Y}\right)^2\right] + \frac{Bi\omega\left(\theta_s - \theta_f\right)}{\left(\omega\theta_f + 1\right)} \quad (6\text{-}290)$$

$$N_{FF} = \frac{A_6\omega}{(\theta_f\omega+1)}[Da^2 + 2A_1 Da\, cosh(SY) + 2A_2 Da\, sinh(SY) + (A_1^2 + A_2^2)\, cosh(2SY) + 2A_1A_2\, sinh(2SY)] \quad (6\text{-}291)$$

$$N_{DI} = \frac{\varphi}{\Phi}\left[\xi^2\left(\frac{\partial\Phi}{\partial X}\right)^2 + \left(\frac{\partial\Phi}{\partial Y}\right)^2\right] + \frac{\varphi\omega}{(\omega\theta_f+1)}\left[\xi^2\left(\frac{\partial\Phi}{\partial X}\right)\left(\frac{\partial\theta_f}{\partial X}\right) + \left(\frac{\partial\Phi}{\partial Y}\right)\left(\frac{\partial\theta_f}{\partial Y}\right)\right] \quad (6\text{-}292)$$

$$N_1 = \frac{k_{e1}\omega^2}{(\omega\theta_1+1)^2}\left[\xi^2\left(\frac{\partial\theta_1}{\partial X}\right)^2 + \left(\frac{\partial\theta_1}{\partial Y}\right)^2\right] \quad (6\text{-}293)$$

To assist the investigation of entropy generation, the equations for the fluid and the solid phases of the porous medium are broken down. Each being the sum of a heat transfer and an interstitial contribution. This permits a comparison between the contributions from different sources of irreversibility. The following equations for the irreversibility of heat transfer in the system result.

$$N_{s,ht} = \frac{\omega^2}{(\omega\theta_s+1)^2}\left[\xi^2\left(\frac{\partial\theta_s}{\partial X}\right)^2 + \left(\frac{\partial\theta_s}{\partial Y}\right)^2\right] \quad (6\text{-}294)$$

$$N_{f,ht} = \frac{k\,\omega^2}{(\omega\theta_f+1)^2}\left[\xi^2\left(\frac{\partial\theta_f}{\partial X}\right)^2 + \left(\frac{\partial\theta_f}{\partial Y}\right)^2\right] \quad (6\text{-}295)$$

The interstitial volumetric entropy generation term can be found by addition of the remaining components of equations to return the following;

$$N_{int} = \frac{Bi\,\omega^2(\theta_f-\theta_s)^2}{(\omega\theta_s+1)(\omega\theta_f+1)}. \quad (6\text{-}296)$$

The volumetric entropy generations for the porous insert as a whole, N_{pm} is the sum of the equations that describe the various irreversibility sources with the porous medium only. As such, N_{pm} contains terms for the combined processes of heat transfer, viscous dissipation, and concentration gradients,

$$N_{pm} = N_{s,ht} + N_{f,ht} + N_{int} + N_{FF} + N_{DI}. \tag{6-297}$$

The total entropy generation in the microreactor, N_{Tot}, is generated from the sum of the parts of volumetric entropy generation, in the ranges in which they are valid. Which is then integrated over the volume of the microchannel with the inclusion of contributions from the walls to yield a numerical value for the system as a whole. That is

$$N_{Tot} = \int_{-1}^{1}\int_{0}^{1}\sum N_i \, dXdY, \qquad i = 1, s, f, FF, DI, 2. \tag{6-298}$$

6.4 Validation

To validate the mathematical model developed in Sections 5.3, it is demonstrated that when the wall thickness and thermal radiation tend to zero, the analytical form of the temperature fields reduce to those presented by Ting et al. [115] with no internal heat generation term. For details, see Appendix B, Section 2.

Additionally, a numerical calculation was performed using Starccm+ and Nusselt numbers calculated using this numerical simulation and the analytical model described in this chapter were found to be in excellent agreement. For further details, see Appendix B, Section 2.

6.5 Discussion

The problem solved in Section 5.2.2 features a large number of dimensionless parameters. To conduct quantitative analyses default values are assigned to them in

Table 6-3 Default values of dimensionless parameters used in figures

Dimensionless parameter	Dimensionless parameter Name	Default value
ε	Porosity	0.95
Bi	Biot Number	1
Br'	Modified Brinkman number	0.00001
γ	Damköhler number	0.5
Da	Darcy number	0.1
Pe	Peclet number	10
Pr	Prandtl number	5
Re	Reynolds number	75
Sr	Soret number	0.7
ξ	Aspect ratio of channel	0.05
k	Thermal conductivity ratio	0.01 0.2 (Total Entropy)
k_{e1}	Dimensionless Wall1 thermal conductivity	0.5
k_{e2}	Dimensionless Wall1 thermal conductivity	0.2
Q	Heat flux ratio	0.75
Q_{w1}	Wall1 heat flux ratio	0.5
Q_{w2}	Wall2 heat flux ratio	0.2
ω	Dimensionless heat flux	0.001
φ	Irreversibility distribution ratio	0.01
Y_1	Lower channel thickness from centre-line	0.9
Y_2	Upper channel thickness from centre-line	0.8

6.5.1 Temperature distribution

Figure 6-2 to Figure 6-4 show contour plots of the dimensionless temperature field in the microreactor including the upper and lower walls. It is important to note that the non-dimensionalisation described by Table 6-1 allows some parts of the system to have negative non-dimensional temperatures. Figure 6-2 to Figure 6-4 show the temperature fields of the fluid and solid phases, and all subfigures include the temperature field of the solid walls. A general feature of these figures is the clear distinction between the temperature fields of the fluid and porous solid phases, rendering a strong deviation from LTE. This is consistent with the previous investigations of internally heat generating porous channels [93,98,108] and highlights the significance of LTNE approach in the current analysis. The effects of variation in the thermal conductivity ratio, k are shown in Figure 6-2.

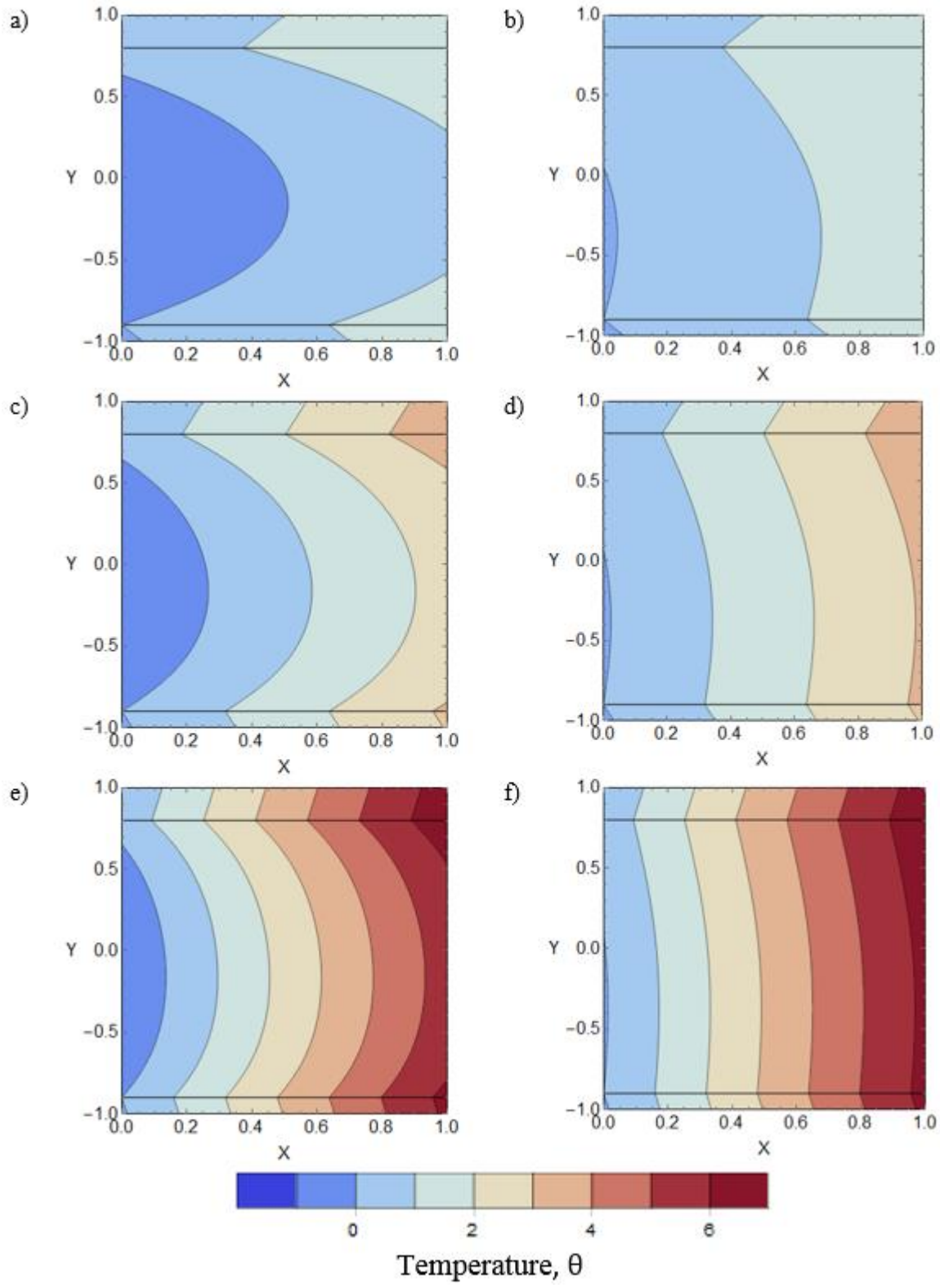

Figure 6-2 Dimensionless temperature contours for varying thermal conductivity ratio, **k** for the fluid and porous solid phase. Fluid phase is shown in a), c), and e) and solid phase is shown in b), d), and f) with $\mathbf{k} = \mathbf{0.02}, \mathbf{0.01}, \mathbf{0.005}$, respectively.

A decrease in k can be accomplished by increasing the thermal conductivity of the porous solid, decreasing that of the fluid or a combination of both. The effect is more heat transmitted to the centre of the microchannel by the solid and less conducted or convected

away by the fluid. Figure 6-2 bears this out, showing an increased temperature range for decreasing k. This result is of practical significance, demonstrating that the respective thermal conductivities of the fluid and porous solid can have a major impact on the temperatures encountered in the microreactor.

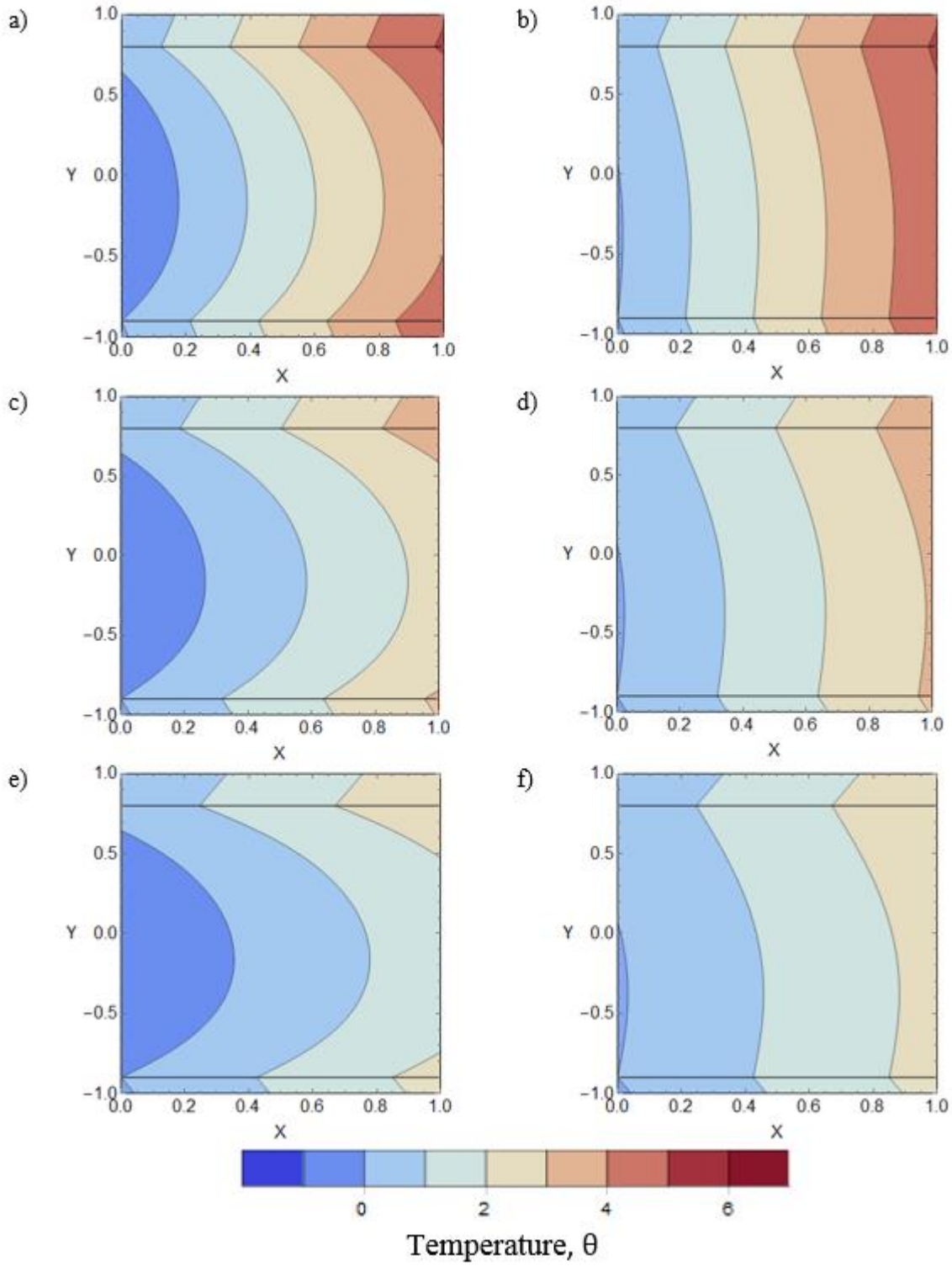

Figure 6-3 Dimensionless temperature contours for varying Reynolds number, **Re**. Fluid phase is shown in a), c), and e) and solid phase is shown in b), d), and f) with $\mathbf{Re} = \mathbf{50}, \mathbf{75}, \mathbf{100}$, respectively.

Increasing Reynolds number represents an increase in the velocity field of the fluid in the microreactor. Figure 6-3 shows the effects of flow velocity upon the dimensionless temperature field of the microreactor. At lower Reynolds numbers, the implied lower velocity allows for longer residence times of the fluid element and hence greater quantities of thermal energy is imparted to the fluid. Further, expectedly, the rate of heat removal from the system by convection is lower at reduced flow velocities. The combination of these effects leads to a significantly larger axial temperature gradient and higher dimensionless temperatures at lower Reynolds numbers. Again, from a practical point of view, control of the fluid velocity within the microreactor allows for variation in the temperature fields within the system.

Consistent with the one-dimensional analyses in microreactors [85,117,205], and also with those in both axial and transverse directions [212], Figure 6-4 shows that increasing the thickness of the upper wall extends the dimensionless temperature range within the microreactor. Although not shown here, a similar result was obtained by varying the lower wall thickness. The corresponding decrease in microchannel thickness gives rise to an increase in velocity field in the channel and a decrease in the volume of fluid. Thus the same total heat flux is being applied to a smaller volume of porous medium, which is hence less able to advect the heat away, leading to higher temperatures. The greater disparity between the temperatures of the two phases towards the centreline is indicative of deviation from local thermal equilibrium, which clearly reflects the necessity of taking an LTNE approach in the current problem. This, in turn, highlights the importance of the extended interface model developed in Section 6.3.

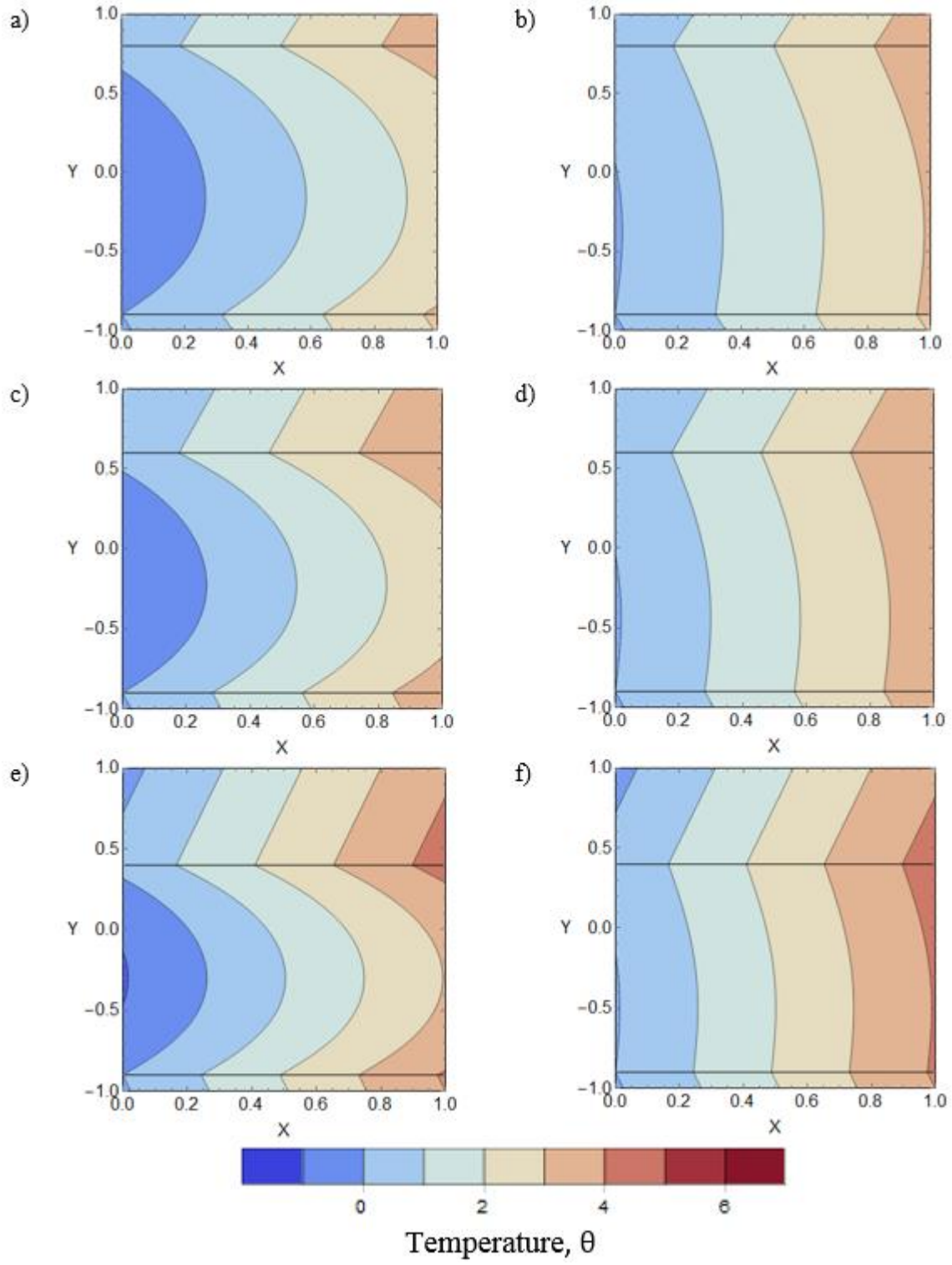

Figure 6-4 Dimensionless temperature contours for varying upper wall thickness, $\mathbf{Y_2}$. Fluid phase is shown in a), c), and e) and solid phase is shown in b), d), and f) with $\mathbf{Y_2} = \mathbf{0.8}, \mathbf{0.6}, \mathbf{0.4}$, respectively.

6.5.2 Nusselt number

Variation of Nusselt number on the wall versus the upper wall thickness is shown in Figure 6-5c and Figure 6-5d as calculated on the lower and upper walls, respectively. Similar examination for the Nusselt number against the lower wall thickness is shown in Figure 6-5a and Figure 6-5b. In all cases, the general trend is towards a significant increase in Nusselt number as the wall thickness decreases. This is in keeping with the findings of the recent works [205,212] and reinforces the emerging notion that the microstructure plays a vital role in determining the thermal characteristics of the microreactor. Variation of the thermal conductivity ratio is monotonically increasing for Nusselt number on the upper wall under the given conditions. However, as the wall thickness increases the Nusselt number on the lower wall behaves in a more complex manner.

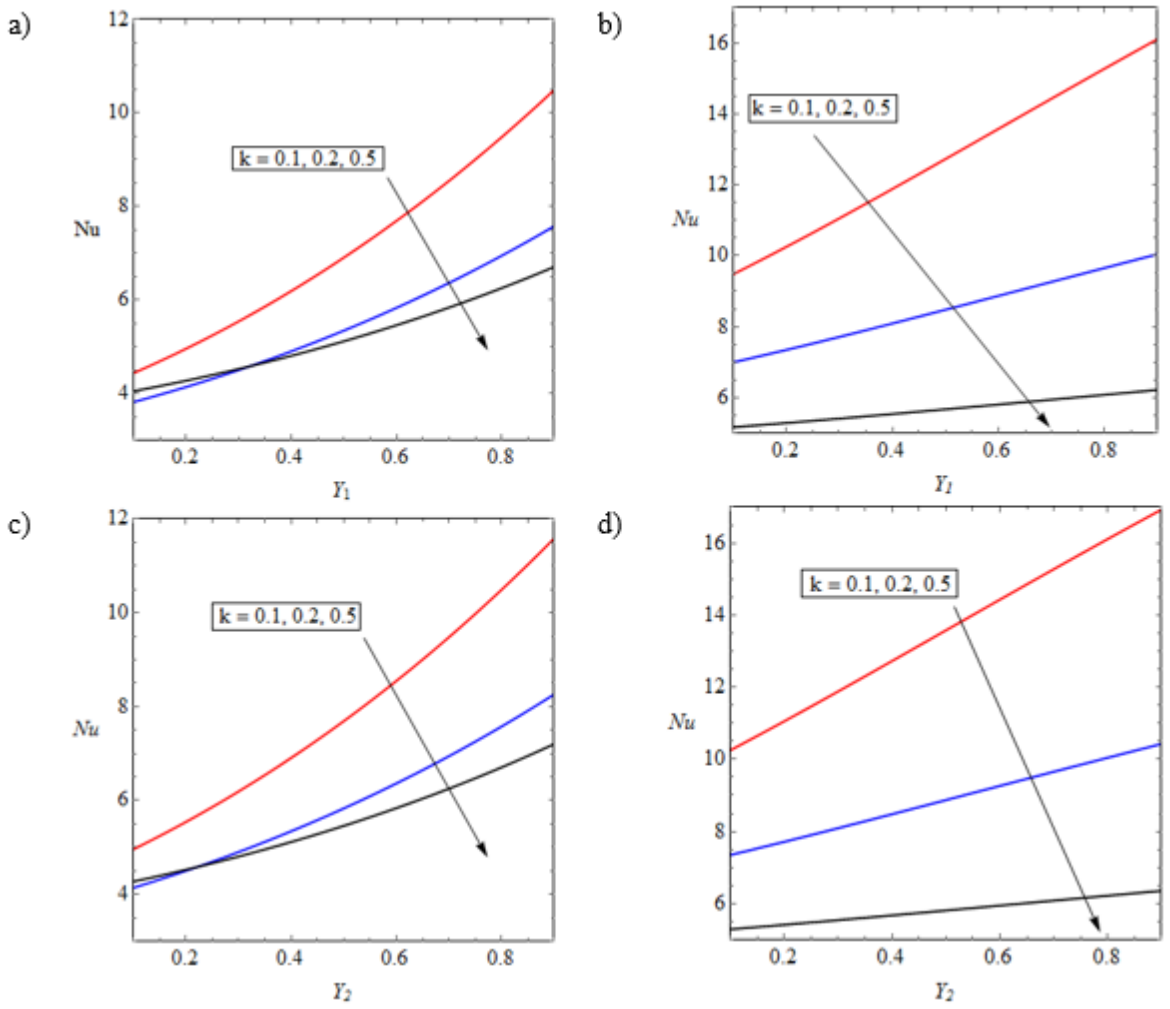

Figure 6-5 Variation of *Nu* versus the lower and upper wall thicknesses, $\mathbf{Y_1}$&$\mathbf{Y_2}$, for different values of thermal conductivity ratio, **k**, at a) & c) the lower wall and b) & d) the upper wall.

For thick walled systems, the behaviour of the system changes with higher thermal conductivity ratios as can be seen in Figure 6-5a and Figure 6-5c, where the curves for $k = 0.2$ and $k = 0.5$ reach first an intersection, then cross over one another. This behaviour indicates the presence of minima in the variation of Nusselt number against thermal conductivity ratio for a given wall thickness above the threshold value. Clearly, existence of such minima enables thermal optimisation of the system.

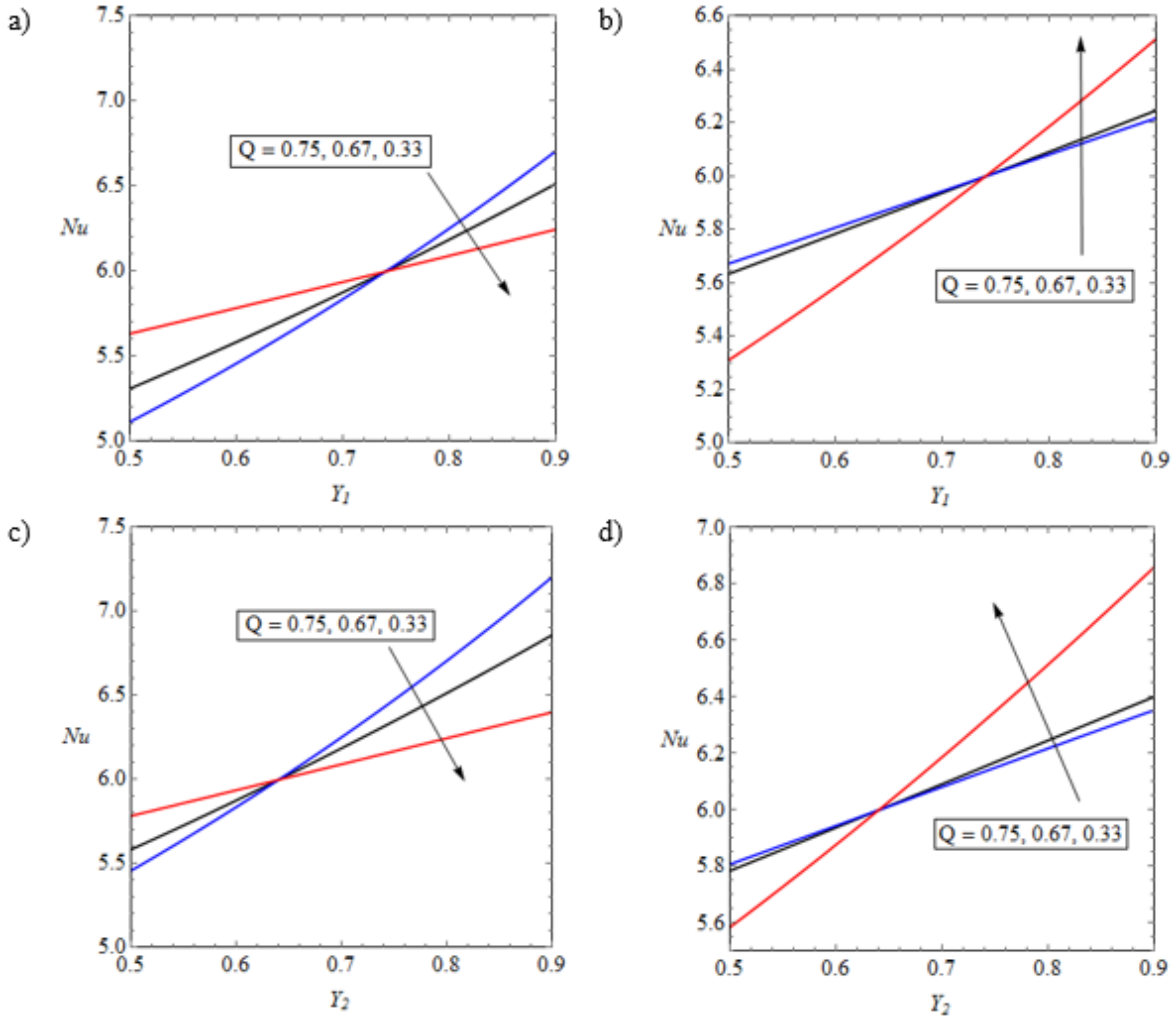

Figure 6-6 Variation of *Nu* versus the lower and upper wall thicknesses, $\mathbf{Y_1}$&$\mathbf{Y_2}$, ($\mathbf{k = 0.5}$) for different values of heat flux ratio, **Q** at a & c) the lower wall and b & d) the upper wall.

Examination of the effects upon the Nusselt number induced by changes in the thermal load are the subject of Figure 6-6. Utilising the findings of Figure 6-5, a value of k was set to 0.5 in Figure 6-6. While maintaining the magnitude of the total thermal load constant, the individual fluxes from the catalyst into the porous microchannel are varied through a measure of their proportionality, Q defined in Table 6-1. The trend in the graphs shows a monotonic increase in Nusselt number as wall thickness decreases for all cases. This holds regardless of whether there is an imbalance of heat flux from the upper or the lower

wall or if the Nusselt number is measured on the upper (Figure 6-6b and Figure 6-6d) or lower wall (Figure 6-6a and Figure 6-6c). Nonetheless, variations in Q appear to have considerable influences upon the numerical value of Nusselt number. Importantly, a feature of all graphs is the point of intersection at which the lines cross regardless of the thermal load balance. Further values of Q were tested for completeness, these demonstrated that the point of intersection holds for all values of Q. This indicates the existence of a critical value of the wall thickness for which the Nusselt number becomes independent of the magnitude of the dimensionless surface heat flux, Q ratio.

6.5.3 Concentration field

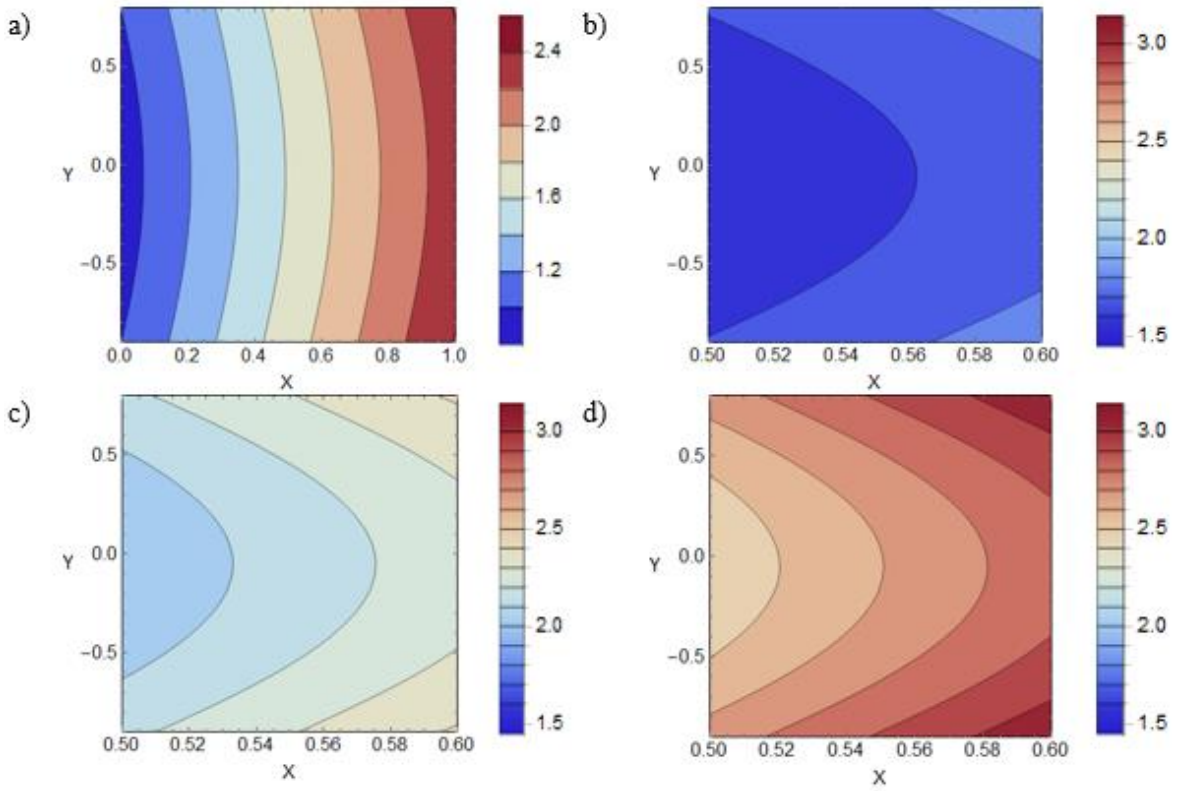

Figure 6-7 Dimensionless concentration contours for varying Damköhler number, $\boldsymbol{\gamma}$ a) showing the full microchannel for $\boldsymbol{\gamma = 0.3}$, b) mid-section of channel, for $\boldsymbol{\gamma = 0.3}$, c) mid-section for $\boldsymbol{\gamma = 0.5}$, and d) mid-section for $\boldsymbol{\gamma = 0.7}$.

The concentration contours along the full length of the microchannel are shown in Figure 6-7a and Figure 6-8a . Due to the high aspect ratio of the microchannel, a more representative visualisation of the concentration contours can be achieved by examining a segment of the microchannel (parts b, c, and d of Figure 6-7 and Figure 6-8). These figures show the advection of species along the length of the microchannel in the flow direction and the axial increase in the concentration due to reaction on the catalyst surfaces. Parts b, c, and d of Figure 6-7 show the effect of increasing Damköhler number on the concentration field.

Clearly, there is an increase in the magnitude and range of the concentration contours, which is indicative of an increase of concentration in the axial direction. This is an anticipated consequence of increasing Damköhler number, since it is directly related to the reaction rate on the catalyst surface. Close examination further reveals an increase in the magnitude and range of the concentration in the transverse direction. It is likely that this is also a result of the enhanced production of species on the catalytic surface coupled with the velocity of the flow causing a greater differential between the centre of the porous microchannel and the channel walls.

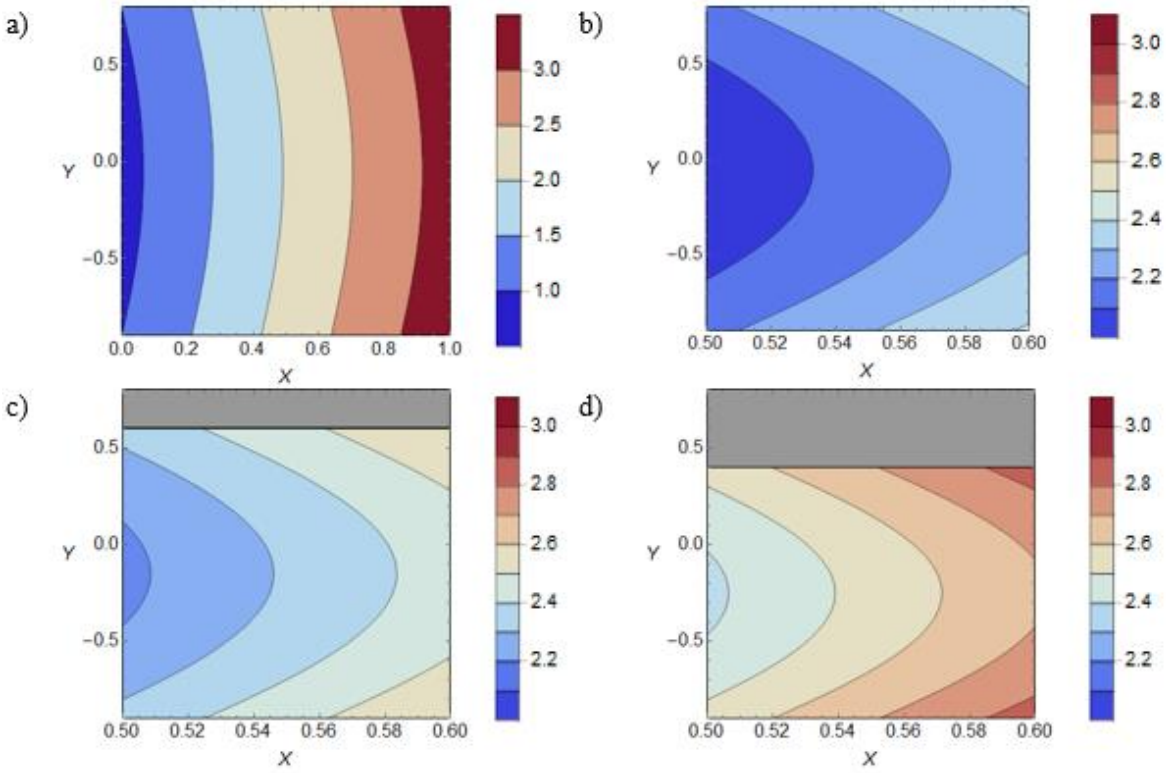

Figure 6-8 Dimensionless concentration contours for varying upper wall thickness, $\mathbf{Y_2}$ a) showing the full microchannel for $\mathbf{Y_2 = 0.8}$, b) mid-section of channel, for $\mathbf{Y_2 = 0.8}$, c) mid-section for $\mathbf{Y_2 = 0.6}$, and d) mid-section for $\mathbf{Y_2 = 0.4}$. The upper wall is coloured in grey to maintain the position of the central axis.

Investigating the effect of thickening of either the upper or the lower wall demonstrates the strong influences of the wall thickness upon the concentration field. Figures 8b to 8d show that increasing thickness of the upper wall can cause a significant increase in the magnitude of the concentration in the microchannel, The associated decrease in volume coupled with the same surface area of catalyst contribute to the observed increased concentration. Additionally, the increased temperatures under these conditions (Figure 6-4) augment mass transfer due to the Soret effect. For microreactor design, this is an important point to note. In the use of microreactors for chemical synthesis, the drive towards increased

yield is a key consideration. Thus, the methods by which the magnitude of the species concentration can be increased are desirable.

6.5.4 Sherwood number

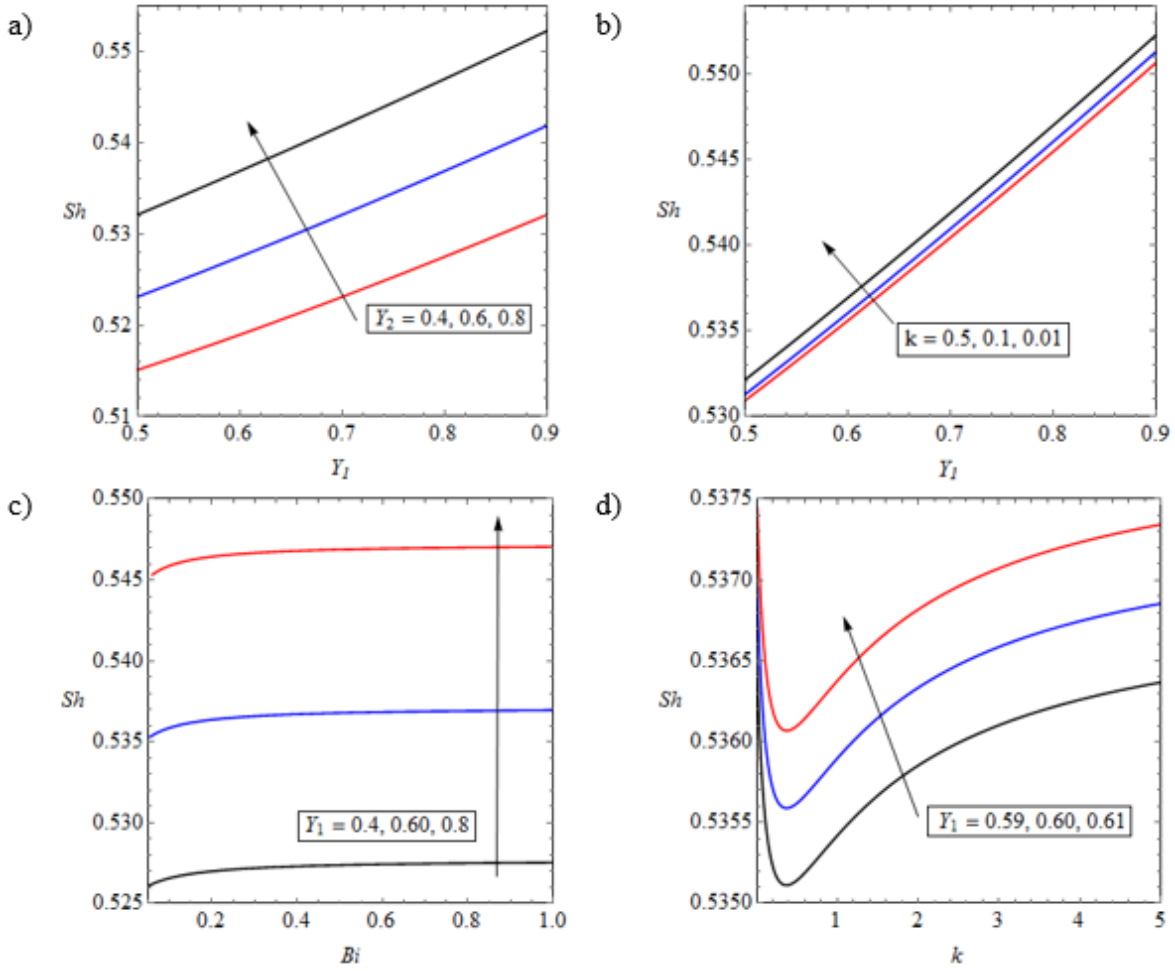

Figure 6-9 Variation in Sherwood number, $\boldsymbol{Sh}$ versus the a) lower wall thickness, $\mathbf{Y_1}$ for different values of upper wall thickness, $\mathbf{Y_2}$, b) lower wall thickness, $\mathbf{Y_1}$ for different values of thermal conductivity ratio, **k** , c) Biot Number,**Bi** for different values of lower wall thickness, $\mathbf{Y_1}$ and d) thermal conductivity ratio, **k** for different values of lower wall thickness, $\mathbf{Y_1}$.

The response of Sherwood number to variation in the microchannel thickness is shown in Figure 6-9a. Here it can be seen that as the microchannel height increases with respect to the wall thickness, there is a corresponding increase in Sherwood number. Increase of heat transfer at thinner walls strengthens the thermal diffusion of mass and enhances the mass transfer process. The graph is nearly a straight line and indicates a linear relationship. It is important to observe the fact that the Sherwood number is constant for a given microchannel thickness. This is best demonstrated by examining the Sherwood number for $Y_1 = 0.5$ and the line for $Y_2 = 0.8$ (which leads to a dimensionless microchannel thickness

of 1.3) and comparing with the Sherwood number for $Y_1 = 0.9$ and the line for $Y_2 = 0.4$ (which also has a dimensional microchannel thickness of 1.3). Clearly, these both have an equal Sherwood number. Evidenced by this is that the symmetry, or lack thereof, for any set of wall thicknesses is not as important as the microchannel thickness.

Thermal conductivity ratio, k also caused a linear increase of Sherwood number with the lower wall thickness, Y_1 as shown in Figure 6-9b. However, the increase in the value of thermal conductivity ratio renders a non-linear response, shown in Figure 6-9d. This behaviour is related to that observed in Figure 6-5, where Nusselt number was found to be much higher at low values of *k*. Higher rates of heat transfer enhances the Soret effect and magnifies the value of Sherwood number. The corresponding decrease in Sherwood number with increasing k is not monotonic, however. The initial rapid decrease between $k = 0.01$ to say, $k = 0.1$ is related to the definition of the thermal conductivity ratio. While this may seem the same as the difference between $k = 2.01$ and $k = 2.1$ it represents something different. At $k = 0.01$ the effective thermal conductivity of the fluid is 100 times smaller than that of the solid, whereas at $k = 0.1$ it is only ten times smaller, so there is a factor of ten difference in the effective thermal conductivity value of the fluid between $k = 0.01$ and $k = 0.1$. This is not the case for $k = 2.01$ and $k = 2.1$, in both cases the effective thermal conductivity of the fluid is about twice that of the solid. This is why there is a sudden drop then a comparatively slower increase. The reason for the turning point in the curve may be due to a balance point at which the value of k leads to a minimal thermal gradient and so the contributions from the Soret effect reach a minimum. This in turn would lead to a minimum in the Sherwood number.

Although not shown here, the relationship between the Damköhler number and the Sherwood number is essentially linear. Further, the Biot number (Figure 6-9c) generally has little effects upon the Sherwood number, except at very low Biot number, where the flow of thermal energy between the solid and fluid phases of the porous medium is greatly inhibited. The observed reduction of Sherwood number at low Biot number demonstrates that consideration should be given to LTNE effects in thermochemical, porous microreactors. It should be clarified that although the qualitative trends discussed here remain almost unchanged, altering the value of Soret number widens the range of changes in Sherwood number.

6.5.5 Local entropy generation

Figure 6-10 and Figure 6-11 represent an investigation of the local entropy generation. They contain six contour plots pertaining to the various terms of equations (6-288) to (6-296), enabling examination of the effects of changing one parameter on separate aspects of the microchannel. Since the entropy contribution from the solid walls is only dependent upon temperature within that particular wall, the entropy generation within the walls is not that enlightening and is therefore omitted. Both Figure 6-10a and Figure 6-10b show asymmetry consistent with the heat flux ratio of the system in which there is a greater heat flux at the upper wall than at the lower wall.

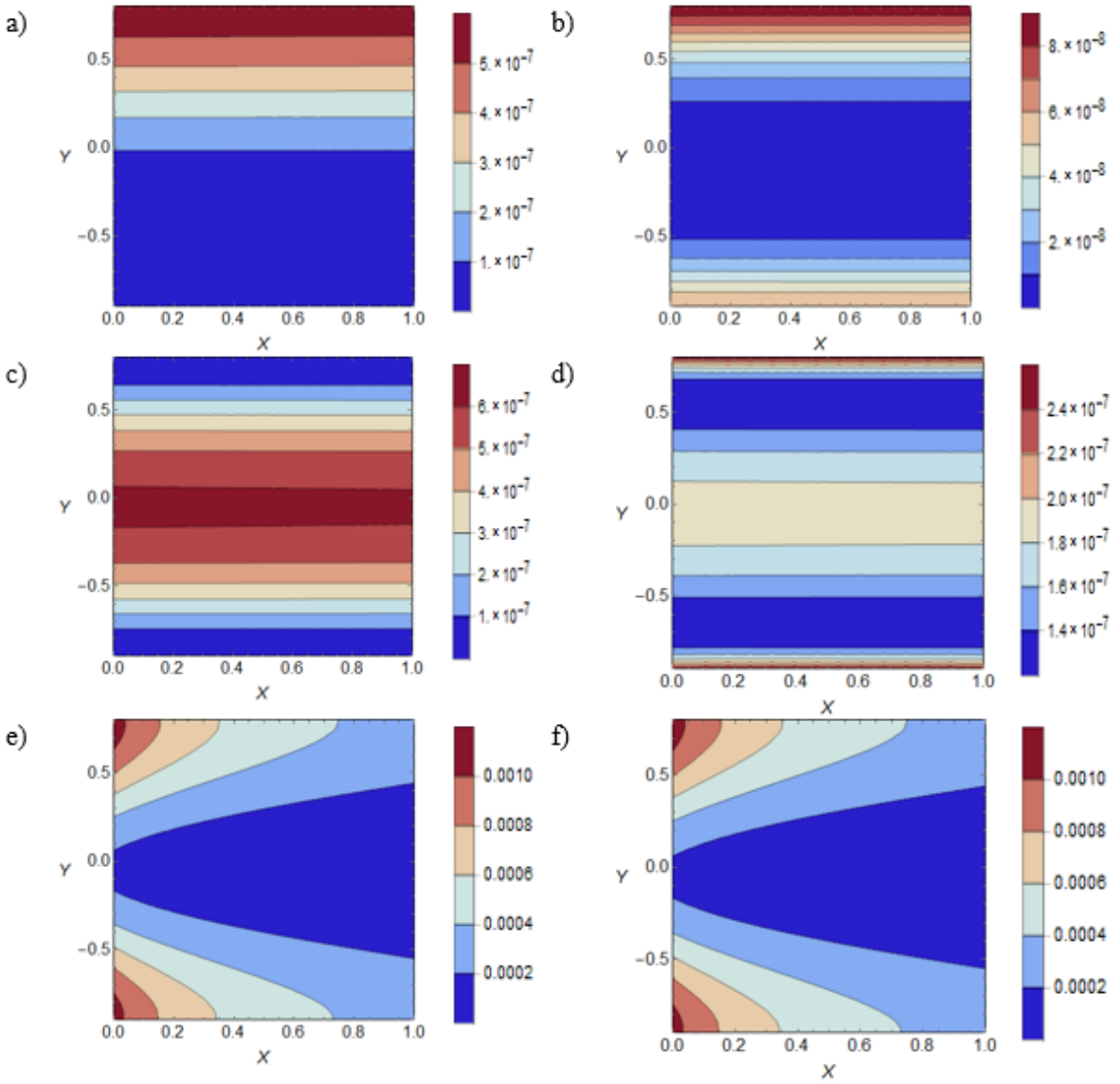

Figure 6-10 Local entropy generation contours for the base configuration showing a)$\mathbf{N_{s,ht}}$, b) $\mathbf{N_{f,ht}}$, c) $\mathbf{N_{int}}$, d)$\mathbf{N_{FF}}$, e) $\mathbf{N_{DI}}$ and f) $\mathbf{N_{PM}}$.

The contours of the entropy generation due to interstitial heat transfer suggest a greater generation of entropy from this source at the centre of the microchannel. This is entirely consistent with Figure 6-2 to Figure 6-5 where the temperature difference between the solid and fluid phases of the porous medium are larger towards the centre of the microchannel and decrease towards the walls. Entropy generation due to hydrodynamic effects, Figure 6-10d, shows that maximum values are encountered at the interface between the fluid and the walls due to the dominance of viscous effects in this vicinity. The irreversibility then decreases rapidly moving away from the wall before building to a moderate level in the centre of the microchannel where the velocity is maximum and thus increases the irreversibility. Entropy generation due to mass transfer is shown in Figure 6-10e, and as expected, the greater levels of irreversibility are to be found on the walls next to the catalytic surfaces. It is worthy of note that the magnitude of the mass transfer contribution is significantly greater than that of other sources. This leads to Figure 6-10f, which shows the combined local entropy generation by the porous insert is dominated by the mass transfer contribution. However, the dominance of mass transfer irreversibility can be overcome by increasing the heat flux or reducing Damköhler number [212].

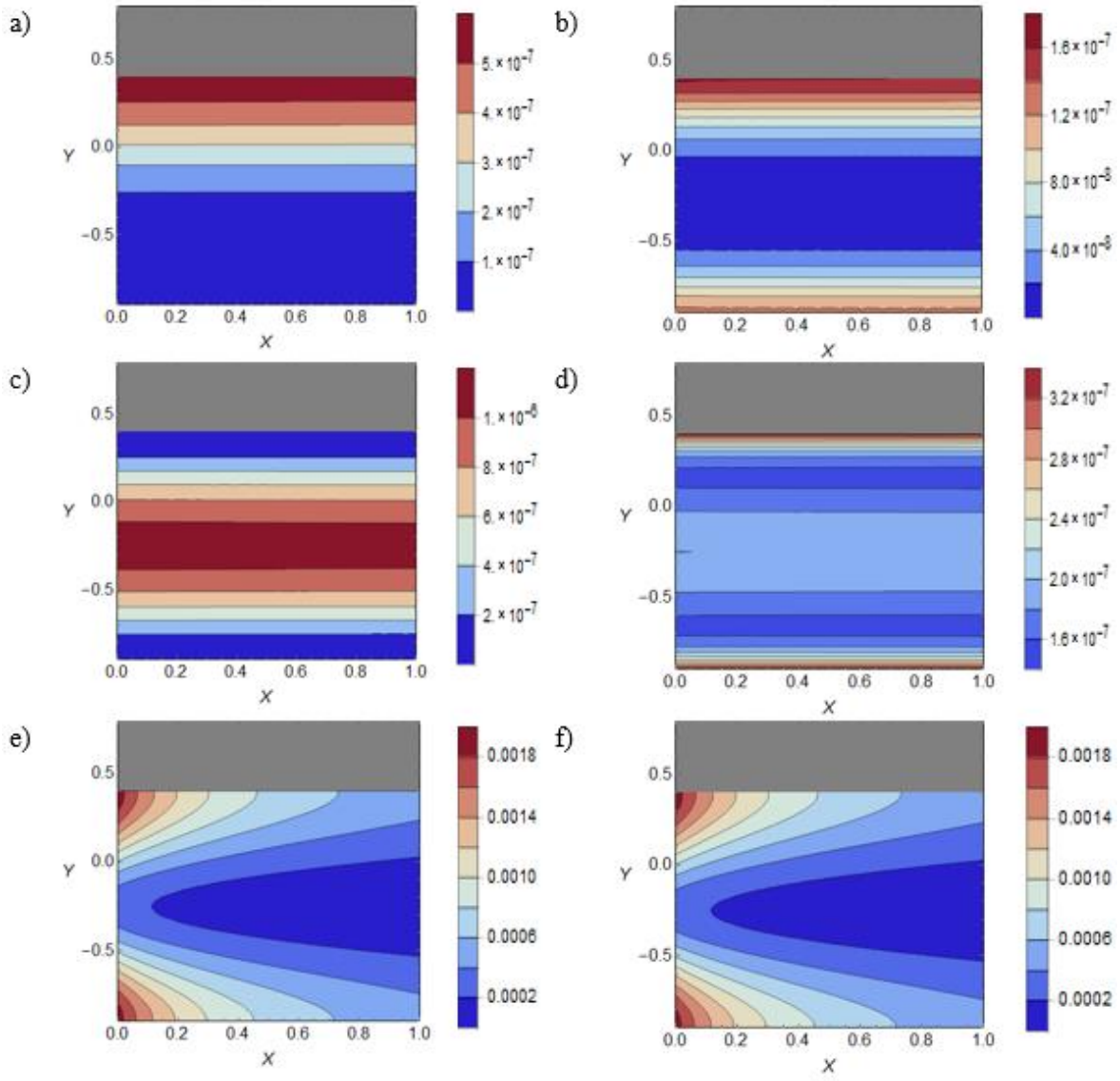

Figure 6-11 Local entropy generation contours for the upper wall thickness, $\mathbf{Y_2 = 0.4}$ showing a)$\mathbf{N_{s,ht}}$, b) $\mathbf{N_{f,ht}}$, c) $\mathbf{N_{int}}$, d)$\mathbf{N_{FF}}$, e) $\mathbf{N_{DI}}$ and f) $\mathbf{N_{PM}}$. The upper wall is coloured in grey to maintain the position of the central axis.

As shown in Figure 6-11, setting the wall thicknesses to be increasingly asymmetric increases the magnitude of the sources of irreversibility. The least affected by this is the solid phase of the porous medium. Other contributions show increases in magnitude of over 50%. The entropy generation due to fluid friction shows an increase in the thickness of the highly irreversible zone along the centreline of the porous insert. Narrowing of the microchannel thickness leading to enhanced velocities at the centre of the insert are the root cause of this effect. An increase in magnitude of the mass transfer irreversibility contribution is to be expected. This can be confirmed by examination of Figure 6-4 and Figure 6-8, which show the effects of increasing the asymmetry of the thick walls upon the temperature and concentration fields, respectively.

6.5.6 Total entropy generation

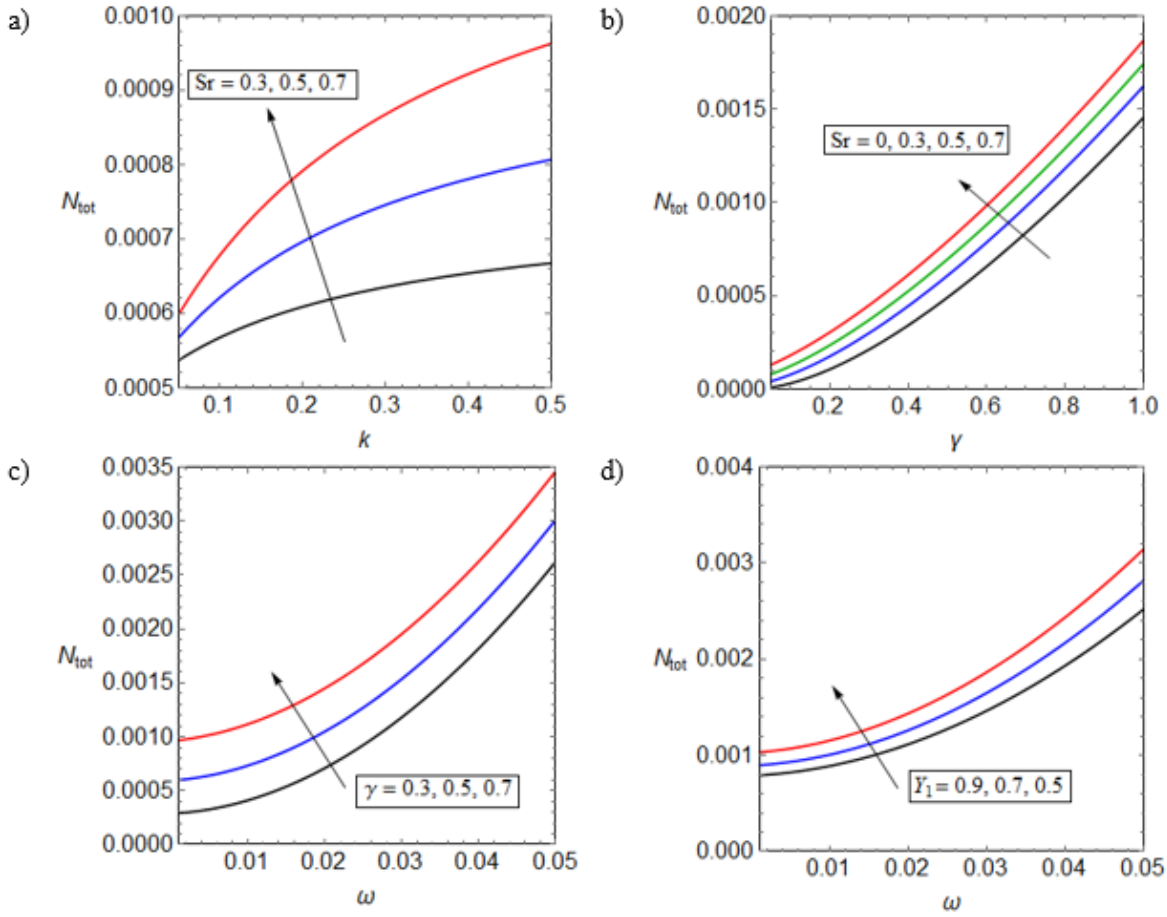

Figure 6-12 Total entropy generation for a) varying thermal conductivity ratio, **k** with different values of Soret number, **Sr** and b) varying Damköhler number, **γ** with different values of Soret number, **Sr**, and varying heat flux, **ω** with different values of c) Damköhler number, **γ** and d) for various values of $\mathbf{Y_1}$.

Calculation of the total entropy generation of the system includes adding all the sources examined above as well as those of the upper and lower walls as defined by equation (5-187). Varying the thermal conductivity ratio appears to have a strong influence upon the total entropy of the system. From Figure 6-12a, it is readily observed that this progression is non-linear in nature and has a more pronounced effect at lower thermal conductivity ratios. As already discussed, low values of thermal conductivity ratio can significantly enhance the rates of heat transfer and thus smoothen the temperature gradients in the system, which reduces the thermal irreversibility of the system. Magnifying the value of Soret number on this graph also result in an increase in the total entropy generation, the magnitude of this increase is most pronounced for higher values of thermal conductivity ratio. The low value of thermal conductivity ratio used as the default value for the previous sections of this study show very small differences and therefore an increased base value for the thermal conductivity was chosen for the purposes of clarity (see Table 6-3).

Figure 6-12b depicts the total rate of entropy generation against Damköhler number for several values of Soret number, illustrating the strong influence of Damköhler number upon the total irreversibility of the system. Higher rates of catalytic reaction at enhanced values of Damköhler number intensify the mass transfer rate and thus magnifies the associated irreversibility. This figure shows that for a given Damköhler number increasing the value of Soret number leads to an increase in the total entropy generation. Nonetheless, regardless of the value of Soret number the total irreversibility always increases monotonically against Damköhler number. Figure 6-12c and Figure 6-12d show variations of the total entropy generation with the dimensionless heat flux, ω. Clearly, increasing the exothermicity of the catalytic reaction, implied by the higher values of ω, strongly intensifies the total rate of entropy generation due to strengthening of the thermal irreversibilities. Increasing the value of Damköhler number (Figure 6-12c) and narrowing the microchannel (Figure 6-12d) further increase the total irreversibility, by promoting the mass transfer and thermal irreversibilities, respectively.

6.6 Conclusion

A two-dimensional, analytical local thermal non-equilibrium model of transport of heat and mass was developed for an asymmetric microreactor, accommodating an exothermic catalytic reaction. The thermal diffusion of mass was taken into account and thus mass transfer was coupled to the thermal fields. The catalyst was placed on the internal surface of the walls and therefore heat of reaction was released on a surface in contact with the solid wall, fluid phase and porous solid phase. Such situation is distinctively different to that of volumetric heat release investigated in the earlier studies, as it provides three different routes for heat diffusion, whilst currently there is no model to describe the heat transfer split amongst these. The issue was resolved by extending an existing phenomenological model of porous interfaces (Model A of Vafai and co-workers [91]). The validity of the extended model was demonstrated by comparing the analytically calculated temperature fields and Nusselt number with those predicted numerically in the limit of very large porosity (See Appendix B, Section 2).

Further, it was shown that the analytical solution could be systematically reduced to the theoretical works on simpler configurations. The extended interface model can be used in future theoretical and numerical studies of microreactors. Additionally, the developed close-form analytical solutions can serve as a means of validation for the relevant theoretical analyses. It was shown that asymmetry in heat transfer in the upper and lower parts of the

system (arising from the thermal and structural asymmetry of the microreactor) had a pronounced effect upon the temperature and concentration fields and that the system can significantly deviates from the local thermal equilibrium. In agreement with previous chapters, wall thickness was shown to be highly influential in the thermal and concentration field. Further, the thermal conductivity ratio also had a strong effect upon the temperature field and rate of heat transfer. The Nusselt number was found to have a singular point for a given wall thickness where any change in heat flux ratio would yield the same Nusselt number. This effect was found to exist on both the upper and lower walls. This singular point could be exploited to allow for greater thermal control of a microreactor.

Exothermicity of the reaction was found to promote the total irreversibility of the system in a monotonic manner. In addition, increasing Damköhler number appeared to have a strong intensifying effect on the total generation of entropy, while the effects of Soret number were less pronounced.

Chapter 7 The Interactions between hydrodynamics and catalytic activities

7.1 Introduction

The preceding chapters dealt with the heat and mass transfer properties of microreactors analytically. Having examined the effect that catalytic surface can have upon the microreactor channel properties, attention is turned to the effect that the microreactor geometry can have upon catalytic activity. The analytical models presented in Chapters 4-6 were limited to a one-way interaction between transport phenomena and catalytic activity. The following numerical studies will permit a two-way coupling between heat and mass ns processes and catalytic activity. Analytic solutions obtained were necessarily constrained by the assumptions inherent in their formulation. Numerical studies permit the relaxation of some of those assumptions and permit the study of flow fields in more complex geometrical configurations of microreactors. The small size of microreactors often complicates conduction of precise measurements and visualisation of fluid processes. Such difficulties are not pertinent to numerical methods, which can then be used to reveal the details of transport processes and the results obtained can aid understanding and design of microsystems [132]. To this end, the multi-cylinder model of Figure 7-1a) was examined followed by the simpler configurations of Figure 7-1b) and c). Comparisons were made to that of the straight channel shown in Figure 7-1d) with and it was ensured that the total catalytic surface remains constant with respect to that in Figure 7-1c) and d) respectively. To gain understanding of the interplays between thermal and hydrodynamic effects, the wavy channel geometries presented in Figure 7-3 were investigated. These geometries retained some of the hydrodynamic features of the multi- and single cylinder systems while not being encumbered with stagnation zones inherent to the cylinder-based systems. Examinations were made of flow structure in the form of streamlines to investigate the hydrodynamics. Once, again, the total catalytic surface in the wave microchannels shown in Figure 7-1(a-d) were maintained constant. In all figures, flow direction is from the left-hand side. Clearly, flow velocity is important to this investigation and in keeping with the assumption of laminar flow, low Reynolds number flows are applied. The Reynolds number, Re for this study is defined as;

$$Re = \frac{v\, D_H \rho}{\mu} \tag{7-299}$$

The hydraulic diameter, D_H defined as follows:

$$D_H = \frac{4A_X}{P_R}, \tag{7-300}$$

where A_X is the cross-sectional area and P_R is the wetted perimeter. Here, v is the velocity at the inlet (normal to the plane of the inlet and uniform). Lean fuel mixtures have less in the way of homogeneous reaction, so any combustion of such lean fuel-air mixtures is most likely to be surface catalytic. In keeping with this a fuel lean air mixture with an equivalence ratio, $\phi = 3.5$ was chosen. For this reason, the density, ρ of the gaseous mixture is, to close approximation, that of air. The available sites on the platinum catalyst are predominantly taken up by oxygen at low temperatures [153] and so the inlet gas temperature was taken to be 600K to reduce temperature gradients. Above a critical temperature of 800K, oxygen desorbs in sufficient quantity so as to allow a significant amount of methane to adsorb onto the surface, permitting the reaction to proceed apace [153]. Thus, the constant wall temperature of 1000K is applied. Due to the highly fuel lean nature of the gas mixture, the dynamic viscosity, μ of air at 600K is a reasonable approximation.

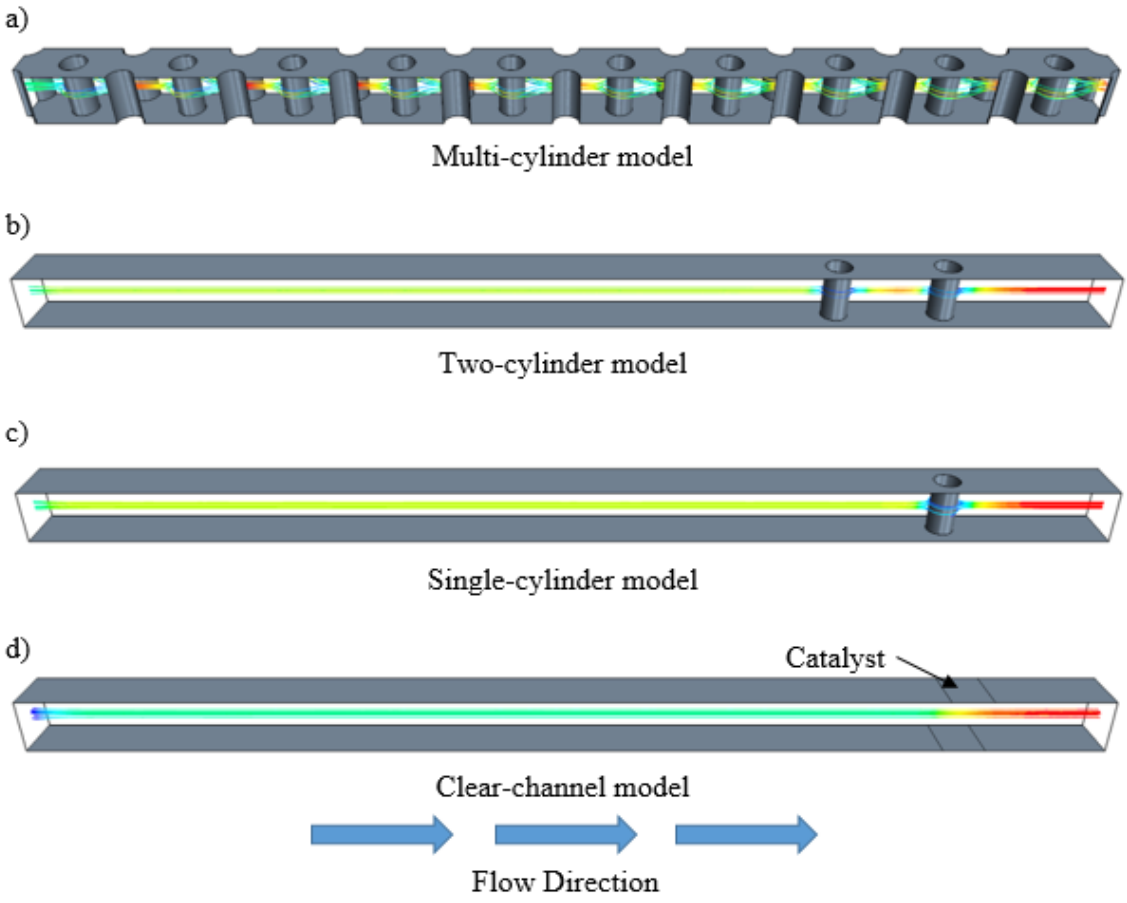

Figure 7-1 Geometry of cylinder models used with representative streamlines showing flow; a) multi-cylinder model, b) Two-cylinder model, c) Single-cylinder model and d) Clear-channel model showing catalyst area.

The number of cells in the computational regime varied with the configuration. For the OoP (Figure 7-3b) case 4 grid densities were examined, 86438 cells, 113955 cells, 163324 cells, and 311417 cells. These are presented in the form of the graph shown in Figure 7-2. To determine the effect of the mesh upon the results the metric of CO2 mass fraction at the catalyst end plane was chosen as this is of key interest in this study. The coarsest of these grids demonstrated reasonable results, but short of the desired accuracy. Both the 113955 and the 163324 grids demonstrated excellent results. The 311417-cell grid only revealed a 0.2% variance to that of the 163324 grid in terms of the chosen metric. As such, the 163324 grid was chosen as a good balance in terms of computational demands while retaining excellent accuracy for the measurements required.

To address possible concerns regarding the use of a laminar model for these configurations, all tests were additionally conducted using a low Reynolds number turbulent model [168]. Since the standard k-ε model is gives good results for high wall cell y^+ values of 30 and above, it does not resolve the viscous sublayer sufficiently accurately. To this end the Standard Two-Layer k-ε and Standard Low-Reynolds number models were developed. Both of these models benefit for an all-y^+ treatment, with the Low Reynolds number also having a low y^+ treatment available. These models have been successfully employed specifically for catalytic surface reaction modelling purposes [151,213] and have been used for this comparison. The results were replicated to within 1% of the values for mass fraction of species and all behaviours observed were reproduced.

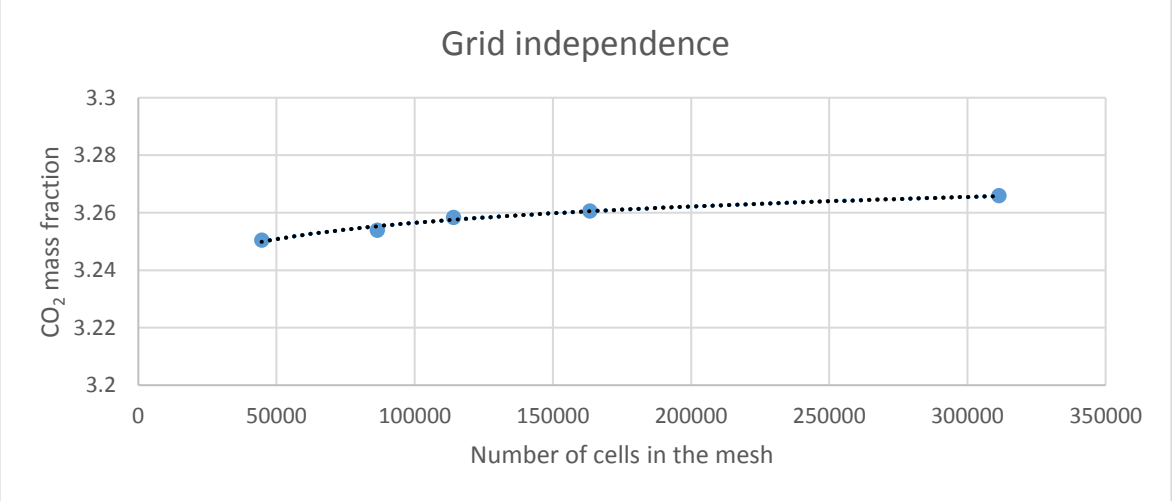

Figure 7-2 Grid independence graph

In order to avoid added complexities due to interactions between the surface reaction and homogeneous reaction mechanisms that might result in obscuring features of interest,

the heterogeneous catalytic mechanism only was examined. This mechanism was originally developed to predict the ignition and steady state combustion of methane over a platinum catalyst [133] and is highly regarded which makes it a very good fit for this investigation. Another possible area, which may obscure the effects of interest in this study, stems from temperature variations and their effects on both gaseous properties and catalytic activity. Such issues are avoided simply by applying a constant temperature boundary condition at the walls. This serves to ensure that any variation in catalytic activity is not due to temperature changes at the surface, thus removing this possible source of error. Similarly, the effect of this is to retain only very small variations in temperature within the channel and so minimise variation of the gaseous physical properties. Geometric complexities are systematically removed from the models in a coherent manner to reveal the hydrodynamic interactions of interest without obfuscating them with other effects. Initially a model containing multiple cylindrical bluff bodies is examined (see Figure 7-1a). The cylinders themselves interact with each other through their impact on the flow field. To minimise this and gain access to information regarding the extent of this interaction, single and two-cylinder models are studied (see Figure 7-1b and c). This includes an investigation into the properties of the catalytic output concerning upstream and downstream facing catalytic surfaces. Following on from this the bluff bodies are removed entirely from the channel such that effects due to wall/cylinder interaction such as stagnation zones are likewise removed. The final phase of the study focused on channels with corrugated surfaces and the variation in the phase of the waves between upper and lower surfaces. This leads to the three models shown in Figure 7-3 in which the upper and lower walls are either in phase, IP (Figure 7-3a), fully out of phase, OoP (Figure 7-3b) or partially out of phase, P1 (Figure 7-3c). It is worth noting that a further partially out of phase geometry can be created by a phase shift in the opposite direction; however this simply leads to the same geometry with the upper and lower walls inverted. Since that makes both of these partially out of phase geometries functionally identical, only one is shown here and considerations for the other are simply the mirror image of that shown. Each model (IP, OoP, and P1) consist of six wavelengths, the first five of which are catalytically active.

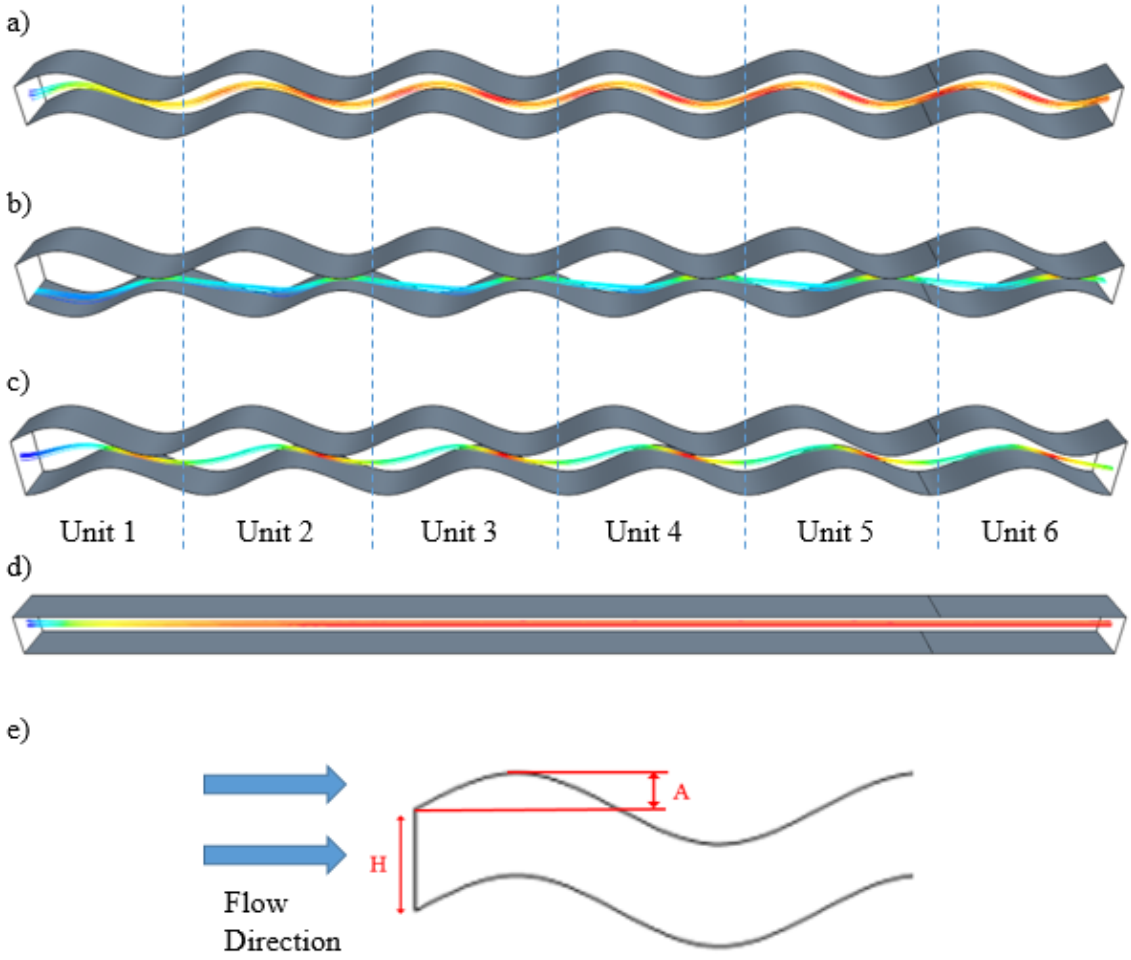

Figure 7-3 Geometry of wavy channels featuring representative streamlines; a) In phase channel, b) Out of phase channel, c) Phase 1 channel, d) clear channel, and illustration of amplitude, A and inlet height, H.

Each wavelength of the configuration will henceforth be described as a 'unit' for descriptive simplicity. These are shown by the dashed lines in Figure 7-3. The purpose of the sixth unit is to maintain hydrodynamic conditions and permit the measurement of product mass fractions at the end of the catalytically active zone, reducing errors from recirculation effects.

7.2 Validation

Due to the complexity of the geometries under examination in this study, the use of OH-LIF or Raman spectroscopy to investigate the boundary layer next to the catalyst an available option. The cylinders themselves in all the cylindrical configurations used prevent use of such techniques and the waved surface models lack have surfaces that do not lie in-plane and so similarly preclude use of these techniques. As such, validation must be achieved against studies that have already been validated against experimental results. In this study, but heat and mass transfer play important roles and so must be separately verified.

7.2.1 Thermal field validation

The validation of the thermal field is made against the work of Bahaidarah et al. [214]. These authors investigated both heat and momentum transfer in waved channels. Two models were used, one an arc-shaped model and the other a sinusoidal model. Of interest for validation purposes is the sinusoidal channel and the thermal properties.

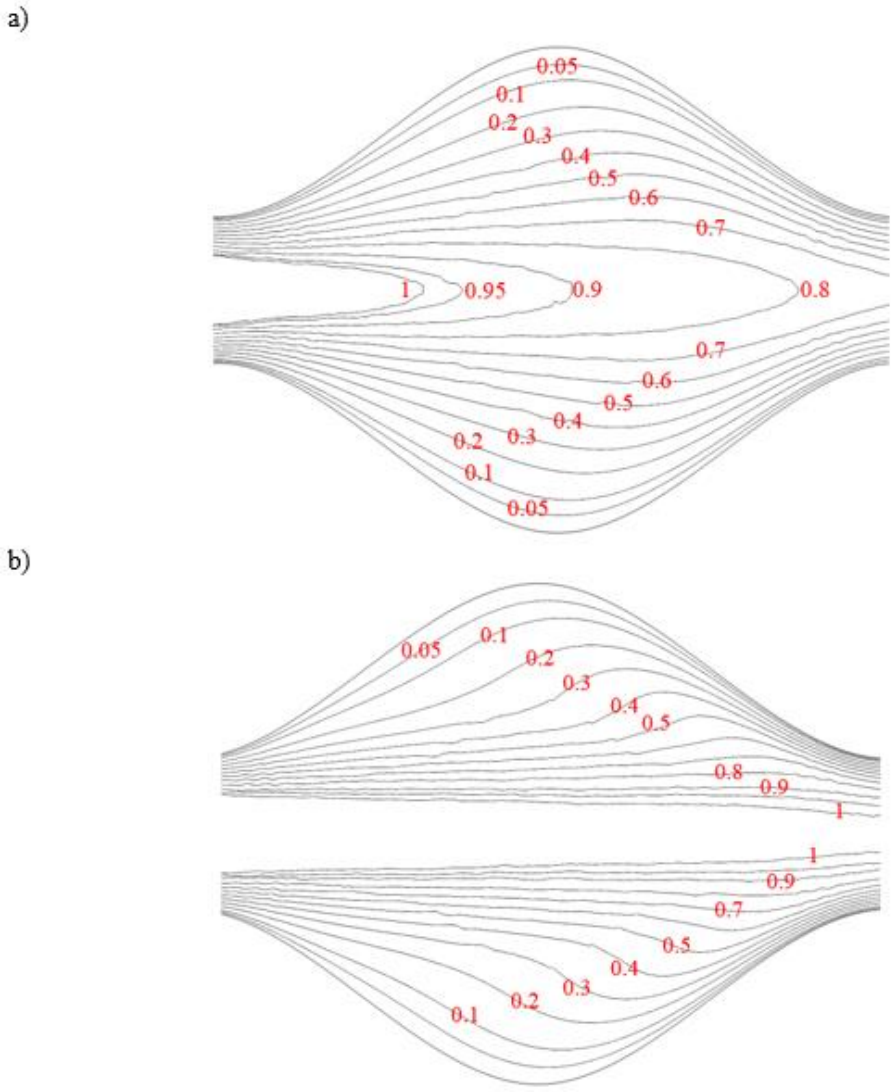

Figure 7-4 Isotherms for the fourth module with $H_{min}/H_{max}=0.3$ and $L/a=8$ for a) $\boldsymbol{Re}$ = 100 and b) $\boldsymbol{Re}$ = 400.

To this end the geometry chosen was that with $H_{min}/H_{max}=0.3$ and $L/a=8$, since this is the closest match to the geometry used herein. Where H_{min} is the minimum height of the channel, H_{max} is the maximum height of the channel, and L/a is the ratio of the wavelength to the amplitude of the sinusoidal waveform of the channel walls. When comparing Figure 7-4a) and b) to figure 8c and 8e respectively of Bahaidarah et al. [214], it is clear that an excellent match is obtained. The normalised isotherms for both the Re =100 and Re =400

coincide with those achieved by Bahaidarah et al. [214] for both these cases. This serves to demonstrate that the thermal modelling of this current study is yielding very good results.

7.2.2 Surface chemistry validation

Validation of the surface chemical model used in this study is achieved by comparison to the work of Deutschmann et al. [153]. The choice of the investigation by Deutschmann et al. for validation purposes is due to its concentration on the surface chemistry and deliberate omission of gas phase reactions in a manner similar to the study presented here. The comparison for validation is made against the steady state single channel simulations performed by these authors using a two dimensional axisymmetric model. Following the authors, a single cylinder of channel length 5 cm and diameter 0.18 cm at initial temperature 300 K and 1 bar pressure was created. Into this was fed a lean mixture of 4% volume methane, 6% volume hydrogen in air at 0.8 ms^{-1} also at 300 K. This permitted the reproduction of the temperature, methane, carbon dioxide and carbon monoxide profiles presented in figure 8 of paper by Deutschmann et al. [153]. The results of this validation are presented in Figure 7-5. In keeping with the work of Deutschmann et al., the radial coordinate has also been enlarged and only the inlet region shown. The aspect ratio has been adjusted so as to match that used in figure 8 of Deutschmann et al. for comparative purposes. Clearly, the results are in excellent agreement with that of Deutschmann et al.

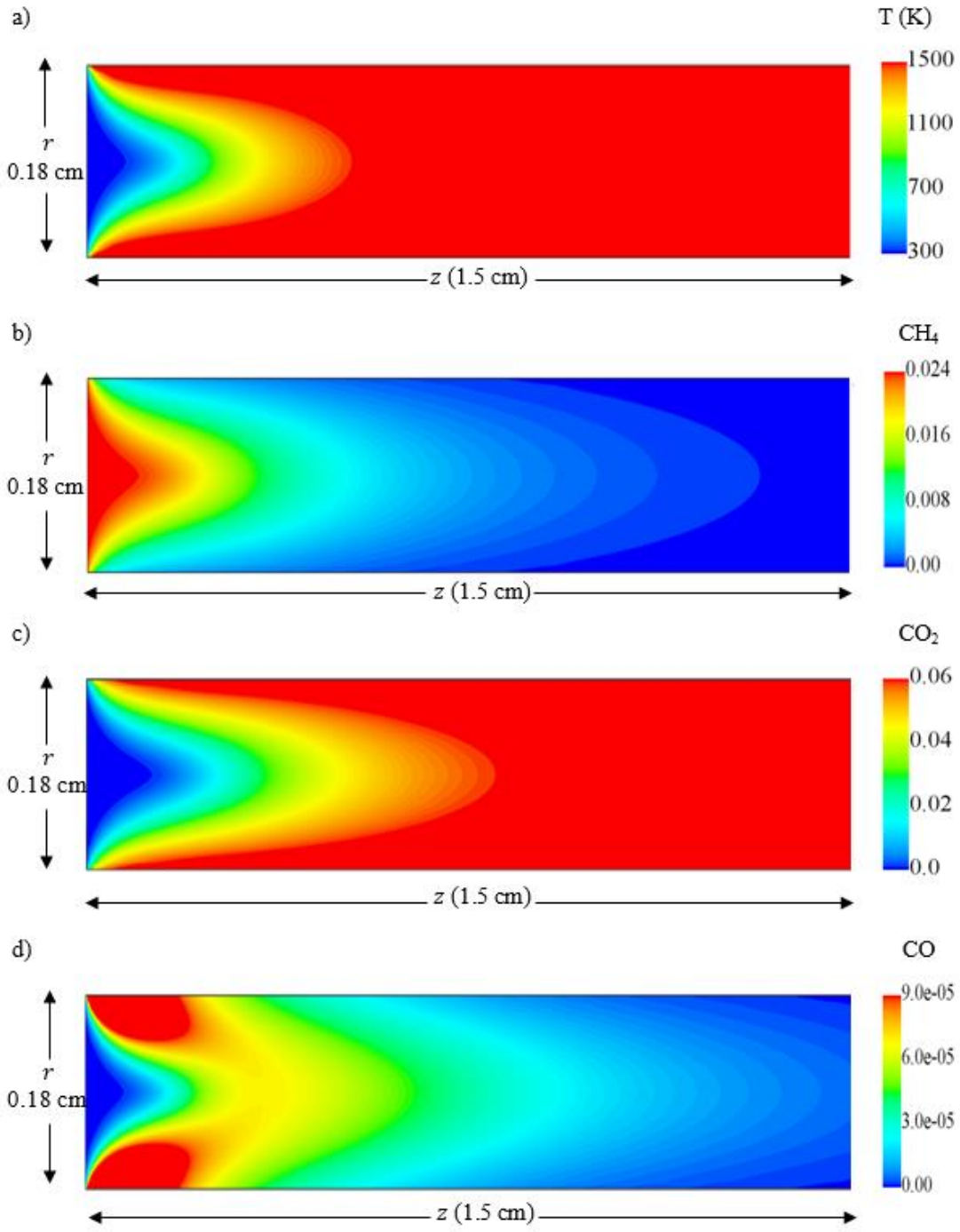

Figure 7-5 Calculated profiles using 4 vol.% CH_4 and 6 vol.% H_2 in air for a) Temperature, b) mass fraction CH_4, c) mass fraction CO_2, and d) mass fraction CO. For comparison, the radial coordinate, ***r*** has been enlarged and only the entrance region is shown.

7.3 Multi-cylinder Model

The first model examined is that of the multi-cylinder model (see Figure 7-1a). This model uses a series of cylindrical bluff bodies to examine flow through a porous medium constructed of such cylinders between two parallel plates. For this configuration, a mesh of 443761 cells was used with an fuel lean inlet equivalence ratio, $\phi = 3.5$. The overall geometry was construct of 10 units, each with a cylindrical pore at the centre, and a quarter of a cylinder at each corner. Each unit is 2mm long, giving an overall length of 2cm for the model. The height of the channel defining the separation of the parallel plates is 1mm and the diameter of the cylinders is 0.5mm. Solid walls made up the upper and lower boundaries, whereas the front and back vertical boundaries used a symmetry condition to represent a continuous series of such cylinders ad infinitum.

Table 7-1 Outlet mass fractions of carbon dioxide (x 10^{-2})

	Re = 50	Re = 150	Re = 250
Walls	7.7765	6.9194	6.1510
Cylinders	7.4370	6.6792	6.2846
All	7.5663	6.8351	6.5825

During the examination of this configuration a series of Reynolds numbers were studied in conjunction with various catalytic coating options. The outlet mass fraction of carbon dioxide as a major product was used as a measure of overall catalytic activity. The results of this are summarised in Table 7-1. The three catalytic coatings cases were Walls: upper and lower walls only coated with catalyst, Cylinders: cylinder surfaces only coated in catalyst and All: both upper and lower walls, and cylinder surfaces coated in catalyst. It is worthy of note at this juncture that the surface area of the combined upper and lower walls is only 2.32% greater than that of the cylinders combined. In keeping with previous results [141], the general trend of decreasing conversion with higher velocities is observed. At low Reynolds number, the relationship between the Walls and Cylinder cases is consistent with their respective surface areas. However, as the high inlet velocities, the Cylinders case outperformed that of the Walls. This suggests that at higher velocities the mass diffusion

effects may be inhibiting the catalytic activity at the surfaces for the Walls case to a greater extent than that of the Cylinders case. The most notable observation from this series of results is that, even though the catalytic surface area for the All case is almost double that of either of the other two cases, the conversion in no way reflects that. In fact, at Reynolds numbers of 50 and 150, the All case showed lower conversion than that of the Walls alone. Only in the higher velocity case did the All case exceed both other cases in terms of carbon dioxide mass fraction and even then, only by a small percentage. The implication of this is that there is more than just surface area influencing the conversion, suggesting that hydrodynamic and thermal effects may be involved. Since this configuration is inherently complex with regards to hydrodynamic and thermal effects, simpler configurations were conceived with a view to gaining a better picture.

7.4 Single and two cylinder models

In order to simplify the system and get a clearer picture of the hydrodynamics, the number of cylinders in the model was reduced to two or fewer (see Figure 7-1b and c). By way of comparison, another configuration was created, the No Cylinder model, where a portion is the upper and lower walls in an otherwise clear parallel plate channel was catalytically active (see Figure 7-1d). The surface area of this active zone was controlled to be equal to the two and one cylinder models as necessary and was placed the same distance from the inlet as the cylinders. Furthermore, the cylinder surfaces created such that the option was available to have only the front (inlet facing) or rear (outlet facing) half catalytically active.

Table 7-2 Outlet mass fractions of carbon dioxide (x 10^{-4})

	Re = 5	Re = 15	Re = 50
No Cylinder	79.029	28.271	8.7522
Single Cylinder	80.649	28.863	9.0600
Two Cylinders	150.53	56.218	17.726
Half Cylinder	42.173	14.770	4.7000
Two Half Cylinders	81.260	28.899	9.0516

Again examining mass fractions of carbon dioxide at the outlet (see Table 7-2) it can be seen that when compared to the No Cylinder model, the Single Cylinder model outperforms at all Reynolds numbers tested. The increase varied with Reynolds number such that at Reynolds number of 5 a 2.1% increase was observed. As the Reynolds number rose to 50, the increase became more notable at 3.5%. Addition of a second cylinder, though doubling the surface area of catalyst in the system does not double the mass fraction of carbon dioxide at outlet at any of the Reynolds numbers examined (Table 7-2). However, as the Reynolds number increases the carbon dioxide mass fraction approaches double the value of the Single Cylinder model. So, the activity of one (or both) of the cylinders in the Two Cylinder model is being decreased. This raises the question as to if certain portions of the cylindrical surface are more active than others. To examine this, the Half Cylinder model was created to examine the effect of having only the rear (outlet) facing side of the cylinder catalytically active. Curiously, by halving the catalytic surface area in this manner, the outlet mass fraction is not halved. It is in fact 5% great than the expected value at Re = 5 and Re = 50, though only 3% at Re = 15. Similarly by adding a second half-coated cylinder, an increase of 8% over the half value for the Two Cylinder model is obtained at Re = 5, for example. In terms of surface area, this model has the same as the Single Cylinder model. However, at low Reynolds number, it shows a small increase in outlet mass fraction against the Single Cylinder model. Thus, it behoves examination of the variance of activity between the front and rear of the catalytic cylinders.

To this end, Figure 7-6 shows the mass fraction of carbon dioxide on a surface region defined at 10^{-5}m out from the Single Cylinders catalytic surface. This permits a view of how the mass fraction of carbon dioxide varies close to the catalytic surface of the cylinder. The most striking feature is the marked difference between front and rear of the cylinder in both cases. It is also worthy of note that the variance in mass fraction of methane is the inverse of that of carbon dioxide as shown in Figure 7-6. The distribution in mass fraction on the cylindrical region is that in the front facing section there is little in the way of carbon dioxide and hence more methane (see Figure 7-7). This is to be expected as the front section is facing the inlet from which the methane is arriving at the catalyst. Examination of Figure 7-6b) and d) show that the area of lowest carbon dioxide concentration vary in both size and magnitude with respect to Reynolds number. This demonstrates that a proportionally larger region of the front face has very low carbon dioxide mass fraction in the Re = 50 case as compared to the Re =15 case. As mentioned, this implies that there is proportionally more methane in this region and as such the Re = 50 is more catalytically active. Turning attention to Figure 7-6a) and b), it can be seen that at the rear of the cylindrical region, significantly

more of the surface has high concentrations of carbon dioxide in the Re = 15 case. Again, this leads to there being less methane able to be converted and thus decreases the catalytic activity in that zone. Further, in the Re = 15 case, the high carbon dioxide (low methane) zone at the rear extends from the base of the cylinder to the top of the cylinder, with marginally more concentrated zones where the cylinder meets the walls (Figure 7-6a). However, in the higher Reynolds number case, the high carbon dioxide concentration zones at the rear are limited to those parts of the cylinder that are close to the walls (Figure 7-6c).

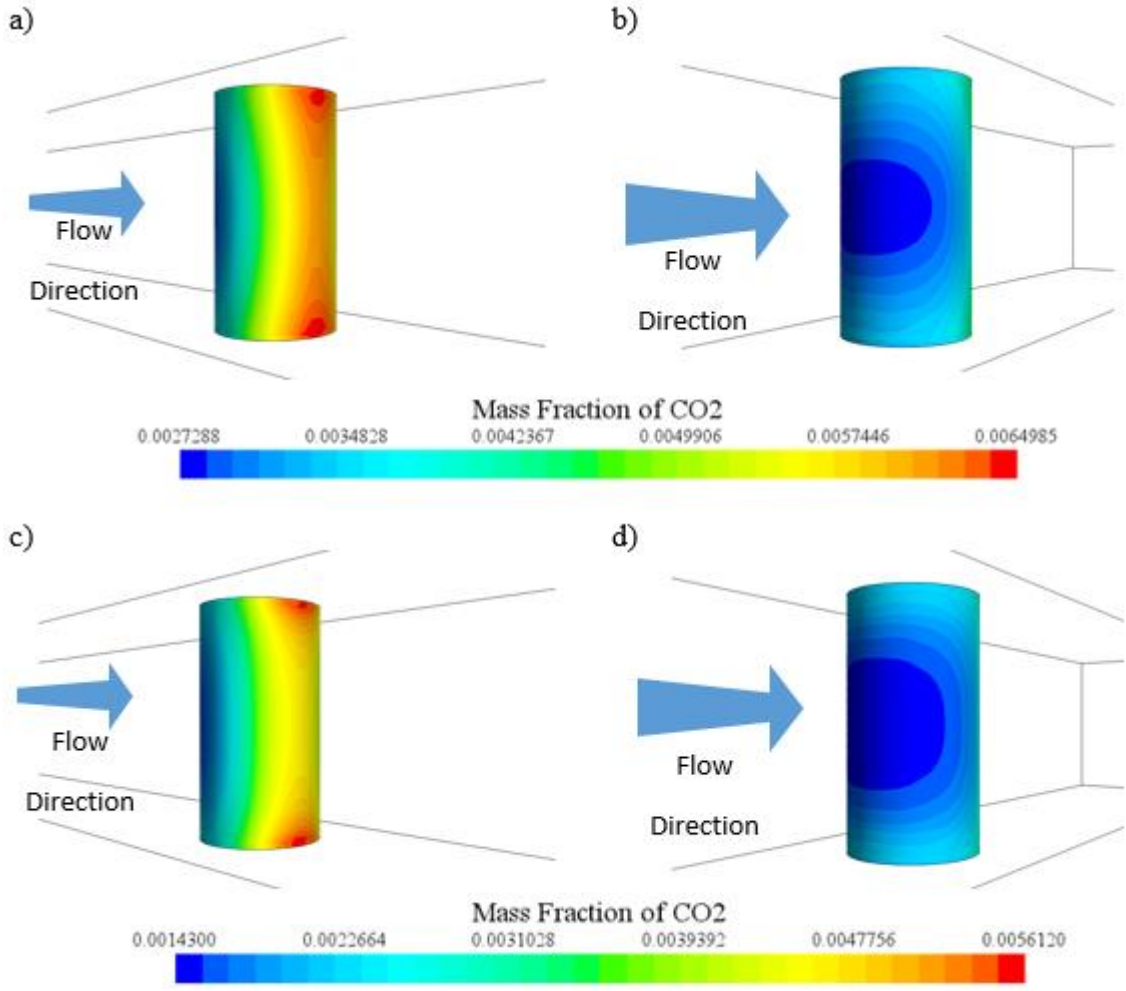

Figure 7-6 Cylindrical region surrounding the single cylinder for showing the mass fraction of CO_2 at; a) $\boldsymbol{Re}$ = 15 rear of cylinder, b) $\boldsymbol{Re}$ = 15 front of cylinder, c) $\boldsymbol{Re}$ = 50 rear of cylinder, and d) $\boldsymbol{Re}$ = 50 front of cylinder.

The hydrodynamics that bring this situation about are the subject of Figure 7-8. Here, 10 streamlines are seeded within a radius of 10^{-4}m of a point towards the base of the front (inlet side) of the cylinder in the Single Cylinder model. Figure 7-8a) shows the velocity streamlines for the case where Re = 5 and as might be expected the flow is very simple with low velocity zones near the walls and cylinder surface. In Figure 7-8b), the velocity

streamlines are shown for the case corresponding to the concentration surface shown in Figure 7-6a) and b), ie. Re = 15. In this diagram, the low velocity streamlines arriving close to the wall at the front of the cylinder curve round the cylinder and almost immediately double back and up the cylinder surface at the rear. An analogous series of streamlines are produced if the streamlines are seeded near the upper wall instead of the lower. This leads to a low velocity zone spanning the full height of the cylinder. Since the velocity here is all very low, the fluid remains in contact with the cylinder for longer time and the proportion of carbon dioxide to methane increases as more methane is converted. This methane then stays in the vicinity of the cylinder for a greater time due again to low velocities in the region and so the concentration of methane available to the catalytic surface of the cylinder in this zone is lessened.

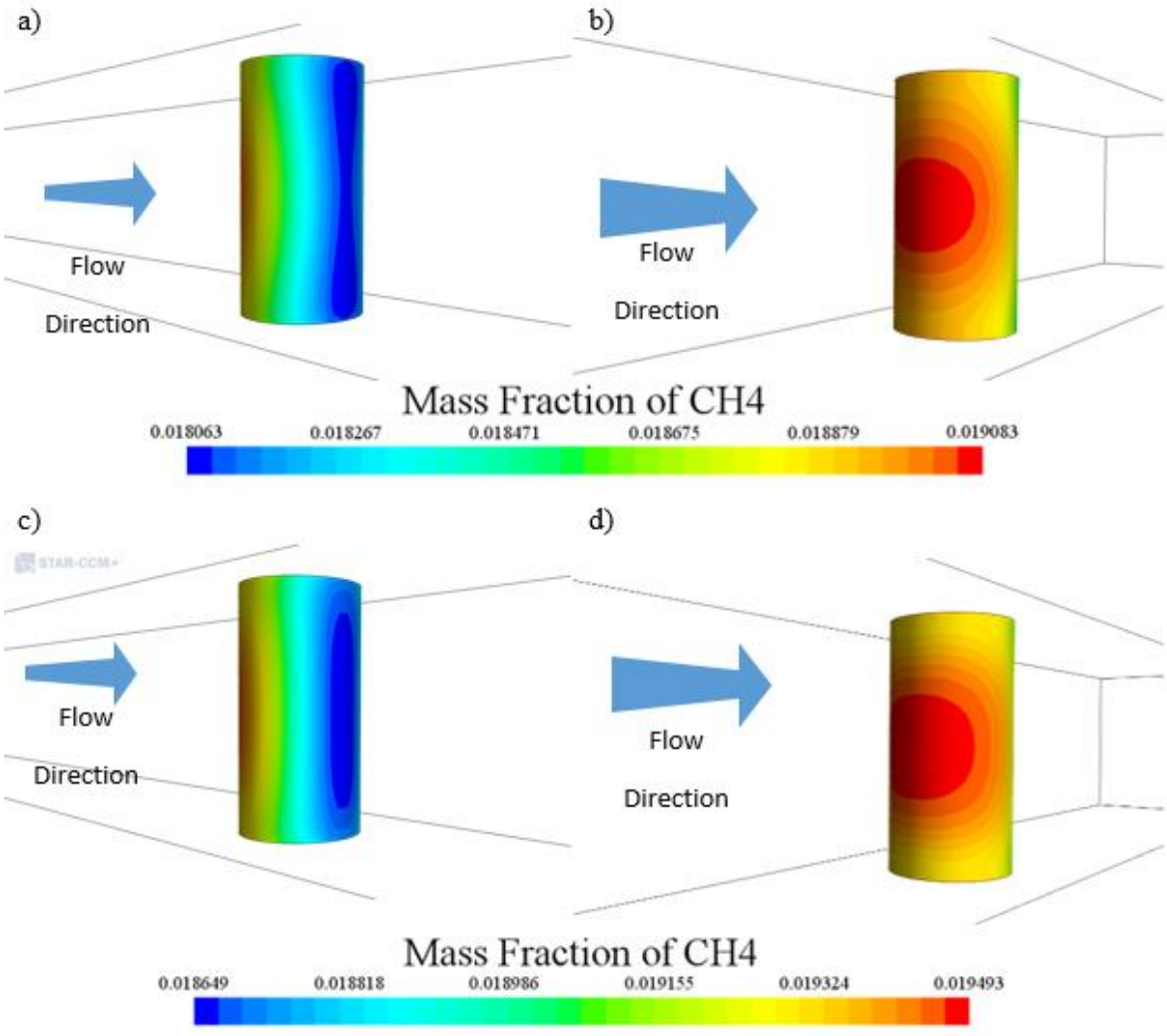

Figure 7-7 Cylindrical region surrounding the single cylinder for showing the mass fraction of CH_4 at; a) Re = 15 rear of cylinder, b) Re = 15 front of cylinder, c) Re = 50 rear of cylinder, and d) Re = 50 front of cylinder.

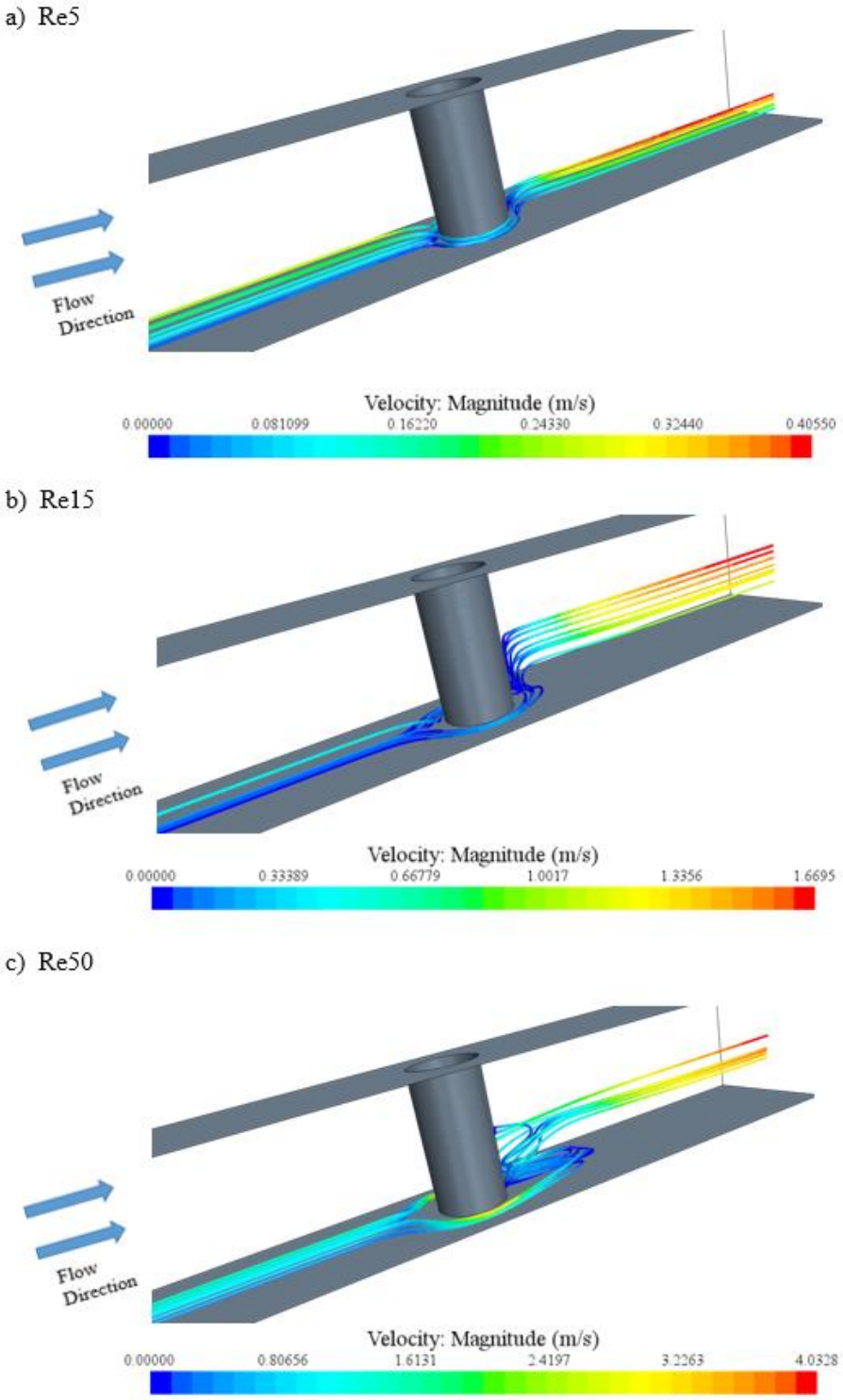

Figure 7-8 Streamlines showing the velocity magnitude for the Single Cylinder model at; a) $\boldsymbol{Re}$ = 5, b) $\boldsymbol{Re}$ = 15, and c) $\boldsymbol{Re}$ = 50.

This gives rise effect described above whereby the high carbon dioxide region shown in Figure 7-6a) runs from wall to wall along the cylinders full height. The streamlines for the Re = 50 system are considerably more complex. However, it can be seen that within the rotation of the flow that the velocities moving away from the wall and up towards the centre of the channel are significantly higher than for the Re = 15 case. This leads to more mixing

and transport of the products away from the cylinder surface, permitting the active sites access to more methane and thus increasing activity. Furthermore, the only low velocity zones are seen low down the cylinder and near to the wall at the rear. Here the effect described for the Re = 15 case again takes effect, but in a much smaller zone. This is borne out by the small zones of high carbon dioxide concentration near the walls in Figure 7-6c) as described previously.

It can be seen by comparison between Figure 7-7a, and Figure 7-8b that the low CH_4 concentration zone in the Re = 15 case extends the full length of the cylinder, in keeping with the streamline for that case. For the Re = 50 case (Figure 7-7c) a different picture emerges, the low CH_4 zone does not extend to the upper and lower walls. Correspondingly, there is a significant flow feature recirculating the flow visible in the streamlines of Figure 7-8c. Here the reaction process is undergoing a reflux like effect whereby unreacted reactants are being returned to the surface to undergo reaction again. This leads to the increased reactant concentration shown in the Re = 50 case along the channel centreline of the rear of the cylinder as compared to that closer to the walls. Correspondingly, the recycled reactant is able to increase the amount of product generated in this zone, which is further confirmed by looking at the increased product mass fraction shown in this same zone in Figure 7-6c.

At the front of the cylinder, the velocity is greatest at the centre of the channel and as such the reactants have a lower residence time in the vicinity of the catalyst. Nearer the walls, however, the velocity slows considerably, this leads to an increase in residence time and as such an increase in generation of product. This is seen for all Reynolds numbers shown. So nearer the walls, there is less reactant and more product near the cylinder since the reactants are being consumed and thereby generating the products.

7.5 Wavy channel models

By creating channels with conditions that replicate zones with flow conditions, but without the added complication created by bluff-body/wall interaction, as described in section 7.3 similar effects can be observed. To this end the configurations shown in Figure 7-3 were created with the amplitude, A as shown in Figure 7-3e) set to 35% of the channel height, H. Streamlines seeded in the low velocity zone of the OP model at Re = 100 in the 5th unit show the velocity variance in the flow, as shown in Figure 7-9b).

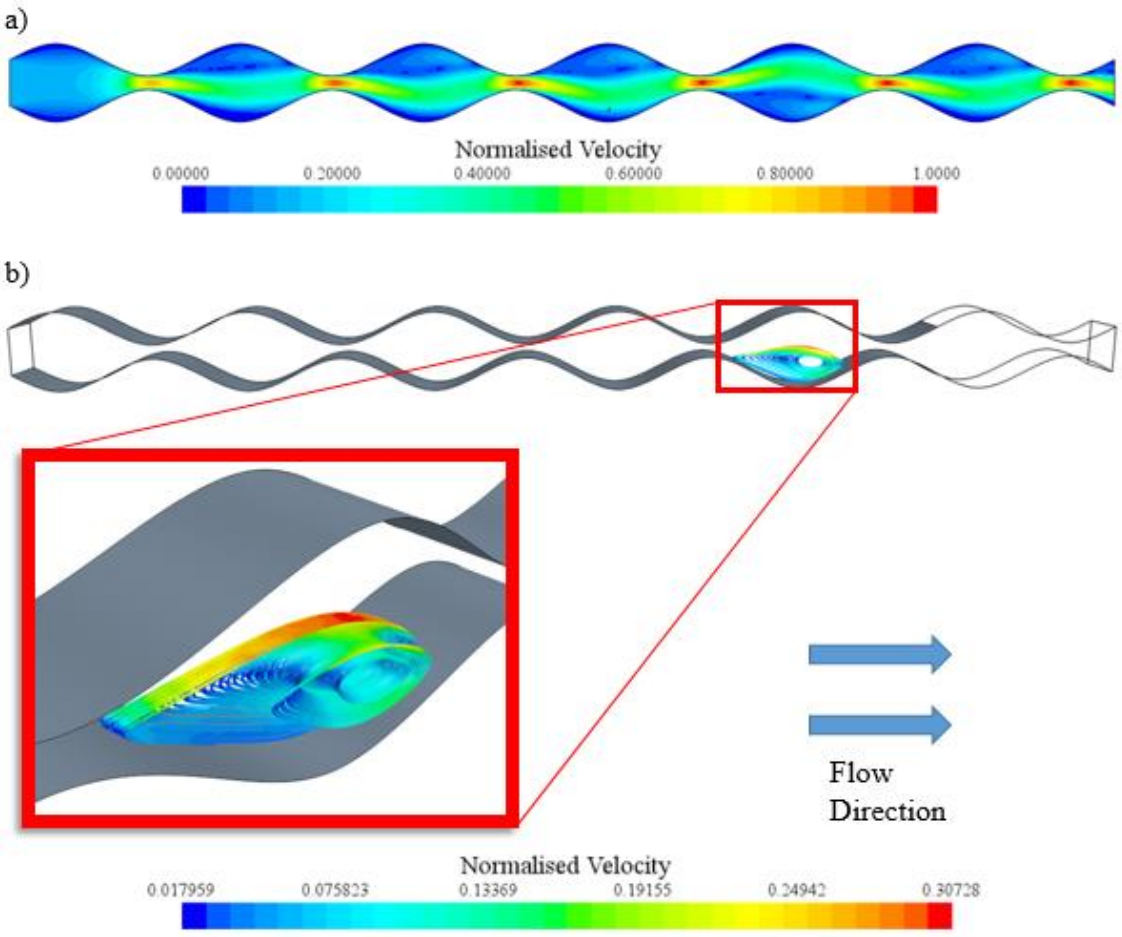

Figure 7-9 Normalised velocity in out of phase model for $\boldsymbol{Re}$ = 100 showing catalytic surface in grey; a) Normalised velocity field in a vertical section along the centre of the channel and b) normalised velocity profile in streamlines in the fifth trough of the channel.

This clearly varies in the z direction as well as the x and y, and would not have been picked up had a two-dimensional simulation been conducted. It also demonstrates the rotation within the flow field that recirculates the product rich (and thereby reactant lean) fluid into the main flow zone and resupply the catalyst with fuel. By examining both parts of Figure 7-9, it is clear that there are two distinct regions to the recirculating flow. Firstly, that on the inlet side, which is very low velocity close to the catalytic surface and very high velocity

towards the centre of the channel. Secondly, as the catalyst surface in the unit rises from the trough, the velocity close to the catalyst surface rises considerably. It is the first of these zones which correspond very closely to the high CO_2 mass fraction zones in Figure 7-10b. Similar flows can be seen in the upper waved surface of units 2 to 4 and correspond to the regions of low velocity flow in Figure 7-9a). Though not shown here to remain concise, smaller features of this kind are observed in the P1 model also, the positions of which are in the low velocity zones shown in Figure 7-13b) which correspond to the high CO_2 mass fraction zones shown in Figure 7-10c). The feature is most prominent in flows of Re = 100 and Re = 150 for both the OoP and P1 models, it is clearly not observed in the Re = 50 models for either case.

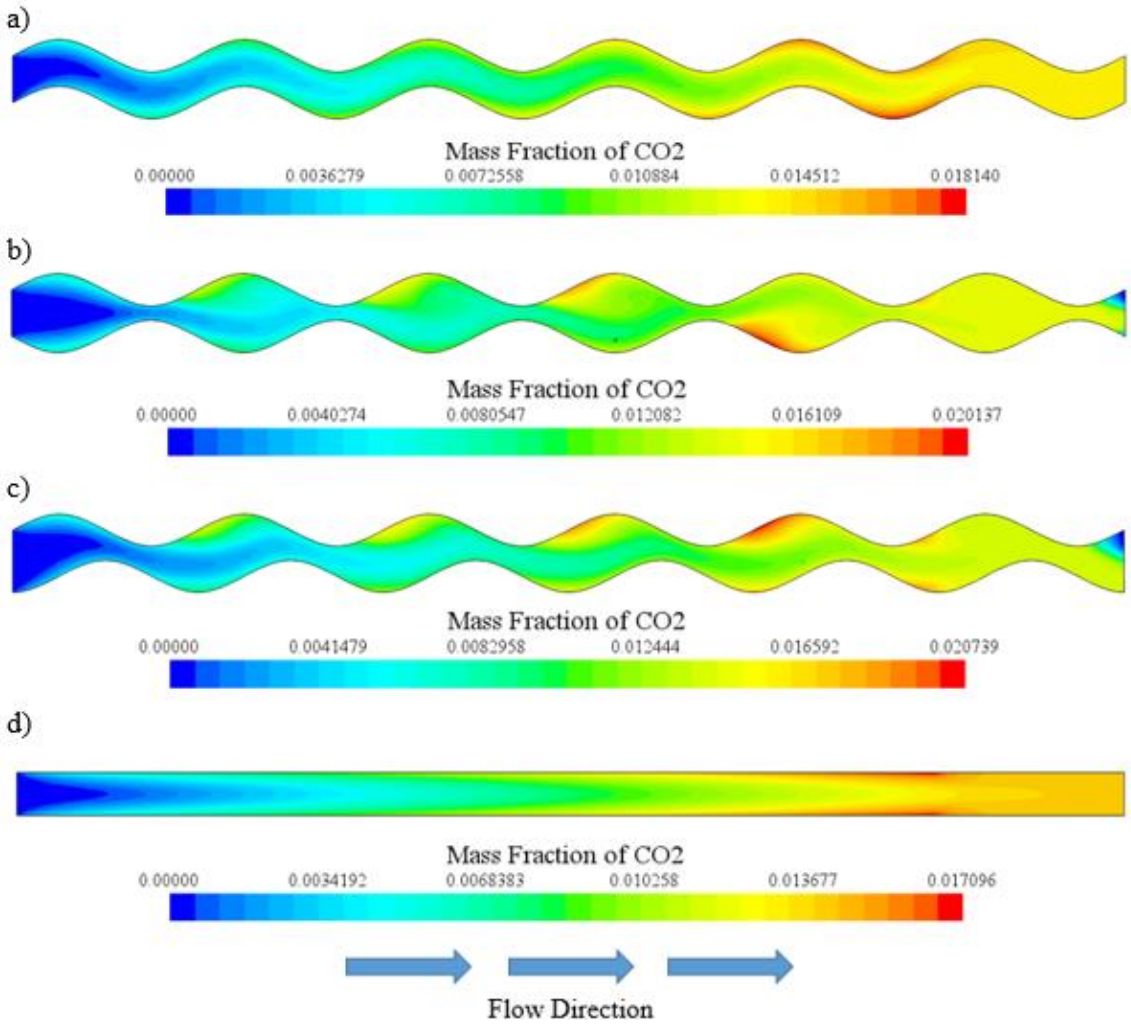

Figure 7-10 Mass fraction of CO_2 along a vertical section in the centre of the channel for at $\boldsymbol{Re}$ =150; a) IP model, b) OoP model, c) P1 model, and d) Clear channel model.

Corresponding to these zones of rotation are high carbon dioxide mass fractions which are clearly visible in Figure 7-10b) and c).Though not completely absent, considerably smaller pockets of higher carbon dioxide concentration can be found in the troughs of the IP model as shown in Figure 7-10a). The steady and constant build-up of carbon dioxide along

the length of the clear channel is seen in Figure 7-10d). For the purposes of outlet mass fraction of carbon dioxide in the manner of the multi-, single-, and two-pore models, such measurements were taken instead at a vertical plane at the end of the catalytically active surface. The reason for this can plainly be seen in Figure 7-10b) and c) where, due to the rotational flow, there is some reversed flow at the outlet itself. As such, the risk of this feature polluting the results must be avoided, hence the choice of a plane sufficiently far from the outlet was chosen for comparison purposes.

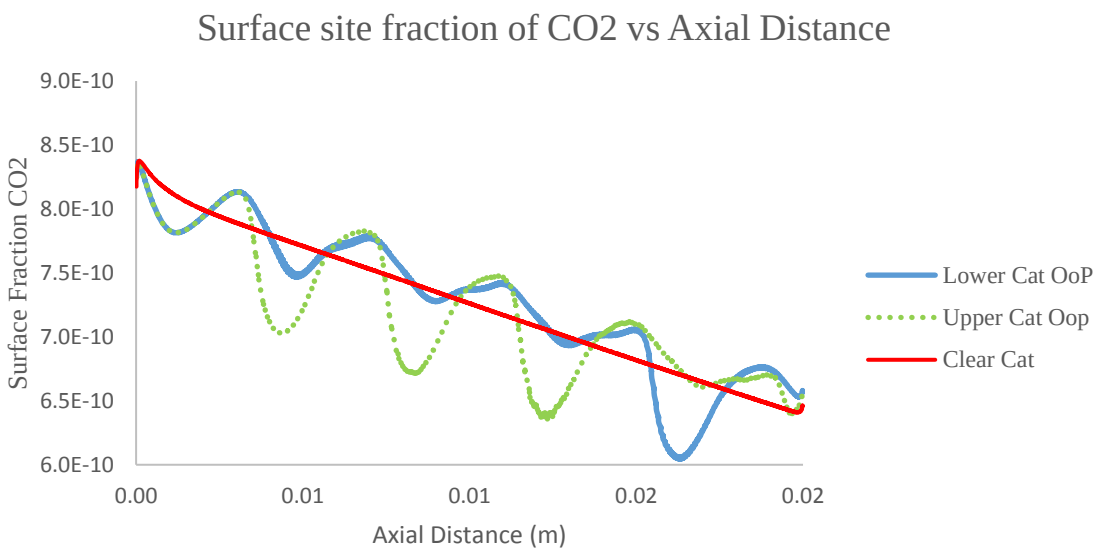

Figure 7-11 Surface site fraction of CO_2 as a function of axial distance for the OoP model with the clear channel values for comparison at $\boldsymbol{Re}$ = 150.

By way of comparison, Figure 7-11 shows the surface site fraction of carbon dioxide along the OoP model, with the clear channel values added for reference. Due to the nature of the geometry of the models, all the wavy channels are of the same length in the axial direction, but the clear channel is longer. This is due to the fact that the clear channel catalytic surface is compose entirely in the axial direction whereas the wavy channels also vary in the transverse direction. To allow for comparisons to be made between all the channels, the clear channel was scaled to the channel length of the wavy channels. Several features of interest present themselves in Figure 7-11, first is the constant decrease in surface fraction of carbon dioxide observed in the clear channel values. It should also be noted that for the clear channel there is no difference between the upper and lower catalytic surface values. Though the upper and lower catalytic surfaces (Upper and Lower Cat respectively) vary along the length of the channel, there is a consistent downward trend. The second point of interest in Figure 7-11 is the way that, after the values begin to diverge from one another, the Upper Cat features three large troughs then one small one, and the Lower Cat has three small troughs then one larger one. These features correspond to the high carbon dioxide regions in Figure 7-10b). Which

in turn correspond to the rotational low velocity zone features shown in Figure 7-12b). The surface site fractions of all the other species showed similar wavelike patterns corresponding to the positions of the aforementioned features. The CO_2 site fractions were chosen for illustrative purposes only and any of the other species site fractions would have been equally representative and demonstrated the same trends.

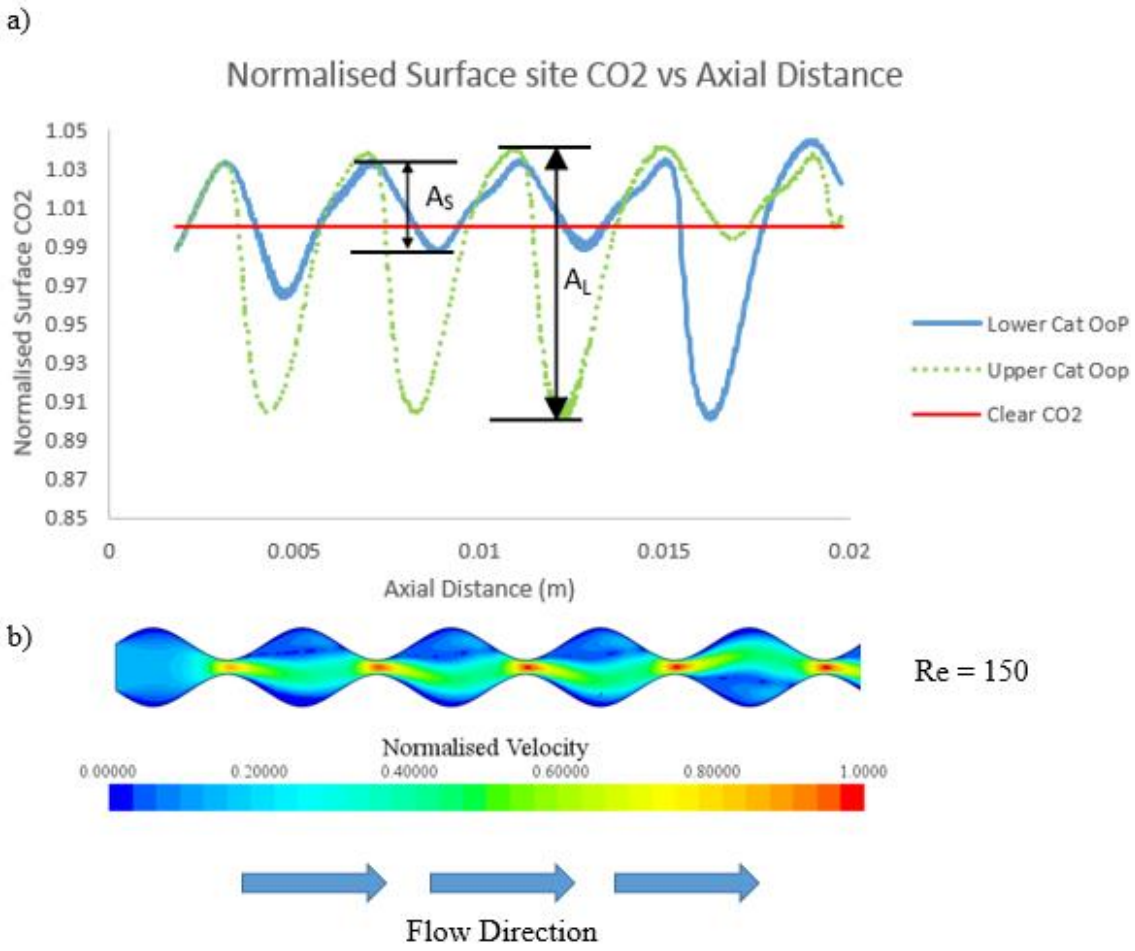

Figure 7-12 Graph of Normalised surface site CO_2 vs Axial Distance of OoP channel, with vertical section of channel for comparison.

To further the study, the values for the site surface fraction of carbon dioxide were normalised with respect to the clear channel values, which constituted a baseline. Due to the different node positions between the clear channel and the channel of interest for a particular figure, the clear channel values were replaced values calculated using a line of best fit. As can be seen in Figure 7-11, the clear channel values are essentially linear. The best-fit line was produced between 0.0018m and 0.0198m, to avoid inlet and catalyst end effects, has an R^2 value of 0.9998 (including all data the R^2 value is 0.996). For the OP case, two waveforms with distinct amplitudes, one small, A_S and another large, A_L of surface site fraction of CO_2 can be identified in Figure 7-12a). For the purposes of this investigation, the catalytic zone of the channels only is examined. When compared to the velocity profile in Figure 7-12b) it

is clear that the larger amplitude waveform corresponds to the larger low velocity zones in the upper portion of the channel for the first 3 wavelengths, then the lower in the final wavelength. Waveform A_S, on the other hand coincides with the smaller low velocity zones and is predominantly representative of areas where the site surface fraction is greater than that of the clear channel case. On the other hand, A_L exhibits site surface CO_2 values considerably lower in comparison to the clear channel case. It becomes especially clear when comparing Figure 7-12a) to Figure 7-10b) that the troughs of A_L correspond to the high CO_2 mass fraction areas.

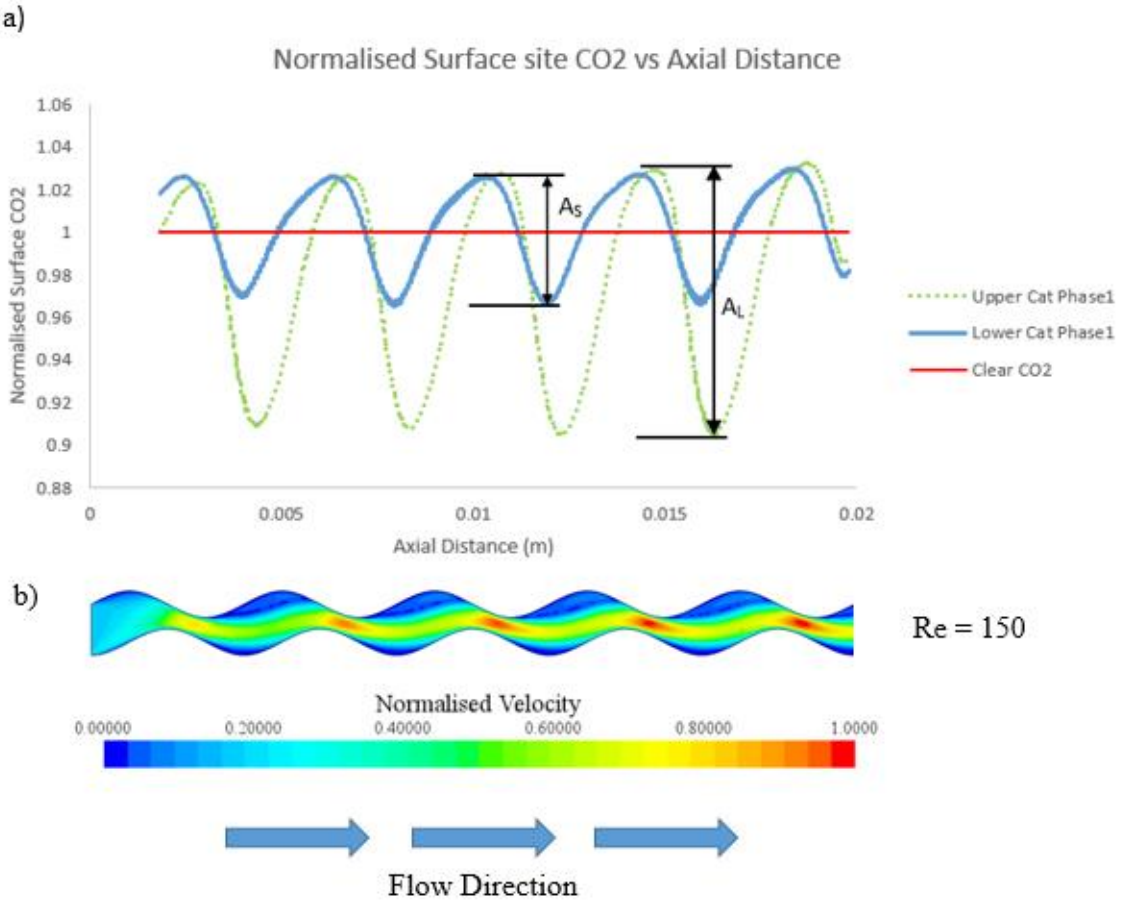

Figure 7-13 Graph of Normalised surface site CO_2 vs Axial Distance of P1 channel, with vertical section of channel for comparison.

A similar picture is formed when the P1 case is considered, Figure 7-13. Here, again, the low velocity zones area formed in two sizes, one larger and the other smaller. The smaller of the zones is of comparable size to that of the smaller zones in the OoP case and results in a variance with the clear channel values of 3% consistently. The larger zones are slightly smaller than those of the OoP case and are associated with a drop of about 9% with respect to the clear channel. This is as compared to a drop of about 11% for the larger zones in the

OoP case. Comparison with Figure 7-10c) show again that these sections of low CO_2 surface site fraction correspond to the areas of high CO_2 mass fraction.

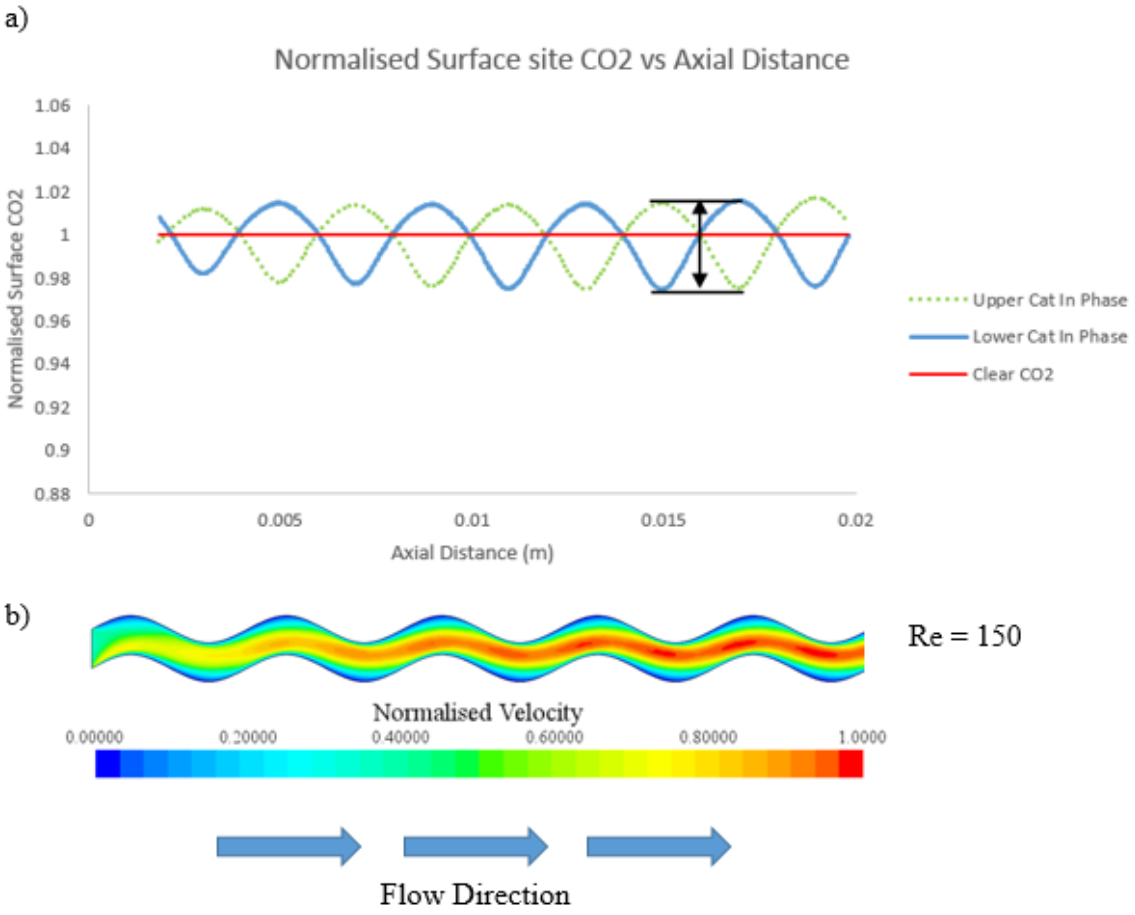

Figure 7-14 Graph of Normalised surface site CO_2 vs Axial Distance of IP channel, with vertical section of channel for comparison.

The symmetric nature of the waveforms in Figure 7-14a) are somewhat unsurprising given the velocity field shown in Figure 7-14b). The low velocity zones shown in Figure 7-14b) again correspond to the areas where the site surface fraction of CO_2 drops below that of the clear channel. This time, however, all such zones are of the same magnitude and as such the resultant graph shows that the upper and lower catalyst have the same waveform with a phase shift. These zones are also very much smaller than that of both the OoP or the IP models and the resulting variance from the clear channel values is correspondingly smaller whether it is a relative increase or decrease. Unsurprisingly at this point, these zones again correspond to the zones in Figure 7-10a) where there is elevated mass fraction of CO_2.

Table 7-3 Outlet mass fractions of carbon dioxide (x 10^{-2})

	Re = 50	Re = 100	Re = 150
Clear Channel	3.2739	1.9656	1.3946
OoP	3.2392	1.9494	1.3924
IP	3.2715	1.9629	1.3921
P1	3.2519	1.9466	1.3846

Measurements for mass fraction of CO_2 taken at the catalyst end show the effect the rotational flow has on the catalytic activity in Table 7-3. For Re = 50 the main hydrodynamic effect observed is jetting which reduces the amount of CO_2 product obtained by 1.2%. In the OoP and P1 case, this is especially prevalent, whereas in the IP case, the flow is almost identical to that of the clear channel. This drop is partially mitigated when the flow feature shown in Figure 7-9b) develops at Re = 100 dropping the deficit to about 0.9% in the OoP case and about 1% in the P1 case. Further increase in the inlet velocity to Re = 150 closes the gap for the OoP case to being on a par with the IP case. For the P1 case, the deficit is also further reduced. The larger magnitude of the feature in the OoP case makes for greater reduction in the deficit than in the P1 case.

7.6 Conclusion

The effect of hydrodynamics on catalytic activity was examined using several geometric configurations. The multi-cylinder model demonstrated that through changing whether the catalytic surface was chosen to be the walls or the cylinders themselves impacted on the mass fraction of product at the channel outlet. Decreasing the complexity of the system permitted closer examination of the catalytic activity of individual cylinders in the single- and two-cylinder models. The results were compared to that of a clear channel with portions of the wall of equal area catalytically active. As the Reynolds number was increase from 5 to 50 a recirculation flow developed, leading to an increase in mass fraction of product at the outlet. Further simplification of the configuration led to the removal of the bluff body entirely, replacing it with a waved catalyst surface. Through use of streamlines and velocity flow field, a picture of a recirculating flow was built up in the OoP and P1 models. The magnitude of this recirculating flow increase as the Reynolds number rose from 100 to 150. It was virtually absent at low flow rates. No such flow was observed in the IP model at any of the Reynolds numbers examined.

The values of the end catalyst mass fractions of CO_2 were less than that of the clear channel for all wavy channel configurations at all inlet mass flow rates. Jetting effects were observed in the OoP and P1 models for all the Reynolds numbers tested. This reduces the amount of reactant that is available to the catalyst and hence there is a corresponding reduction in catalytic activity and product mass fraction. However, this is steadily mitigated as the Reynolds number increased until it almost completely accounted for in the OoP case at Re = 150 by the recirculating flow. The clear channel shows linear reduction in CO_2 surface site fraction in the axial direction. The wavy channels show waveform variation in this value both above and below that of the baseline set by the clear fluid channel. This indicates a variance in catalytic activity dependent on position on the wavy channel catalyst surface, which is influenced by the hydrodynamics of the flow. The overall values for mass fraction of CO_2 at the catalyst end plane were lower than those seen in the clear channel for all waved channel configurations. Had the site surface fraction indicated a consistently lower catalytic activity than that of the clear channel then it could simply be put down to jetting effects. However, the surface site fraction of CO_2 was on occasion larger and sometimes smaller than its equivalent position on the clear channel. The coincidence of these phases of increased and decreased site surface fraction of product with the reflux features like the one shown in Figure 7-1 indicates the influence of hydrodynamics on the catalyst activity.

Chapter 8 Conclusion

The work presented in this thesis has investigated heat and mass transfer in a model microreactor analytically in two dimensions. The analytical treatment was under LTNE conditions and accounts for viscous dissipation (in the two-dimensional studies), local entropy generation and total entropy of the system. A numerical investigation was carried out upon configurations involving multiple cylinders, two cylinders and a single cylinder in a parallel plate channel. Followed by a further investigation into the coupling of hydrodynamic effects with catalytic activity in a channel with wavy walls. The findings of these studies are presented in section 8.1 and a recommendation for future work in section 8.2.

8.1. Conclusion

Initially a one-dimensional model of a single channel microreactor was examined analytically in chapter 4. In this model, asymmetric thick walls subjected to unequal fixed temperature conditions enclosed a microchannel partially filled with a porous material. Volumetrically uniform energy source terms were present in both solid and fluid phases. It was observed that the presence of such sources of heat generation caused significant deviation from the LTE condition, especially with variance of the thickness of the porous medium. Additionally, the thickness of both the porous insert and the enclosing walls were found to impact the Nusselt number, resulting in extremum in the values of the Nusselt number. Heat source terms had an inverse correlation with Nusselt number, whereas the porosity had a positive correlation. Varying either wall or porous insert thickness facilitated the production of minima in the total entropy of the system.

Chapter 5 features two-dimensional analytical studies of heat and mass transfer processes within porous microchannels. Examinations were carried out for Case 1, a heterogeneous catalytic process and Case 2, a homogeneously reactive system. Each featured a double-diffusive model for a zeroth order reaction with attention paid to the Soret effect. Analytical solutions were obtained to the linked thermal and mass transfer equations, which permitted a further investigation into the second law response of the system to parametric variation.

Homogeneous and heterogeneous reaction systems were found to both conform to the relationship between wall thickness and Nusselt number whereby increasing wall

thickness served to lower the Nusselt number. This finding serves to indicate the important role played by the thickness of the enclosing structure with regards to management of thermal conditions within microreactors.

The commonality between the heterogeneous and homogeneous reactions did not end there, however. It was additionally found by virtue of a second law analysis that both cases saw a dominance in irreversibility by that of mass transfer processes over thermal processes. Further, the entropy contribution due to mass transfer could be magnified by increasing either the Damköhler number or the Soret number. This situation could be overcome through ramping up the imposed heat flux or reducing the Damköhler number. Under certain conditions, the entropy contribution from the fluid friction component could be similarly great in magnitude.

A knock-on effect of this is the increase in total entropy generation in both cases associated with increased Damköhler and Soret numbers. Similarly, the thickness of the enclosing structure was found to influence the total entropy of the system in both cases. In Case 1, thermal conductivity ratio was found to have a strong influence on the total entropy generation. While in Case 2 the radiation parameter had an analogous effect on the total entropy of the system.

An existing LTNE model is extended to permit the analysis of a catalytic surface interfacing between a fluid filled porous medium and a solid enclosing structure is presented in chapter 6. This novel model allows the study of heat emitted by an exothermic reaction, taking place on the surface, to be split between not only the porous solid and fluid phases, but additionally the thick walled enclosing structure. In agreement with the results of chapter 5, the thickness of the enclosing structure was found to be a vital parameter with regards to both heat and mass transfer, and by extension entropy generation. The Nusselt number was found to have a singular point by which any variation in heat flux yielded the same value for the Nusselt number for a given wall thickness. Even though the system is geometrically asymmetric, such a point was found to exist for both the upper and lower walls. The Sherwood number demonstrated a response that indicated that the microchannel thickness is of greater importance than the asymmetry of the system, yielding the same value for the same channel thickness regardless of the geometric symmetry of the system.

A numerical model of channel incorporating cylindrical structure, and later waved surfaces, is the focus of chapter 7. A study of the effect of the cylinders on the mass fraction

of the product of the lean combustion of methane in air is undertaken. Increasing Reynolds number from 5 to 50 saw the development of a recirculating flow and an accompanying increase in mass fraction of carbon dioxide at the outlet. Removing the complexity of these bluff bodies, to reduce obscuring of hydrodynamic effect resulted in the development of channels with wavy walls. The wavy upper and lower walls with either in phase (IP), out of phase (OoP) or partially out of phase (P1). These were compared with a baseline of a channel with straight walls, but equal catalytic surface. For the OoP and P1 models, jetting effects were observed in the velocity field, reducing the contact with the catalytic surfaces and thus reducing the carbon dioxide mass fraction at the catalyst-end measuring plane. This effect steadily reduced as the Reynolds number increased to 150 and a reflux zone developed in the trough regions of the wavy surfaces. Comparison of surface site fraction of carbon dioxide for the channels as compared to the clear channel revealed regions where the fraction was greater than the corresponding value for the clear channel. These regions coincided with the reflux features observed. It also showed regions where lower values were recorded. Such variance being indicative of the hydrodynamics of the flow influencing the catalytic activity at the surface.

8.2. Recommendations for future work

Use of LTNE conditions in the analytical study of microreactor performance is still a very open area of research interest. Future investigations in this area, utilising the extended model presented in chapter 6 would find ideal application in systems of multiple microreactors. In such systems, microreactors featuring exothermic reactions are place above and below those featuring endothermic reaction processes. Simple modification of the model would allow it to be applicable to endothermic reactions. Thus the optimisation of such multi-microreactor systems could be performed.

Relaxation of certain limitations imposed by the underlying assumptions could yield interesting results and increase the accuracy of the model. One such assumption would be the use of a constant effective diffusion coefficient. By relating the diffusion coefficient to the tortuosity and porosity, for example, of the porous medium a model that closer represented a working microreactor could be achieved. Another addition could be that of consideration of dispersion upon both the thermal and concentration fields. This would entail examining the effects of dispersion on the effective thermal conductivity of the fluid. How this interacts with the heat transfer properties of the porous medium could then be

investigated. With such consideration in place when coupled with the thermophoresis, the impact on the mass transport within the microchannel could also be pursued.

It would be a worthwhile endeavour to examine the situation for increased reaction orders. One dimensional analytical models for first order reactions in a one-dimensional analysis have already been conducted [198]. Extension to two-dimensional models would certainly be an advantageous step to be undertaken. Further reaction orders could also be considered, allowing the analysis to be used for a wider range of reactions that might be of interest for chemical synthesis using microreactors.

A further assumption that is made within the models presented has been that the catalytic activity is not susceptible to temperature change. Many catalysts are subject to changes in activity with temperature and the relaxing of this assumption would permit the more accurate modelling of such catalysts. This would entail some serious reconsideration of the mass balance as the input to the channel would no longer be constant. As such another relationship leading to the generation of species within the channel would have to be explored. Perhaps starting with a simple linear model of increased catalytic activity with temperature, further relationships between temperature and catalytic activity could then be examined.

In order to further advance the models presented and any further models created, it would be advantageous to be able to conduct experimental studies of microreactors. This would serve both as an experimental validation technique for the models and also be able to highlight areas in which improvement may be made.

Using the information provided by the study into hydrodynamic influence on catalytic activity, further studies of waved surfaces could be performed involving changes of wavelength of corrugation between upper and lower walls. Further, these walls could be modelled as thick walls and a conjugate heat transfer study could be performed. This would entail the removal of the fixed wall temperature condition imposed in the study presented in this work. That would permit temperature effects on the catalytic activity to also be taken into account. The combination of the effects of temperature sensitivity of catalyst and the hydrodynamic influence observed could yield further information on the how the interplay between the two phenomena function within working microreactors.

Conclusion

Moving beyond the steady state condition into the examination of transient phenomena could also provide interesting information on the development of the flow structures observed in the numerical simulations presented in Chapter 7.

Appendix A

Closed-form constants for Chapter 5

Provided here is a list of the closed form constants $D_1 - D_4$ pertinent to Equations (5-141), (5-144), (5-145).

$D_1 = \frac{SY_1}{SY_1 \cosh(SY_1) - \sinh(SY_1)}$
$D_2 = Br' D_1^2 S^2$
$D_3 = \frac{D_1}{Y_1} - D_2 \cosh(SY_1)$
$D_4 = -\frac{D_1}{Y_1} \cosh(SY_1).$

Table A- 1 Closed-form constants for velocity equations chapter 5

Similarly, $E_1 - E_{14}$, pertinent to equations (5-151), (5-152), (5-153), and (5-154) can be defined as follows.

$E_1 = \dfrac{2QY_1 - k_{e2}\theta_{w2}}{k_{e2}}$,	$E_2 = \dfrac{2Q}{k_{e2}}$,
$E_3 = \dfrac{BiD_2 - 4D_2S^2}{16kS^4 - 4kS^2\alpha^2}$,	$E_4 = \dfrac{BiD_3 - D_3S^2}{kS^4 - kS^2\alpha^2}$,
$E_5 = \dfrac{-[D_4 + 2E_6k + (D_3 + E_4kS^2)\cosh(SY_1) + (D_2 + 4E_3kS^2)\cosh(2SY_1)]\mathrm{sech}(\alpha Y_1)}{k\alpha^2}$,	
$E_6 = \dfrac{-BiD_4}{2k\alpha^2}$,	$E_7 = \dfrac{\theta_{w2}}{2Y_1}$,
$E_8 = \dfrac{1}{2k\alpha^2}\big[2D_4 + 2E_6k(2 - Y_1^2\alpha^2) + k\alpha^2\theta_{w2} + 2\big(D_3 + E_4k(S^2 - \alpha^2)\big)\cosh(SY_1) + 2\big(D_4 + E_3k(4S^2 - \alpha^2)\big)\cosh(2SY_1)\big]$,	
$E_9 = \dfrac{BiD_2}{16kS^4 - 4kS^2\alpha^2}$,	$E_{10} = \dfrac{BiD_3}{kS^4 - kS^2\alpha^2}$,
$E_{11} = \dfrac{-[2E_6 + E_{10}S^2\cosh(SY_1) + 4E_9S^2\cosh(2SY_1)]\mathrm{sech}(\alpha Y_1)}{\alpha^2}$,	
$E_{12} = \dfrac{1}{2\alpha^2}[4E_6 - 2E_6Y_1^2\alpha^2 + \alpha^2\theta_{w2} + 2E_{10}(S^2 - \alpha^2)\cosh(SY_1) + 2E_9(4S^2 - \alpha^2)\cosh(2SY_1)]$,	
$E_{13} = \dfrac{2(Q-1)Y_1}{k_{e1}}$,	$E_{14} = \dfrac{2(Q-1)}{k_{e1}}$

Table A- 2 Closed-form constants for temperature equations for the heterogeneous case

Homogeneous case

The closed form constants $D_1 - D_4$, are identical to those for the heterogeneous case. Provided here is a list of the closed form temperature coefficients $E_1 - E_{12}$.

$E_1 = \frac{-Y_1}{k_{e1}}$,	$E_2 = \frac{1}{k_{e1}}$,
$E_3 = \frac{BiD_2 - 4D_2S^2 - 4BiD2S^2Rd}{16k(1+Rd)S^4 - 4k(1+Rd)S^2\alpha^2}$,	$E_4 = \frac{BiD_3 - D_3S^2}{k(1+Rd)S^4 - k(1+Rd)S^2\alpha^2}$,
$E_5 = \frac{-[D_4 + 2E_6k + (D_3 + E_4kS^2)\cosh(SY_1) + (D_2 + 4E_3kS^2)\cosh(2SY_1)]\mathrm{sech}(\alpha Y_1)}{k\alpha^2}$,	
$E_6 = \frac{-BiD_4}{2k(1+Rd)\alpha^2}$,	$E_7 = 0$,
$E_8 = \frac{1}{2k(1+Rd)\alpha^2}\big[2D_4 + 2E_6k(1+Rd)(2 - Y_1^2\alpha^2) + 2\big(D_3 + E_4k(1+Rd)(S^2 - \alpha^2)\big)\cosh(SY_1) + 2\big(D_4 + E_3k(1+Rd)(4S^2 - \alpha^2)\big)\cosh(2SY_1)\big]$,	
$E_9 = \frac{BiD_2}{16k(1+Rd)S^4 - 4k(1+Rd)S^2\alpha^2}$,	$E_{10} = \frac{BiD_3}{k(1+Rd)S^4 - k(1+Rd)S^2\alpha^2}$,
$E_{11} = \frac{-[2E_6 + E_{10}S^2\cosh(SY_1) + 4E_9S^2\cosh(2SY_1)]\mathrm{sech}(\alpha Y_1)}{\alpha^2}$,	
$E_{12} = \frac{1}{2\alpha^2}[4E_6 - 2E_6Y_1^2\alpha^2 + 2E_{10}(S^2 - \alpha^2)\cosh(SY_1) + 2E_9(4S^2 - \alpha^2)\cosh(2SY_1)]$,	

Table A- 3 Closed-form constants for the temperature equations for the homogeneous case

Provided below is a list of the closed form concentration equation coefficients $F_1 - F_5$.

Appendix A

$F_1 = \dfrac{D_2 k(Bi - 4(1+Rd)S^2)Sr}{4S^2 Y_1 \varepsilon(-Bi(1+k+Rd) + 4k(1+Rd)S^2)}$
$F_2 = \dfrac{D_3 k(Bi - (1+Rd)S^2)Sr}{S^2 Y_1 \varepsilon(-Bi(1+k+Rd) + k(1+Rd)S^2)} - \dfrac{\gamma}{SY_1^2(SY_1\cosh(SY_1) - \sinh(SY_1))}$
$F_3 = \dfrac{E_5 kSr}{Y_1 \varepsilon}$
$F_4 = -\dfrac{D_4 kSr}{2Y_1\varepsilon(1+k+Rd)} - \dfrac{\gamma(S(Y_1-1)\cosh(SY_1) - \sinh(SY_1))}{2Y_1^2(SY_1\cosh(SY_1) - \sinh(SY_1))}$
$F_5 = \dfrac{E_8 kSr}{Y_1\varepsilon} + \dfrac{\left(2\gamma + S^2Y_1^2(Y_1(2+\gamma)-\gamma)\right)\cosh(SY_1) - SY_1^2(2+\gamma)\sinh(SY_1)}{2SY_1^2(SY_1\cosh(SY_1) - \sinh(SY_1))} - \dfrac{kSr}{Y_1\varepsilon}\left[E_8 - \dfrac{D_4 Y_1^2}{2(1+k+Rd)} + \dfrac{D_3(Bi-(1+Rd)S^2)\cosh(SY_1)}{S^2(-Bi(1+k+Rd)+k(1+Rd)S^2)} + \dfrac{D_2(Bi-4(1+Rd)S^2)\cosh(2SY_1)}{4S^2(-Bi(1+k+Rd)+4k(1+Rd)S^2)} + E_5\cosh(\alpha Y_1)\right]$

Table A- 4 Closed-form coefficients for the concentration equations for the homogeneous case

Appendix A

Closed-form constants for Chapter 6

Provided here is a table of the closed-form constants, used in Chapter 6.

$$A_1 = \frac{Da[\sinh(SY_1) + \sinh(SY_2)]}{\cosh(SY_2)\sinh(SY_1) + \cosh(SY_1)\sinh(SY_2)},$$

$$A_2 = \frac{Da[\cosh(SY_2) - \cosh(SY_1)]}{\cosh(SY_2)\sinh(SY_1) + \cosh(SY_1)\sinh(SY_2)},$$

$$A_3 = \frac{S(Y_1 + Y_2)}{DaS(Y_1 + Y_2) + A_1(\sinh(SY_1) + \sinh(SY_2)) + A_2(\cosh(SY_2) - \cosh(SY_1))},$$

$$A_4 = \frac{SA_3}{2}[2Da^2S(Y_1 + Y_2) + 4A_2Da(\cosh(SY_2) - \cosh(SY_1)) + 2A_1A_2(\cosh(2SY_2) - \cosh(2SY_1)) + 4A_1Da(\sinh(SY_1) + \sinh(SY_2)) + (A_1^2 + A_2^2)(\sinh(2SY_1) + \sinh(2SY_2))],$$

$$A_5 = \frac{A_3(1 + Br'A_4)}{(Y_1 + Y_2)},$$

$$A_6 = A_3^2 Br'^{S^2},$$

$$B_1 = (A_1^2 + A_2^2)A_6,$$

$$B_2 = 2A_1A_2A_6,$$

$$B_3 = (2A_1A_6Da - A_1A_5),$$

$$B_4 = (2A_2A_6Da - A_2A_5),$$

$$B_5 = Da(A_6Da - A_5),$$

$$C_1 = \frac{\mathrm{Q}_{w2}2\mathrm{Y}_2}{\mathrm{k}_{e2}} + \theta_{w2},$$

$$C_2 = \frac{\mathrm{Q}_{w2}}{\mathrm{k}_{e2}},$$

$$C_3 = \frac{B_1Bi}{16kS^4 - 4kS^2\alpha^2},$$

$$C_4 = \frac{B_3Bi}{kS^4 - kS^2\alpha^2},$$

$$C_5 = \frac{1}{k\alpha^4(4S^4 - 5S^2\alpha^2 + \alpha^4)}\, Bi\,\mathrm{csch}\big((Y_1 + Y_2)\alpha\big)\big[\big(B_5(4S^4 - 5S^2\alpha^2 + \alpha^4) + \alpha^2(B_3(-4S^2 + \alpha^2)\cosh(2SY_2) + B_1(-S^2 + \alpha^2)\cosh(2SY_2) + B_4(-4S^2 + \alpha^2)\sinh(2SY_2) + B_2(-S + \alpha)(S + \alpha)\sinh(2SY_2))\big)\sinh(\alpha Y_1) + (B_3\alpha^2(-4S^2 + \alpha^2)\cosh(SY_1) + B_1\alpha^2(-S + \alpha)(S + \alpha)\cosh(2SY_1) + (4S^2 - \alpha^2)(B_5(S - \alpha)(S + \alpha) + B_4\alpha^2\sinh(SY_1)) + B_2(S - \alpha)\alpha^2(S + \alpha)\sinh(2SY_1))\sinh(\alpha Y_2)\big],$$

Appendix A

$C_6 = \frac{B_2 Bi}{16kS^4 - 4kS^2\alpha^2}$,	$C_7 = \frac{B_4 Bi}{kS^4 - kS^2\alpha^2}$,

$$C_8 = \frac{1}{k\alpha^4(4S^4 - 5S^2\alpha^2 + \alpha^4)} Bi\ \mathrm{csch}\big((Y_1 + Y_2)\alpha\big)\big[\cosh(\alpha Y_2)\left(-B_5(4S^4 - 5S^2\alpha^2 + \alpha^4)\right.$$
$$+ \alpha^2(B_3(4S^2 - \alpha^2)\cosh(SY_1) + B_1(S - \alpha)(S + \alpha)\cosh(2SY_1)$$
$$+ B_4(-4S^2 + \alpha^2)\sinh(SY_1) + B_2(-S^2 + \alpha^2)\sinh(2SY_1))\big)$$
$$+ \cosh(\alpha Y_1)\left(B_5(4S^4 - 5S^2\alpha^2 + \alpha^4)\right.$$
$$+ \alpha^2(B_3(-4S^2 + \alpha^2)\cosh(SY_2) + B_1(-S^2 + \alpha^2)\cosh(2SY_2)$$
$$+ B_4(-4S^2 + \alpha^2)\sinh(SY_2) + B_2(-S + \alpha)(S + \alpha)\sinh(2SY_2))\big)\big],$$

$$C_9 = -\frac{B_5 Bi}{2k\alpha^2},$$

$$C_{10} = \frac{1}{4kS^2(Y_1 + Y_2)\alpha^2}\Big(2S^2\big(B_5\mathrm{Bi}\big(-{Y_1}^2 + {Y_2}^2\big) + 2k\alpha^2\theta_{w2}\big)$$
$$+ \mathrm{Bi}\big(-4B_3\cosh(SY_1) - B_1\cosh(2SY_1) + 4B_3\cosh(SY_2)$$
$$+ B_1\cosh(2SY_2) + 4B_4(\sinh(SY_1) + \sinh(SY_2))$$
$$+ B_2(\sinh(2SY_1) + \sinh(2SY_2))\big)\Big),$$

$$C_{11} = \frac{1}{4kS^2(Y_1 + Y_2)\alpha^4}\Big(2S^2(B_5\mathrm{Bi}(Y_1 + Y_2)(-2 + Y_1Y_2\alpha^2) + 2kY_1\alpha^4\theta_{w2})$$
$$+ \mathrm{Bi}\alpha^2\big(4B_3Y_2\cosh(SY_1) + B_1Y_2\cosh(2SY_1)$$
$$- 2Y_2(2B_4 + B_2\cosh(SY_1))\sinh(SY_1)$$
$$+ Y_1(4B_3\cosh(SY_2) + B_1\cosh(2SY_2) + 4B_4\sinh(SY_2)$$
$$+ B_2\sinh(2SY_2))\big)\Big),$$

$C_{12} = \frac{B_1(\mathrm{Bi} - 4S^2)}{4kS^2(4S^2 - \alpha^2)}$,	$C_{13} = -\frac{B_3(-\mathrm{Bi} + S^2)}{kS^2(S^2 - \alpha^2)}$,

$$C_{14} = \frac{1}{k\alpha^4(4S^4 - 5S^2\alpha^2 + \alpha^4)}(\mathrm{Bi}$$
$$- \alpha^2)\mathrm{csch}\big((Y_1 + Y_2)\alpha\big)\Big(\big(B_5(4S^4 - 5S^2\alpha^2 + \alpha^4)$$
$$+ \alpha^2(B_3(-4S^2 + \alpha^2)\cosh(SY_2) + B_1(-S^2 + \alpha^2)\cosh(2SY_2)$$
$$+ B_4(-4S^2 + \alpha^2)\sinh(SY_2)$$
$$+ B_2(-S + \alpha)(S + \alpha)\sinh(2SY_2))\big)\sinh(\alpha Y_1)$$
$$+ (B_3\alpha^2(-4S^2 + \alpha^2)\cosh(SY_1) + B_1\alpha^2(-S + \alpha)(S + \alpha)\cosh(2SY_1)$$
$$+ (4S^2 - \alpha^2)(B_5(S - \alpha)(S + \alpha) + B_4\alpha^2\sinh(SY_1))$$
$$+ B_2(S - \alpha)\alpha^2(S + \alpha)\sinh(2SY_1))\sinh(\alpha Y_2)\Big),$$

$C_{15} = \frac{B_2(\mathrm{Bi} - 4S^2)}{4kS^2(4S^2 - \alpha^2)}$,	$C_{16} = -\frac{B_4(-\mathrm{Bi} + S^2)}{kS^2(S^2 - \alpha^2)}$,

$$C_{17} = \frac{1}{k\alpha^4(4S^4 - 5S^2\alpha^2 + \alpha^4)}(\mathrm{Bi} - \alpha^2)\mathrm{csch}((Y_1 + Y_2)\alpha)(\cosh(\alpha Y_2) - B_5(4S^4$$
$$- 5S^2\alpha^2 + \alpha^4) + \alpha^2(B_3(4S^2 - \alpha^2)\cosh(SY_1) + B_1(S - \alpha)(S$$
$$+ \alpha)\cosh(2SY_1) + B_4(-4S^2 + \alpha^2)\sinh(SY_1) + B_2(-S^2$$
$$+ \alpha^2)\sinh(2SY_1))) + \cosh(\alpha Y_1)\,(B_5(4S^4 - 5S^2\alpha^2 + \alpha^4) + \alpha^2(B_3(-4S^2$$
$$+ \alpha^2)\cosh(SY_2) + B_1(-S^2 + \alpha^2)\cosh(2SY_2) + B_4(-4S^2$$
$$+ \alpha^2)\sinh(SY_2) + B_2(-S + \alpha)(S + \alpha)\sinh(2SY_2)))),$$

Appendix A

$$C_{18} = -\frac{B_5 \mathrm{Bi}}{2k\alpha^2},$$

$$C_{19} = C_{11},$$

$$C_{20} = \frac{1}{4kS^2(Y_1+Y_2)\alpha^4}\Big(2S^2(B_5(Y_1+Y_2)(-2\mathrm{Bi}+(2+\mathrm{Bi}Y_1Y_2)\alpha^2)+2kY_1\alpha^4\theta_{\mathrm{w2}}) + \mathrm{Bi}\alpha^2\big(4B_3Y_2\cosh(SY_1)+B_1Y_2\cosh(2SY_1) - 2Y_2(2B_4+B_2\cosh(SY_1))\sinh(SY_1) + Y_1(4B_3\cosh(SY_2)+B_1\cosh(2SY_2)+4B_4\sinh(SY_2) + B_2\sinh(2SY_2))\big)\Big),$$

$$C_{21} = \frac{Q_{\mathrm{w1}}Y_1}{k_{\mathrm{e1}}},$$

$$C_{22} = \frac{Q_{\mathrm{w1}}}{k_{\mathrm{e1}}},$$

$$C_{23} = \frac{1}{4kS^2(Y_1+Y_2)\alpha^2}\mathrm{Bi}\big(-2B_5S^2{Y_1}^2+2B_5S^2{Y_2}^2-4B_3\cosh(SY_1)-B_1\cosh(2SY_1) + 4B_3\cosh(SY_2)+B_1\cosh(2SY_2)+4B_4\sinh(SY_1)+B_2\sinh(2SY_1) + 4B_4\sinh(SY_2)+B_2\sinh(2SY_2)\big),$$

$$\theta_{\mathrm{w2}} = ((Y_1+Y_2)/(1+k))\Big(Q - \big(2C_9Y_2+2C_{18}kY_2+(C_7+C_{16}k)S\cosh(SY_2) + 2(C_6+C_{15}k)S\cosh(2SY_2)+C_8\alpha\cosh(\alpha Y_2)+C_{17}k\alpha\cosh(\alpha Y_2) + C_4S\sinh(SY_2)+C_{13}kS\sinh(SY_2)+2C_3S\sinh(2SY_2) + 2C_{12}kS\sinh(2SY_2)+C_5\alpha\sinh(\alpha Y_2)+C_{14}k\alpha\sinh(\alpha Y_2) + (C_{23}+kC_{23})\big)\Big),$$

$$D_1 = \frac{C_{12}k\mathrm{Sr}(Y_1+Y_2)}{(Y_1+Y_2)^2\varepsilon},$$

$$D_2 = \frac{(C_{13}k\mathrm{Sr}S^2(Y_2+Y_1)+2A_1A_3\gamma\varepsilon)}{S^2(Y_1+Y_2)^2\varepsilon},$$

$$D_3 = \frac{C_{14}k\mathrm{Sr}(Y_1+Y_2)}{(Y_1+Y_2)^2\varepsilon},$$

$$D_4 = \frac{C_{15}k\mathrm{Sr}(Y_1+Y_2)}{(Y_1+Y_2)^2\varepsilon},$$

$$D_5 = \frac{(C_{16}kS^2\mathrm{Sr}(Y_1+Y_2)+2A_2A_3\gamma\varepsilon)}{S^2(Y_1+Y_2)^2\varepsilon},$$

$$D_6 = \frac{C_{17}k\mathrm{Sr}(Y_1+Y_2)}{(Y_1+Y_2)^2\varepsilon},$$

$$D_7 = \frac{(C_{18}k\mathrm{Sr}(Y_1+Y_2)+A_3\mathrm{Da}\gamma\varepsilon)}{(Y_1+Y_2)^2\varepsilon},$$

$$D_8 = \frac{1}{S(Y_1+Y_2)^2\varepsilon}\Big(C_{19}kS\mathrm{Sr}Y_1+C_{19}kS\mathrm{Sr}Y_2+A_3\mathrm{Da}SY_1\gamma\varepsilon-A_3\mathrm{Da}SY_2\gamma\varepsilon - 2A_2A_3\gamma\varepsilon\cosh\Big(\frac{1}{2}S(-Y_1+Y_2)\Big)-2A_1A_3\gamma\varepsilon\sinh\Big(\frac{1}{2}S(-Y_1+Y_2)\Big)\Big),$$

$$
\begin{aligned}
D_9 = \frac{1}{S^2(Y_1+Y_2)^2\varepsilon}\Bigg(& C_{19}kS^2\mathrm{Sr}{Y_1}^2 - C_{18}kS^2\mathrm{Sr}{Y_1}^3 + C_{19}kS^2\mathrm{Sr}Y_1Y_2 - C_{18}kS^2\mathrm{Sr}{Y_1}^2Y_2 \\
& + S^2{Y_1}^2\varepsilon + 2S^2Y_1Y_2\varepsilon + S^2{Y_2}^2\varepsilon - A_3\mathrm{Da}S^2Y_1Y_2\gamma\varepsilon \\
& - C_{13}kS^2\mathrm{Sr}Y_1\ \cosh(SY_1) - C_{13}kS^2\mathrm{Sr}Y_2\ \cosh(SY_1) \\
& - 2A_1A_3\gamma\varepsilon\ \cosh(SY_1) - C_{12}kS^2\mathrm{Sr}Y_1\ \cosh(2SY_1) \\
& - C_{12}kS^2\mathrm{Sr}Y_2\ \cosh(2SY_1) - 2A_2A_3SY_1\gamma\varepsilon\ \cosh\left(\frac{1}{2}S(-Y_1+Y_2)\right) \\
& - C_{14}kS^2\mathrm{Sr}Y_1\ \cosh(\alpha Y_1) - C_{14}kS^2\mathrm{Sr}Y_2\ \cosh(\alpha Y_1) \\
& + C_{16}kS^2\mathrm{Sr}Y_1\sinh(SY_1) + C_{16}kS^2\mathrm{Sr}Y_2\sinh(SY_1) + 2A_2A_3\gamma\varepsilon\sinh(SY_1) \\
& + C_{15}kS^2\mathrm{Sr}Y_1\sinh(2SY_1) + C_{15}kS^2\mathrm{Sr}Y_2\sinh(2SY_1) \\
& - 2A_1A_3SY_1\gamma\varepsilon\sinh\left(\frac{1}{2}S(-Y_1+Y_2)\right) + C_{17}kS^2\mathrm{Sr}Y_1\sinh(\alpha Y_1) \\
& + C_{17}kS^2\mathrm{Sr}Y_2\sinh(\alpha Y_1)\Bigg).
\end{aligned}
$$

Table A- 5 Closed-form coefficients for the concentration equations for Chapter 6

Appendix B

Section 1: Validation for Chapter 5 temperature solutions

Section 1.1 Heterogeneous case

To validate the mathematical model developed in Section 5.2.2, it is demonstrated here that when the wall thickness tends to zero, the temperature fields reduce to that presented by Ting et al. [115] with no internal heat generation term. To produce a system equivalent to that of Ref. [115], we set $h_1 = h_2$, that is in terms of non-dimensional parameters; $Y_1 = 1$ and also $q'''_{gen} = 0$, which renders $\Omega_{gen} = 0$. The momentum equations (5-133) to (5-135) can clearly be seen to reduce to the corresponding equations. Utilising these, equation (5-139) becomes (where the subscript, T is used to indicate the equivalence to Ting's work),

$$\frac{d\bar{T}_{nf}}{dx} = \frac{1}{2\rho_{nf}C_{p,nf}\bar{u}h_2^2}\left[h_2 q_1'' + h_2 q_2'' + \frac{2\mu_{eff}S^3\bar{u}^2\,cosh(S)}{S\,cosh\,(S) - sinh(S)}\right] = \Omega_T \tag{B-301}$$

This is the same as the axial thermal gradient found by Ting et al. [115] with no heat generation term. Next, the radial thermal equations can be determined from equations (5-141) and (5-142) using the given conditions to yield the coupled equations:

$$k\theta''_{nf} + Bi\left(\theta_s - \theta_{nf}\right) + D'_2\,cosh(2SY) + D'_3\,cosh(SY) + D'_4 = 0 \tag{B-302}$$

$$\theta''_s - Bi\left(\theta_s - \theta_{nf}\right) = 0 \tag{B-303}$$

Where the modified coefficients (which are shown by use of a prime) are:

$D'_1 = \dfrac{S}{S\cosh(S) - \sinh(S)}$	$D'_2 = Br' D'^2_1 S^2$
$D'_3 = D'_1 - D'_2\cosh(S)$	$D'_4 = -D'_1\cosh(S)$

Table B- 1 Closed-form coefficients for validation coupled temperature equations

The coefficients $D'_1 - D'_4$ are the same as those calculated by Ting et al. for the coupled thermal equations investigated therein under the previously stated conditions. Thus, it follows that the final nanofluid and porous solid thermal equations, equations (5-147) and (5-148) may be recast using these conditions to give the following:

$$\theta_{nf}(Y) = E_3' \cosh(2SY) + E_4' \cosh(SY) + E_5' \cosh(\alpha Y) + E_6' Y^2 + E_7' Y + E_8' \quad \text{(B-304)}$$

$$\theta_s(Y) = E_9' \cosh(2SY) + E_{10}' \cosh(SY) + E_{11}' \cosh(\alpha Y) + E_6' Y^2 + E_7' Y + E_{12}' \quad \text{(B-305)}$$

Where the new coefficients are defined as:

$E_3' = \dfrac{D_2'(4S^2 - Bi)}{4S^2(-4kS^2 + Bik + Bi)}$,	$E_4' = \dfrac{D_3'(S^2 - Bi)}{S^2(k\alpha^2 - kS^2)}$,
$E_5' = \dfrac{-[D_4' + 2E_6'k + (D_3' + E_4'kS^2)\cosh(S) + (D_2' + 4E_3'kS^2)\cosh(2S)]\mathrm{sech}(\alpha)}{Bi(k+1)}$,	
$E_6' = \dfrac{-D_4'}{2(k+1)}$,	$E_7' = \dfrac{\theta_{w2}'}{2}$,
$E_8' = \dfrac{1}{2k\alpha^2}\big[2D_4' + 2E_6'k(2-\alpha^2) + k\alpha^2\theta_{w2}' + 2\big(D_3' + E_4'k(S^2-\alpha^2)\big)\cosh(S) + 2\big(D_4' + E_3'k(4S^2-\alpha^2)\big)\cosh(2S)\big]$,	
$E_9' = \dfrac{BiE_3'}{Bi - 4S^2}$,	$E_{10}' = \dfrac{BiE_4'}{Bi - S^2}$,
$E_{11}' = \dfrac{-[2E_6' + E_{10}'S^2\cosh(S) + 4E_9'S^2\cosh(2S)]\mathrm{sech}(\alpha)}{\alpha^2}$,	
$E_{12}' = \dfrac{1}{2\alpha^2}[4E_6' - 2E_6'\alpha^2 + \alpha^2\theta_{w2} + 2E_{10}'(S^2-\alpha^2)\cosh(S) + 2E_9'(4S^2-\alpha^2)\cosh(2S)]$,	

Table B- 2 Closed-form coefficients for validation of temperature equations

With the appropriate rearranging of terms, these coefficients show that equations (B-304) and (B-305) are analytically identical to the nanofluid and porous solid thermal equations presented in the work by Ting et al. [115].

Appendix B

Section 1.2 Homogeneous case

To validate the mathematical model developed in Sections 5.3, it is demonstrated here that when the wall thickness and thermal radiation tend to zero, the analytical form of the temperature fields reduce to those presented by Ting et al. [115] with no internal heat generation term. To produce a system equivalent to that of Ref. [115], we set $h_1 = h_2$, $q_r = 0$. That is in terms of non-dimensional parameters; $Y_1 = 1$, $Rd = 0$, and also from Ting's work; $q'''_{gen} = 0$, which renders $\Omega_{gen} = 0$.

Utilising these, equation (5-203) becomes (where the subscript, T is used to indicate the equivalence to Ting's work),

$$\frac{d\bar{T}_{nf}}{dx} = \frac{1}{\rho_{nf} C_{p,nf} \bar{u} h_2^2}\left[h_2 q_1'' + \frac{\mu_{eff} S^3 \bar{u}^2 cosh(S)}{S\,cosh\ (S) - sinh(S)}\right] = \Omega_T \tag{B-306}$$

This is the same as the axial thermal gradient found by Ting et al. [115] with no heat generation term. Next, the radial thermal equations can be determined from equations (5-207) and (5-208) using the given conditions to yield the coupled equations:

$$k\theta''_{nf} + Bi\left(\theta_s - \theta_{nf}\right) + D'_2\, cosh(2SY) + D'_3\, cosh(SY) + D'_4 = 0 \tag{B-307}$$

$$\theta''_s - Bi\left(\theta_s - \theta_{nf}\right) = 0 \tag{B-308}$$

Where the modified coefficients (which are shown by use of a prime) are identical to those shown in Table B- 1. Thus coefficients $D'_1 - D'_4$ are the same as those calculated by Ting et al. for the coupled thermal equations investigated therein under the previously stated conditions. Thus, it follows that the final nanofluid and porous solid thermal equations, equations (5-210) and (5-211) may be redefined using these conditions into;

$$\theta_{nf}(Y) = E'_3\, cosh(2SY) + E'_4\, cosh(SY) + E'_5\, cosh(\alpha Y) + E'_6 Y^2 + E'_7 Y + E'_8 \tag{B-309}$$

$$\theta_s(Y) = E'_9\, cosh(2SY) + E'_{10}\, cosh(SY) + E'_{11}\, cosh(\alpha Y) + E'_6 Y^2 + E'_7 Y + E'_{12} \tag{B-310}$$

Where the new coefficients are defined as:

<table>
<tr><td>$E'_3 = \dfrac{D'_2(4S^2 - Bi)}{4S^2(-4kS^2 + Bik + Bi)}$,</td><td>$E'_4 = \dfrac{D'_3(S^2 - Bi)}{S^2(k\alpha^2 - kS^2)}$,</td></tr>
<tr><td colspan="2">$E'_5 = \dfrac{-[D'_4 + 2E'_6 k + (D'_3 + E'_4 kS^2)\cosh(S) + (D'_2 + 4E'_3 kS^2)\cosh(2S)]\mathrm{sech}(\alpha)}{Bi(k+1)}$,</td></tr>
<tr><td>$E'_6 = \dfrac{-D'_4}{2(k+1)}$,</td><td>$E'_7 = 0$,</td></tr>
<tr><td colspan="2">$E'_8 = \dfrac{1}{2k\alpha^2}\big[2D'_4 + 2E'_6 k(2 - \alpha^2) + 2\big(D'_3 + E'_4 k(S^2 - \alpha^2)\big)\cosh(S) + 2\big(D'_4 + E'_3 k(4S^2 - \alpha^2)\big)\cosh(2S)\big]$,</td></tr>
</table>

$E_9' = \frac{BiE_3'}{Bi - 4S^2}$,	$E_{10}' = \frac{BiE_4'}{Bi - S^2}$,
$E_{11}' = \frac{-[2E_6' + E_{10}'S^2\cosh(S) + 4E_9'S^2\cosh(2S)]\mathrm{sech}(\alpha)}{\alpha^2}$,	
$E_{12}' = \frac{1}{2\alpha^2}[4E_6' - 2E_6'\alpha^2 + 2E_{10}'(S^2 - \alpha^2)\cosh(S) + 2E_9'(4S^2 - \alpha^2)\cosh(2S)]$,	

Table B- 3 Closed-form coefficients for validation of temperature equations for the homogeneous case

With the appropriate rearranging of terms, the above coefficients indicate that equations (B-309) and (B-310) are analytically identical to the nanofluid and porous solid thermal equations in the work by Ting et al. [115] with a temperature at the upper wall equal to zero due to the equality of the external heat flux at the bottom and top walls.

Section 2: Validation for Chapter 6 temperature solutions

Analytical Validation

To validate the mathematical model developed in Section 2, it is demonstrated that when the wall thicknesses are equal and there is no exothermic catalytic reaction, the temperature fields reduce to that presented by Hunt et al. [212] and Ting et al. [115] . To produce a system equivalent to that of Ref. [212], we set $h_1 = h_2$. It is also necessary to reverse the directions of q_{w1} and q_{w2} and set their magnitudes equal to q_1 and q_2 respectively, which in terms of non-dimensional parameters leads to $Q_{w1} = 2(Q - 1)$ and $Q_{w2} = -2Q$. Accounting for the difference in parameter definitions of Br', Re and θ_i then the axial thermal gradient, Equation (6-258) becomes:

$$\theta_i(X) = \frac{X\,[1 + A_4'Br']}{2Re\,Pr\,k\,Y_1\xi} \qquad i = 1, 2, s, f \tag{B-311}$$

Where

$$A_4' = \frac{2S^3 {Y_1}^2 \cosh(SY_1)}{S\,Y_1\cosh(SY_1) - \sinh(SY_1)}. \tag{B-312}$$

This is the same as the axial thermal gradient found by Hunt et al. [212] where A_4' represents the coefficient of the modified Brinkman number. Next, the radial thermal equations can be determined from equations (6-260) and (6-261) using the given conditions to yield the coupled equations:

$$k\theta_f'' + Bi\left(\theta_s - \theta_f\right) + B_1' \cosh(2SY) + B_2' \sinh(2SY) + B_3' \cosh(SY) + B_4' \sinh(SY) + B_5' = 0 \quad \text{(B-313)}$$

$$\theta_s'' - Bi\left(\theta_s - \theta_f\right) = 0 \quad \text{(B-314)}$$

where, taking into consideration the difference in parameter definitions of Br' and θ_i , the modified coefficients (which are shown by use of a prime) are:

$$B_1' = \frac{Br'S^4Y_1^2}{(SY_1\cosh(SY_1) - \sinh(SY_1))^2} \quad \text{(B-315)}$$

$$B_2' = 0 \quad \text{(B-316)}$$

$$B_3' = -\frac{S\,\mathrm{sech}(SY_1)\,[SY_1(2Br'S^2Y_1 - 1) + \tanh(SY_1)]}{2(-SY_1 + \tanh(SY_1))^2} \quad \text{(B-317)}$$

$$B_4' = 0 \quad \text{(B-318)}$$

$$B_5' = -\frac{S}{SY_1 - \tanh(SY_1)} \quad \text{(B-319)}$$

The coefficients $B_1' - B_4'$ once rearranged are identical to the equivalent coefficients calculated by Hunt et al. for the coupled thermal equations investigated therein under the previously stated conditions. Thus, the final fluid and porous solid thermal equations, equations (6-265) to (6-268) under these conditions yield the following.

$$\theta_2(Y) = C_1' + C_2'Y \qquad Y_2 < Y \leq 1 \quad \text{(B-320)}$$

$$\theta_s(Y) = C_3' \cosh(2SY) + C_4' \cosh(SY) + C_5' \cosh(\alpha Y) + C_6' \sinh(2SY) + C_7' \sinh(SY) + C_8' \sinh(\alpha Y) + C_9'Y^2 + C_{10}'Y + C_{11}' \qquad -Y_1 \leq Y < Y_2 \quad \text{(B-321)}$$

$$\theta_f(Y) = C'_{12}\,cosh(2SY) + C'_{13}\,cosh(SY) + C'_{14}\,cosh(\alpha Y) + C'_{15}\,sinh(2SY) + C'_{16}\,sinh(SY) + C'_{17}\,sinh(\alpha Y) + C'_{18}Y^2 + C'_{19}Y + C'_{20} \qquad -Y_1 \le Y < Y_2 \qquad \text{(B-322)}$$

$$\theta_1(Y) = C'_{21} + C'_{22}Y \qquad -1 \le Y < -Y_1 \qquad \text{(B-323)}$$

where the new coefficients are defined as:

$C'_1 = \frac{Y_2 Q_{w2}}{2k_{e2}} + \theta'_{w2}$,	$C'_2 = -\frac{Q_{w2}}{k_{e2}}$,
$C'_3 = \frac{B'_1 Bi}{16kS^4 - 4kS^2\alpha^2}$,	$C'_4 = \frac{B'_3 Bi}{kS^4 - kS^2\alpha^2}$,
$C'_5 = \frac{1}{(k\alpha^4(4S^4 - 5S^2\alpha^2 + \alpha^4))}\,[Bi(B'_3\alpha^2(\alpha^2 - 4S^2)\cosh(SY_1) + (S^2 - \alpha^2)(4S^2B'_5 - B'_5\alpha^2 - B'_1\alpha^2\cosh(2SY_1)))\text{sech}(\alpha Y_1)]$,	
$C'_6 = C'_7 = C'_8 = 0$,	$C'_9 = \frac{-B'_5 Bi}{2k\alpha^2}$,
$C'_{10} = \frac{\theta'_{w2}}{2Y_1}$,	
$C'_{11} = \frac{1}{2kS^2\alpha^4}[2S^2(B'_5 Bi(Y_1^2\alpha^2 - 2) + k\alpha^4\theta'_{w2}) + 4B'_3 Bi\alpha^2\cosh(SY_1) + B'_1 Bi\alpha^2\cosh(2SY_1)]$,	
$C'_{12} = \frac{B'_1(Bi - 4S^2)}{4kS^2(4S^2 - \alpha^2)}$,	$C'_{13} = -\frac{B'_3(S^2 - Bi)}{kS^4 - kS^2\alpha^2}$,
$C'_{14} = \frac{1}{(k\alpha^4(4S^4 - 5S^2\alpha^2 + \alpha^4))}\,[(Bi - \alpha^2)(B'_3\alpha^2(\alpha^2 - 4S^2)\cosh(SY_1) + (S^2 - \alpha^2)(4S^2B'_5 - B'_5\alpha^2 - B'_1\alpha^2\cosh(2SY_1)))\text{sech}(\alpha Y_1)]$,	
$C'_{15} = C'_{16} = C'_{17} = 0$,	$C'_{18} = \frac{-B'_5 Bi}{2k\alpha^2}$,

$C'_{19} = \frac{\theta'_{w2}}{2Y_1}$,	
$C'_{20} = \frac{1}{4kS^2\alpha^4}[2S^2(B'_5 Bi(Y_1^2\alpha^2 - 2) + k\alpha^4\theta'_{w2}) + 4B'_3 Bi\alpha^2\cosh(SY_1) + B'_1 Bi\alpha^2\cosh(2SY_1)]$,	
$C'_{21} = \frac{Q_{w1}Y_1}{k_{e1}}$,	$C'_{22} = \frac{Q_{w1}}{k_{e1}}$.

Table B- 4 Closed-form constants for the validation of the temperature equations for Chapter 6

With rearrangement of terms and taking into consideration the difference in parameter definitions of Br' and θ_i, the above coefficients show that equations (B-320) to (B-323) are analytically identical to the thermal equations derived in the investigation by Hunt et al. [212], which itself could be rigorously reduced to the results of Ting et al.[115].

Numerical Validation

For comparison purposes a model was developed in the computational multi-physics software, STAR-CCM+ of a microchannel 12mm in length, 800μm in height enclosed between walls of 50μm thickness. Steady, two-dimensional continuity, momentum and energy equations for the fluid and solid walls were solved on a grid consisting of 98344 cells.

Continuity equation:

$$\boldsymbol{\nabla} \cdot (\rho \boldsymbol{v}) = 0. \tag{B-324}$$

Momentum equation:

$$\boldsymbol{\nabla} \cdot (\rho \boldsymbol{v} \otimes \boldsymbol{v}) = \boldsymbol{\nabla} \cdot \boldsymbol{\sigma}. \tag{B-325}$$

Energy equation:

$$\boldsymbol{\nabla} \cdot (\rho E \boldsymbol{v}) = \boldsymbol{\nabla} \cdot (\boldsymbol{v} \cdot \boldsymbol{\sigma}) - \boldsymbol{\nabla} \cdot \boldsymbol{q} + S_{\boldsymbol{E}}. \tag{B-326}$$

where; $\otimes$ represents the Kronecker product, $\boldsymbol{\sigma}$ is the stress tensor, E is the total energy per unit mass, $\boldsymbol{q}$ is the heat flux and $S_{\boldsymbol{E}}$ is an energy source term.

Grid independency tests confirmed the adequacy of this grid. Standard no slip velocity and no jump temperature boundary conditions were implemented. Using an interface between the walls and the fluid flowing within the microchannel the thermal specification of conjugate heat transfer was applied. A heat source interface was implemented at the boundary between each wall and the fluid within the microchannel. The heat flux into the wall and into the fluid from this heat source was measured. Thermal conductivity within the walls was set to 18 $WK^{-1}m^{-1}$ to represent a ceramic and the fluid chosen was considered to be water. A mass flow rate was calculated to give a Reynolds number of 7. These figures permitted the development of an analytical model using the temperature equations derived in Section 6.3.7, using a porosity of 0.999, and a Darcy number of 1000 to represent the flow inside a clear conduit. The analytically and computationally predicted temperature fields are shown in Figure B- 1, featuring a good agreement. Further, for the configuration shown in Figure B- 1, the Nusselt number calculated by equation (6-273) is 4.29 and that obtained computationally is 4.45. Once again, this shows an excellent agreement between the two models. It is worth recalling that consideration of a clear microchannel (instead of a porous one) was to avoid using any interface model on the surface of the walls.

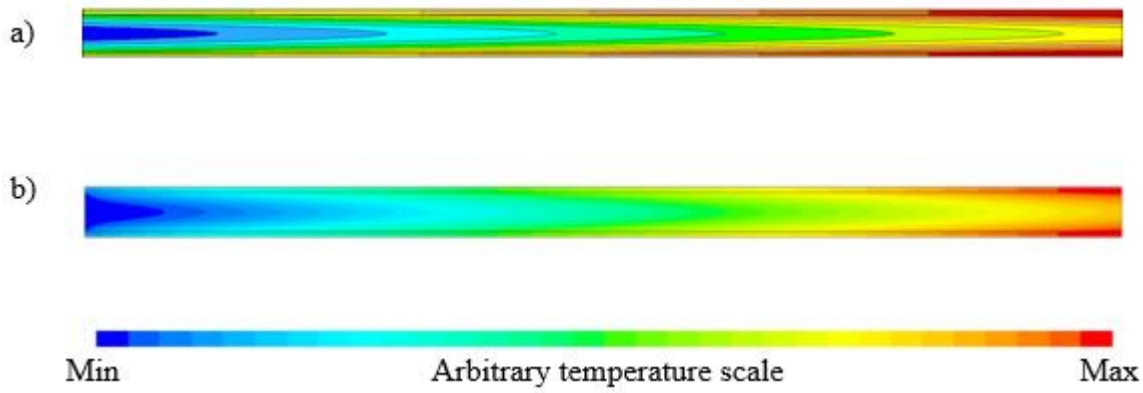

Figure B- 1 Comparison between the temperature fields in the microreactor, predicted: a) analytically and b) numerically.

Appendix C

Low Reynolds Number Turbulent Results

Contained in Appendix C are a compendium of figures and table created using results generated by a low Reynolds number turbulent model rather than a laminar model. They are presented here for comparative purposes and demonstrate that use of a turbulent model changes the results by only a small fraction and that all the observations and conclusions presented in chapter 7 hold true under these modelling conditions.

For comparison with Figure 7-5 to Figure 7-7 and Table 7-3 of chapter 7.

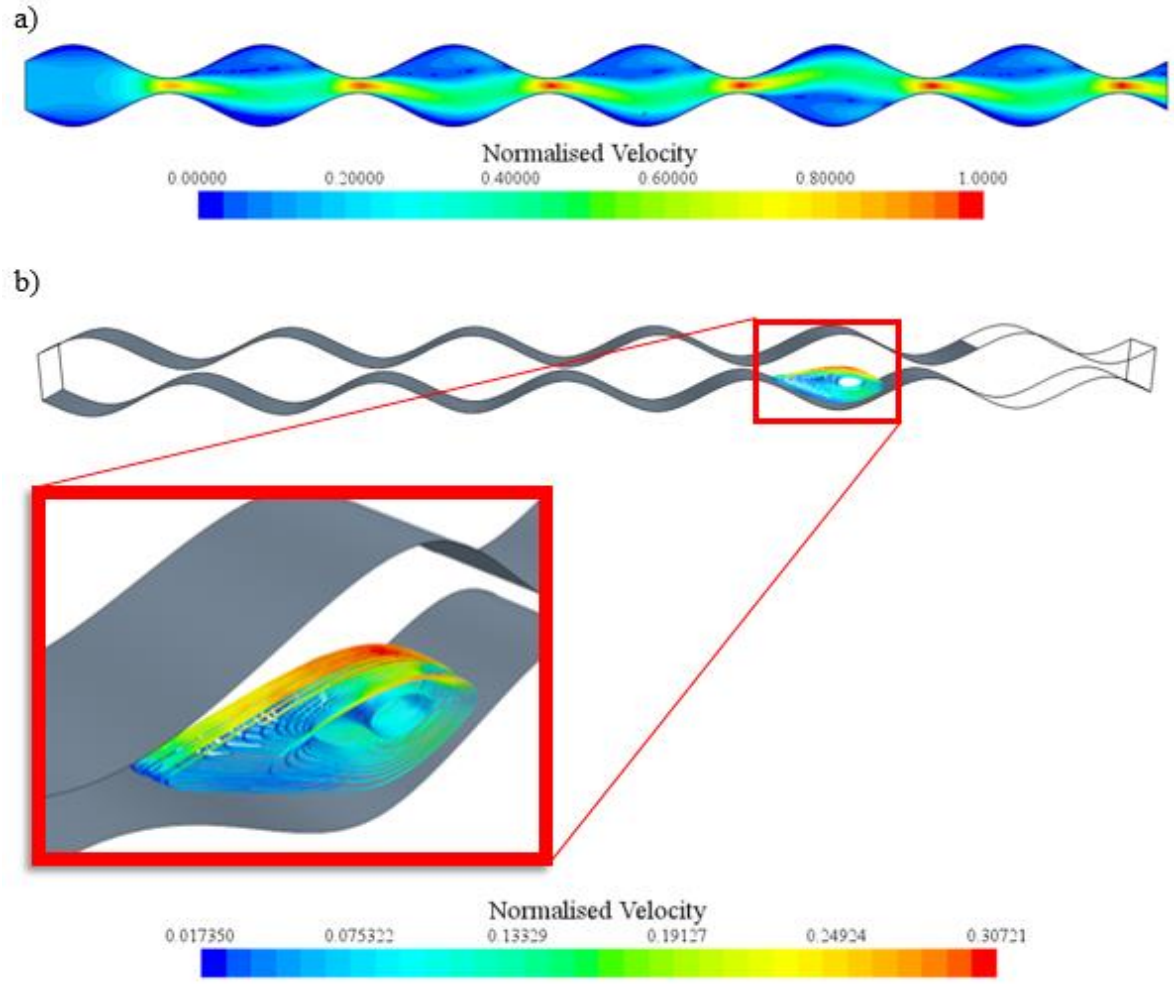

Figure C- 1 Normalised velocity in out of phase model for Re = 100 showing catalytic surface in grey using Low Re turbulent model; a) Normalised velocity field in a vertical section along the centre of the channel and b) normalised velocity profile in streamlines in the fifth trough of the channel.

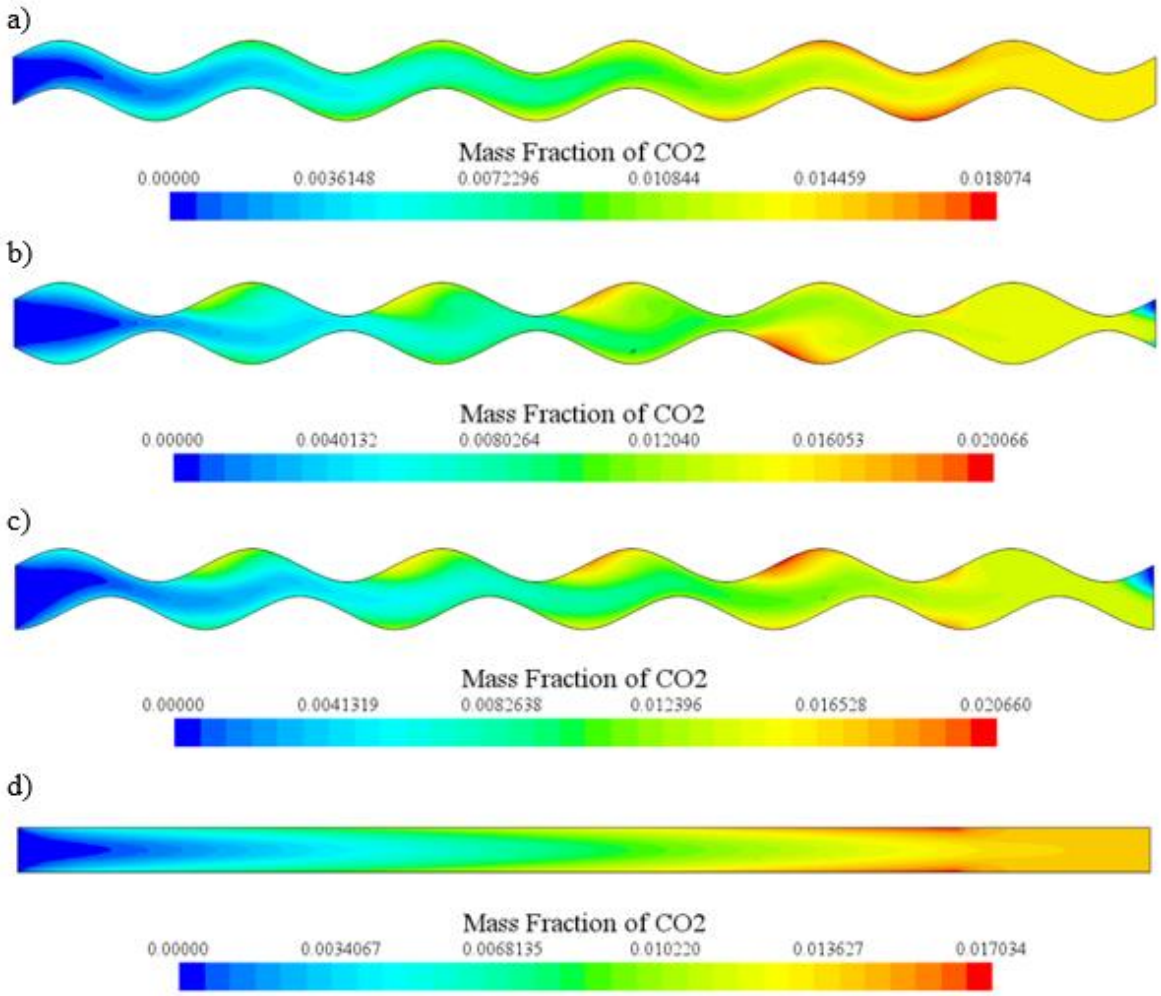

Figure C- 2 Mass fraction of CO_2 along a vertical section in the centre of the channel for at Re =150 for Low Re turbulent model for; a) IP model, b) OoP model, c) P1 model, and d) Clear channel model.

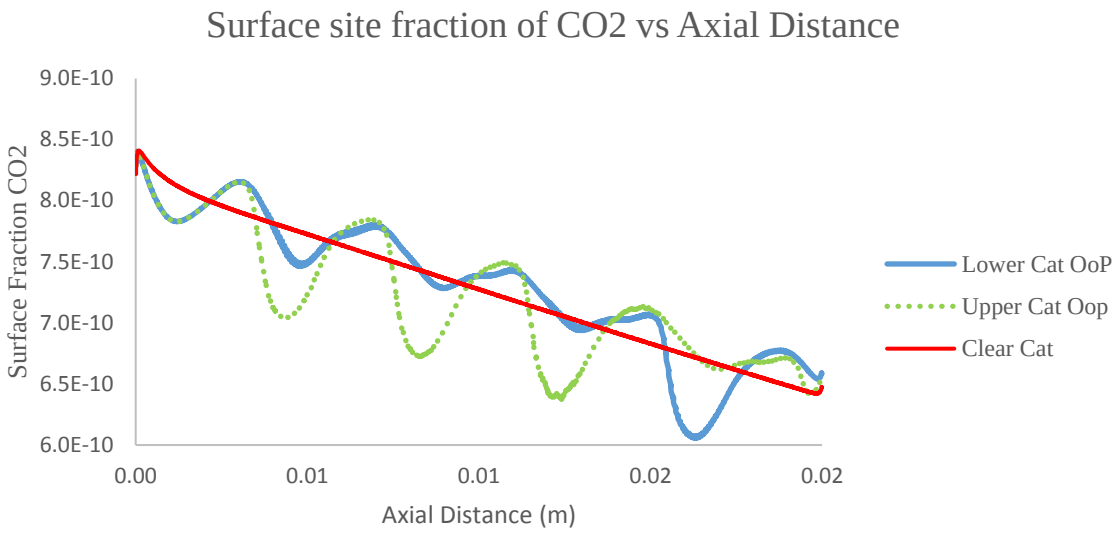

Figure C- 3 Surface site fraction of CO_2 as a function of axial distance for the OoP model with the clear channel values for comparison at $\boldsymbol{Re}$ = 150 for low Re turbulent model.

	Re = 50	Re = 100	Re = 150
Clear Channel	3.2629	1.9590	1.3900
OoP	3.2277	1.9425	1.3877
IP	3.2605	1.9564	1.3876
P1	3.2410	1.9402	1.3802

Table C- 1 Outlet mass fractions of carbon dioxide (x 10^{-2}) for low Re turbulent model

Bibliography

[1] UK Renewable Energy Roadmap, 2011. https://assets.publishing.service.gov.uk/government/uploads/system/uploads/attachment_data/file/48128/2167-uk-renewable-energy-roadmap.pdf (accessed January 31, 2019).

[2] Energy - Electricity Generation, (n.d.). https://www2.gov.scot/Topics/Statistics/Browse/Business/TrendElectricity (accessed January 31, 2019).

[3] High Level Summary of Statistics Trends - Chart data, (n.d.). https://www2.gov.scot/Topics/Statistics/Browse/Business/TrendData (accessed January 31, 2019).

[4] H. Kevin, BEIS Document Template - Standard Numbering, 2018. www.nationalarchives.gov.uk/doc/open-government- (accessed January 31, 2019).

[5] Electricity generation | Energy Charts, (n.d.). https://www.energy-charts.de/energy.htm?source=all-sources&period=annual&year=2018 (accessed January 31, 2019).

[6] E.U. Roadmap, E./ Eu, I. Roadmap, European Renewable Energy Council Mapping Renewable Energy Pathways towards 2020, n.d. www.inextremis.be (accessed January 31, 2019).

[7] 2050 Pathways - GOV.UK, (n.d.). https://www.gov.uk/guidance/2050-pathways-analysis (accessed September 19, 2019).

[8] 2050 Energy Strategy | Energy, (n.d.). https://ec.europa.eu/energy/en/topics/energy-strategy-and-energy-union/2050-energy-strategy (accessed September 19, 2019).

[9] UK energy in brief 2019 - GOV.UK, (n.d.). https://www.gov.uk/government/statistics/uk-energy-in-brief-2019 (accessed September 19, 2019).

[10] A. Chatzivasileiadi, E. Ampatzi, I. Knight, Characteristics of electrical energy storage technologies and their applications in buildings, Renew. Sustain. Energy Rev. 25 (2013) 814–830. doi:10.1016/J.RSER.2013.05.023.

[11] P.D. Lund, J. Lindgren, J. Mikkola, J. Salpakari, Review of energy system flexibility measures to enable high levels of variable renewable electricity, Renew. Sustain. Energy Rev. 45 (2015) 785–807. doi:10.1016/J.RSER.2015.01.057.

[12] R.. Dell, D.A.. Rand, Energy storage — a key technology for global energy sustainability, J. Power Sources. 100 (2001) 2–17. doi:10.1016/S0378-7753(01)00894-1.

[13] C.W. Gellings, W.M. Smith, Integrating demand-side management into utility planning, Proc. IEEE. 77 (1989) 908–918. doi:10.1109/5.29331.

[14] E. Hsieh, R. Anderson, Grid flexibility: The quiet revolution, Electr. J. 30 (2017) 1–8. doi:10.1016/J.TEJ.2017.01.009.

[15] E. Ela, M. Milligan, A. Bloom, A. Botterud, A. Townsend, T. Levin, B.A. Frew, Wholesale electricity market design with increasing levels of renewable generation: Incentivizing flexibility in system operations, Electr. J. 29 (2016) 51–60. doi:10.1016/J.TEJ.2016.05.001.

[16] US Department of Energy, Global Energy Database, (n.d.). http://www.energystorageexchange.org/ (accessed February 5, 2019).

[17] V. Koritarov, T. Veselka, J. Gasper, B. Bethke, A. Botterud, J. Wang, M. Mahalik, Z. Zhou, C. Milostan, J. Feltes, Y. Kazachkov, T. Guo, G. Liu, B. Trouille, P. Donalek, K. King, E. Ela, B. Kirby, I. Krad, V. Gevorgian, Modeling and Analysis of Value of Advanced Pumped Storage Hydropower in the United States, (n.d.). http://www.academia.edu/20597409/Modeling_and_Analysis_of_Value_of_Advanced_Pumped_Storage_Hydropower_in_the_United_States (accessed February 5, 2019).

[18] I. Stadler, M. Sterner, Urban Energy Storage and Sector Coupling, Urban Energy Transit. (2018) 225–244. doi:10.1016/B978-0-08-102074-6.00026-7.

[19] Grid Balancing | Beacon Power, (n.d.). http://beaconpower.com/grid-balancing/ (accessed February 28, 2019).

[20] F. Farret, M. Simoes, Integration of alternative sources of energy, 2006. https://books.google.com/books?hl=en&lr=&id=a8BJ3zYYd3MC&oi=fnd&pg=PR7&ots=KjRQAk6Nq3&sig=rse7vpshVejJE_Tr9IIhMk5dA44 (accessed July 8, 2019).

[21] P. Droege, Urban energy transition : from fossil fuels to renewable power, Elsevier, 2008.

[22] S. Succar, R.W.-P. environmental institute report, undefined 2008, Compressed air energy storage: theory, resources, and applications for wind power, Citeseer. (n.d.). http://citeseerx.ist.psu.edu/viewdoc/download?doi=10.1.1.374.7597&rep=rep1&type=pdf (accessed July 8, 2019).

[23] P. Bérest, B. Brouard, Safety of Salt Caverns Used for Underground Storage Blow Out; Mechanical Instability; Seepage; Cavern Abandonment INTRODUCTION: SOLUTION-MINED CAVERNS, 2003. https://ogst.ifpenergiesnouvelles.fr/articles/ogst/pdf/2003/03/berest_58n3.pdf (accessed July 8, 2019).

[24] D.C. Goodall, B. [illegible]berg, T.L. Brekke, Fundamentals of gas containment in unlined rock caverns, Rock Mech. Rock Eng. 21 (1988) 235–258. doi:10.1007/BF01020278.

[25] C. Bullough, C. Gatzen, C. Jakiel, M. Koller, A. Nowi, S. Zunft, Advanced Adiabatic Compressed Air Energy Storage for the Integration of Wind Energy, 2004. https://www.nrc.gov/docs/ML1129/ML11294A554.pdf (accessed March 21, 2019).

[26] H. Chen, T.N. Cong, W. Yang, C. Tan, Y. Li, Y. Ding, Progress in electrical energy storage system: A critical review, Prog. Nat. Sci. 19 (2009) 291–312. doi:10.1016/J.PNSC.2008.07.014.

[27] R.B. Schainker, Executive overview: energy storage options for a sustainable energy future, in: IEEE Power Eng. Soc. Gen. Meet. 2004., IEEE, n.d.: pp. 2310–2315. doi:10.1109/PES.2004.1373298.

[28] News Releases : October 31, 2018 : Hitachi Global, (n.d.). https://www.hitachi.com/New/cnews/month/2018/10/181031a.html (accessed September 19, 2019).

[29] M. Beaudin, H. Zareipour, A. Schellenberglabe, W. Rosehart, Energy storage for mitigating the variability of renewable electricity sources: An updated review, Energy Sustain. Dev. 14 (2010) 302–314. doi:10.1016/J.ESD.2010.09.007.

[30] J. McDowall, Integrating energy storage with wind power in weak electricity grids, J. Power Sources. 162 (2006) 959–964. doi:10.1016/J.JPOWSOUR.2005.06.034.

[31] B. Guo, M. Niu, X. Lai, L. Chen, Application research on large-scale battery energy storage system under Global Energy Interconnection framework, Glob. Energy Interconnect. 1 (2018) 79–86. doi:10.14171/J.2096-5117.GEI.2018.01.010.

[32] M. Jentsch, T. Trost, M. Sterner, Optimal Use of Power-to-Gas Energy Storage Systems in an 85% Renewable Energy Scenario, Energy Procedia. 46 (2014) 254–261. doi:10.1016/J.EGYPRO.2014.01.180.

[33] U. Bünger, J. Michalski, F. Crotogino, O. Kruck, Compendium of Hydrogen Energy Large-scale underground storage of hydrogen for the grid integration of renewable energy and other applications, (2016). doi:10.1016/B978-1-78242-364-5.00007-5.

[34] S. Schiebahn, T. Grube, M. Robinius, V. Tietze, B. Kumar, D. Stolten, Power to gas: Technological overview, systems analysis and economic assessment for a case study in Germany, Int. J. Hydrogen Energy. 40 (2015) 4285–4294. doi:10.1016/J.IJHYDENE.2015.01.123.

[35] W. Kreuter, H. Hofmann, Electrolysis: The important energy transformer in a world of sustainable energy, Int. J. Hydrogen Energy. 23 (1998) 661–666. doi:10.1016/S0360-3199(97)00109-2.

[36] J. Mergel, M. Carmo, D.F.-T. to renewable energy, undefined 2013, Status on technologies for hydrogen production by water electrolysis, Wiley Online Libr. (n.d.). https://onlinelibrary.wiley.com/doi/pdf/10.1002/9783527673872#page=449 (accessed July 28, 2019).

[37] A. Ursua, L.M. Gandia, P. Sanchis, Hydrogen Production From Water Electrolysis: Current Status and Future Trends, Proc. IEEE. 100 (2012) 410–426. doi:10.1109/JPROC.2011.2156750.

[38] R. Bhandari, C.A. Trudewind, P. Zapp, Life cycle assessment of hydrogen production via electrolysis – a review, J. Clean. Prod. 85 (2014) 151–163. doi:10.1016/J.JCLEPRO.2013.07.048.

[39] Ø. Ulleberg, T. Nakken, A. Eté, The wind/hydrogen demonstration system at Utsira in Norway: Evaluation of system performance using operational data and updated hydrogen energy system modeling tools, Int. J. Hydrogen Energy. 35 (2010) 1841–1852. doi:10.1016/J.IJHYDENE.2009.10.077.

[40] G. Gahleitner, Hydrogen from renewable electricity: An international review of power-to-gas pilot plants for stationary applications, Int. J. Hydrogen Energy. 38 (2013) 2039–2061. doi:10.1016/J.IJHYDENE.2012.12.010.

[41] K. Stangeland, D. Kalai, Z. Yu, CO2 Methanation: The Effect of Catalysts and Reaction Conditions, Energy Procedia. 105 (2017) 2022–2027. doi:10.1016/J.EGYPRO.2017.03.577.

[42] M. Belimov, D. Metzger, P. Pfeifer, On the temperature control in a microstructured packed bed reactor for methanation of CO/CO $_2$ mixtures, AIChE J. 63 (2017) 120–129. doi:10.1002/aic.15461.

[43] K.P. Brooks, J. Hu, H. Zhu, R.J. Kee, Methanation of carbon dioxide by hydrogen reduction using the Sabatier process in microchannel reactors, Chem. Eng. Sci. 62 (2007) 1161–1170. doi:10.1016/J.CES.2006.11.020.

[44] O. Görke, P. Pfeifer, K. Schubert, Highly selective methanation by the use of a microchannel reactor, Catal. Today. 110 (2005) 132–139. doi:10.1016/J.CATTOD.2005.09.009.

[45] T. Schaaf, J. Grünig, M.R. Schuster, T. Rothenfluh, A. Orth, Methanation of CO2 - storage of renewable energy in a gas distribution system, Energy. Sustain. Soc. 4 (2014) 2. doi:10.1186/s13705-014-0029-1.

[46] J.R. Rostrup-Nielsen, Industrial relevance of coking, Catal. Today. 37 (1997) 225–232. doi:10.1016/S0920-5861(97)00016-3.

[47] C.H. Bartholomew, Mechanisms of catalyst deactivation, Appl. Catal. A Gen. 212 (2001) 17–60. doi:10.1016/S0926-860X(00)00843-7.

[48] J. Kopyscinski, T.J. Schildhauer, S.M.A. Biollaz, Production of synthetic natural gas (SNG) from coal and dry biomass – A technology review from 1950 to 2009, Fuel. 89 (2010) 1763–1783. doi:10.1016/J.FUEL.2010.01.027.

[49] W. SHEN, Criteria for stable Ni particle size under methanation reaction conditions: Nickel transport and particle size growth via nickel carbonyl, J. Catal. 68 (1981) 152–165. doi:10.1016/0021-9517(81)90048-8.

[50] J. Kopyscinski, T.J. Schildhauer, S.M.A. Biollaz, Methanation in a fluidized bed reactor with high initial CO partial pressure: Part I—Experimental investigation of hydrodynamics, mass transfer effects, and carbon deposition, Chem. Eng. Sci. 66 (2011) 924–934. doi:10.1016/J.CES.2010.11.042.

[51] J. Lefebvre, M. Götz, S. Bajohr, R. Reimert, T. Kolb, Improvement of three-phase methanation reactor performance for steady-state and transient operation, Fuel Process. Technol. 132 (2015) 83–90. doi:10.1016/J.FUPROC.2014.10.040.

[52] T. Wang, J. Wang, Y. Jin, Slurry Reactors for Gas-to-Liquid Processes: A Review, (2007). doi:10.1021/ie070330t.

[53] M. Sudiro, A. Bertucco, G. Groppi, E. Tronconi, Simulation of a structured catalytic reactor for exothermic methanation reactions producing synthetic natural gas, Comput. Aided Chem. Eng. 28 (2010) 691–696. doi:10.1016/S1570-7946(10)28116-6.

[54] T.J. Schildhauer, S.M.A. Biollaz, SCCER BIOSWEET-ThE SWISS COmpETEnCE CEnTER fOR EnERgy RESEaRCh On BIOEnERgy Reactors for Catalytic Methanation in the Conversion of Biomass to Synthetic Natural Gas (SNG), Chimia (Aarau). 69 (2015)

603–607. doi:10.2533/chimia.2015.603.

[55] G. Kolb, V. Hessel, Micro-structured reactors for gas phase reactions, Chem. Eng. J. 98 (2004) 1–38. doi:10.1016/J.CEJ.2003.10.005.

[56] V. Hessel, A. Renken, J.C. Schouten, J.I. Yoshida, Micro Process Engineering: A Comprehensive Handbook, 2013. doi:10.1002/9783527631445.

[57] V. Hessel, S. Hardt, H. Löwe, Chemical Micro Process Engineering: Fundamentals, Modelling and Reactions, 2004. doi:10.1002/3527603042.fmatter.

[58] X. Yao, Y. Zhang, L. Du, J. Liu, J. Yao, Review of the applications of microreactors, Renew. Sustain. Energy Rev. 47 (2015) 519–539. doi:10.1016/j.rser.2015.03.078.

[59] G. Kolb, Review: Microstructured reactors for distributed and renewable production of fuels and electrical energy, Chem. Eng. Process. Process Intensif. 65 (2013) 1–44. doi:10.1016/J.CEP.2012.10.015.

[60] F. Yao, Y. Chen, G.P. Peterson, Hydrogen production by methanol steam reforming in a disc microreactor with tree-shaped flow architectures, Int. J. Heat Mass Transf. 64 (2013) 418–425. doi:10.1016/j.ijheatmasstransfer.2013.04.057.

[61] A. Kück, M. Steinfeldt, K. Prenzel, P. Swiderek, a V Gleich, J. Thöming, Green nanoparticle production using micro reactor technology, in: J. Phys. Conf. Ser., 2011: p. 012074. doi:10.1088/1742-6596/304/1/012074.

[62] N.S. Kaisare, D.G. Vlachos, A review on microcombustion: Fundamentals, devices and applications, Prog. Energy Combust. Sci. 38 (2012) 321–359. doi:10.1016/j.pecs.2012.01.001.

[63] D.M. Roberge, L. Ducry, N. Bieler, P. Cretton, B. Zimmermann, Microreactor technology: A revolution for the fine chemical and pharmaceutical industries?, Chem. Eng. Technol. 28 (2005) 318–323. doi:10.1002/ceat.200407128.

[64] A. Tanimu, S. Jaenicke, K. Alhooshani, Heterogeneous catalysis in continuous flow microreactors: A review of methods and applications, Chem. Eng. J. 327 (2017) 792–821. doi:10.1016/j.cej.2017.06.161.

[65] E. V. Rebrov, J.C. Schouten, M.H.J.M. de Croon, Single-phase fluid flow distribution and heat transfer in microstructured reactors, Chem. Eng. Sci. 66 (2011) 1374–1393. doi:10.1016/j.ces.2010.05.044.

[66] N. Kockmann, Transport phenomena in micro process engineering, Springer, 2008.

[67] R. Guettel, T. Turek, Assessment of micro-structured fixed-bed reactors for highly exothermic gas-phase reactions, Chem. Eng. Sci. 65 (2010) 1644–1654. doi:10.1016/j.ces.2009.11.002.

[68] E.R. Delsman, M.H.J.M. de Croon, G.D. Elzinga, P.D. Cobden, G.J. Kramer, J.C. Schouten, The influence of differences between microchannels on microreactor performance, Chem. Eng. Technol. 28 (2005) 367–375. doi:10.1002/ceat.200407126.

[69] J. Li, S.K. Chou, Z.W. Li, W.M. Yang, Experimental investigation of porous media combustion in a planar micro-combustor, Fuel. 89 (2010) 708–715. doi:10.1016/j.fuel.2009.06.026.

[70] M. Torabi, N. Karimi, G.P. Peterson, S. Yee, Challenges and progress on the modeling of entropy generation in porous media: A review, Int. J. Heat Mass Transf. 114 (2017) 31–46. doi:http://dx.doi.org/10.1016.

[71] H. Namkung, X. Yuan, G. Lee, D. Kim, T.J. Kang, H.T. Kim, Reaction characteristics through catalytic steam gasification with ultra clean coal char and coal, J. Energy Inst. 87 (2014) 253–262. doi:10.1016/j.joei.2014.03.003.

[72] Y. Elias, P. Rudolf von Rohr, W. Bonrath, J. Medlock, A. Buss, A porous structured reactor for hydrogenation reactions, Chem. Eng. Process. Process Intensif. 95 (2015) 175–185. doi:10.1016/j.cep.2015.05.012.

[73] A. Avril, C.H. Hornung, A. Urban, D. Fraser, M. Horne, J.-P. Veder, J. Tsanaktsidis, T. Rodopoulos, C. Henry, D.R. Gunasegaram, Continuous flow hydrogenations using novel catalytic static mixers inside a tubular reactor, React. Chem. Eng. 2 (2017) 180–188. doi:10.1039/C6RE00188B.

[74] J.-I. Yoshida, A. Nagaki, T. Iwasaki, S. Suga, Enhancement of Chemical Selectivity by Microreactors, (n.d.). doi:10.1002/ceat.200407127.

[75] T. Fukuyama, Y. Hino, N. Kamata, I. Ryu, Quick Execution of [2+2] Type Photochemical Cycloaddition Reaction by Continuous Flow System Using a Glass-made Microreactor, Chem. Lett. 33 (2004) 1430–1431. doi:10.1246/cl.2004.1430.

[76] V. Kumar, M. Paraschivoiu, K.D.P. Nigam, Single-phase fluid flow and mixing in microchannels, Chem. Eng. Sci. 66 (2011) 1329–1373. doi:10.1016/j.ces.2010.08.016.

[77] V. Hessel, A. Renken, J.C. Schouten, J.-I. Yoshida, eds., Micro Process Engineering, Wiley-VCH Verlag GmbH & Co. KGaA, Weinheim, Germany, 2009. doi:10.1002/9783527631445.

[78] M.J. Stutz, D. Poulikakos, Effects of microreactor wall heat conduction on the reforming process of methane, Chem. Eng. Sci. 60 (2005) 6983–6997. doi:10.1016/j.ces.2005.06.012.

[79] T. Wirth, Microreactors in Organic Chemistry and Catalysis, (2013) 470.

[80] Y. Hao, X. Du, L. Yang, Y. Shen, Y. Yang, Numerical simulation of configuration and catalyst-layer effects on micro-channel steam reforming of methanol, Int. J. Hydrogen Energy. 36 (2011) 15611–15621. doi:10.1016/j.ijhydene.2011.09.038.

[81] X. Yao, Y. Zhang, L. Du, J. Liu, J. Yao, Review of the applications of microreactors, Renew. Sustain. Energy Rev. 47 (2015) 519–539. doi:10.1016/j.rser.2015.03.078.

[82] H. Ammar, B. Garnier, A. Ould el Moctar, H. Willaime, F. Monti, H. Peerhossaini, Thermal analysis of chemical reactions in microchannels using highly sensitive thin-film heat-flux microsensor, Chem. Eng. Sci. 94 (2013) 150–155. doi:10.1016/j.ces.2013.02.055.

[83] R. Sui, N.I. Prasianakis, J. Mantzaras, N. Mallya, J. Theile, D. Lagrange, M. Friess, An

experimental and numerical investigation of the combustion and heat transfer characteristics of hydrogen-fueled catalytic microreactors, Chem. Eng. Sci. 141 (2016) 214–230. doi:10.1016/j.ces.2015.10.034.

[84] S. Schwolow, J.Y. Ko, N. Kockmann, T. Roder, Enhanced heat transfer by exothermic reactions in laminar flow capillary reactors, Chem. Eng. Sci. 141 (2016) 356–362. doi:10.1016/j.ces.2015.11.022.

[85] M. Torabi, M. Torabi, G.P. Peterson, Entropy Generation of Double Diffusive Forced Convection in Porous Channels with Thick Walls and Soret Effect, Entropy. 19 (2017) 171. doi:10.3390/e19040171.

[86] M. Torabi, K. Zhang, Temperature distribution, local and total entropy generation analyses in MHD porous channels with thick walls, Energy. 87 (2015) 540–554. doi:10.1016/j.energy.2015.05.009.

[87] M. Kaviany, Principles of heat transfer in porous media, 2012.

[88] D. Nield, A. Bejan, Convection in Porous Media, (2013).

[89] K. Vafai, Handbook of porous media, 2015.

[90] K. Wang, K. Vafai, D. Wang, Analytical characterization of gaseous slip flow and heat transport through a parallel-plate microchannel with a centered porous substrate, Int. J. Numer. Methods Heat Fluid Flow. 26 (2016) 854–878. doi:10.1108/HFF-09-2015-0364.

[91] B. Alazmi, K. Vafai, Constant wall heat flux boundary conditions in porous media under local thermal non-equilibrium conditions, Int. J. Heat Mass Transf. 45 (2002) 3071–3087. doi:10.1016/S0017-9310(02)00044-3.

[92] D.-Y. Lee, K. Vafai, Analytical characterization and conceptual assessment of solid and fluid temperature differentials in porous media, Int. J. Heat Mass Transf. 42 (1999) 423–435. doi:10.1016/S0017-9310(98)00185-9.

[93] N. Karimi, D. Agbo, A. Talat Khan, P.L. Younger, On the effects of exothermicity and endothermicity upon the temperature fields in a partially-filled porous channel, Int. J. Therm. Sci. 96 (2015) 128–148. doi:10.1016/j.ijthermalsci.2015.05.002.

[94] K. Yang, K. Vafai, Analysis of temperature gradient bifurcation in porous media – An exact solution, Int. J. Heat Mass Transf. 53 (2010) 4316–4325. doi:10.1016/j.ijheatmasstransfer.2010.05.060.

[95] M. Torabi, C. Dickson, N. Karimi, Theoretical investigation of entropy generation and heat transfer by forced convection of copper–water nanofluid in a porous channel — Local thermal non-equilibrium and partial filling effects, Powder Technol. 301 (2016) 234–254. doi:10.1016/j.powtec.2016.06.017.

[96] Y. Mahmoudi, N. Karimi, Numerical investigation of heat transfer enhancement in a pipe partially filled with a porous material under local thermal non-equilibrium condition, Int. J. Heat Mass Transf. 68 (2014) 161–173. doi:10.1016/j.ijheatmasstransfer.2013.09.020.

[97] C. Dickson, M. Torabi, N. Karimi, First and second law analyses of nanofluid forced

convection in a partially-filled porous channel – The effects of local thermal non-equilibrium and internal heat sources, Appl. Therm. Eng. 103 (2016) 459–480. doi:10.1016/j.applthermaleng.2016.04.095.

[98] M. Torabi, N. Karimi, K. Zhang, G.P. Peterson, Generation of entropy and forced convection of heat in a conduit partially filled with porous media – Local thermal non-equilibrium and exothermicity effects, Appl. Therm. Eng. 106 (2016) 518–536. doi:10.1016/j.applthermaleng.2016.06.036.

[99] Y. Mahmoudi, N. Karimi, K. Mazaheri, Analytical investigation of heat transfer enhancement in a channel partially filled with a porous material under local thermal non-equilibrium condition: Effects of different thermal boundary conditions at the porous-fluid interface, Int. J. Heat Mass Transf. 70 (2014) 875–891. doi:10.1016/J.IJHEATMASSTRANSFER.2013.11.048.

[100] A. Elliott, M. Torabi, N. Karimi, S. Cunningham, On the effects of internal heat sources upon forced convection in porous channels with asymmetric thick walls, Int. Commun. Heat Mass Transf. 73 (2016) 100–110. doi:10.1016/j.icheatmasstransfer.2016.02.016.

[101] K. Hooman, Heat and fluid flow in a rectangular microchannel filled with a porous medium, Int. J. Heat Mass Transf. 51 (2008) 5804–5810. doi:10.1016/j.ijheatmasstransfer.2008.05.010.

[102] B. Buonomo, O. Manca, G. Lauriat, Forced convection in micro-channels filled with porous media in local thermal non-equilibrium conditions, Int. J. Therm. Sci. 77 (2014) 206–222.

[103] R.-Y. Chein, L.-C. Chen, Y.-C. Chen, J.N. Chung, Heat transfer effects on the methanol-steam reforming with partially filled catalyst layers, Int. J. Hydrogen Energy. 34 (2009) 5398–5408. doi:10.1016/j.ijhydene.2009.04.049.

[104] R.-Y. Chein, Y.-C. Chen, J.N. Chung, Thermal resistance effect on methanol-steam reforming performance in micro-scale reformers, Int. J. Hydrogen Energy. 37 (2012) 250–262. doi:10.1016/j.ijhydene.2011.09.070.

[105] R.-Y. Chein, Y.-C. Chen, H.-J. Zhu, J.N. Chung, Numerical Simulation of Flow Disturbance and Heat Transfer Effects on the Methanol-Steam Reforming in Miniature Annulus Type Reformers, Energy & Fuels. 26 (2012) 1202–1213. doi:10.1021/ef201498t.

[106] R. Chein, Y.-C. Chen, J.N. Chung, Axial heat conduction and heat supply effects on methanol-steam reforming performance in micro-scale reformers, Int. J. Heat Mass Transf. 55 (2012) 3029–3042. doi:10.1016/j.ijheatmasstransfer.2012.02.022.

[107] G. Arzamendi, P.M. Diéguez, M. Montes, J.A. Odriozola, E. Falabella Sousa-Aguiar, L.M. Gandía, Computational fluid dynamics study of heat transfer in a microchannel reactor for low-temperature Fischer–Tropsch synthesis, Chem. Eng. J. 160 (2010) 915–922. doi:10.1016/j.cej.2009.12.028.

[108] M. Torabi, N. Karimi, K. Zhang, Heat transfer and second law analyses of forced convection in a channel partially filled by porous media and featuring internal heat sources, Energy. 93 (2015) 106–127. doi:10.1016/j.energy.2015.09.010.

[109] N. Karimi, D. Agbo, A. Khan, P. Younger, On the effects of exothermicity and endothermicity upon the temperature fields in a partially-filled porous channel, Int. J.

Therm. (2015).

[110] G. Ibáñez, A. López, J. Pantoja, J. Moreira, J. Reyes, Optimum slip flow based on the minimization of entropy generation in parallel plate microchannels, Energy. (2013).

[111] M. Torabi, G.P. Peterson, Effects of velocity slip and temperature jump on the heat transfer and entropy generation in micro porous channels under magnetic field, Int. J. Heat Mass Transf. 102 (2016) 585–595. doi:10.1016/j.ijheatmasstransfer.2016.06.080.

[112] T.W. Ting, Y.M. Hung, N. Guo, Viscous dissipative forced convection in thermal non-equilibrium nanofluid-saturated porous media embedded in microchannels, Int. Commun. Heat Mass Transf. 57 (2014) 309–318. doi:10.1016/j.icheatmasstransfer.2014.08.018.

[113] T.W. Ting, Y.M. Hung, N. Guo, Field-synergy analysis of viscous dissipative nanofluid flow in microchannels, Int. J. Heat Mass Transf. 73 (2014) 483–491. doi:10.1016/j.ijheatmasstransfer.2014.02.041.

[114] T.W. Ting, Y.M. Hung, N. Guo, Entropy generation of nanofluid flow with streamwise conduction in microchannels, Energy. 64 (2014) 979–990. doi:10.1016/j.energy.2013.10.064.

[115] T.W. Ting, Y.M. Hung, N. Guo, Entropy generation of viscous dissipative nanofluid convection in asymmetrically heated porous microchannels with solid-phase heat generation, Energy Convers. Manag. 105 (2015) 731–745. doi:10.1016/j.enconman.2015.08.022.

[116] G. Ibáñez, S. Cuevas, Entropy generation minimization of a MHD (magnetohydrodynamic) flow in a microchannel, Energy. 35 (2010) 4149–4155. doi:10.1016/j.energy.2010.06.035.

[117] M. Torabi, A. Elliott, N.K. Karimi, Thermodynamics analyses of porous microchannels with asymmetric thick walls and exothermicity: An entropic model of micro-reactors, J. Therm. Sci. Eng. Appl. (2017). doi:10.1115/1.4036802.

[118] B.R. Bakshi, T.G.P. Gutowski, D.P. Sekulić, Thermodynamics and the destruction of resources, Cambridge University Press, 2011.

[119] M. Torabi, K. Zhang, N. Karimi, G. Peterson, Entropy generation in thermal systems with solid structures–A concise review, Int. J. Heat Mass Transf. (2016).

[120] M. Mahdavi, M. Saffar-Avval, S. Tiari, Z. Mansoori, Entropy generation and heat transfer numerical analysis in pipes partially filled with porous medium, Int. J. Heat Mass Transf. 79 (2014) 496–506. doi:10.1016/j.ijheatmasstransfer.2014.08.037.

[121] M. Siavashi, H.R. Talesh Bahrami, H. Saffari, Numerical investigation of flow characteristics, heat transfer and entropy generation of nanofluid flow inside an annular pipe partially or completely filled with porous media using two-phase mixture model, Energy. 93 (2015) 2451–2466. doi:10.1016/j.energy.2015.10.100.

[122] Y.S. Chee, T.W. Ting, Y.M. Hung, Entropy generation of viscous dissipative flow in thermal non-equilibrium porous media with thermal asymmetries, Energy. 89 (2015) 382–401. doi:10.1016/j.energy.2015.05.118.

[123] Y. Wenming, J. Dongyue, C.K.Y. Kenny, Z. Dan, P. Jianfeng, Combustion process and entropy generation in a novel microcombustor with a block insert, Chem. Eng. J. 274 (2015) 231–237. doi:10.1016/j.cej.2015.04.034.

[124] U. Rana, S. Chakraborty, S.K. Som, Thermodynamics of premixed combustion in a heat recirculating micro combustor, Energy. 68 (2014) 510–518. doi:10.1016/j.energy.2014.02.070.

[125] D. Jiang, W. Yang, K.J. Chua, Entropy generation analysis of H2/air premixed flame in micro-combustors with heat recuperation, Chem. Eng. Sci. 98 (2013) 265–272. doi:10.1016/j.ces.2013.05.038.

[126] W.-H. Chen, T.-C. Cheng, C.-I. Hung, Numerical predictions on thermal characteristic and performance of methanol steam reforming with microwave-assisted heating, Int. J. Hydrogen Energy. 36 (2011) 8279–8291. doi:10.1016/j.ijhydene.2011.04.145.

[127] A. Bejan, Fundamentals of exergy analysis, entropy generation minimization, and the generation of flow architecture, Int. J. Energy Res. (2002).

[128] S.K. Som, A. Datta, Thermodynamic irreversibilities and exergy balance in combustion processes, Prog. Energy Combust. Sci. 34 (2008) 351–376. doi:10.1016/j.pecs.2007.09.001.

[129] T.W. Ting, Y.M. Hung, N. Guo, Entropy generation of viscous dissipative nanofluid flow in thermal non-equilibrium porous media embedded in microchannels, Int. J. Heat Mass Transf. 81 (2015) 862–877. doi:10.1016/j.ijheatmasstransfer.2014.11.006.

[130] M. Torabi, K. Zhang, N. Karimi, G.P. Peterson, Entropy generation in thermal systems with solid structures – A concise review, Int. J. Heat Mass Transf. 97 (2016) 917–931. doi:10.1016/j.ijheatmasstransfer.2016.03.007.

[131] H. Abbassi, Entropy generation analysis in a uniformly heated microchannel heat sink, Energy. 32 (2007) 1932–1947. doi:10.1016/j.energy.2007.02.007.

[132] X. Kang, R.J. Gollan, P.A. Jacobs, A. Veeraragavan, On the influence of modelling choices on combustion in narrow channels, Comput. Fluids. 144 (2017) 117–136. doi:10.1016/J.COMPFLUID.2016.11.017.

[133] O. Deutschmann, R. Schmidt, F. Behrendt, J. Warnatz, NUMERICAL MODELING OF CATALYTIC IGNITION, (1996) 1747–1754.

[134] S.M. Peyghambarzadeh, S.H. Hashemabadi, A.R. Chabi, M. Salimi, Performance of water based CuO and Al2O3 nanofluids in a Cu–Be alloy heat sink with rectangular microchannels, Energy Convers. Manag. 86 (2014) 28–38. doi:10.1016/J.ENCONMAN.2014.05.013.

[135] M. Götz, J. Lefebvre, F. Mörs, A. McDaniel Koch, F. Graf, S. Bajohr, R. Reimert, T. Kolb, Renewable Power-to-Gas: A technological and economic review, Renew. Energy. 85 (2016) 1371–1390. doi:10.1016/J.RENENE.2015.07.066.

[136] H. Pennemann, G. Kolb, Review: Microstructured reactors as efficient tool for the operation of selective oxidation reactions, Catal. Today. 278 (2016) 3–21. doi:10.1016/J.CATTOD.2016.04.032.

[137] D.C. Walther, J. Ahn, Advances and challenges in the development of power-generation systems at small scales, Prog. Energy Combust. Sci. 37 (2011) 583–610. doi:10.1016/J.PECS.2010.12.002.

[138] Y. Lei, W. Chen, J. Lei, Combustion and direct energy conversion inside a micro-combustor, Appl. Therm. Eng. 100 (2016) 348–355. doi:10.1016/j.applthermaleng.2016.01.162.

[139] M. Zanfir, A. Gavriilidis, Catalytic combustion assisted methane steam reforming in a catalytic plate reactor, Chem. Eng. Sci. 58 (2003) 3947–3960. doi:10.1016/S0009-2509(03)00279-3.

[140] J. Warnatz, M.D. Allendorf, R.J. Kee, M.E. Coltrin, A model of elementary chemistry and fluid mechanics in the combustion of hydrogen on platinum surfaces, Combust. Flame. 96 (1994) 393–406. doi:10.1016/0010-2180(94)90107-4.

[141] J. Chen, L. Yan, W. Song, D. Xu, Effect of heat and mass transfer on the combustion stability in catalytic micro-combustors, Appl. Therm. Eng. 131 (2018) 750–765. doi:10.1016/J.APPLTHERMALENG.2017.12.059.

[142] S. Raimondeau, D. Norton, D.G. Vlachos, R.I. Masel, Modeling of high-temperature microburners, Proc. Combust. Inst. 29 (2002) 901–907. doi:10.1016/S1540-7489(02)80114-6.

[143] M.-T. Lee, C.P. Grigoropoulos, R. Greif, A study of the transport phenomena in a wall-coated micro steam-methanol reformer, Int. J. Hydrogen Energy. 39 (2014) 2008–2017. doi:10.1016/j.ijhydene.2013.11.107.

[144] D.A. Hickman, L.D. Schmidt, Steps in CH4 oxidation on Pt and Rh surfaces: High-temperature reactor simulations, AIChE J. 39 (1993) 1164–1177. doi:10.1002/aic.690390708.

[145] F.P. Incropera, D.P. DeWitt, T.L. Bergman, A.S. Lavine, Fundamentals of Heat and Mass Transfer, John Wiley & Sons, 2007. doi:10.1016/j.applthermaleng.2011.03.022.

[146] W.M. Deen, Analysis of transport phenomena, Oxford University Press, 1998.

[147] O. Deutschmann, F. Behrendt, J. Warnatz, Modelling and simulation of heterogeneous oxidation of methane on a platinum foil, Catal. Today. 21 (1994) 461–470. doi:10.1016/0920-5861(94)80168-1.

[148] N.E. McGuire, N.P. Sullivan, O. Deutschmann, H. Zhu, R.J. Kee, Dry reforming of methane in a stagnation-flow reactor using Rh supported on strontium-substituted hexaaluminate, Appl. Catal. A Gen. 394 (2011) 257–265. doi:10.1016/J.APCATA.2011.01.009.

[149] C. Karakaya, O. Deutschmann, Kinetics of hydrogen oxidation on Rh/Al2O3 catalysts studied in a stagnation-flow reactor, Chem. Eng. Sci. 89 (2013) 171–184. doi:10.1016/j.ces.2012.11.004.

[150] H. Karadeniz, C. Karakaya, S. Tischer, O. Deutschmann, Numerical modeling of stagnation-flows on porous catalytic surfaces: CO oxidation on Rh/Al2O3, Chem. Eng. Sci.

104 (2013) 899–907. doi:10.1016/j.ces.2013.09.038.

[151] O. Deutschmann, Modeling of the Interactions Between Catalytic Surfaces and Gas-Phase, Catal. Letters. 145 (2015) 272–289. doi:10.1007/s10562-014-1431-1.

[152] O. Deutschmann, L.D. Schmidt, Modeling the partial oxidation of methane in a short-contact-time reactor, AIChE J. 44 (1998) 2465–2477. doi:10.1002/aic.690441114.

[153] O. Deutschmann, L.. Maier, U. Riedel, A.. Stroemman, R.. Dibble, Hydrogen assisted catalytic combustion of methane on platinum, Catal. Today. 59 (2000) 141–150. doi:10.1016/S0920-5861(00)00279-0.

[154] I. Cerri, G. Saracco, V. Specchia, Methane combustion over low-emission catalytic foam burners, Catal. Today. 60 (2000) 21–32. doi:10.1016/S0920-5861(00)00313-8.

[155] T. Numaguchi, K. Shoji, S. Yoshida, Hydrogen effect on α-Al2O3 supported Ni catalyst for steam methane reforming reaction, Appl. Catal. A Gen. 133 (1995) 241–262. doi:10.1016/0926-860X(95)00188-3.

[156] R. Quiceno, J. Pérez-Ramírez, J. Warnatz, O. Deutschmann, Modeling the high-temperature catalytic partial oxidation of methane over platinum gauze: Detailed gas-phase and surface chemistries coupled with 3D flow field simulations, Appl. Catal. A Gen. 303 (2006) 166–176. doi:10.1016/J.APCATA.2006.01.041.

[157] C.R.H. de Smet, M.H.J.M. de Croon, R.J. Berger, G.B. Marin, J.C. Schouten, An experimental reactor to study the intrinsic kinetics of catalytic partial oxidation of methane in the presence of heat-transport limitations, Appl. Catal. A Gen. 187 (1999) 33–48. doi:10.1016/S0926-860X(99)00181-7.

[158] M.-F. Reyniers, C.R.H. de Smet, P.G. Menon, G.B. Marin, Catalytic Partial Oxidation. Part I. Catalytic Processes to Convert Methane: Partial or Total Oxidation, CATTECH. 6 (2002) 140–149. doi:10.1023/A:1021279211358.

[159] J.-H. Cho, C.S. Lin, C.D. Richards, R.F. Richards, J. Ahn, P.D. Ronney, Demonstration of an external combustion micro-heat engine, Proc. Combust. Inst. 32 (2009) 3099–3105. doi:10.1016/J.PROCI.2008.07.017.

[160] C. Amador, A. Gavriilidis, P. Angeli, Flow distribution in different microreactor scale-out geometries and the effect of manufacturing tolerances and channel blockage, Chem. Eng. J. 101 (2004) 379–390. doi:10.1016/J.CEJ.2003.11.031.

[161] D. Tondeur, L. Luo, Design and scaling laws of ramified fluid distributors by the constructal approach, Chem. Eng. Sci. 59 (2004) 1799–1813. doi:10.1016/j.ces.2004.01.034.

[162] O. Tonomura, S. Tanaka, M. Noda, M. Kano, S. Hasebe, I. Hashimoto, CFD-based optimal design of manifold in plate-fin microdevices, Chem. Eng. J. 101 (2004) 397–402. doi:10.1016/J.CEJ.2003.10.022.

[163] B.-J. Zhong, J.-H. Wang, Experimental study on premixed CH4/air mixture combustion in micro Swiss-roll combustors, Combust. Flame. 157 (2010) 2222–2229. doi:10.1016/j.combustflame.2010.07.014.

[164] W.M. Yang, S.K. Chou, K.J. Chua, J. Li, X. Zhao, Research on modular micro combustor-radiator with and without porous media, Chem. Eng. J. 168 (2011) 799–802. doi:10.1016/J.CEJ.2010.12.083.

[165] A. Fan, J. Wan, Y. Liu, B. Pi, H. Yao, W. Liu, Effect of bluff body shape on the blow-off limit of hydrogen/air flame in a planar micro-combustor, Appl. Therm. Eng. 62 (2014) 13–19. doi:10.1016/j.applthermaleng.2013.09.010.

[166] Y. Yan, Z. He, Q. Xu, L. Zhang, L. Li, Z. Yang, J. Ran, Numerical study on premixed hydrogen/air combustion characteristics in micro–combustor with slits on both sides of the bluff body, Int. J. Hydrogen Energy. 44 (2019) 1998–2012. doi:10.1016/j.ijhydene.2018.11.128.

[167] J. Mantzaras, Progress in non-intrusive laser-based measurements of gas-phase thermoscalars and supporting modeling near catalytic interfaces, Prog. Energy Combust. Sci. 70 (2019) 169–211. doi:10.1016/J.PECS.2018.10.005.

[168] J. Mantzaras, Understanding and modeling of thermofluidic processes in catalytic combustion, Catal. Today. 117 (2006) 394–406. doi:10.1016/J.CATTOD.2006.06.047.

[169] K. Vafai, C.L. Tien, Boundary and inertia effects on flow and heat transfer in porous media, Int. J. Heat Mass Transf. 24 (1981) 195–203. doi:10.1016/0017-9310(81)90027-2.

[170] S. Whitaker, The method of volume averaging, 1998.

[171] K. Vafai, Handbook of porous media, Marcel Dekker, New York, 2000.

[172] † D. G. Norton, ‡ and E. D. Wetzel, † D. G. Vlachos*, Fabrication of Single-Channel Catalytic Microburners: Effect of Confinement on the Oxidation of Hydrogen/Air Mixtures, (2004). doi:10.1021/IE049798B.

[173] S. Mahmud, R.A. Fraser, Flow, thermal, and entropy generation characteristics inside a porous channel with viscous dissipation, Int. J. Therm. Sci. 44 (2005) 21–32. doi:10.1016/j.ijthermalsci.2004.05.001.

[174] G. Ibáñez, A. López, J. Pantoja, J. Moreira, Combined effects of uniform heat flux boundary conditions and hydrodynamic slip on entropy generation in a microchannel, Int. J. Heat Mass Transf. 73 (2014) 201–206. doi:10.1016/j.ijheatmasstransfer.2014.02.007.

[175] G. Ibáñez, Entropy generation in MHD porous channel with hydrodynamic slip and convective boundary conditions, Int. J. Heat Mass Transf. 80 (2015) 274–280. doi:10.1016/j.ijheatmasstransfer.2014.09.025.

[176] G. Ibáñez, A. López, J. Pantoja, J. Moreira, Entropy generation analysis of a nanofluid flow in MHD porous microchannel with hydrodynamic slip and thermal radiation, Int. J. Heat Mass Transf. 100 (2016) 89–97. doi:10.1016/j.ijheatmasstransfer.2016.04.089.

[177] W.-H. Chen, T.-C. Cheng, C.-I. Hung, Modeling and simulation of microwave double absorption on methanol steam reforming for hydrogen production, Int. J. Hydrogen Energy. 36 (2011) 333–344. doi:10.1016/j.ijhydene.2010.09.009.

[178] M. Michael F, Radiative Heat Transfer, Acad. Press. (2003) 882.

[179] H.C. Brinkman, The Viscosity of Concentrated Suspensions and Solutions, J. Chem. Phys. 20 (1952) 571–571. doi:10.1063/1.1700493.

[180] K. Khanafer, K. Vafai, A critical synthesis of thermophysical characteristics of nanofluids, Int. J. Heat Mass Transf. 54 (2011) 4410–4428. doi:10.1016/j.ijheatmasstransfer.2011.04.048.

[181] K. Khanafer, K. Vafai, M. Lightstone, Buoyancy-driven heat transfer enhancement in a two-dimensional enclosure utilizing nanofluids, Int. J. Heat Mass Transf. 46 (2003) 3639–3653. doi:10.1016/S0017-9310(03)00156-X.

[182] E.L. Cussler, Diffusion: Mass Transfer in Fluid Systems - E. L. Cussler, Edward Lansing Cussler - Google Books, (n.d.).

[183] G.R. Kefayati, Simulation of double diffusive natural convection and entropy generation of power-law fluids in an inclined porous cavity with Soret and Dufour effects (Part II: Entropy generation), Int. J. Heat Mass Transf. 94 (2016) 582–624. doi:10.1016/J.IJHEATMASSTRANSFER.2015.11.043.

[184] A. Mchirgui, N. Hidouri, M. Magherbi, A. Ben Brahim, Second law analysis in double diffusive convection through an inclined porous cavity, Comput. Fluids. 96 (2014) 105–115. doi:10.1016/j.compfluid.2014.03.008.

[185] O. Deutschmann, Computational Fluid Dynamics Simulation of Catalytic Reactors, in: Handb. Heterog. Catal., Wiley-VCH Verlag GmbH & Co. KGaA, Weinheim, Germany, 2008: pp. 1811–1828. doi:10.1002/9783527610044.hetcat0097.

[186] M.E. Coltrin, R.J. Kee, F.M. Rupley, Surface CHEMKIN (Version 4. 0): A Fortran package for analyzing heterogeneous chemical kinetics at a solid-surface---gas-phase interface, Albuquerque, NM, and Livermore, CA, 1991. doi:10.2172/6128661.

[187] U. Dogwiler, P. Benz, J. Mantzaras, Two-dimensional modelling for catalytically stabilized combustion of a lean methane-air mixture with elementary homogeneous and heterogeneous chemical reactions, Combust. Flame. 116 (1999) 243–258. doi:10.1016/S0010-2180(98)00036-4.

[188] S.-X. Zhang, Y.-L. He, G. Lauriat, W.-Q. Tao, Numerical studies of simultaneously developing laminar flow and heat transfer in microtubes with thick wall and constant outside wall temperature, Int. J. Heat Mass Transf. 53 (2010) 3977–3989. doi:10.1016/j.ijheatmasstransfer.2010.05.017.

[189] A. Amiri, Analysis of dispersion effects and non-thermal equilibrium , non- Darcian , variable porosity incompressible flow through porous media, Analysis. 37 (1994).

[190] B. Alazmi, K. Vafai, Analysis of variants within the porous media transport models, J. Heat Transfer. (2000).

[191] M. Torabi, K. Zhang, G. Yang, J. Wang, P. Wu, Heat transfer and entropy generation analyses in a channel partially filled with porous media using local thermal non-equilibrium model, Energy. (2015).

[192] M. Bovand, S. Rashidi, J.A. Esfahani, Heat transfer enhancement and pressure drop penalty

in porous solar heaters: Numerical simulations, Sol. Energy. 123 (2016) 145–159. doi:10.1016/j.solener.2015.10.054.

[193] P. Forooghi, M. Abkar, M. Saffar-Avval, Steady and unsteady heat transfer in a channel partially filled with porous media under thermal non-equilibrium condition, Transp. Porous Media. (2011).

[194] X. Du, Y. Shen, L. Yang, Y. Shi, Y. Yang, Experiments on hydrogen production from methanol steam reforming in the microchannel reactor, Int. J. Hydrogen Energy. 37 (2012) 12271–12280. doi:10.1016/j.ijhydene.2012.06.027.

[195] N. Verma, D. Mewes, A. Luke, Lattice Boltzmann study of velocity, temperature, and concentration in micro-reactors, Int. J. Heat Mass Transf. 53 (2010) 3175–3185. doi:10.1016/j.ijheatmasstransfer.2010.03.009.

[196] F. Wang, J. Zhou, G. Wang, Transport characteristic study of methane steam reforming coupling methane catalytic combustion for hydrogen production, Int. J. Hydrogen Energy. 37 (2012) 13013–13021. doi:10.1016/j.ijhydene.2012.05.062.

[197] N. Meynet, A. Bentaib, V. Giovangigli, Impact of oxygen starvation on operation and potential gas-phase ignition of passive auto-catalytic recombiners, Combust. Flame. 161 (2014) 2192–2202. doi:10.1016/j.combustflame.2014.02.001.

[198] M.H. Matin, I. Pop, Forced convection heat and mass transfer flow of a nanofluid through a porous channel with a first order chemical reaction on the wall, Int. Commun. Heat Mass Transf. 46 (2013) 134–141. doi:10.1016/j.icheatmasstransfer.2013.05.001.

[199] P.S. Reddy, A.J. Chamkha, Soret and Dufour effects on MHD convective flow of Al2O3-water and TiO2-water nanofluids past a stretching sheet in porous media with heat generation/absorption, Adv. Powder Technol. 27 (2016) 1207–1218. doi:10.1016/j.apt.2016.04.005.

[200] A. Bahloul, N. Boutana, P. Vasseur, Double-diffusive and Soret-induced convection in a shallow horizontal porous layer, J. Fluid Mech. 491 (2003) 325–352. doi:10.1017/S0022112003005524.

[201] D. Ingham, I. Pop, Transport phenomena in porous media III, 2005.

[202] J.B. Mena, A.A. Ubices De Moraes, Y.R. Benito, G. Ribatski, J.A.R. Parise, Extrapolation of Al2O3-water nanofluid viscosity for temperatures and volume concentrations beyond the range of validity of existing correlations, Appl. Therm. Eng. 51 (2013) 1092–1097. doi:10.1016/j.applthermaleng.2012.11.002.

[203] M. Torabi, K. Zhang, G. Yang, J. Wang, P. Wu, Heat transfer and entropy generation analyses in a channel partially filled with porous media using local thermal non-equilibrium model, Energy. 82 (2015) 922–938. doi:10.1016/j.energy.2015.01.102.

[204] S. Sharada, P.L. Suryawanshi, R. Kumar P., S.P. Gumfekar, T.B. Narsaiah, S.H. Sonawane, Synthesis of palladium nanoparticles using continuous flow microreactor, Colloids Surfaces A Physicochem. Eng. Asp. 498 (2016) 297–304. doi:10.1016/j.colsurfa.2016.03.068.

[205] G. Hunt, N. Karimi, M. Torabi, Analytical investigation of heat transfer and classical

entropy generation in microreactors – The influences of exothermicity and asymmetry, Appl. Therm. Eng. 119 (2017) 403–424. doi:10.1016/j.applthermaleng.2017.03.057.

[206] P. Atkins, J. De Paula, Atkins' physical chemistry, 2009. doi:10.1021/ed056pA260.1.

[207] R. V. Chaudhari, P.A. Ramachandran, Influence of Mass Transfer on Zero-Order Reaction in a Catalytic Slurry Reactor, Ind. Eng. Chem. Fundam. 19 (1980) 201–206. doi:10.1021/i160074a013.

[208] D. Albani, G. Vilé, M.A. Beltran Toro, R. Kaufmann, S. Mitchell, J. Pérez-Ramírez, Structuring hybrid palladium nanoparticles in metallic monolithic reactors for continuous-flow three-phase alkyne hydrogenation, React. Chem. Eng. 1 (2016) 454–462. doi:10.1039/C6RE00114A.

[209] C.J. Ho, D.S. Chen, W.M. Yan, O. Mahian, Buoyancy-driven flow of nanofluids in a cavity considering the Ludwig-Soret effect and sedimentation: Numerical study and experimental validation, Int. J. Heat Mass Transf. 77 (2014) 684–694. doi:10.1016/j.ijheatmasstransfer.2014.05.059.

[210] L. Govone, M. Torabi, G. Hunt, N. Karimi, Non-equilibrium thermodynamic analysis of double diffusive, nanofluid forced convection in catalytic microreactors with radiation effects, Entropy. 19 (2017). doi:10.3390/e19120690.

[211] R.C. Givler, S.A. Altobelli, A determination of the effective viscosity for the Brinkman–Forchheimer flow model, J. Fluid Mech. 258 (1994) 355. doi:10.1017/S0022112094003368.

[212] G. Hunt, N. Karimi, M. Torabi, Two-dimensional analytical investigation of coupled heat and mass transfer and entropy generation in a porous, catalytic microreactor, Int. J. Heat Mass Transf. 119 (2018). doi:10.1016/j.ijheatmasstransfer.2017.11.118.

[213] J. Mantzaras, C. Appel, P. Benz, U. Dogwiler, Numerical modelling of turbulent catalytically stabilized channel flow combustion, Catal. Today. 59 (2000) 3–17. doi:10.1016/S0920-5861(00)00268-6.

[214] H.M.S. Bahaidarah, N.K. Anand, H.C. Chen, NUMERICAL STUDY OF HEAT AND MOMENTUM TRANSFER IN CHANNELS WITH WAVY WALLS, Numer. Heat Transf. Part A Appl. 47 (2005) 417–439. doi:10.1080/10407780590891218.